

NORTHWESTERN UNIVERSITY

Reimagining Solid Acid Fuel Cells: From Electrolyte Discovery to Cathode
Design

A DISSERTATION

SUBMITTED TO THE GRADUATE SCHOOL
IN PARTIAL FULFILLMENT OF THE REQUIREMENTS

For the degree

DOCTOR OF PHILOSOPHY

Field of Materials Science and Engineering

By

Louis Shen Wang

EVANSTON, ILLINOIS

June 2023

Acknowledgements

My time in graduate school has been the most intellectually fulfilling experience of my life, and I am eternally grateful to all those who have contributed to my growth at Northwestern University. As cliché as it is to say that a PhD teaches you how to think, I am astounded by how much I've learned from Sossina about how to think – as a scientist, an explorer, and a communicator – and how much I still have yet to learn. I am incredibly grateful for Sossina's balanced mentorship; she pushed me when I needed to be pushed, and yet also allowed me the freedom to follow my own curiosity and explore new directions of research. I can only hope to one day come close to attaining the level of insight and knowledge that Sossina possesses. Seldom have I left a discussion with Sossina not feeling inspired by a new perspective or in awe of the depth of her understanding and critical thinking. Additionally, throughout my PhD, Sossina has tirelessly supported me in opportunities both within and outside of research, and I cannot thank her enough for the time and effort she has invested in my development.

I have been blessed to work with fantastic coworkers in the Haile group. I am grateful for the mentorship I received from Sheel Sanghvi on the synthesis and characterization of solid acid electrolytes and from Austin Plymill and Ara Jo on the fabrication of solid acid fuel cells. Each of these mentors was incredibly generous with the time and energy they spent teaching me in lab, and I cannot thank them enough for their patience as I invariably fumbled every procedure. I am also grateful to the members of the Haile group who I've worked with or mentored, including Grace Xiong, Paul Chery, Dylan Bardgett, Trevor Worthy, Tiffany Miao, and Arthur Shih, who have deepened my understanding of science and pushed me to develop as a teacher and communicator. Additionally, I would like to thank Elise Goldfine for her generosity in helping

with x-ray experiments and Dalton Cox for invaluable discussions about fuel cells and specifically fuel cell modeling, which eventually led to the work in Chapter 5. I also had the pleasure of sharing an office Connor Carr, Jill Wenderott, and Emanuela Mastronardo, and I'm so appreciative of the fun times we enjoyed in the office.

Thank you to our collaborators at Florida State University, Professor Yan-Yan Hu and Dr. Sawankumar Patel, for their tireless NMR work. Our conclusions in characterizing solid acid electrolytes rests heavily upon the work that they conducted. I am also very grateful for the warm welcome that the folks at SAFCell, Dr. Calum Chisholm and Mandy Abbott, extended to me during my month-long internship. The work they have done for the last 20 years has been a constant source of inspiration for me during my PhD.

I must also thank the underappreciated facility managers at Northwestern who afford the students incredible opportunities and resources. There are too many to recount each one in detail so in summary I am grateful for the contributions of: Jerry Carsello, Sumit Kewalramani, Tirzah Abbott, Elizabeth King, Neil Schweitzer, Serkan Butun, Nasir Basit, Becky Sponenburg, Christos Malliakas, Charlotte Stern, and Bruce Buchholz.

Outside of the lab, I am grateful to have been able to contribute to founding a high school research program at Northwestern for underprivileged local students. I am so appreciative of the graduate students in the Materials Science department who devoted an immense amount of time and energy to take a risk in trying to start a new student led program. Thank you to Lauren Walters, Alex Kane, Dalton Cox, Sean Koyama, Alexander Evenchik, Dilara Meli, Adam Ladd, Mitchell Walker, Santiago Arauzo, Hyeonseon Choi, Broderick Lewis, David Garcia, and Dylan Bardgett. Thank you as well to the faculty members who sponsored this program and advocated

for us when there was little reason or incentive for doing so: Professors Ian McCue, Ryan Truby, and Sossina Haile. Additionally, thank you to the organizers at Colorado School of Mines who funded our program: Professor Eric Toberer and Emily Freed. I hope that the passion to improve diversity and equity in STEM and society more broadly continues to burn strongly at Northwestern.

I don't know that I would have made it through graduate school without the incredible friendship of Tyler Gish, James Male, Jennie Glerum, Elise Goldfine, Dalton Cox, Broderick Lewis, Thomas Schmitt, Travis Schmauss, Kha Phi, William Chang, Kaitlin Yang, and Stone Yan. I am boundlessly grateful for the companionship that these dear friends have offered in helping me through the isolating nature of graduate school.

I am blessed to have two supportive parents who nurtured a love for learning from a very young age and encouraged me to explore the world in all of its facets. My father was the first to encourage me to pursue scientific research, and my journey down this path started through summer high school research program that he introduced to me. I thank my parents for their constant support and interest in my work. I am blessed to have a loving brother whose considerateness and generosity is unmatched.

Lastly, I don't know how I got so lucky to have found a girlfriend as amazing as Lisa Lieu. She is the most loving, kind, and caring person I know, and I am so grateful for the life that we share. I can only hope to repay the incredible amount of support she has given me these past few years.

ABSTRACT

Reimagining Solid Acid Fuel Cells: From Electrolyte Discovery to Cathode Design

Solid acid fuel cells confer unique advantages over nearby technologies, such as polymer electrolyte membrane fuel cells (PEMFCs) or solid oxide fuel cells (SOFCs), due to the solid acid electrolyte – a solid-state, anhydrous, intermediate-temperature proton conductor. Despite these encouraging unique properties, solid acid fuel cells have performed unfavorably in comparison to the aforementioned technologies both due to constraints specific to the electrolyte as well as the electrochemical kinetics at the cathode.

In the first chapter, a review is conducted of the properties of solid acid electrolytes including the superprotonic transition and the related structures, proton transport properties, and degradation behavior. Focus is placed on cesium dihydrogen phosphate (CDP), as this solid acid compound is currently the only technologically relevant electrolyte. Additionally, the foundational methods for characterizing solid acid electrolytes – x-ray diffraction, differential scanning calorimetry and thermogravimetric analysis, and electrochemical impedance spectroscopy – are discussed.

In Chapters 2 and 3, a new approach to the modification of solid acid phases is demonstrated with substantial impact on the phase behavior and structure of the materials. By introducing off-stoichiometry in CDP, we discovered a new remarkable superprotonic phase and revealed that the superprotonic phase of CDP is highly amenable to non-stoichiometry. The new superprotonic compound $\text{Cs}_7(\text{H}_4\text{PO}_4)(\text{H}_2\text{PO}_4)_8$, or CPP features extraordinary H_4PO_4^+ cations on select Cs sites of a structure that otherwise resembles cubic superprotonic CDP. CPP was found

to be stable in dry Ar atmospheres from 90- 151 °C, but the material's conductivity is only moderate in comparison to that of CDP. In the composition space between CDP and CPP, the cubic superprotonic phase of CDP was found to accommodate cesium deficiency in the form of Cs vacancies which were charge balanced by excess protons. The non-stoichiometric cubic phase, α -CDP(ss), displayed eutectoid phase behavior, forming at 155 °C at its eutectoid composition, $x = 0.18$. The proton conductivity of the α -CDP(ss) phase was found to be relatively insensitive to composition; when coupled with the eutectoid phase behavior, this result presents the opportunity to extend the lower operating temperature limit of CDP-based devices. More generally, the non-stoichiometry demonstrated here in CDP presents a powerful new approach to the modification of solid acids.

The later half of the thesis is devoted to solid acid electrochemical devices, with a focus on fuel cells. Chapter 4 provides a review of solid acid devices (SADs) and highlights the progress made thus far in SAFCs. Additionally, the fundamental principles underlying fuel cell operation and the important electrochemical techniques for characterizing SAFCs are summarized.

In Chapter 5, the limitations of the SAFC cathode are examined through the lens of a 1-D model. Key to the modeling approach taken here was the experimental measurement of parameters characterizing the cathode, including the measurement of electrochemical kinetic parameters for the oxygen reduction reaction on Pt nanoparticle catalysts. The measurements crucially revealed that the primary factor hampering SAFC performance compared to that of PEMFCs is a low cathodic charge transfer coefficient, and that this factor more than negates the effect of thermal enhancement of the exchange current density. The 1-D model was used to

examine the internal mechanisms of the cathode and used to evaluate the impacts of various advances in materials properties and changes in cathode microstructure. In addition to the critical importance of the charge transfer coefficient, it was found that significant improvements to cell performance could be achieved by discovering a solid acid electrolyte with reduced humidification requirements.

Table of Contents

Chapter 1: Introduction to Solid Acids Electrolytes	16
1.1 Advantages of Solid Acid Electrolytes	16
1.2 Superprotonic Solid Acid Electrolytes: Structure and Chemistry	17
1.3 Properties of CsH ₂ PO ₄ (CDP).....	19
1.4 CDP composite electrolytes	24
1.5 Characterization Techniques for Solid Acid Electrolytes	25
1.5.1 X-ray Diffraction	25
1.5.2 Differential Scanning Calorimetry and Thermogravimetric Analysis	31
1.5.3 Electrochemical Impedance Spectroscopy	34
Chapter 2: Structure and properties of Cs₇(H₄PO₄)(H₂PO₄)₈: A new superprotonic solid acid featuring the unusual polycation (H₄PO₄)⁺	42
2.1 Introduction.....	42
2.2 Crystal Synthesis and Structure Determination	43
2.2.1 Methods	43
2.2.2 Results: Structure of Cs ₇ (H ₄ PO ₄)(H ₂ PO ₄) ₈	46
2.3 Phase Formation and Stability Range.....	52
2.3.1 Methods	52
2.3.2 Results: Thermodynamics of CPP Formation.....	54
2.4 Conductivity	58
2.4.1 Methods	58
2.4.2 Results.....	59
2.5 Discussion of CPP Phase Formation	62
2.6 Conclusion and Summary	63
Supplemental Information	65
Chapter 3: Phase Behavior and Superprotonic Conductivity in the System (1-x)CsH₂PO₄ – xH₃PO₄: Discovery of Off-stoichiometric α-[Cs_{1-x}H_x]H₂PO₄	83
3.1 Introduction.....	83
3.2 Methods.....	85
3.2.1 Thermal Analysis.....	86
3.2.2 X-ray Diffraction	86

	10
3.2.3	NMR..... 87
3.2.4	Impedance Spectroscopy..... 88
3.3	Results and Discussion..... 88
3.3.1	Direct Characterization of Phase Behavior..... 89
3.3.2	Solvus Line Determination 105
3.3.3	Structure and Chemistry of α -CDP(ss) 108
3.3.4	Conductivity 110
3.4	Summary and Conclusions 113
	Supplemental Information 115
	Chapter 4: Review of Solid Acid Devices..... 136
4.1	Basic Principles of Fuel Cells and Electrochemical Devices 136
4.1.1	Fuel Cell Efficiency..... 139
4.1.2	Polarization Losses 141
4.1.2.1	Experimental OCV and Leak currents 141
4.1.2.2	Ohmic Losses..... 144
4.1.2.3	Charge Transfer Kinetics losses 144
4.1.3	Regions of the Polarization Curve 147
4.2	Solid Acid Fuel Cells..... 148
4.2.1	SAFC Cathodes..... 151
4.2.2	Anode 154
4.3	Alternative Fuels 156
4.4	Prospective Electrolytic Applications 159
4.5	Electrochemical Characterization of SAFCs..... 163
4.5.1	Open Circuit Voltage..... 163
4.5.2	Potential Sweep Methods 164
4.5.3	Impedance Spectroscopy..... 166
4.5.4	Chronoamperometry/Chronopotentiometry 169
	Chapter 5: Understanding SAFC Cathode Limitations through Experimentally Informed 1-D Modeling 171
5.1	Background 171
5.2	Methods..... 173

5.2.1	Description of 1-D Cathode Model.....	173
5.2.1.1	Strategies for Interpreting Model Results.....	181
5.2.2	Measuring and Calculating Model Parameters.....	182
5.2.2.1	Measuring ORR kinetics of Pt Nanoparticles.....	184
5.2.2.2	Microstructural Properties.....	187
5.2.2.3	Charge Transport.....	188
5.2.2.4	Gas Diffusion.....	189
5.2.3	Experimental Measurements of a SAFC.....	191
5.3	ORR Kinetics of Pt Nanoparticles: Results and Discussion.....	192
5.4	Modelling SAFC behavior.....	201
5.4.1	Validation of the Model.....	201
5.4.2	Case Studies of SAFC Cathode Performance.....	206
5.4.2.1	Cathodic Charge Transfer Coefficient α	206
5.4.2.2	Proton Conductivity of the Electrolyte.....	209
5.4.2.3	Required Humidification.....	210
5.4.2.4	Operating Temperature.....	213
5.4.2.5	Exchange Current Density and Active Pt Surface Area.....	215
5.4.2.6	Cathode Thickness.....	217
5.4.2.7	Cell Pressure.....	218
5.5	Conclusions.....	219
	Supplemental Information.....	221
	Appendix A: Transmission Line Modeling of Impedance from SAFC Cathodes.....	232
	Appendix B: Stabilizing Pd catalysts with Oxide Barrier Layers.....	241
	B.1 Background.....	241
	B.2 Stabilizing Pd.....	242
	B.3 Flat Cathodes.....	247
	B.4 Porous Cathodes.....	256

List of Figures:

Figure 1.1. Advantages of solid acid electrolytes.	17
Figure 1.2. Structure, Transport, and Stability properties of CsH ₂ PO ₄	20
Figure 1.3. Example Impedance Spectra.	36
Figure 1.4. Impedance Spectra of Superprotonic Solid Acid Electrolytes.....	39
Figure 2.1. Crystal structure of CPP or Cs ₇ (H ₄ PO ₄)(H ₂ PO ₄) ₈	47
Figure 2.2. High temperature ³¹ P NMR spectra of CPP.....	51
Figure 2.3. Variable-temperature ¹ H MAS NMR of CPP.....	51
Figure 2.4. High temperature powder x-ray diffraction patterns of CPP.....	55
Figure 2.5. Differential scanning calorimetry and thermogravimetric profiles collected on CPP.....	55
Figure 2.6. Dehydration Behavior of CPP captured with variable humidity DSC/TGA.....	56
Figure 2.7. Phase diagram for CPP or Cs ₇ (H ₄ PO ₄)(H ₂ PO ₄) ₈	58
Figure 2.8. Conductivity of CPP.....	60
Figure 2.S-1. ³¹ P NMR spectra of CPP at 120 oC with and without 1H-decoupling.....	71
Figure 2.S-2. Why CPP? Comparison of CPP structure vs hypothetical 2 × 2 × 2 supercell.....	72
Figure 2.S-3. Lattice parameter of Cs ₇ (H ₄ PO ₄)(H ₂ PO ₄) ₈ at various temperatures.....	75
Figure 2.S-4. Averaged Superprotonic reaction DSC peaks to obtain thermodynamic values.....	76
Figure 2.S-5. Metastability of CPP as shown in DSC signal from a repeated thermal cycling.....	78
Figure 2.S-6. EIS spectra for the low high temperature responses of Cs ₇ (H ₄ PO ₄)(H ₂ PO ₄) ₈	79
Figure 2.S-7. TGA/DSC measurements on CsH ₅ (PO ₄) ₂ sample.....	80
Figure 2.S-8. Schematic of proposed formation (a) Gibbs free energies, ΔG _f , (b) enthalpies, ΔH _f , and (c) entropies, ΔS _f , for the CsH ₂ PO ₄ – CsH ₅ (PO ₄) ₂ phase space at 100 °C.	81
Figure 3.1. Phase diagram of the (1-x)CsH ₂ PO ₄ – xH ₃ PO ₄ system in the Cs-rich region.....	89
Figure 3.2. Phase transformation behavior of CPP to α- CDP(ss). (a) TGA/DSC profiles; (b) high temperature XRD patterns.	92
Figure 3.3 Phase transformation behavior of (1-x)CsH ₂ PO ₄ – xH ₃ PO ₄ at x = 0.18, the eutectoid composition: (a & c) high temperature XRD patterns and lattice constants; (b)TGA/DSC profiles.....	94
Figure 3.4. High temperature ³¹ P NMR measurements of (1-x)CsH ₂ PO ₄ – xH ₃ PO ₄ at x = 0.18, the eutectoid composition: (a) spectra; (b) chemical shifts; (c) and T1 relaxation times.	97
Figure 3.5. High temperature ¹ H NMR measurements of (1-x)CsH ₂ PO ₄ – xH ₃ PO ₄ at x = 0.18, the eutectoid composition: (a) spectra; and (b) chemical shifts.....	98
Figure 3.6. Phase transformation behavior of (1-x)CsH ₂ PO ₄ – xH ₃ PO ₄ at x = 0.07: (a) TGA/DSC profiles; (b) XRD patterns; and (c) lattice constants and weight fraction.....	101
Figure 3.7. Lattice parameters of the α-CDP(ss) phase of various sample compositions, x: (a) thermal evolution of the lattice parameter; (b) lattice parameters of α-CDP(ss) as a function of composition extrapolated to 170 °C.....	104
Figure 3.8. Determination of the solvus boundary: temperature dependence of the cell parameter of α-CDP(ss) at the solvus boundary and inferred solvus compositions of α-CDP(ss).	107
Figure 3.9. Schematic of the α-CDP(ss) structure.	109
Figure 3.10. Conductivity of materials in the (1-x)CsH ₂ PO ₄ – xH ₃ PO ₄ system.....	111

Figure 4.1. Schematic of the charge transport mechanisms in a standard hydrogen SAFC.....	137
Figure 4.2. Polarization curve of a SAFC with delineated voltage loss contributions.	139
Figure 4.3. Schematic of the balance of leak and fuel cell currents at the cathode.	143
Figure 4.4. Marcus theory description of the kinetics of a single electron transfer reaction	147
Figure 4.5. Cross sectional SEM image of a SAFC.....	149
Figure 4.6. Schematics representing solid acid devices. (a) methanol fuel cell. (b) ammonia fuel cell. (c) steam electrolysis cell. (d) CO ₂ reduction electrolysis cell. (e) ammonia synthesis electrolysis cell	156
Figure 4.7. Transmission line model for a porous electrode with a proton conducting electrolyte.	169
Figure 5.1. Example solution to the model boundary value problem. Profiles for ORR reaction rate, CDP and Pt phase potentials, electron and proton currents, and oxygen and steam concentrations.....	182
Figure 5.2. Tafel curves collected from MEA A.	192
Figure 5.3. Data analysis used to extract Tafel parameters from experimental polarization curves.....	195
Figure 5.4. Plot of the local reaction rate functions for SAFCs vs PEMFCs.....	200
Figure 5.5. Comparison of the modeled polarization curves using Tafel parameters from MEAs A, B, and C vs experimental fuel cell	201
Figure 5.6. Internal mechanisms derived from 1-D model at two potentials.....	205
Figure 5.7. Case study: cathodic charge transfer coefficient..	207
Figure 5.8. Case study: proton conductivity..	209
Figure 5.9. Case study: humidity..	212
Figure 5.10. Case study: temperature.....	214
Figure 5.11. Case study: exchange current density and active area density.	216
Figure 5.12. Case study: cathode thickness.	218
Figure 5.13. Case study: Pressure.	219
Figure 5S.-1. Procedure for the fabrication of flat cathode MEAs.....	221
Figure 5S.-2. Flat Cathode MEA assembly	223
Figure 5S.-3. Tafel fitting data for MEA A.	224
Figure 5S.-4. Tafel Fitting for MEA B.	225
Figure 5S.-5. Tafel Fitting for MEA C.	226
Figure 5S.-6. Measurements of density of porous SAFC cathodes	227
Figure 5S.-7. Van der Pauw measurement of electronic conductivity in porous SAFC cathode.	228
Figure A.1. EIS spectra collected from the SAFC studied in Chapter 5 at various cell potentials.....	232
Figure A.2. Summary of the transmission line impedance model.	233
Figure A.3. Impedance spectra fit using a transmission line model (TLM).	235
Figure A.4. Modeled polarization curves using conductivity values determined from the TLM fitting ..	240
Figure B.1. SEM images after each stage of the process to create catalyst oxide CDP particles.....	242
Figure B.2. ALD pulse sequences Ta ₂ O ₅ and TiO ₂ deposition.....	244
Figure B.3. ³¹ P NMR spectra of annealed Pd CDP samples.	246
Figure B.4. ³¹ P NMR spectra of Pd TiO ₂ CDP and Pd Ta ₂ O ₅ CDP after annealing.	247
Figure B.5. Flat cathode cells with Pt catalyst films deposited either by (a) sputtering or (b) MOCVD.	250
Figure B.6. Performance of Pd _{0.84} Pt _{0.16} TiO ₂ flat cathodes compared with that of a standard Pt flat cathode.....	253
Figure B.7. EIS results from cells with Pd _{0.84} Pt _{0.16} TiO ₂ flat cathodes.....	255
Figure B.8. Performance of a Pd _{0.84} Pt _{0.16} TiO ₂ cathode where the catalyst was deposited by MOCVD.	256

Figure B.9. Performance of a porous cathode with $\text{Pd}_{0.84}\text{Pt}_{0.16}$ catalyst.....	258
Figure B.10. Cell geometry employed in the measurement of catalyst oxide CDP cathodes.	259
Figure B.11. Performance of porous cathodes composed of Pt TiO_2 CDP particles.....	261

List of Tables:

Table 1.1. Basic EIS circuit elements.	38
Table 2.1. Structure of Cs ₇ (H ₄ PO ₄)(H ₂ PO ₄) ₈ with atomic positions and site occupancies.	48
Table 2.2. Thermodynamic quantities for the superprotonic reaction forming CPP	55
Table 2.S-1. Details from the single crystal diffraction and structure solution and refinement.	65
Table 2.S 2. Structure of Cs ₇ (H ₄ PO ₄)(H ₂ PO ₄) ₈ with atomic positions, site occupancy, and anisotropic thermal displacement parameters	67
Table 2.S-3. P-O bond length and O-P-O bond angles for phosphates in CPP.	68
Table 2.S-4. ³¹ P NMR details for the resonances in each scan temperature.	70
Table 2.S-5. Flow rates for various humidified atmospheres in TGA/DSC measurements.	74
Table 5.1. Coupled differential equations and boundary conditions constituting the boundary value problem that describes the cathode.	180
Table 5.2. Summary of the model parameters, the values determined, and the method of measurement or calculation.	183
Table 5.3. Binary diffusion coefficients.	190
Table 5.4. Knudsen diffusion coefficients.	190
Table 5.5. Summary of the Tafel parameters from MEAs A, B, and C.	196
Table 5.6. Comparison of the Tafel Parameters from SAFCs vs PEMFCs.	199
Table 5S.-1. Calculation methods for gas diffusion coefficients.	230
Table A.1. Fit TLM parameters from the impedance spectra of a porous cathode.	239
Table B.1. Transmission line model fitting results for EIS spectra from Pt TiO ₂ CDP cathodes and standard Pt cathodes.	263

Chapter 1: Introduction to Solid Acids Electrolytes

1.1 Advantages of Solid Acid Electrolytes

Solid acid electrolytes are a unique class of ionic conductors that compare favorably with commercial polymer electrolytes in several key attributes. Solid acid electrolytes are solid-state, anhydrous, proton-conductors at intermediate temperatures (200 – 300 °C). Each one of these attributes presents technological advantages (Figure 1.1). A solid-state, anhydrous electrolyte provides effective separation of the gas atmospheres across the device, with no possibility for the dissolution and crossover of water-soluble species. Furthermore, the transport of protons without relying on a carrier water molecule allows solid acid devices to operate without delicate water management across the cell, as is required in devices based on hydrated ionomers. Proton conducting electrolytes are advantageous both in fuel cells and electrolyzers; in the former, the reaction products are produced at the cathode and do not dilute the fuel stream, whereas in the latter the products are generated at the fuel electrode and do not need separation from the reactants. The most distinctive advantage of solid acid devices is operation at intermediate temperatures at which rapid reaction kinetics and tolerance of gas stream impurities are achieved while still allowing for facile thermal cyclability and relaxed material constraints of auxiliary components.

This chapter will review the structure, chemistry, transport properties, and idiosyncrasies of solid acid electrolytes, with a focus on the most prominent solid acid thus far, CsH_2PO_4 . A review of the solid acid composite electrolytes is then conducted. Finally, an overview of the methods for characterizing solid acids is presented.

Advantages of Solid Acid Electrolytes

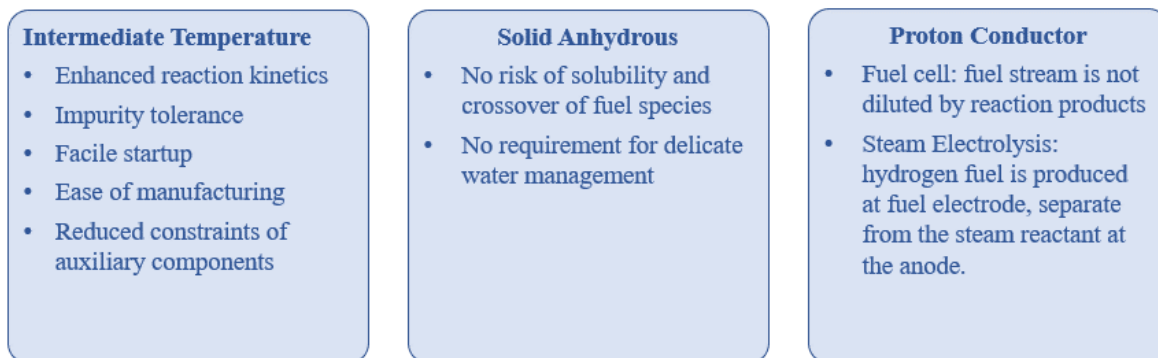


Figure 1.1. Advantages of solid acid electrolytes.

1.2 Superprotonic Solid Acid Electrolytes: Structure and Chemistry

While the term solid acid can be used to describe a broad range of acidic compounds, it is used here to describe ionic compounds composed of metal cations and protonated oxyanions, where the metal cations are typically alkali metals and the oxyanions are typically PO_4 , SO_4 , and SeO_4 groups. At room temperature, solid acids commonly have low proton conductivities and crystallize in structures with fixed hydrogen-bonding networks. However, certain solid acids exhibit a unique phase transition upon heating, called the superprotonic transition, in which the material transforms into a superprotonic phase with oxyanion orientational disorder. The rapid rotation of the oxyanion in this superprotonic phase allows for long range proton transport through the Grotthuss mechanism and allows these compounds to achieve liquid-like conductivities ($10^{-2} \text{ S cm}^{-1}$). Superprotonic phases have been found to fall into three structure types: tetragonal ($I\frac{4_1}{a}md$), cubic ($Pm\bar{3}m$), and trigonal ($R\bar{3}m$). Compounds which form the

tetragonal $I\frac{4_1}{a}md$ phases are typically of the composition $MHAO_4$, including $CsHSO_4$,¹ $RbHSO_4$,² $CsHSeO_4$, and $RbHSeO_4$. Compounds with trigonal $R\bar{3}m$ superprotonic phases are typically of the composition $M_3H(AO_4)_2$, including $Cs_3H(SeO_4)_2$, $Rb_3H(SeO_4)_2$, and $K_3H(SeO_4)_2$.³ Finally, compounds which form cubic $Pm\bar{3}m$ phases include CsH_2PO_4 , RbH_2PO_4 ,^{4,5} CsH_2AsO_4 , $CsH(PO_3H)$,⁶ and $Cs_2(HSO_4)(H_2PO_4)$.⁷ While an extensive number of superprotonic compounds exist, nearly all are not suitable for application in fuel cells due to the decomposition of SO_4 and SeO_4 groups in reducing H_2 atmospheres, forming H_2S and H_2Se respectively.⁸ In fact, of the compounds which exhibit the requisite chemical stability, only two feature an accessible superprotonic phase – CsH_2PO_4 , and $Cs_7(H_4PO_4)(H_2PO_4)_8$ or CPP.⁹ CPP was only recently discovered by the authors and its conductivity is an order-of-magnitude lower than that of CDP. Thus, the development of solid acid devices has almost exclusively relied on CDP.

The thermodynamics of the superprotonic transition of course adhere to the equilibrium thermodynamics of phase transitions, namely that the change in Gibbs free energy at the phase transition temperature is zero. Rearranging the enthalpic and entropic terms in the Gibbs free energy expression then produces the equation: $T_{sp} = \Delta H / \Delta S$ which dictates the temperature at which the superprotonic transition occurs. While the enthalpy of the transition is a difficult term to predict or control, the change in entropy, ΔS , remarkably follows a simple framework. The change in entropy of a superprotonic phase transition can be largely predicted by the change in configurational entropy arising from the highly disordered superprotonic state. The configurational entropy is calculated by the Boltzmann equation for entropy, $S = k_B \ln(\Omega_{config})$ where Ω_{config} is the number of configurations for a state or phase. The low

temperature solid acid phase is characterized by limited disorder and often the configurational entropy can be calculated by just considering the presence or absence of a double minima in the proton potential. In contrast, the superprotonic phase has an abundance of configurational entropy owing to the numerous permutations of oxyanion orientations and proton positions. The number of configurations of the superprotonic phase was shown to follow Pauling's ice rules for entropy:

$$\Omega_{config} = (\#proton\ configurations) * (probability\ of\ open\ proton\ site)^{\#protons} \\ * (\#oxyanion\ orientations)$$

Predictions of the superprotonic transition entropy made from the change in configurational entropy were shown to be remarkably accurate across the entire cesium hydrogen sulfate-phosphate system.¹⁰⁻¹²

A large body of literature has been established examining the impact of chemistry on structure, transition temperature, stability, and proton transport, and I will not attempt to provide a comprehensive review of solid acid chemistry here. However, it should be noted that significant technological advances in solid acid device performance might be realized with the discovery of a superprotonic solid acid phase with any of the following attributes in addition to the requisite chemical stability: proton conductivity significantly greater than 10^{-2} S cm⁻¹, large thermal stability window, absence of a requirement for humidification.

1.3 Properties of CsH₂PO₄ (CDP)

Below its superprotonic transition, CDP exists as an ionically-insulating monoclinic phase (*P2₁/m*). Upon undergoing the superprotonic transition at 228 °C, CDP transforms into a

cubic ($Pm\bar{3}m$) structure with Cs cations distributed a simple cubic lattice and orientationally disordered phosphate groups at the center of the unit cells. The superprotonic transition in CDP results in a three order-of-magnitude increase in proton conductivity, with the cubic phase exhibiting conductivity values greater than 2×10^{-2} S/cm. As previously stated, proton transport occurs in CDP by the Grotthuss mechanism – a coupled sequence of inter-phosphate proton hopping and phosphate group reorientation. Molecular dynamics simulations have suggested that phosphate group reorientation is rate limiting, with time constants on the order of tens of ps whereas roughly ten protons jumps occur every ps.¹³⁻¹⁵ The cubic superprotonic structure also implies free rotation of the phosphate group, as opposed to rotation around an axis, and thus isotropic proton diffusivity.

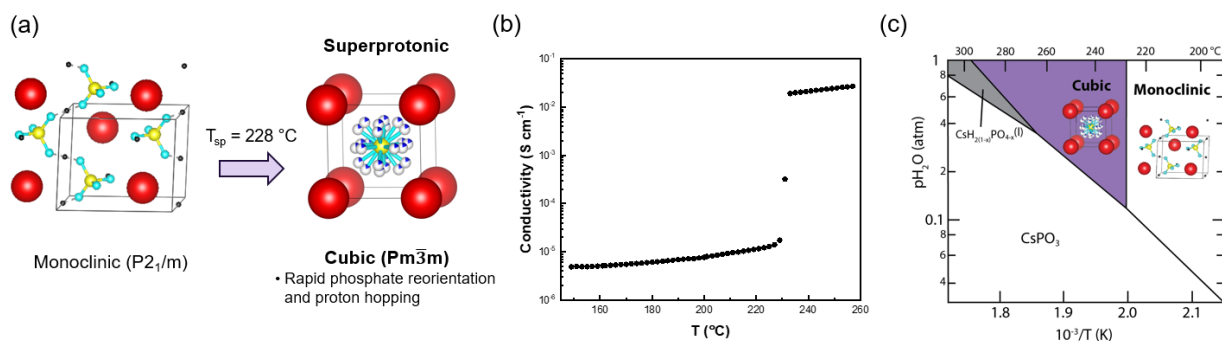


Figure 1.2. (a) Structures of the low temperature monoclinic and superprotonic cubic phase of CDP. (b) Thermal conductivity trend of CDP where the increase in conductivity at 230 °C reflects the superprotonic transition. (c) $\text{pH}_2\text{O} - T$ phase diagram of CDP.¹⁶

While proton transport in CDP is quite favorable, the material exhibits some unusual characteristics which both hinder device performance and can impede entry into this space. Chief among these is the tendency for CDP to dehydrate into CsPO_3 at temperatures close to its superprotonic transition. CsPO_3 is not protonically conductive, and thus dehydration must be

avoided to maintain device operation. While stabilization of the superprotonic phase can be achieved by active humidification to increase the dehydration temperature, significant steam partial pressures ($p_{\text{H}_2\text{O}} > 0.2 \text{ atm}$) are required to create a comfortable operating temperature window. The high steam partial pressures hinder device performance on several fronts: (1) the open circuit voltage of the device is reduced; (2) the concentration of reactant gas species is diluted; and (3) an energy penalty is incurred in the vaporization of water. Providing the high levels of humidification required to stabilize the superprotonic phase of CDP can be a source of consternation for those trying to enter the field and so here we describe a simple setup to achieve this. In this setup, the gas stream is humidified by passing through a water bubbler, with temperature control independent of the CDP-containing sample chamber. The gas lines connecting this humidifying bubbler to the sample chamber as well as the exhaust lines should be wrapped in a resistive heater rope and kept above $100 \text{ }^\circ\text{C}$ so as to prevent condensation. Finally, the exhaust gas should be passed into a room temperature bubbler for controlled condensation. The components of this setup are relatively inexpensive, and controlling humidity in this way is very straightforward – the gas stream picks up the vapor pressure of water at the humidifying bubbler temperature, so long as the bubbler temperature is not too high or the gas flow rate too fast. This approach is amenable for simple modification of existing fuel cell measurement stations as well as integration into many in-situ characterization techniques such as x-ray diffraction, Raman spectroscopy, differential scanning calorimetry, thermogravimetric analysis, etc.

However, the introduction of humidification also needs to be prudently managed, as CDP is hygroscopic and water soluble. It is recommended that active humidification only be

introduced above 130 °C, and that below this temperature, active dry gas flow is maintained to flush out residual water content. In the most extreme cases, exposure to high levels of humidification below 130 °C, can cause deliquescence, the dissolution of the water-soluble compound due to condensation. Even ambient atmospheric humidity can be problematic. Exposure to particularly humid ambient conditions can cause the material to adsorb significant amounts of water, resulting in particle agglomeration and coarsening. This issue is felt both in the fabrication of high performance electrodes, where maintaining high active surface area is crucial, as well as in the densification of electrolyte samples, where water vapor trapped in internal voids can produce protrusions in the electrolyte when heated. It is thus recommended that CDP be stored in a desiccator or glovebox when not being handled.

The mechanical properties of the CDP present additional challenges. While the low temperature monoclinic phase of CDP is brittle, the superprotonic cubic phase is highly plastic and therefore susceptible to deformation. The low failure strength of the cubic phase prompts the fabrication of electrolyte layers around 50 μm thick to ensure reproducible stable gas atmosphere separation. This restriction places a lower bound on the electrolyte ohmic resistance of $\sim 0.2 \Omega \text{ cm}^2$. The superprotonic phase transition is also accompanied by a $\sim 4\%$ volume expansion. While this expansion helps to ensure effective sealing across the device on heating, the reverse transition on cooling produces microcracks in the electrolyte that result in gas crossover. Fortunately, the cracks are “healed” upon reheating through the superprotonic transition, and stability over repeated cycling has been demonstrated. Nevertheless, it is strongly recommended that hydrogen and air, or any combination of fuel and oxidant, only be supplied once the cell has reached temperatures above the superprotonic transition.

Chemical doping of the cation site in CDP with Rb, K, and to a lesser extent, Ba, and NH_4 have been explored.¹⁷⁻²⁰ Individual doping of Rb, K, and Ba each resulted in reduced thermal stability of the superprotonic phase against dehydration. Experiments I conducted showed that the NH_4^+ cation decomposes to evolve NH_3 at elevated temperatures, producing a cation deficient CDP sample of composition $(1-x)\text{CsH}_2\text{PO}_4 - x\text{H}_3\text{PO}_4$. This off-stoichiometric CDP phase space was recently shown to feature several unexpected behaviors. Firstly, a new superprotonic line compound was discovered of composition $\text{Cs}_7(\text{H}_4\text{PO}_4)(\text{H}_2\text{PO}_4)_8$, termed CPP, which will be the focus of Chapter 2. CPP exhibits no ordered low temperature phase, but rather forms upon the solid state reaction of CDP and $\text{CsH}_5(\text{PO}_4)_2$ at 90 °C and is stable up to 150 °C without active humidification.⁹ The structure of CPP is remarkable in that it largely resembles that of cubic CDP but features highly unusual H_4PO_4^+ cations on select Cs sites. However the proton conductivity of the material is only $\sim 10^{-3} \text{ S cm}^{-1}$, an order of magnitude lower than those of CDP, and thus no attempts have yet been made to incorporate the material in a practical device. It should also be noted that the temperature range in which CPP is stable is too low to offer significant benefits over PEM and phosphoric acid devices. The cubic superprotonic phase of CDP was also revealed to be able to accommodate high amounts of non-stoichiometry, $[\text{Cs}_{1-x}\text{H}_x]\text{H}_2\text{PO}_4$, displaying eutectoid phase behavior, which will be the focus of Chapter 3.²¹ The eutectoid phase behavior allows samples to exhibit elevated conductivities as early as 155 °C, with increases in temperature resulting in a gradual increase in the proton conductivity up to $10^{-2} \text{ S cm}^{-1}$ above 230 °C.²¹ The decomposition behavior of non-stoichiometric CDP remains to be clearly defined. While application of non-stoichiometric CDP in devices has not been seriously investigated, the materials may have inadvertently been studied in several instances. For

example, composites of SiP_2O_7 and CDP have been studied by Kikuchi et al^{22,23}, and the reaction of the two compounds at elevated temperatures produced $\text{CsH}_5(\text{PO}_4)_2$, which likely reacted with CDP to form the non-stoichiometric cubic phase of CDP. The conductivity results shown in those studies are consistent with this hypothesis, although the authors made no suggestion of this behavior.

1.4 CDP composite electrolytes

Composites of CDP have been extensively studied as a means of improving the superprotonic phase stability, mechanical properties, or low temperature conductivity of the electrolyte. The addition of non-conductive heterogeneous dopants in all reported cases thus far has resulted in reduced proton conductivities in the superprotonic temperature range as expected from the dilution of the conductive phase. Nevertheless, the improvement of other properties may justify the reduction in proton transport. A variety of polymer composites with CDP have been explored with the aim of improving the mechanical stability.²⁴⁻³² While addition of polymers has generally shown to improve the failure stress of composites at room temperature, the behavior at superprotonic temperatures requires elucidation, most critically for composites of polymers that exist as melts at superprotonic temperatures, ie. PVDF. Nevertheless, improved mechanical robustness at low temperatures has opened new avenues for fabrication of the electrolyte layer, such as tape casting. Using this approach, Qing et al. and Ponomareva et al. have demonstrated remarkably flexible freestanding electrolyte films of $\sim 100 \mu\text{m}$ thickness.^{25,31} CDP composites with oxides, such as SiO_2 , ZrO_2 ,³³ and Al_2O_3 ,^{20,34,35} have also been highly investigated.^{20,22,23,33-37} The addition of SiO_2 has been shown to improve conductivities at

temperatures below the superprotonic transition, while conversely reducing the conductivity in the superprotonic state.³⁶⁻³⁸ Otomo et al have suggested that the elevated conductivities at low temperatures arise from the oxide-CDP interface where interfacial defects in CDP create a more disordered local state.³⁷ However, this explanation has not been experimentally substantiated despite frequent reference in studies of CDP composites. Several other studies have investigated additives which feature sulfates, phosphates or pyrophosphates, such as SiP_2O_7 ,^{22,23,39-41} SnP_2O_7 ,⁴² or SiO_2 modified with sulfate/phosphate surface species.³⁶ These studies reported significantly elevated conductivities at temperatures below the superprotonic transition, but as previously stated, these results are actually due to chemical reaction of the sulfate and phosphate groups with CDP. Some studies have claimed that the addition of oxides has improved the stability of CDP against dehydration; I find these claims to be dubious and unsubstantiated.³³

1.5 Characterization Techniques for Solid Acid Electrolytes

The investigation of solid acid electrolytes relies heavily on three foundational techniques: x-ray diffraction, differential scanning calorimetry and thermogravimetric analysis, and electrochemical impedance spectroscopy. A brief introduction to the principles of each technique is presented below along with helpful insights into the application of these techniques in the characterization of solid acids.

1.5.1 X-ray Diffraction

X-ray diffraction (XRD) is an essential tool in the structural characterization and phase diagram mapping of solid acid systems. XRD can offer a wealth of structural and microstructural information about a sample including space group, lattice parameters, atomic positions, site

occupancy, composition of phases, phase fractions, crystallite size, and strain. XRD can be conducted both on powder and single crystal solid acid samples, where the former is recommended for refinement or identification of known phases whereas the latter is indispensable for the structure solution of new phases. The investigation of the high temperature superprotonic phase behavior in solid acids relies primarily on humidified high temperature XRD.

Powder XRD is most often conducted on a laboratory diffractometer in the θ - 2θ geometry, where the arms of the x-ray source and detector are moved symmetrically in concert on a fixed vertical plane. The angle of either the source or the detector from the plane of the sample is called θ . Diffraction patterns are commonly presented by plotting the intensities of the collected x-rays as a function of 2θ . The relevant signals interpreted from a diffraction pattern can be roughly described as the position, intensity, and shape of the peaks.

The peaks in the diffraction pattern are formed by the constructive interference of scattered x-rays from the periodic array of atoms in the crystal lattice. Constructive interference occurs when the scattering length difference between two atoms is a multiple of the x-ray wavelength such that the scattered x-rays aligned crest-to-crest or perfectly in phase. The conditions under which diffraction will occur are dependent on the vectors connecting scattering atoms, the vectors of the incident x-rays and detector, and the wavelength of the x-rays, λ . These latter two are often combined and expressed as the scattering vector Q , where Q is the difference between the incident and measurement vectors divided by the wavelength of the x-ray, ie. $Q = \frac{S_i - S_o}{\lambda}$. Plotting the diffraction pattern in terms of the scattering vector Q rather than 2θ allows the result to be generalized across different x-ray sources and measurement geometries. In a θ - 2θ

measurement, the diffraction condition can be expressed by the flawed but simple Bragg's "law": $n\lambda = 2d\sin(\theta)$ where d is the interplanar spacing and diffraction occurs when n can be satisfied by an integer value. Bragg's law is an insufficient but necessary condition for diffraction in the θ - 2θ geometry, as while Bragg's law can frequently predict the position of peaks in a θ - 2θ measurement, it fails to describe the intensity the peaks. This flaw is most glaring in the case of systematic absences where Bragg's law fails to note that the intensity of the peak is zero.

In contrast to the simple reflected x-ray behavior suggested by Bragg's law, scattering of x-rays from excited electrons occurs in all directions. Therefore the diffraction condition is not limited to only occur on the plane of the θ - 2θ measurement, and because of the omnidirectional scattering it is possible to collect 2D diffraction patterns. Additionally, scattering is produced from every illuminated atom, not only those that lie on the diffracting plane, and thus the measured intensity of every reflection is influenced by every atomic position in the crystal structure. The peak positions of a crystalline phase are determined only by the space group and lattice constants of the phase, and thus it is possible to determine these properties without knowledge of the peak intensities or the chemistry of the material.

The relative intensities of peaks can reveal information about the chemical composition of a phase. The scattering strength of an atom is called its atomic scattering factor and roughly scales with atomic number. In practice, the scattering factor of each atom has been experimentally measured as a function of scattering vector. The relative scattering strength of different atoms is used to calculate the relative intensities of peaks. It is therefore possible to refine occupancy of sites or chemical composition from the relative peak intensities. However, in order to do so accurately with powder diffraction data, the sample should exhibit a good

statistical representation of the orientations of the crystal; in other words preferential orientation of the crystallites must be kept to a minimum. This is because the relative intensities of the measured peaks are influenced not only by the inherent intensity of the reflections but also by the relative frequency that the reflections are represented in the sampled collection of grain orientations. There are several approaches to overcoming preferential orientation effects in order to achieve a statistical sampling of the reflections. Firstly, the sample should be well ground to reduce the particle size to about a micron. This ensures that a large number of crystallites are sampled, increasing the probability that good statistics are achieved without running into peak broadening from size effects. Secondly, the sample should be continuously rotated during the measurement if possible. Transmission XRD measurements with sample rotation are also notably much less prone to preferential orientation effects, but unfortunately such measurements are difficult to do with solid acids due to the heavy alkali metal cations. Preferential orientation effects are sometimes unavoidable given the particle shape, and in such cases the effect should be accounted for in the refinement of the data. Additionally, because the measured intensities reflect the representation of reflections, it is possible to refine the phase fractions of different phases from the relative intensities of the peaks of each phase, if preferential orientation effects are minimal or well accounted for.

The shape of the peaks is an indicator of the harshness of the diffraction condition. In theory, the diffraction condition for an infinite perfect crystal should be exactly defined such that the peak is a delta function. In practice however, the minimum observed peak width is set by the characteristic instrument broadening. Peak broader than the instrument broadening are indicative of a relaxation in the diffraction condition such that scattering at angles slightly off of the ideal

diffraction condition are not eliminated by destructive interference. This effect can occur due to small crystallite size or strain within the crystal. The diffraction condition is made harsher by large crystal lattices because scattering from a large number of planes reduces the tolerated phase shift difference between scattered x-rays before total destructive interference is observed. The crystallite size can be calculated from the peak broadening by the Scherrer equation:

$$D = \frac{K\lambda}{\beta \cos\theta}$$

Where D is the crystallite diameter, K is a crystallite shape factor often taken to be 1, λ is the wavelength of the x-ray, β is the observed full width half max of the peak, and θ is the measurement angle. Strain also results in peak broadening because the lattice is stretched or compressed, breaking the periodicity required for the diffraction condition.

High temperature XRD measurements are essential in identifying the high temperature phase behavior in solid acids – phase transition temperatures, superprotonic structures, structural and chemical evolution, etc. High temperature measurements are conducted at specific temperature steps and thus often provide only crude temperature resolution. Nevertheless, the measurements can provide a rough estimate of the temperature of phase transitions. Phase boundary mapping in systems such as eutectoids is a crucial yet challenging task, and there are several approaches to tackling the issue. The first and most crude approach is to measure samples of various compositions and track the temperatures at which phases appear or disappear.

Achieving good resolution in either composition or temperature with this approach is difficult as this requires a large number of sample compositions and fine temperature intervals. The second approach is to calculate the phase boundary from the lever rule using the refined phase fractions at each temperature. In theory it should be possible to establish a highly accurate phase boundary

with only a few sampled compositions using this approach. However, accurately refining phase fractions can be challenging in high temperature measurements of solid acids because of large preferential orientation effects. Solid acids are highly prone to coarsening especially in the superprotonic state, and thus preferential orientation effects become significant even when the initial sample was well prepared. Finally, as demonstrated in Chapter 3, the chemical and thermal expansion trends can be utilized to calculate the composition of a phase based on the lattice parameters. The drawback of this approach is that it can be difficult to establish chemical and thermal expansion trends.

A few practical recommendations for the methodology of XRD sample preparation and data collection and refinement are provided below:

- Solid acid samples are water soluble and thus all sample holders and tools should be dry prior to use.
- In order to minimize preferential orientation effects, thorough grinding of the sample is recommended in a mortar and pestle for roughly 5 minutes. Additionally, it is recommended to rotate the sample during measurement.
- If the aim of a measurement is to observe the solid state reaction of two phases, it is best to grind together the materials and press them together in a composite pellet to ensure intimate contact of the reactants. Otherwise it is highly likely that unreacted precursor phases will remain above the reaction temperature. Pressing a pellet unfortunately often results in higher preferential orientation.
- If low signal intensity is not an issue, it is best to use a nickel filter to eliminate the $k\beta$ peaks. $k\beta$ peaks are a result of diffraction from the $k\beta$ emission line from the x-ray source. The

shorter $k\beta$ wavelength results in an additional set of lower angle $k\beta$ peaks. Although easy to identify, these peaks result in messier data and sometimes erroneous conclusions about impurities.

- It is best if the sample displacement is refined early in the refinement process using a known phase with a known lattice constant. Subsequently the sample displacement should be fixed.
- The phase fractions refined in GSAS are calculated on a unit cell basis. This fact should be accounted for if using the refined phase fractions in calculations such as the lever rule.
- In high temperature XRD measurements, humidified gas should only be introduced at temperatures above 130 °C and upon cooling the station should be flushed with dry gas before cooling below 130 °C.

1.5.2 Differential Scanning Calorimetry and Thermogravimetric Analysis

Differential Scanning Calorimetry (DSC) and thermogravimetric analysis (TGA) are crucial tools in assessing the thermodynamics, phase behavior, and stability of solid acid phases. The two techniques are often coupled together to provide simultaneous enthalpic and gravimetric data about a sample over a temperature profile. The DSC/TGA measurements were conducted here were done using a Netzsch STA F3.

To conduct a DSC/TGA measurement, a background scan is first collected using the identical temperature and atmosphere profile of the sample measurement. In the background scan, two empty identical pans are placed onto the sample holder. The background DSC and TGA signals are subsequently subtracted from the sample scan data to correct for effects such as thermal drift and buoyancy. Samples are prepared by hand pressing a powders into a pan, in this

case a Pt pan, and then loading the sample pan and empty reference pan onto the sample carrier. The sample carrier and pans are then enclosed under the instrument furnace and subjected to the designed gas atmosphere and temperature profile.

DSC/TGA measurements of solid acid samples are frequently conducted under highly humidified gas conditions. In our measurements, this is achieved with the Netzsch water vapor generator. Water vapor can be deleterious to the instrument if allowed to condense, and therefore the introduction and evacuation of the water vapor should be prudently managed. It is recommended that water vapor only be introduced at temperatures above 120 °C and only after a 1 hour hold at the temperature to allow for equilibration and heating of the external steam lines. Introducing humidity also produces a jolt on the DSC/TGA signals and thus it is recommended that the sample be allowed to equilibrate at a fixed temperature for 30 minutes after the introduction of humidity. Upon cooling, the sample should be held at a temperature greater than 120 °C while the humidification is shut off and the chamber is flushed with a dry inert gas for at least 1 hour. A key often-overlooked factor in humidified measurements is the condensation of the humidified gas at the exhausted. If left unchecked, the condensation of the humidified gas at the furnace exhaust port can result in water temporarily blocking the port. This produces a slight pressure build up that is then suddenly released when the water drips out of the port. While one might imagine this effect to be slight, in reality the sudden release of pressure causes massive spikes in the TG data that seriously obfuscate data analysis. The issue is best managed by applying an external heater to the exhaust port that is turned on with the other external heated lines prior to the introduction of humidification. It should also be noted that the external heated lines should not be turned on until the equilibration temperature (120 °C or above) and the

system should be allowed to equilibrate for 30 minutes after turning on the lines because the heat from these lines is palpable in the system.

The TG signal is simply measured as the mass loss as a function of time. The DSC signal is collected as the difference between the voltage signals from the thermocouples attached to the sample and reference pan holders. The voltage differential signals are correlated to heat values using a calibration curve established from the melting of known metal standards. In measuring the thermodynamics of phase transitions, it is recommended that if possible the phase transition is induced multiple times over several cycles of heating and cooling. The first phase transition is often noticeably impacted by microstructural factors such as particle size or strain and will produce transition temperatures and enthalpies far from those of the subsequent transitions. Therefore, its best to throw out the data from the first cycle and average the results from the later cycles. The integrated DSC peak produces the enthalpy of the phase transition and the onset of the peak is the measured temperature of transition. The two values can then be used to calculate the entropy of transition from $\Delta S = \Delta H/T$. In solid acid samples, the decomposition or dehydration temperature is often of interest and this value can be determined by the onset of mass loss or the onset of the DSC peak corresponding to dehydration. The relationship between the dehydration temperature and humidity is also revealing of the thermodynamics of dehydration. The relationship follows the equation:¹⁶

$$\ln(pH_2O) = -\frac{\Delta G^0}{RT} = \frac{\Delta S^0}{R} - \frac{\Delta H^0}{RT}$$

Where ΔG^0 , ΔH^0 , ΔS^0 are the standard Gibbs free energy, enthalpy, and entropy of the dehydration reaction. These thermodynamic values are typically relatively constant over the

temperature ranges measured and thus an Arrhenius plot of the dehydration data ($\ln(p\text{H}_2\text{O})$ vs $1/T$) often exhibits linear behavior.

1.5.3 Electrochemical Impedance Spectroscopy

Electrochemical impedance spectroscopy (EIS) is a technique which provides timescale resolved characterization of the various electrochemical processes within a system. EIS involves applying a sinusoidal perturbation of either the current or potential across a system and measuring the response of the other signal. When the potential is controlled the measurement is termed potentiostatic, and when the current is controlled the measurement is galvanostatic. A basic framework for understanding EIS is presented below using potentiostatic EIS as an example.

In potentiostatic EIS, a potential perturbation is applied of the form:

$$V(t) = V_0 \cos(\omega t) = V_0 e^{i\omega t}$$

where V_0 is the amplitude of the voltage perturbation and ω is the frequency.

The corresponding current response will take a similar sinusoidal form, but with a phase shift θ :

$$I(t) = I_0 \cos(\omega t + \theta) = I_0 e^{i(\omega t + \theta)}$$

The impedance of the system is calculated as from the ratio of these two terms:

$$Z(\omega) = \frac{V(t)}{I(t)} = |Z| e^{-i\theta}$$

where $|Z|$ is termed the impedance modulus and is the ratio of the amplitudes of the potential and current profiles. The impedance can be separated into real, Z' , and imaginary, Z'' , components as:

$$Z(\omega) = |Z| \cos(\theta) - i|Z| \sin(\theta) = Z' - iZ''$$

$|Z|$, Z' , Z'' , and θ are all dependent on the frequency of the impedance measurement, ω . An impedance measurement is composed of the impedance values from a set of measurements conducted over a range of frequencies that ideally spans the entire range of timescales for the processes of interest.

Impedance spectra are commonly plotted using two representations: the Nyquist plot or the Bode plot. In the Nyquist plot, the data are plotted with the real impedance against the imaginary, Z' vs $-Z''$. The Bode plot is actually composed of two separate plots: one in which the impedance modulus $|Z|$ is plotted as a function of frequency and the other in which the phase shift angle, θ , is plotted as a function of frequency. The Bode plot is technically a more complete representation of the data than the Nyquist plot, as it includes the frequency information while also capturing the real and imaginary impedances, that can be calculated from the modulus and the phase shift angle. However, the Nyquist plot is more commonly presented as the shape of the data in the Nyquist representation is often telling about the nature of the processes observed.

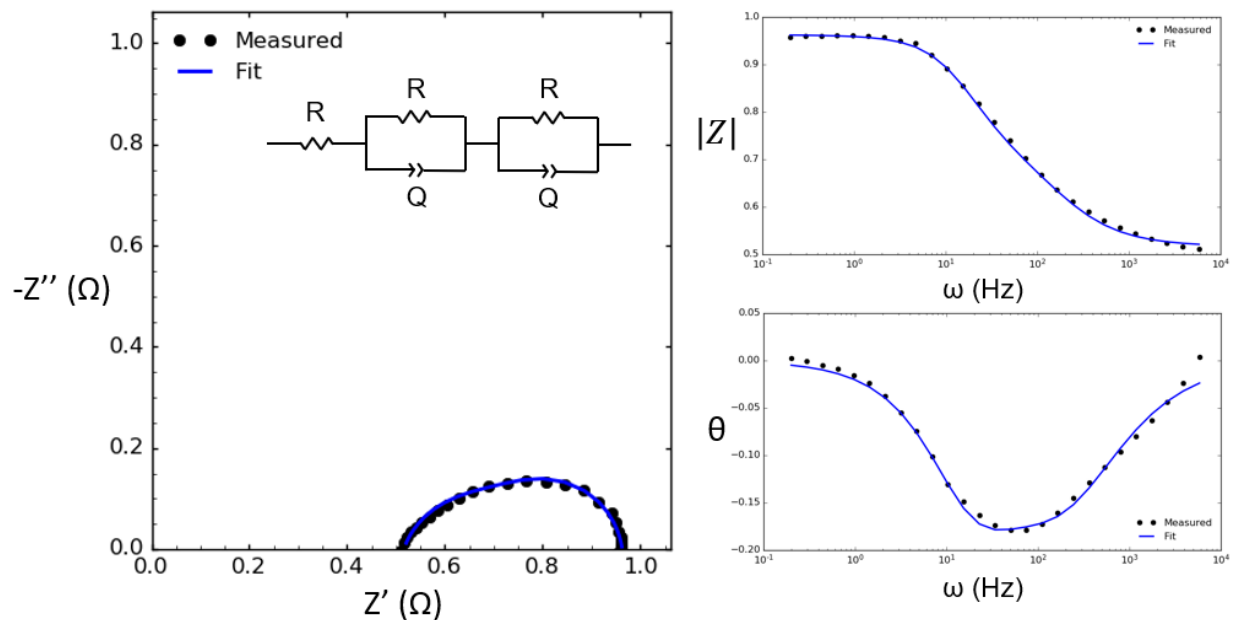


Figure 1.3. (left) Nyquist plot. (right) Bode plot.

Impedance data are frequently fit with equivalent circuit models using simple circuit elements such as resistors and capacitors. Ideally the parameters describing these elements are related back to physical properties such as the conductivity of a material or the capacitance of interfacial charging, however with complex spectra designation of physical meaning can be quite difficult. A list of common circuit elements employed to model phenomena such as diffusion or charge transfer resistance are provided in

Table 1.1. For a more detailed account of the basic EIS circuit elements, their mathematical derivation, and their form in the Nyquist representation, readers are encouraged to read Chapter 2 in Dr. Mary Louie's thesis.⁴³

Table 1.1. Basic EIS circuit elements.

Circuit Element	Impedance
Resistor R	R
Inductor L	$i\omega L$
Capacitor C	$\frac{1}{i\omega C}$
Constant Phase Element Q	$\frac{1}{Q(i\omega)^n}$
R-C circuit (parallel)	$\frac{1/R}{(1/R)^2 + (\omega C)^2} + \frac{-i\omega C}{(1/R)^2 + (\omega C)^2}$
Infinite-length Warburg	$\frac{R_0}{(i\omega\tau)^n}$
Finite-length Warburg	$R_0 \frac{\tanh[(i\omega\tau)^n]}{(i\omega\tau)^n}$
Blocked Warburg	$R_0 \frac{\coth[(i\omega\tau)^n]}{(i\omega\tau)^n}$

The impedance spectra of solid acid electrolytes typically takes two forms: that of semicircular arc below the superprotonic transition and that of an ohmic offset in the superprotonic phase. The semicircular arc is characteristic of electrolyte behavior and is fit with an RQ circuit. In the superprotonic phase the timescale of proton diffusion in the material is too rapid to be characterized by the frequency capabilities of the impedance spectrometer and thus the electrolyte response simply appears as an ohmic offset. The spectra collected in the superprotonic phase reflect instead the blocked Warburg diffusion behavior of the silver electrodes. The measured resistance of the electrolyte sample is then used to calculate the conductivity of the material using the dimensions of the pellet sample:

$$\sigma = \frac{L}{A * R}$$

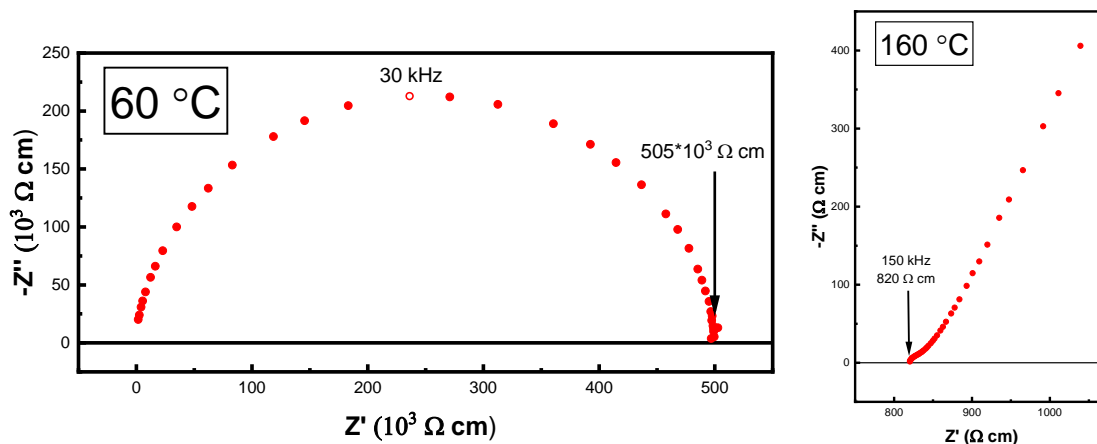


Figure 1.4. (left) impedance spectra of a solid acid electrolyte below its superprotonic transition temperature. (right) impedance spectra of a solid acid electrolyte in its superprotonic phase. These spectra were collected on a CPP sample.⁹

A wonderful Nature Reviews Methods Primers article was written on the subject of proper experimental methods for collecting impedance data.⁴⁴ A few salient points from that article will be mentioned here.

In general, two conditions must be met in order to collect meaningful impedance spectra. The first is that the voltage-current response should exhibit a proportionate linear behavior, meaning if the sample were held at specific voltages within the EIS scan range the measured current responses should exhibit a linear trend with voltage. In reality, very few electrochemical systems satisfy this condition, but an approximate linear response can be achieved if the perturbation amplitude is kept to a minimum. However, the amplitude must still be large enough to achieve reasonable signal-to-noise ratio. In the samples studied here, amplitudes of 10 - 20 mV were found to be suitable. The second condition for meaning EIS data is that the sample behavior should remain stable over the course of the measurement.

The satisfaction of these two requirements can be validated using the Kramers-Kronig relations. If the two conditions are satisfied, the Kramers-Kronig relations allow for calculation of either the real or imaginary component of the impedance response given only the other component. Therefore, comparison of the calculated vs measured impedance values provides a measure of the validity of the measurement. According to the Kramers Kronig relations, the imaginary component of the impedance can be calculated from the real component using:

$$Z''(\omega) = -\frac{2\omega}{\pi} \int_0^{\infty} \frac{Z'(x) - Z'(\omega)}{x^2 - \omega^2} dx$$

And the real impedance can be calculated from the imaginary impedance data using:

$$Z'(\omega) = Z''(\omega) + \frac{2}{\pi} \int_0^{\infty} \frac{xZ''(x) - \omega Z''(\omega)}{x^2 - \omega^2} dx$$

A complication frequently incurred in measuring EIS data is a large inductance effect from the wires leading to the sample. Although it is in theory possible to fit an inductor to remove this effect, it is best to avoid the complication altogether if possible. A simple approach to minimize the inductance effect is to braid together the current carrying wires and braid together the voltage perturbation wires so that the induction effect is cancelled out as the wires repeatedly cross. The inductance is quite sensitive to the specific braiding pattern, and it is recommended that when setting up the station various braiding patterns are trialed to determine the one of lowest inductance.

The proper preparation of solid acid electrolyte samples for impedance can also be challenging. Solid acid samples are typically prepared by uniaxially pressing powders of the material to form a circular pellet roughly 1 mm in thickness and then sputtering silver electrodes on either face of the pellet. However, many solid acids, CDP included, are quite brittle at room

temperature and fracture upon removal of the pellet from the die. A simple trick to help remedy this issue is to apply a film of Kapton tape to the face of both die punches. The smooth Kapton film helps to avoid the pellet being stuck to the die. Another common issue is low density in the pellet samples. I have found that the simplest way to achieve high density CDP pellets is to “hobo hot press” the samples. In “hobo hot pressing”, the filled die is stored in an oven at 130 °C for at least 3 hrs, and then carefully removed with thermally insulating gloves, and pressed at 4 tons (for a 3/4” diameter sample) for 10 minutes. The die should then be allowed to naturally cool for ~20 minutes before removing the sample. Densities of ~95 % theoretical density should be achieved using this method. A major challenge in forming solid acid samples is avoiding adsorbed water vapor on the surface of the solid acid powders. Adsorbed water presents an issue because trapped water vapor inside the pellet will escape when the sample is heated and form surface protrusions that deform the pellet. Many solid acids are highly hygroscopic and will easily adsorb water if exposed to atmospheric humidity, so it is strongly recommended that solid acid samples are stored in a desiccator, an oven above 120 °C, or in a glovebox. Even then, it is sometimes necessary to form the pellet itself in the glovebox, as exposure to the ambient atmosphere while filling the die can be enough to cause issues.

Chapter 2: Structure and properties of $\text{Cs}_7(\text{H}_4\text{PO}_4)(\text{H}_2\text{PO}_4)_8$: A new superprotonic solid acid featuring the unusual polycation $(\text{H}_4\text{PO}_4)^+$

Adapted with permission from: Wang, L. S., Patel, S. V., Sanghvi, S. S., Hu, Y. Y. & Haile, S. M. Structure and Properties of $\text{Cs}_7(\text{H}_4\text{PO}_4)(\text{H}_2\text{PO}_4)_8$: A New Superprotonic Solid Acid Featuring the Unusual Polycation $(\text{H}_4\text{PO}_4)^+$. *J. Am. Chem. Soc.* **142**, 19992-20001.

2.1 Introduction

Superprotonic solid acids are crystalline phases characterized by orientationally-disordered acidic oxyanion groups which undergo rapid reorientation around fixed central atoms. The coupling of this motion with inter-oxyanion proton hopping produces a variant of the Grotthuss mechanism and results in high proton mobilities along with long-range proton transport. Amongst known superprotonic conductors, cesium dihydrogen phosphate, CsH_2PO_4 , or CDP, is particularly suited for implementation as a fuel cell electrolyte, because in addition to its high proton conductivity, it displays chemical stability against reaction with both oxygen and hydrogen. Accordingly, CDP has been heavily studied in this capacity.⁴⁵⁻⁵¹ The superprotonic phase of CDP features a CsCl-like arrangement of Cs cations and orientationally disordered phosphate anions. The phase occurs at temperatures above 228 °C, but requires active humidification ($\sim p\text{H}_2\text{O} > 0.2 \text{ atm}$) to prevent dehydration.¹⁶ Several authors have sought to use chemical modification to expand the stability window of the superprotonic CDP phase and reduce the humidification requirements. The various approaches have included cation site doping with Rb, K,¹⁷ NH_4 ⁵², and Ba¹⁹, as well as ‘heterogeneous’ doping by introducing components such as $\text{Cs}_2\text{HPO}_4 \cdot \text{H}_2\text{O}$ ⁵³, $\text{Ba}(\text{H}_2\text{PO}_4)_2$ ⁵⁴, SiO_2 ⁵⁵, SiP_2O_7 ²³, and even $\text{Cs}_5\text{H}_5\text{N}_5\text{O}$ ⁵⁶. Of particular relevance to the present work is a study that was conducted by Ponomareva et al. on the impact of Cs deficiency on CDP, achieved by addition of excess $\text{CsH}_5(\text{PO}_4)_2$ or H_3PO_4 .⁵⁷ While the

authors reported unusually high proton conductivities at temperatures below the superprotonic transition temperature of CDP, the phase behavior was not characterized.

Here we report the discovery of a new superprotonic compound: heptacesium tetra-hydroxyphosphonium octa-dihydrogenphosphate, $\text{Cs}_7(\text{H}_4\text{PO}_4)(\text{H}_2\text{PO}_4)_8$, or CPP. The compound was revealed as part of a systematic study of the phase behavior in the CDP- $\text{CsH}_5(\text{PO}_4)_2$ system. As described below, CPP is thermodynamically stable at temperatures as high as 151 °C even without humidification and can be produced by either solid state reaction or high temperature crystallization from aqueous solution. The structure of $\text{Cs}_7(\text{H}_4\text{PO}_4)(\text{H}_2\text{PO}_4)_8$ is rather remarkable in that it contains the tetra-hydroxyphosphonium cation, H_4PO_4^+ . This polycation is an exceptionally rare species, especially in crystalline solids. The first supported report of its occurrence in a crystalline material was in $\text{H}_4\text{PO}_4^+\text{ClO}_4^-$ but the structure was not characterized.⁵⁸ To our knowledge, the only prior crystallographic studies of the H_4PO_4^+ ion have been in KH_2PO_4 ,⁵⁹ a result which has been questioned,⁶⁰ and in $\text{P}(\text{OH})_4^+\text{MF}_6^-$ (M= As, Sb)⁶⁰. In both crystalline and liquid system, the occurrence of tetra-hydroxyphosphonium is attributed to the presence of strong acids capable of donating protons to the phosphate group.⁶⁰⁻⁶³ The absence of such groups in $\text{Cs}_7(\text{H}_4\text{PO}_4)(\text{H}_2\text{PO}_4)_8$ renders the present discovery particularly surprising. Here we evaluate the proton transport, thermodynamics, and stability of this new compound.

2.2 Crystal Synthesis and Structure Determination

2.2.1 Methods

The compounds CsH_2PO_4 (CDP) and $\text{CsH}_5(\text{PO}_4)_2$ were independently prepared as precursors for the synthesis of CPP. Crystals of both materials were grown from evaporation of aqueous solutions of stoichiometric quantities of Cs_2CO_3 and phosphoric acid at ambient

conditions. Stoichiometric mixtures of CDP and $\text{CsH}_5(\text{PO}_4)_2$ (5:2 molar ratio) were homogenized by grinding, pressed into dense compacts at 275 MPa, and annealed at 130 °C for 3 days under dry N_2 gas flow. After annealing, the densified samples were immediately transferred to an N_2 atmosphere glovebox and further ground into a powder. As shown below, this series of processing steps returns the initial precursor phases: CDP and $\text{CsH}_5(\text{PO}_4)_2$. All subsequent references to powder precursor samples are to materials prepared in this way.

Crystals of $\text{Cs}_7(\text{H}_4\text{PO}_4)(\text{H}_2\text{PO}_4)_8$ were grown for single crystal x-ray diffraction from the powder precursor samples using a high temperature deliquescence and crystallization procedure.⁶⁴ Approximately 1 g of the powder sample of CDP and $\text{CsH}_5(\text{PO}_4)_2$ was heated to 102 °C in a tube furnace. A highly humidified gas stream ($p_{\text{H}_2\text{O}} = \sim 0.93$ atm) was then supplied to the sample, achieved by bubbling 40 sccm (standard cubic cm per min) Ar through 98 °C water. The sample was held under this condition for 6 h to achieve complete deliquescence, forming a concentrated liquid solution. The temperature was then slowly increased to 130 °C in 5 °C steps with a 2 h hold at each step, while maintaining the humidified atmosphere. The water gradually evaporated, and the target phase crystallized. The crystals were stored and transported to the diffractometer in a small mobile oven kept at 130 °C. During diffraction measurements, the selected crystal was preserved by a flow of argon heated to 130 °C. In order to maintain the high temperature structure, exposure to ambient temperature was limited to only the steps of crystal selection and mounting.

Single crystal x-ray diffraction data for structure solution were collected using Mo $K\alpha$ radiation ($\lambda = 0.71073$ Å) on a Bruker Kappa APEX with a CCD (charge-coupled device) area detector. Absorption corrections were applied using SADABS-2016/2. A total of 9772

reflections were captured, from which a cubic unit cell with $a = 20.1994(9)$ Å was established.

The space group was determined as $Pm\bar{3}n$ using Xprep (SHELX).⁶⁵ The formula unit was defined as 7 cesium atoms, 9 phosphorus atoms, and 36 oxygen atoms, with 8 formula units per unit cell, where the protons have been left out of the structure refinement.

The structure of CPP was solved by direct methods (SHELXS) and refined by least squares minimization (SHELXL).⁶⁵ Direct structure solution generated an asymmetric unit with five Cs and three P atom sites. An additional P atom site was subsequently identified, producing, as a consequence of the site multiplicities, the anticipated Cs:P ratio of 7:9. All atoms were initially refined with isotropic thermal displacements. Oxygen positions were found using successive Fourier difference maps, while restraining oxygen thermal displacements to $U_{\text{iso}} = 0.08$ Å² and P-O bond lengths to 1.58 Å. Significant attention was paid to establishing the oxygen site occupancies during structure refinement. Ultimately, a value of 1/3 for all oxygen sites produced the most sensible coordination environments and overall stoichiometry. In the final stages of the analysis, variable anisotropic thermal displacement parameters were introduced, and the structure was refined until convergence. Final respective R_1 and wR_2 values of 4.28% and 12.12% were achieved. Details of the diffraction experiment, structure solution, and refinement are summarized in Table 2.S-1.

Further structural characterization was carried out by high-temperature solid-state ¹H and ³¹P magic angle spinning (MAS) nuclear magnetic resonance (NMR) spectroscopy, which also provided insight into the material dynamics. MAS NMR spectra were collected on a Bruker spectrometer at a Larmor frequency of 300 MHz for ¹H and 121 MHz for ³¹P, using a 4 mm Bruker MAS probe at a sample spinning rate of 8 kHz. A powder mixture of the precursors

(CDP:CsH₅(PO₄)₂ = 5:2 molar ratio) was packed into a zirconia rotor for placement into the probe. Variable-temperature ¹H and ³¹P NMR spectra were collected between room temperature and 145 °C. For ¹H NMR, a single $\pi/2$ -pulse of 5.70 μ s was applied with a recycle delay of 500 sec. For ³¹P NMR, a single $\pi/2$ -pulse of 2.98 μ s was applied with a recycle delay of 1000 sec. For measurements taken between 120 – 145 °C, in which the CPP phase was observed, the recycle delay for both ¹H and ³¹P was set to 50 sec. In a separate series of measurements, 24-kHz ¹H-decoupling was applied during the collection of ³¹P NMR spectra between room temperature and 120 °C. In the ¹H-decoupled ³¹P NMR measurements, again, a single $\pi/2$ -pulse of 2.98 μ s was applied but with a 300 sec recycle delay. In all measurements, 10 minutes of temperature equilibration were allowed at each step prior to data acquisition. The ³¹P NMR shifts were calibrated using 85 wt% H₃PO₄ with a ³¹P resonance at 0 ppm. The ¹H NMR shifts were calibrated using adamantane with a ¹H resonance at 1.83 ppm. Temperature control was achieved using a heated dry N₂ gas stream, and temperature values were calibrated using ²⁰⁷Pb NMR of Pb(NO₃)₂.

2.2.2 Results: Structure of Cs₇(H₄PO₄)(H₂PO₄)₈

The cubic structure adopted by Cs₇(H₄PO₄)(H₂PO₄)₈ (Figure 2.1a-c, Table 2.1, Table 2.S-2) bears significant similarities to that of superprotonic CDP. Like the latter, CPP has a CsCl-like structure with orientationally disordered H₂PO₄⁻ groups residing on the anion sites. In contrast to CDP, however, one of every eight *cation* sites of the CsCl substructure is occupied by an orientationally disordered PO₄ group. The regular placement of these groups results in a 4 × 4 × 4 superstructure relative to CDP with a reduced symmetry space group of Pm $\bar{3}$ n.

Electrostatic considerations argue that these PO_4 groups must be polycations of chemistry H_4PO_4^+ , a conclusion supported by NMR studies described below. Using these site-charge assumptions, the asymmetric unit contains five Cs cations, two H_4PO_4^+ cations (centered around P1 and P2), and two H_2PO_4^- anions (centered around P3 and P4). Due to the high degree of orientational disorder associated with the phosphate groups, it was not possible to resolve the proton positions from the diffraction analysis.

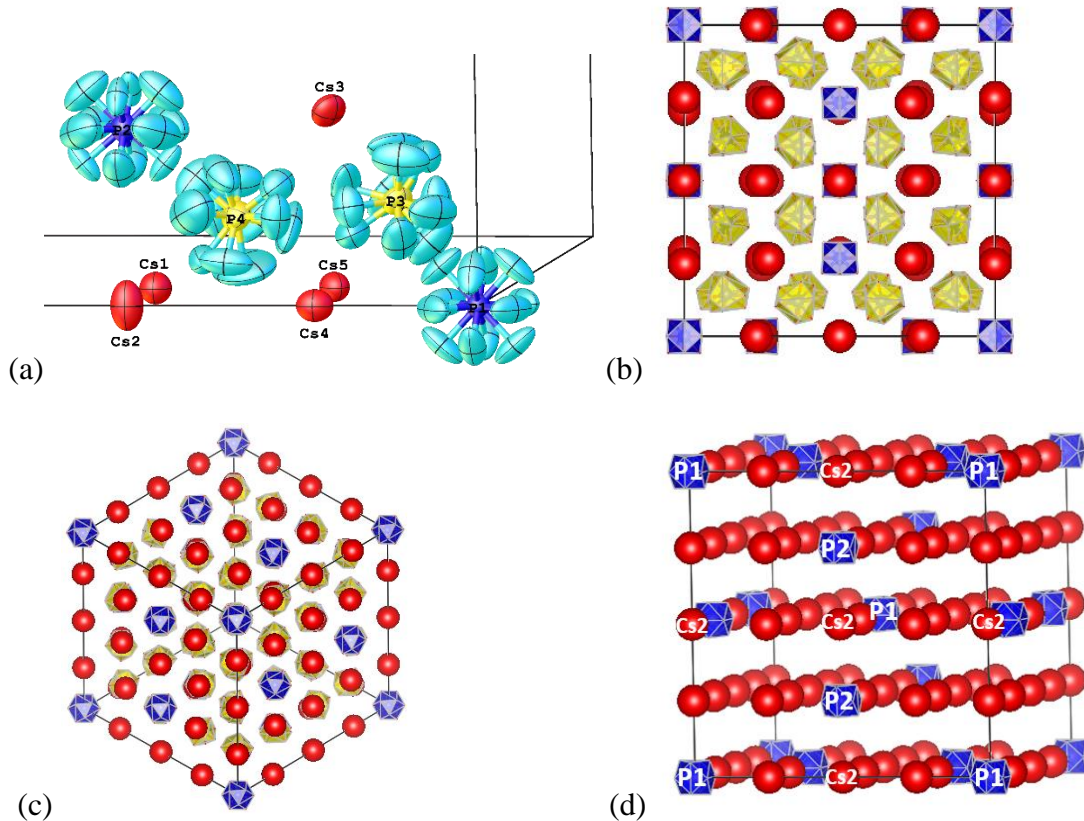


Figure 2.1. Crystal structure of $\text{Cs}_7(\text{H}_4\text{PO}_4)(\text{H}_2\text{PO}_4)_8$: (a) rendition of the asymmetric unit, depicting atomic displacements; (b) projection of the unit cell along [100]; (c) projection along [111]; and (d) idealized depiction of the arrangement of species on the cation sites. In (a) unlabeled atoms are oxygen; in (b), (c) and (d), H_nPO_4 groups are shown as polyhedra, with those about P1 and P2, the polycations, shown in blue, and those about P3 and P4, the polyanions (not depicted in (d)), shown in yellow; Cs atoms are shown in red.

Table 2.1. Structure of $\text{Cs}_7(\text{H}_4\text{PO}_4)(\text{H}_2\text{PO}_4)_8$ with atomic positions and site occupancies. Anisotropic thermal displacements are provided in Table 2.S1.

Atom	x	y	z	Occupancy
Cs1	0.25	0.5	0	1
Cs2	0	0.5	0	1
Cs3	0.25	0.25	0.25	1
Cs4	0	0.23261(6)	0	1
Cs5	0.27088(4)	0.24886(3)	0	1
P1	0	0	0	1
P2	0.5	0.25	0	1
P3	0.13502(8)	0.13502(8)	0.13502(8)	1
P4	0.13421(9)	0.36442(9)	0.11283(9)	1
O1	-0.0517(12)	0.0557(11)	0	1/3
O2	0.086(3)	0.077(2)	0.1237(8)	1/3
O3	0.1974(9)	0.0903(9)	0.1222(18)	1/3
O4	0.1974(7)	0.1299(13)	0.0906(7)	1/3
O5	0.2086(6)	0.1540(14)	0.1397(14)	1/3
O6	0.0902(7)	0.3012(6)	0.1155(13)	1/3
O7	0.1178(11)	0.3028(7)	0.1576(8)	1/3
O8	0.1488(14)	0.2922(6)	0.0952(13)	1/3
O9	0.1979(8)	0.3720(15)	0.1563(8)	1/3
O10	0.1981(8)	0.4078(10)	0.1141(17)	1/3
O11	0.2080(5)	0.3480(10)	0.1004(12)	1/3
O12	0.1242(9)	0.4182(13)	0.1647(13)	1/3
O13	0.0952(14)	0.3781(11)	0.1767(9)	1/3
O14	0.0799(15)	0.4181(15)	0.1234(13)	1/3
O15	0.1214(13)	0.4109(7)	0.0529(7)	1/3
O16	0.0869(7)	0.3724(17)	0.0529(7)	1/3
O17	0.150(2)	0.357(2)	0.0391(8)	1/3
O18	0.4420(8)	0.2005(9)	0	1/3
O19	0.5532(11)	0.3020(11)	0	1/3
O20	0.4463(5)	0.25	-0.0537(5)	1/3

The geometric parameters characterizing the PO_4 tetrahedra are summarized in Table 2.S-3. The 1/3 occupancy of oxygen atoms about the P3 and P4 atoms can be readily mapped to three distinct orientations for these anion phosphates (Table 2.S-3). The average P-O bond lengths in these units are 1.552(11) Å (P3) and 1.548(11) Å (P4), in agreement with the values reported for H_2PO_4^- tetrahedra by Ichikawa et al.⁶⁶ In the case of the P1 and P2 H_4PO_4^+ groups, six

orientations are inferred, with each oxygen position being relevant to two unique orientations. The P-O(H) bond lengths of the H_4PO_4^+ cations, in which all four P-O bonds are presumed to be protonated, have average values of 1.535(11) Å (P1) and 1.528(15) Å (P2). These bond distances, which are notably shorter than the analogous distances in the polyanion groups, are consistent with the values of around 1.53 Å reported for $\text{P}(\text{OH})_4^+\text{MF}_6^-$.⁶⁰

The ^1H -decoupled high-temperature ^{31}P NMR spectra, acquired between 110 - 120 °C, Figure 2.2 and Table 2.S-4, show 4 distinct phosphorus resonances. The -7 ppm resonance corresponds to the phosphorus signal of monoclinic CDP and diminishes in intensity with increasing temperature as the transformation to CPP reaches completion. The features of the remaining three resonances are largely temperature invariant and are attributed to CPP. The most prominent of these appears at -1.2 ppm and closely matches both the position and the breadth of the phosphorus signal of superprotonic CDP (-1.8 ppm).⁶⁷ Thus, we assign this resonance (p34) to the anion-site phosphorus atoms (P3, P4); the chemical environments of these two distinct atoms are apparently too similar to enable their resolution, although there is a hint of a shoulder on the down-shift side of the main peak. The two other phosphorus resonances at 3.3 ppm (p1) and 2.3 ppm (p2) are assigned to the cation-site phosphorus atoms P1 and P2 respectively. The assignment is in agreement with previous ^{31}P NMR studies of H_4PO_4^+ cations in concentrated acidic solutions which reported chemical shifts of approximately 2 ppm relative to phosphoric acid.^{62,63,68} A downshift relative to the anion-site phosphorus resonance is also consistent with the expectation that further protonating a phosphate group will draw electron density away from the central P, thereby reducing its electron shielding. The ratio of integrated peak intensities, with p1 : p2 : p34 = 1 : 2.91 : 31.05, closely matches that expected from the structure

determination (1 : 3 : 32). The sharpness of the p1, p2, and p34 resonances is indicative of the rapid rotation of each phosphate tetrahedra. This motion is further apparent in the XRD refined thermal displacement parameters of the oxygen atoms, which are enlarged in the direction normal to the P-O bonds in comparison to those of the cesium and phosphorus atoms (Figure 2.1a). The rotation of the H_4PO_4^+ polycation creates a relatively isotropic cation, which presumably facilitates its substitutional replacement of Cs^+ in the structure.

The ^1H MAS NMR spectra acquired at temperatures at which the CPP phase is stable, between 120 to 145 °C, are shown in Figure 2.3. The spectra contained only one major resonance centered around 13.4 ppm, which is split into two peaks due to ^1H - ^{31}P J-coupling of ~50 Hz. The splitting is consistent with that of the p1 and p2 resonances in the ^{31}P NMR spectra without ^1H -decoupling (Figure 2.S-1). The local chemical environments of the protons on the polycation (H_4PO_4^+) and polyanion (H_2PO_4^-) groups are undoubtedly distinct, and their differentiation by NMR would be expected. Indeed, the ^{31}P NMR spectra without ^1H -decoupling (Figure 2.S-1) show strong ^1H - ^{31}P coupling only about the p1 and p2 peaks of the polycation phosphorous species. Thus, the single proton resonance indicates rapid proton exchange between all sites, including exchange between polycation and polyanion proton sites. That the individual proton chemical environments cannot be resolved implies that the exchange rate is very fast, estimated to be on the order of 10^8 Hz.

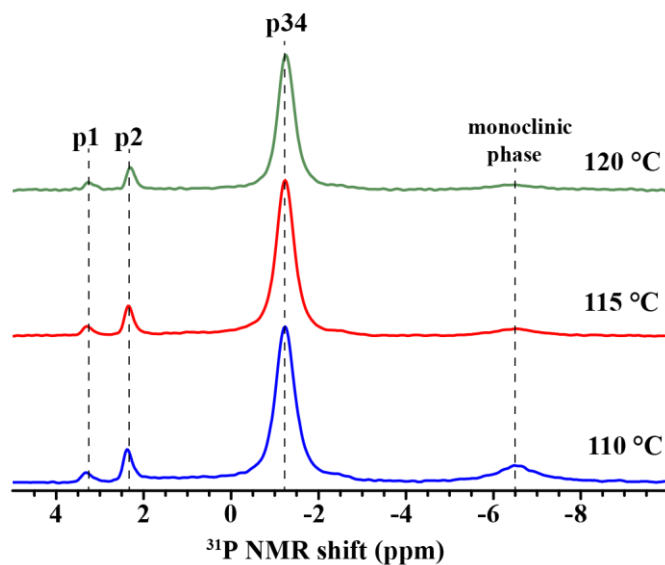


Figure 2.2. Variable-temperature ^1H -decoupled ^{31}P NMR spectra collected between 110 and 120 $^\circ\text{C}$. Peaks p1 and p2 are attributed to the polycations about P1 and P2, respectively, whereas peak p34 is attributed to the polyanions about P3 and P4.

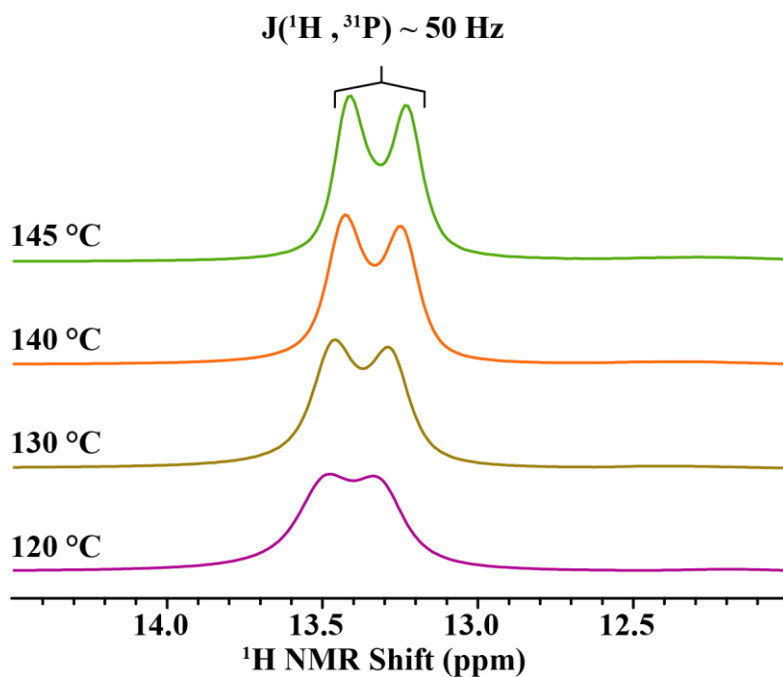


Figure 2.3. Variable-temperature ^1H MAS NMR spectra acquired between 120 to 145 $^\circ\text{C}$. A single split resonance is observed, which is indicative of rapid proton transfer between the polycation and polyanion phosphate groups.

The manner in which the H_4PO_4^+ cations are arranged within the CPP structure is of some note, Figure 2.1d. Within the $4 \times 4 \times 4$ superstructure cell the polycations reside on the corner and body-centered sites (P1), as well as two sites on each of the unit cell faces (P2). In principle, a simpler arrangement with equivalent stoichiometry can be achieved by placing the H_4PO_4^+ cations at the corners of a $2 \times 2 \times 2$ supercell. Adoption of the observed, more complex arrangement may result because it minimizes the extent to which H_4PO_4^+ cations interact. In both the hypothetical and observed arrangements, the shortest distance between H_4PO_4^+ cations, which presumably corresponds to the highest energy interaction, is equal to twice the substructure lattice constant ($2a_{\text{sub}}$). In the hypothetical $2 \times 2 \times 2$ supercell, each H_4PO_4^+ cation is involved in 6 such interactions. In the observed structure, interactions at this short distance ($2a_{\text{sub}}$) are observed only between P2 H_4PO_4^+ cations, with each P2 cation neighboring two other P2 species. The second nearest neighbor distances are conversely shorter in CPP, (Figure 2.S-2), and an energy minimization argument for the cation arrangement in CPP implies that the interaction energy between H_4PO_4^+ cations must drop relatively steeply with distance. It is of some interest to note the Cs2 atom, which lies directly along the short P2-P2 distance, has a displacement ellipsoid that is elongated in the direction of the polycation groups, Figure 2.1a. We suggest that motion of this Cs atom accommodates the reorientation of the bulky H_4PO_4^+ species.

2.3 Phase Formation and Stability Range

2.3.1 Methods

The high temperature phase behavior of CPP was investigated using high temperature x-ray powder diffraction (HTXRD) under both ambient air and active humidification. Samples

were prepared by pressing precursor powders of CDP and $\text{CsH}_5(\text{PO}_4)_2$ (5:2 molar ratio) into thin compacts (~0.1 mm thick, 57 MPA) in order to enhance inter-particle contact and facilitate solid state reaction. A Rigaku SmartLab Gen 3 9kW instrument ($\text{CuK}\alpha$, 45 kV, 160 mA) equipped with an Anton Paar XRK900 furnace was used for data collection under ambient air. Samples were heated at a ramp rate of 1 °C/min and held at each measurement temperature for 15 minutes prior to data collection ($10^\circ 2\theta$ /min, and 0.1° step size). Patterns were recorded at 10°C increments between 90 and 140 °C, and again at 5°C increments in this temperature range on cooling. HTXRD measurements under controlled humidity were performed using an in-house constructed stage,¹⁷ mounted on a Rigaku Ultima diffractometer ($\text{CuK}\alpha$, 40 kV, 44 mA). The sample was exposed to a humidified atmosphere ($p_{\text{H}_2\text{O}} = 0.4$ atm) at temperatures above 130 °C by introducing 25 sccm of N_2 , bubbled through a 80 °C water bath prior to entering the sample chamber. Humidification was introduced only at temperatures above 130 °C in order to prevent condensation of water vapor in the stage. Data were collected at temperatures between 130 and 165 °C, with a ramp rate of 1 °C/min and a 15 minute hold at each temperature prior to data collection ($5^\circ 2\theta$ /min, and 0.3° step size).

The thermodynamic properties of CPP were studied by simultaneous thermogravimetric analysis (TGA) and differential scanning calorimetry (DSC) using a Netzsch STA F3 equipped with a water vapor generator. Measurements were performed under nominally dry Ar and under seven different H_2O partial pressures of between 0.05 and 0.6 atm using Ar as a carrier gas (Table 2.S-5). Ground powder samples (50 – 60 mg) were loaded into a Pt pan and heated at a rate of 1 °C/min. For measurements under humidified atmospheres, the sample was heated to

130 °C and held for 2 hours before water vapor was introduced. Again, humidification was applied only at 130 °C and higher so as to avoid water condensation.

2.3.2 Results: Thermodynamics of CPP Formation

The HTXRD data (Figure 2.4) and thermal analysis results (Figure 2.5) reveal that CDP and $\text{CsH}_5(\text{PO}_4)_2$ react at elevated temperatures to form CPP. Specifically, the diffraction data show retention of the two reactant phases at 90 °C, whereas at 110 °C only CPP is observed. The DSC profile reveals that this structural change is accompanied by a distinct thermal event that initiates at 90 °C (and completes by ~ 110 °C). Notably, no weight loss is observed during the DSC transition, consistent with a solid state transformation. The temperature (T_{rxn}), enthalpy ($\Delta_{\text{rxn}}H$), and entropy ($\Delta_{\text{rxn}}S = \Delta_{\text{rxn}}H/T_{\text{rxn}}$), of the reaction were found to be 89.5 ± 1.2 °C, 47 ± 5 kJ/mol, and 130 ± 14 J/mol-K, Table 2.2, respectively, as averaged over 8 measurements, Figure 2.S-4.

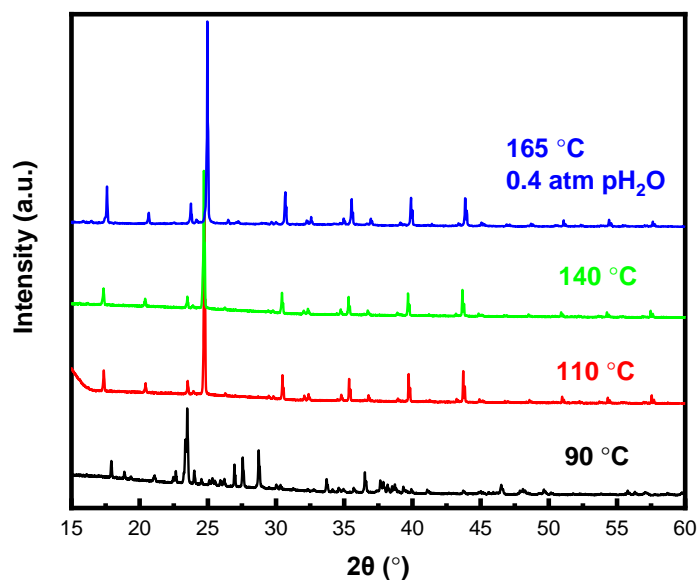


Figure 2.4. Powder x-ray diffraction patterns collected at 90, 110, and 140 °C under ambient atmosphere, and at 165 °C under 0.4 atm p_{H₂O}. The pattern collected at 90 °C is a superposition of the patterns of the monoclinic phases of CsH₂PO₄ and CsH₅(PO₄)₂. Patterns at 110, 140, and 165 °C are fully indexed to cubic Cs₇(H₄PO₄)(H₂PO₄)₈.

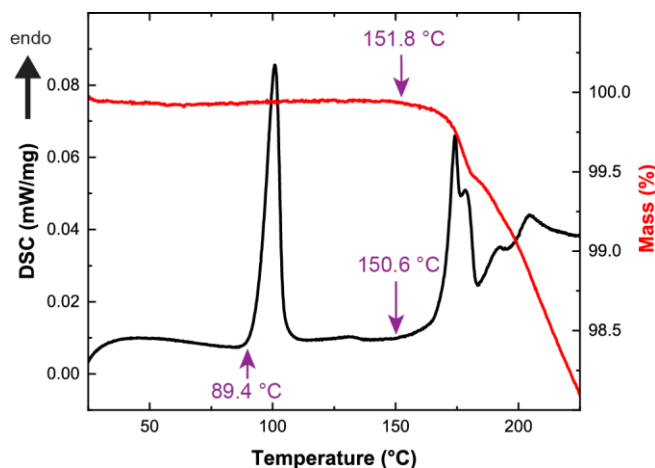


Figure 2.5. Differential scanning calorimetry and thermogravimetric profiles collected from a 5:2 CDP:CsH₅(PO₄)₂ sample heated at 1 °C/min under flowing dry Ar. Here, the DSC peaks for superprotonic reaction (89 °C) and decomposition (151 °C) frame the stability window of Cs₇(H₄PO₄)(H₂PO₄)₈ under nominally dry conditions.

Table 2.2. Thermodynamic quantities for the superprotonic reaction forming CPP. Values reported for the CDP phase transition are provided for comparison.¹⁷

	Cs ₇ (H ₄ PO ₄)(H ₂ PO ₄) ₈	Normalized per cube	CsH ₂ PO ₄
Superprotonic Onset (°C)	90(1.2)		228
Enthalpy (kJ/mol)	48(4)	6.0(0.5)	11.5
Entropy (J/mol K)	130(11)	16(1.4)	22.9

*The number in parentheses is the standard deviation for the measured value expressed in the final digit(s)

Further heating beyond the reaction temperature resulted in conventional thermal expansion behavior (thermal expansion coefficient $\alpha = 3.8(9) \times 10^{-5} \text{ K}^{-1}$, $a = 20.2032(2) \text{ \AA}$ @130 °C, Figure 2.S-3). Retention of CPP was observed in the diffraction data collected in the absence of active humidification up to 140 °C, Figure 2.4, and the onset of CPP decomposition at 151 °C was evident in coincident mass loss and endothermic events (Figure 2.5). Thus, CPP is

stable over a large temperature window (90 - 151 °C) in nominally dry conditions. This stands in marked contrast to CDP, the only other compound with a superprotonic phase composed of oxyanions that are solely PO_4 groups, which has a superprotonic phase with a negligible window of stability under dry conditions.

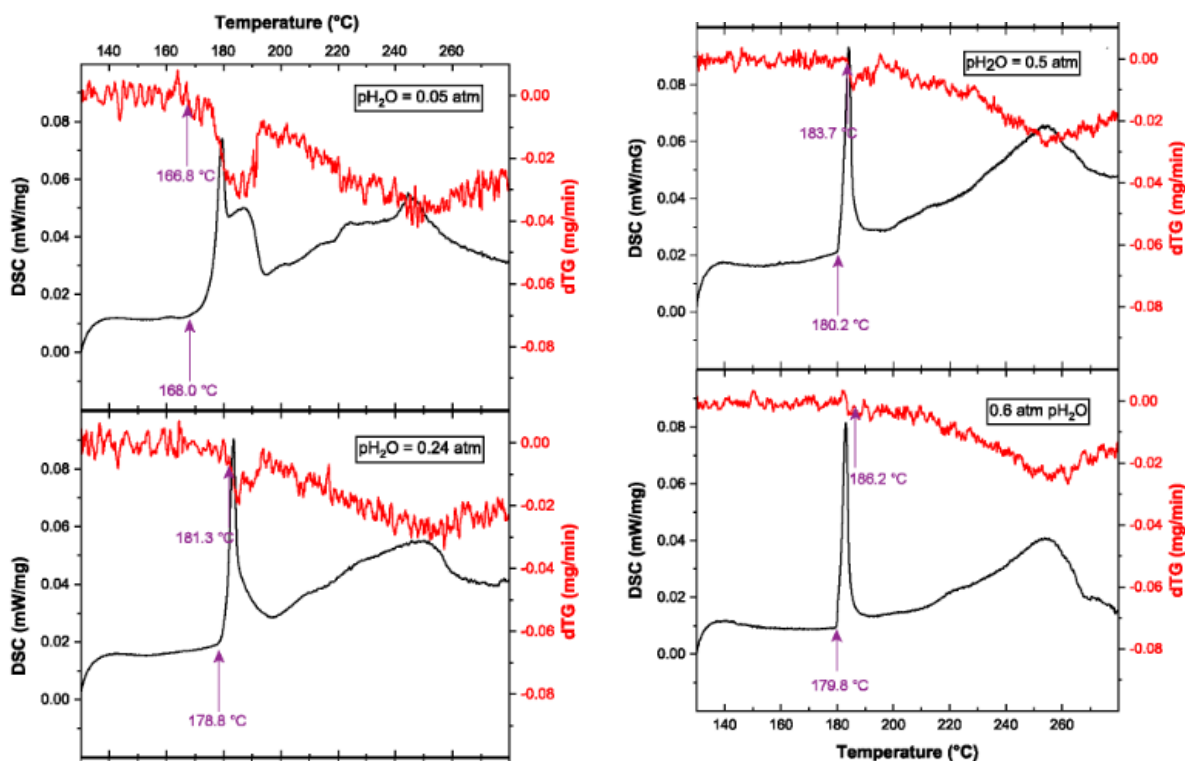


Figure 2.6. Differential scanning calorimetry and differential thermogravimetric profiles collected from $\text{Cs}_7(\text{H}_4\text{PO}_4)(\text{H}_2\text{PO}_4)_8$ (formed in situ by reaction between stoichiometric quantities of CDP and $\text{CsH}_5(\text{PO}_4)_2$) at a heating rate of 1 °C/min under flowing humidified Ar with water vapor partial pressure of (a) 0.05 atm; (b) 0.24 atm; (c) 0.5 atm; and (d) 0.6 atm, revealing the decomposition characteristics of $\text{Cs}_7(\text{H}_4\text{PO}_4)(\text{H}_2\text{PO}_4)_8$ as well as a solid state phase transformation at an onset temperature of 180 °C.

Active humidification resulted in suppression of the mass loss reaction, as evidenced in the differential mass loss curves of Figure 2.6. Such behavior implies the decomposition occurs by dehydration, typical of this general class of materials. Diffraction data collected at 165 °C

under 0.4 atm p_{H_2O} , Figure 2.4, confirmed retention of the cubic CPP phase to this higher temperature. Close examination of the DSC curves of Figure 2.6 reveals that those collected with $p_{H_2O} \leq 0.5$ atm are characterized by two overlapping thermal anomalies in the vicinity of the onset of mass loss. The first produces a sharp DSC peak at an onset temperature of 180 °C that is relatively insensitive to humidification and which can be seen to occur without mass loss in the data collected at $p_{H_2O} = 0.6$ atm. It was later revealed by the work in Chapter 3 that this sharp enthalpic event corresponded to a phase transition into a non-stoichiometric form of the cubic phase of CDP. The properties of the non-stoichiometric cubic phase and the phase transition will be extensively discussed in Chapter 3. The second DSC peak is much broader than the first and coincides with the broad peak in the dTG curves. Both of these broad peaks shift to higher temperatures and diminish in intensity with increasing p_{H_2O} . At $p_{H_2O} = 0.5$ atm, the broad DSC peak is barely visible, whereas at $p_{H_2O} = 0.05$ it is the dominant thermal event, and even initiates at a temperature lower than the solid-state transition. Based on these results, a proposed phase stability diagram for $Cs_7(H_4PO_4)(H_2PO_4)_8$ is presented in Figure 2.7. Here, the dehydration temperature is defined using the onset of the dTG mass loss signal and the solid-state phase transition temperature is defined from the onset of the sharp DSC signal. The observed linear trend of the dehydration temperatures in the Arrhenius representation can be fit to extract the enthalpy and entropy of dehydration using the equation:¹⁶

$$\ln(p_{H_2O}) = -\frac{\Delta G^0}{RT} = \frac{\Delta S^0}{R} - \frac{\Delta H^0}{RT}$$

The extracted ΔS^0 and ΔH^0 values are 473 J/mol and 220 kJ/mol respectively for a reaction producing 1 mol of steam. Decomposition leading to a liquid dehydrate is proposed based on the

nature of the product obtained from the thermal analysis experiments, which had the appearance of vitrified droplet.

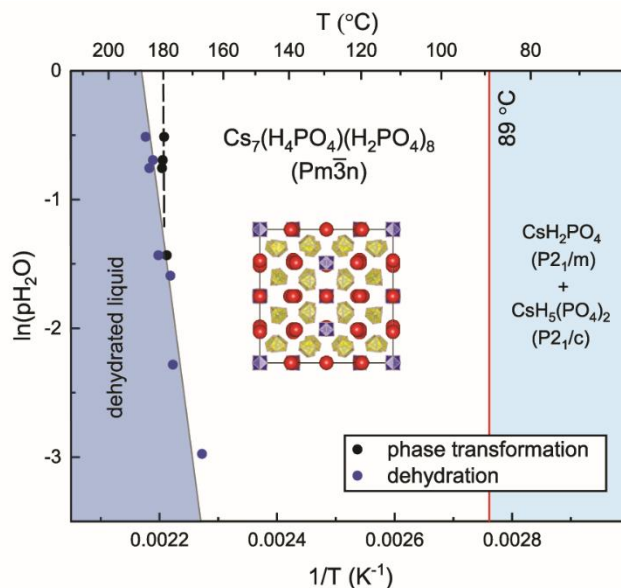


Figure 2.7. Phase diagram for $\text{Cs}_7(\text{H}_4\text{PO}_4)(\text{H}_2\text{PO}_4)_8$. Dehydration temperatures are identified according to the onset of mass loss detected in the dTG profile. Phase transformation temperatures are identified according to the onset of the sharp DSC signal, limited to measurements with $p\text{H}_2\text{O} \geq 0.24$ atm.

2.4 Conductivity

2.4.1 Methods

Conductivity measurements were made by A.C. impedance spectroscopy using an Agilent 4284A LCR analyzer. Data were collected using a 20 mV amplitude (under zero bias) over a 10^5 - 20 Hz frequency range. A dense compact, 1 mm in thickness, was prepared by pressing mixed powders of CDP and $\text{CsH}_5(\text{PO}_4)_2$ (5:2 molar ratio) in a 15 mm die to achieve 93% theoretical density. Electrodes were applied by sputtering 100 nm of Ag on each side. Data were collected under flowing N_2 (40 sccm) over the temperature range 60 - 170 °C. At temperatures of 140 °C and higher, the supply gas was humidified by bubbling through a water

bath at 80 °C to achieve $p_{\text{H}_2\text{O}} = 0.4$ atm. The sample was heated at a rate of 2 °C/min in 5-10 °C increments and was held at temperature for 30 minutes prior to measurement.

Impedance spectra were analyzed using the commercial software package Zview. As is typical of solid acid proton conductors,⁴⁸ at low temperatures, the spectra displayed a semi-circular arc in the Nyquist representation and could be simulated using a single RQ parallel circuit, where R is a resistor (equal to the bulk electrolyte resistance) and Q is a constant phase element ($Z_Q = Q_0^{-1}(i\omega)^{-n}$ where Q_0 is a constant, i is $\sqrt{-1}$, ω is frequency, and n is a constant between 0 and 1)⁶⁹. Despite the composite nature of the material, the impedance arc was rather ideal, consistently displaying an n value of ~ 0.9 . At high temperatures, the characteristic frequency for proton transport exceeded the frequency range of the impedance analyzer, again a typical feature of solid acid superprotonic materials, and a linear response reflecting the electrode was obtained in the Nyquist plot (Figure 2.S-5). These spectra were described using a Warburg diffusion element in series with a resistor, where the latter was taken as the bulk electrolyte resistance. Conductivity values were calculated using the fitted resistances and the sample dimensions, which were unchanged after measurement.

2.4.2 Results

The conductivity values as measured in two successive heating cycles are plotted in Arrhenius form in Figure 2.8. In the first heating cycle, a dramatic increase in conductivity between 90 and 110 °C due to the formation of CPP is evident, with the conductivity rising in this narrow temperature regime by about three orders of magnitude. Following the formation of the CPP phase, the conductivity is linear in the Arrhenius representation, with an activation

energy for charge transport of 0.652(4) eV (62.9(4) kJ/mol). In both the subsequent cooling (not shown) and second heating stages, the data followed the 1st cycle linear trend for temperatures ranging between 90 – 170 °C. No drop in conductivity corresponding to a reverse transition was observed on cooling. Introduction of humidification during the 2nd heating cycle had no impact of the magnitude of the conductivity, but acted to prevent dehydration and enabled measurement to ~170 °C.

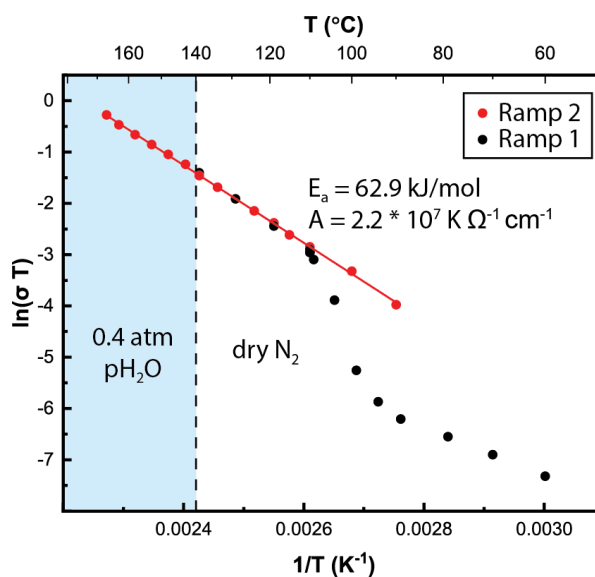


Figure 2.8. Conductivity of $\text{Cs}_7(\text{H}_4\text{PO}_4)(\text{H}_2\text{PO}_4)_8$ as measured over two successive heating cycles and plotted in Arrhenius form. The solid line is a fit to the measured data, from which the activation energy and pre-exponential factor for proton transport in $\text{Cs}_7(\text{H}_4\text{PO}_4)(\text{H}_2\text{PO}_4)_8$ were determined.

Significantly, despite the many similarities between CPP and superprotonic CDP, the activation energy for proton transport of the new material is substantially larger than that of CDP (0.652 vs. 0.398 eV)¹⁷. Concomitantly, the conductivity of CPP is lower, although some of the difference is attributable to the lower temperatures at which CPP is stable in comparison to

superprotonic CDP. Nevertheless at 170 °C, close to the high temperature limit at which CPP is stable under moderate humidification ($T = 180$ °C, $p_{\text{H}_2\text{O}} = 0.4$ atm), the conductivity is $\sim 2 \times 10^{-3}$ S cm^{-1} , an order of magnitude lower than that of CDP at 250 °C.¹⁷ The key structural feature shared between CPP and CDP is the presence of orientationally disordered H_2PO_4^- anion groups which participate, presumably in both compounds, in the Grotthuss mechanism of proton transport. The key distinction is the presence of H_4PO_4^+ cations in CPP, implying that this species must be responsible, either directly or indirectly, for the lower proton conductivity in this material. The ^1H NMR spectra, as discussed above (Figure 2.3), reveal that fast proton exchange occurs between polyanions and polycations, indicating that long range proton motion involves the unusual polycation species. Furthermore, as also noted above, strong ^1H - ^{31}P coupling is observed about the phosphorous atoms in the polycation groups (Figure 2.S-1), but not those in the polyanion groups. This distinction indicates stronger H-P chemical interactions for the polycation groups than the polyanion groups, which may in turn reflect a longer mean residence time for protons at the polycation sites (than at the polyanion sites). The participation of the polycations may thus directly impact long range proton transport by effectively creating proton trapping sites.

Several indirect impacts of the polycation species may also contribute or even be the primary cause of the diminished conductivity and high activation energy in CPP. In CDP, molecular dynamics simulations have pointed to PO_4 reorientation as the rate limiting step for proton transport.¹⁵ In CPP, the presence of somewhat anisotropic H_4PO_4^+ cations with probable hydrogen bonds to the polyanions, and/or the apparently fewer number of accessible polyanion orientations (3 vs. 6) may plausibly suppress the reorientation rate. On the other hand (or perhaps

in conjunction), a shallower minimum for polyanion rotation relative to CDP could result in a decrease in the zero point energy of this unit and thereby an increase in activation energy. Alternatively, the larger distance between polyanion groups ($a_{\text{CPP}} > 4 a_{\text{CDP}}$) may render the proton transfer between these units unfavorable such that this step becomes rate-limiting. The structural and macroscopic transport measurements reported here set the stage for a future focused mechanistic study.

2.5 Discussion of CPP Phase Formation

The formation of a stable compound that bears the H_4PO_4^+ cation is surprising. The rarity of previous observations of this cation suggests that this species is energetically unfavorable. At first glance, one might assume CPP to be stabilized by the high degree of rotational disorder on both anion and cation sites, particularly because the compound forms at temperatures below which the analogous cubic phase of CDP exists. However, the entropy of the reaction to form CPP is moderate in comparison, for example, to the entropy of the superprotonic transition of CDP, Table 2.2. In both cases - phase formation and superprotonic transition - the reactants display near-zero orientational disorder in their respective poly-ion groups, and thus the transition/reaction entropy can be largely attributed to the rotational disorder in the high temperature state.¹¹ The moderate entropy of CPP appears to result from the limited number of orientations of the H_2PO_4^- anion groups in this compound, only 3, as opposed to the 6 orientations that occur in CDP. Ruling out entropy as the driving factor, the ready formation of CPP must be a consequence of enthalpic considerations. As shown in Table 2.2, the enthalpy of the reaction is small, approximately half that of the enthalpy of the superprotonic transition of

CDP, implying that the enthalpy penalty to form CPP is low. The presence of the energetically unfavorable H_4PO_4^+ cation in CPP suggests that the enthalpy of formation of CPP (from the elements) must be at least as high, if not higher, than that of superprotonic CDP. Thus, we propose that the low reaction enthalpy is a consequence of a high enthalpy of formation of the reactant, $\text{CsH}_5(\text{PO}_4)_2$. This interpretation is supported by the observation that $\text{CsH}_5(\text{PO}_4)_2$ decomposes/melts at a relatively low temperature of $\sim 130\text{ }^\circ\text{C}$ under inert atmosphere (Figure 2.S-7). In contrast, CDP under similar conditions is stable to $\sim 224\text{ }^\circ\text{C}$.⁷⁰ Schematic diagrams of the thermodynamic relations underlying the arguments presented here are given in Figure 2.S-8 (derivatives of Hess law diagrams) along with further discussion. Finally, we note that although the reverse transformation was not extensively studied, in no case was a low symmetry form of CPP encountered. Instead, a gradual return to the precursor compounds occurred.

2.6 Conclusion and Summary

The structure, thermodynamic and proton transport properties of superprotonic $\text{Cs}_7(\text{H}_4\text{PO}_4)(\text{H}_2\text{PO}_4)_8$ (CPP), a new compound, are presented in this work. The compound forms at $90\text{ }^\circ\text{C}$ from reaction of CDP and $\text{CsH}_5(\text{PO}_4)_2$. Single crystal diffraction studies in concert with NMR spectroscopy revealed rotationally disordered H_4PO_4^+ polycations as periodic features on the cation lattice – replacing Cs on one of every eight cation sites. The regular, periodic placement of the H_4PO_4^+ cations reduces the symmetry of the cubic structure to $\text{Pm}\bar{3}$ n from the ideal $\text{Pm}\bar{3}$ m space group of the CsCl structure type and creates a $4 \times 4 \times 4$ supercell of cubic CDP-like unit cells. The occurrence of CPP, with the enthalpically unfavorable H_4PO_4^+ unit, is proposed to be the consequence of a high enthalpy of formation of $\text{CsH}_5(\text{PO}_4)_2$, as opposed to a

high entropy of formation of CPP. The low formation temperature contributes to the wide window of thermal stability of CPP, which extends under nominally dry conditions up to ~151 °C. This phase behavior stands in contrast to that of CDP, the only other superprotonic solid acid formed of entirely phosphate polyanion groups, which has a negligible window of stability in the superprotonic phase under nominally dry conditions. Despite the high degree of polyanion disorder in CPP and its overall structural similarity to CDP, the activation energy for proton transport is high and the conductivity is moderate. This is an apparent consequence of the participation of the polycation groups in the long-range proton transport. Thus, in terms of the application of CPP as an electrolyte, it remains to be seen whether the advantages offered, namely operation at reduced temperatures without the requirement of active humidification, can outweigh the advantages of high conductivity and higher operating temperatures offered by CDP and other inorganic proton conductors such as SnP_2O_7 and analogs.⁷¹

Supplemental Information

Table 2.S-1. Details from the single crystal diffraction and structure solution and refinement.

Crystal data	
Chemical formula	Cs ₇ (H ₄ PO ₄)(H ₂ PO ₄) ₈
Chemical formula weight (g/mol)	1805.26
Crystal system	Cubic
Space Group	Pm-3n
a (Å)	20.1994
V (Å ³)	8241.7
Z	8
Density (g/cm ³)	2.877
Radiation Source	Mo Kα
Wavelength (Å)	0.71073
No. of reflections for cell parameters	9772
θ range (°)	2.255-22.671
Absorption correction μ (mm ⁻¹)	6.573
F(000)	6464
Temperature (K)	403
Crystal size (mm)	0.46 x 0.257 x 0.251
Crystal color	Colorless
Crystal mount	Glued on glass fiber
Data collection	
Diffractometer	Bruker Kappa APEX, CCD area detector
Data collection method	ω and φ scans
Absorption correction	SADABS-2016/2 (Bruker,2016/2)
T _{min}	0.4636
T _{max}	0.7455
No. of measured reflections	1671__
No. of observed reflections	1108
Criterion for observed reflections	I > 2 σ(I)
R _{int}	0.0670
θ _{max} (°)	27.199
Range of h,k,l	-25 < h < 21
	-25 < k < 25
	-25 < l < 25
Refinement	
Refinement	least-squares on F ²
R[F ² > 2σ(F ²)]	0.0428
wR(F ²)	0.1212
S	1.064

No. of reflections used in refinement	1671
No. of parameters used	203
Weighting scheme	$w=1/[\sigma^2(F_o^2) + (0.0645P)^2 + 16.7845P]$ where $P=(F_o^2 + 2F_c^2)/3$
Anisotropic thermal parameters	All atoms. H atoms not included in structure.
Extinction coefficient	0.00010(2)
Source of atomic scattering factors	International Tables Vol C Tables 4.2.6.8 and 6.1.1.4
Programs	
Structure solution	SHELXS (Sheldrick, 2008)
Structure refinement	SHELXL 2018/3 (Sheldrick, 2008)
Structure depiction	VESTA

Atom	x	y	z	occupancy	U11	U22	U33	U23	U13	U12
Cs1	0.25	0.5	0	1	0.1011(9)	0.0901(5)	0.0901(5)	0	0	0
Cs2	0	0.5	0	1	0.0835(9)	0.0945(9)	0.222(2)	0	0	0
Cs3	0.25	0.25	0.25	1	0.0953(4)	0.0953(4)	0.0953(4)	-0.0204(3)	-0.0204(3)	-0.0204(3)
Cs4	0	0.23261(6)	0	1	0.0848(6)	0.1224(8)	0.0913(7)	0	0	0
Cs5	0.27088(4)	0.24886(3)	0	1	0.1048(6)	0.0867(5)	0.0765(4)	0	0	0.0200(3)
P1	0	0	0	1	0.0492(12)	0.0492(12)	0.0492(12)	0	0	0
P2	0.5	0.25	0	1	0.0634(14)	0.071(2)	0.0634(14)	0	0	0
P3	0.13502(8)	0.13502(8)	0.13502(8)	1	0.0759(7)	0.0759(7)	0.0759(7)	-0.0134(7)	-0.0134(7)	-0.0134(7)
P4	0.13421(9)	0.36442(9)	0.11283(9)	1	0.0772(10)	0.0795(11)	0.0782(10)	-0.0084(8)	0.0113(8)	0.0056(7)
O1	-0.0517(12)	0.0557(11)	0	1/3	0.147(17)	0.119(16)	0.068(9)	0	0	0.091(11)
O2	0.086(3)	0.077(2)	0.1237(8)	1/3	0.17(2)	0.17(3)	0.108(13)	-0.002(19)	-0.02(2)	-0.097(15)
O3	0.1974(9)	0.0903(9)	0.1222(18)	1/3	0.107(13)	0.087(12)	0.30(4)	0.002(18)	0.017(19)	-0.009(11)
O4	0.1974(7)	0.1299(13)	0.0906(7)	1/3	0.088(10)	0.150(16)	0.065(8)	0.006(10)	0.006(7)	0.009(12)
O5	0.2086(6)	0.1540(14)	0.1397(14)	1/3	0.078(10)	0.22(3)	0.23(3)	-0.146(18)	-0.005(13)	-0.041(13)
O6	0.0902(7)	0.3012(6)	0.1155(13)	1/3	0.070(9)	0.078(9)	0.186(19)	-0.011(11)	-0.015(11)	-0.005(7)
O7	0.1178(11)	0.3028(7)	0.1576(8)	1/3	0.145(17)	0.103(12)	0.098(12)	-0.011(9)	0.016(11)	-0.017(12)
O8	0.1488(14)	0.2922(6)	0.0952(13)	1/3	0.26(3)	0.067(10)	0.22(2)	-0.037(12)	0.12(2)	0.007(13)
O9	0.1979(8)	0.3720(15)	0.1563(8)	1/3	0.105(12)	0.20(2)	0.100(13)	-0.006(15)	-0.002(10)	-0.037(14)
O10	0.1981(8)	0.4078(10)	0.1141(17)	1/3	0.101(12)	0.116(15)	0.24(3)	0.040(19)	-0.001(16)	-0.001(11)
O11	0.2080(5)	0.3480(10)	0.1004(12)	1/3	0.050(7)	0.154(17)	0.180(19)	-0.099(14)	0.011(8)	0.014(8)
O12	0.1242(9)	0.4182(13)	0.1647(13)	1/3	0.090(13)	0.156(19)	0.16(2)	-0.046(16)	0.047(12)	-0.028(12)
O13	0.0952(14)	0.3781(11)	0.1767(9)	1/3	0.17(2)	0.138(18)	0.114(14)	0.052(12)	0.062(14)	0.054(16)
O14	0.0799(15)	0.4181(15)	0.1234(13)	1/3	0.24(3)	0.21(3)	0.19(3)	-0.03(2)	-0.05(2)	0.09(3)
O15	0.1214(13)	0.4109(7)	0.0529(7)	1/3	0.172(19)	0.074(9)	0.073(9)	0.000(7)	0.018(11)	0.016(10)
O16	0.0869(7)	0.3724(17)	0.0529(7)	1/3	0.068(9)	0.25(3)	0.066(9)	0.019(14)	0.000(7)	0.002(13)
O17	0.150(2)	0.357(2)	0.0391(8)	1/3	0.40(6)	0.39(6)	0.096(15)	-0.03(2)	0.10(2)	0.08(4)
O18	0.4420(8)	0.2005(9)	0	1/3	0.091(11)	0.118(13)	0.041(7)	0	0	-0.066(10)
O19	0.5532(11)	0.3020(11)	0	1/3	0.18(2)	0.145(19)	0.091(14)	0	0	-0.089(18)
O20	0.4463(5)	0.25	-0.0537(5)	1/3	0.183(17)	0.119(18)	0.183(17)	-0.036(14)	-0.10(2)	0.036(14)

Table 2.S 2. Structure of $\text{Cs}_7(\text{H}_4\text{PO}_4)(\text{H}_2\text{PO}_4)_8$ with atomic positions, site occupancy, and anisotropic thermal displacement parameters.

Table 2.S-3. P-O bond length and O-P-O bond angles for (a) P1, (b) P2, (c) P3, and (d) P4. Symmetry codes are provided below each table.

(a) P1

	Length (Å)	Angles (°)			Length (Å)		
O1 ^{4,1}	1.535(11)	86(2)	119.91(10)	119.91(10)	2.09(5)	2.657(19)	2.657(19)
O1 ^{5,7}	1.535(11)		119.91(10)	119.91(10)			
O1 ^{6,8}	1.535(11)			86(2)			
O1 ^{7,9}	1.535(11)						
	P1	O1 ^{5,7}	O1 ^{6,8}	O1 ^{7,9}	O1 ^{5,7}	O1 ^{6,8}	O1 ^{7,9}
	Length (Å)	Angles (°)			Length (Å)		
O1 ^{0,10}	1.535(11)	94(2)	119.91(10)	119.91(10)	2.25(4)	2.657(19)	2.657(19)
O1 ^{1,11}	1.535(11)		119.91(10)	119.91(10)			
O1 ^{2,0}	1.535(11)			94(2)			
O1 ^{3,1}	1.535(11)						
	P1	O1 ^{1,11}	O1 ^{2,0}	O1 ^{3,1}	O1 ^{1,11}	O1 ^{2,0}	O1 ^{3,1}

	Length (Å)	Angles (°)			Length		
O1 ^{9,8}	1.535(11)	86(2)	119.91(10)	119.91(10)	2.09(5)	2.657(19)	2.657(19)
O1 ^{11,10}	1.535(11)		119.91(10)	119.91(10)			
O1 ^{4,5}	1.535(11)			94(2)			
O1 ^{2,3}	1.535(11)						
	P1	O1 ^{11,10}	O1 ^{4,5}	O1 ^{2,3}	O1	O1	O1

¹ x,-y,0; ² y,0,-x; ³ y,0,x; ⁴ -y,0,-x; ⁵ -y,0,x; ⁶ -x,y,0; ⁷ -x,-y,0; ⁸ 0, -x,y; ⁹ 0,-x,-y; ¹⁰ 0,x,y; ¹¹ 0,x,-y; ¹² y,0,x

(b) P2

Orientation 1-4	Length (Å)	Angles (°)		
O18 ^{0,2,6,1}	1.540(11)	84.8(10)	122.6(4)	122.6(4)
O19 ^{1,6,2,0}	1.502(14)		120.4(6)	120.4(6)
O20 ^{2,0,5,7}	1.534(15)			90
O20 ^{7,5,2,0}	1.534(15)			
	P2	O19	O20	O20

¹ 1-x,y,-z; ² 1/2-z, 1/2-y, 1/2-x; ⁴ 1/2-z, 1/2-y, -1/2+x; ⁵ 1-x,y,z; ⁶ 1/2+z, 1/2-y, -1/2+x; ⁷ x,y,-z;

Orientation 5	Length (Å)	Angles (°)		
O18	1.540(11)	99.119	114.885	114.885
O18 ¹	1.540(11)		114.89	114.89
O18 ²	1.540(11)			99.106
O18 ⁶	1.540(11)			
	P2	O18 ¹	O18 ²	O18 ⁶

Orientation 6	Length (Å)	Angles (°)		
O19	1.502(14)	91(2)	119.2(12)	119.2(12)
O19 ¹	1.502(14)		119.2(12)	119.2(12)
O19 ⁶	1.502(14)			91(2)
O19 ²	1.502(14)			
	P2	O19 ¹	O19 ⁶	O19 ²

(c) P3

	Length (Å)	Angles (°)		
O2 ^{0,1,2}	1.549(11)	115(2)	112(2)	110.3(9)
O3 ^{2,0,1}	1.572(14)		81.7(10)	123.2(13)
O4 ^{0,1,2}	1.550(12)			111.2(12)
O5 ^{1,2,0}	1.538(11)			
	P3	O3 ^{2,0,1}	O4 ^{0,1,2}	O5 ^{1,2,0}

¹y,z,x; ²z,x,y**(d) P4**

1	Length (Å)	Angles (°)		
O6	1.557(11)	112.4(10)	119.1(13)	115.3(12)
O11	1.547(9)		113.1(9)	99.4(14)
O12	1.523(12)			94.7(14)
O15	1.552(11)			
	P4	O11	O12	O15

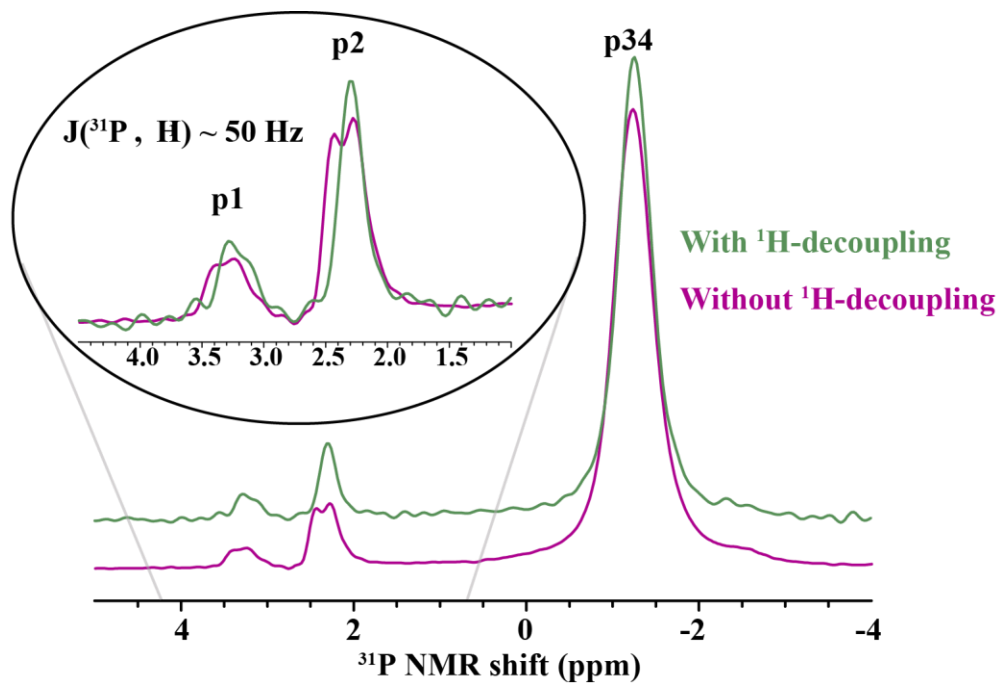
2	Length (Å)	Angles (°)		
O8	1.530(10)	112.3(14)	117.8(12)	92.0(17)
O10	1.560(12)		108.0(18)	117.7(13)
O13	1.536(12)			108.7(13)
O16	1.550(11)			
	P4	O10	O13	O16

3	Length (Å)	Angles (°)		
O7	1.574(11)	85.9(11)	108.9(16)	121.7(19)
O9	1.564(11)		115.7(15)	112.4(18)
O14	1.557(13)			110.5(18)
O17	1.531(12)			
	P4	O9	O14	O17

T (°C)	Chemical Shift (ppm)			Integral			Integral ratios			Broadening	
	p1	p2	p34	p1	p2	p34	p34: (p1 + p2)	p2:p1	p1	p2	p34
110	3.325	2.372	1.198	2.89(5)	8.35(2)	88.76	7.90	2.89	37.1	30.3	64.0
115	3.324	2.365	1.201	2.95(6)	8.32(2)	88.72	7.87	2.82	37.9	30.1	59.5
120	3.261	2.319	1.236	2.75(18)	8.31(4)	88.94	8.04	3.02	50.0	25.8	51.1
Average				2.86	8.33	88.81	7.94	2.91			

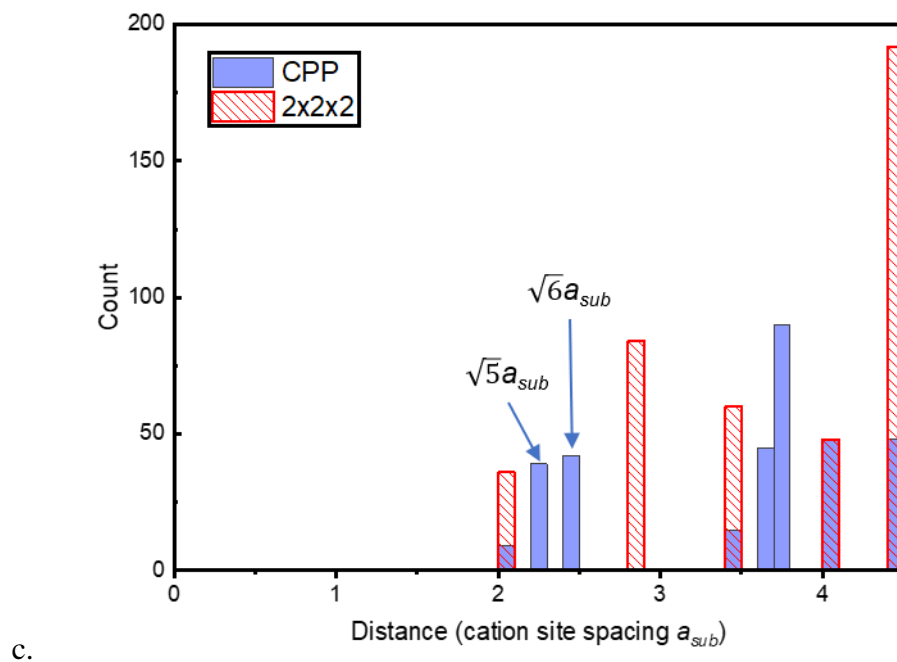
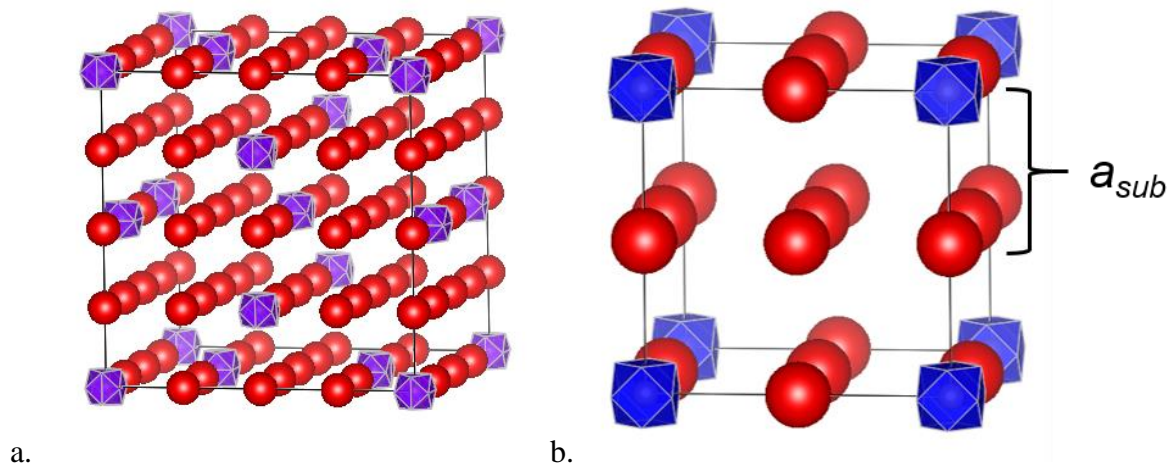
Table 2.S-4. ³¹P NMR details for the resonances in each scan temperature.

Figure 2.S-1. Comparison of ^{31}P MAS NMR spectra of $\text{Cs}_7(\text{H}_4\text{PO}_4)(\text{H}_2\text{PO}_4)_8$ collected at $120\text{ }^\circ\text{C}$ with and without ^1H -decoupling.



Without ^1H -decoupling, the p1 and p2 resonances are split due to ^1H - ^{31}P J-coupling with an amplitude of $\sim 50\text{ Hz}$. The amplitude is consistent with that observed in the ^1H NMR spectra (Figure 2.3). ^1H - ^{31}P J-coupling is also manifested in the slight broadening of the p34 resonance. ^1H -decoupling removes the J-coupling effect, yielding narrower resonances and removal of the splitting.

Figure 2.S-2. Analysis of the H_4PO_4^+ - H_4PO_4^+ interactions in the (a) CPP structure vs the (b) hypothetical $2 \times 2 \times 2$ supercell structure.



A $12 \times 12 \times 12$ array of cation sites was populated using the H_4PO_4^+ arrangement of each structure. All of the interaction distances involving H_4PO_4^+ cations within the central $4 \times 4 \times 4$

cation sites, including those interactions extending from the central $4 \times 4 \times 4$ sites into the larger $12 \times 12 \times 12$ array, were calculated, and the frequency of each interaction distance is plotted in (c).

As shown in (c), the closest H_4PO_4^+ - H_4PO_4^+ interaction for either structure occurs at a distance of 2 cations sites ($2a_{sub}$). However, the frequency of these interactions in the CPP structure is only a quarter of that in the hypothetical $2 \times 2 \times 2$ structure. In the $2 \times 2 \times 2$ structure, each H_4PO_4^+ cation has six $2a_{sub}$ interactions, whereas in the CPP structure only adjacent P2 H_4PO_4^+ cations interact at this distance. However, the CPP arrangement features several more interactions at distances only slightly larger than $2a_{sub}$ – namely interactions between P2 and P1 H_4PO_4^+ cations ($\sqrt{5}a_{sub}$) and interactions between P2 cations on adjacent faces of the unit cell ($\sqrt{6}a_{sub}$). The adoption of the CPP structure suggests that the $2a_{sub}$ interactions induce significantly more lattice strain than the $\sqrt{5}a_{sub}$ and $\sqrt{6}a_{sub}$ interactions and that lattice strain falls off rapidly with increasing interaction distance.

Table 2.S-5. Ar and water vapor flow rates for various humidified atmospheres in TGA/DSC measurements.

pH₂O (atm)	Water mass flow rate (g/h)	Carrier Ar flow rate (sccm)	Protective Ar flow rate (sccm)
0.05	0.3	85.5	20
0.10	0.4	59.7	20
0.20	1.3	95.3	20
0.24	1.1	59.7	20
0.47	3.1	59.7	20
0.5	3.5	59.7	20
0.6	5.1	59.7	20

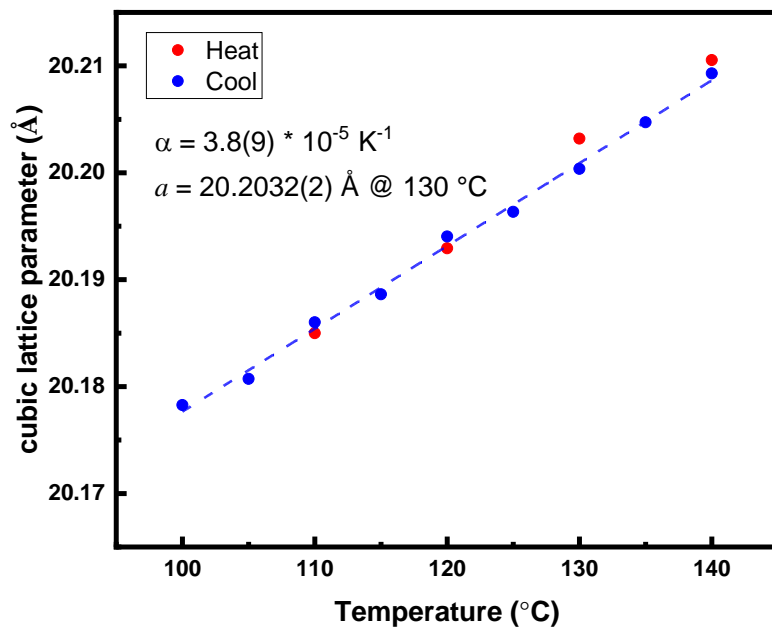
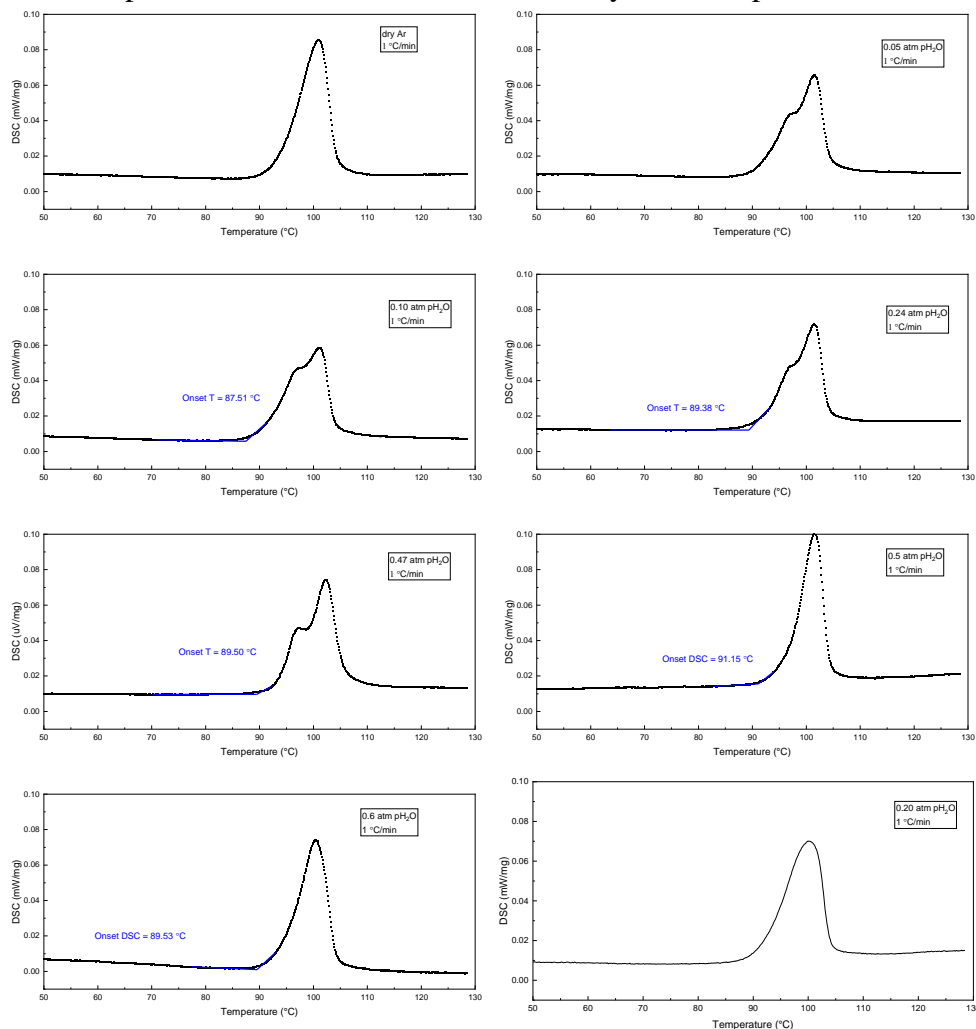
Figure 2.S-3. Lattice parameter of $\text{Cs}_7(\text{H}_4\text{PO}_4)(\text{H}_2\text{PO}_4)_8$ at various temperatures.

Figure 2.S-4. Superprotonic reaction DSC peaks averaged to obtain thermodynamic values for the reaction. All samples were heated at 1 °C/min under dry Ar atmosphere.



Variations in the shape of the recorded DSC profiles are attributed to variable particle-to-particle contact in the as-prepared compacts, which would be expected to influence the course of the solid state reaction. The reaction onset temperature, in contrast, was insensitive to such microstructural effects.

Although several of these scans produced sharp singular DSC peaks, several others featured a superprotonic reaction event that was split into two overlapping peaks with the signal broadened to higher temperatures. These dual reaction peaks are likely a result of particle

agglomeration inhibiting the kinetics of the solid-state reaction, which are highly dependent on intimate interfacial contact between the monoclinic phases of CDP and $\text{CsH}_5(\text{PO}_4)_2$. We suspect that exposure to atmospheric humidity is causing particle agglomeration, which delays a portion of the reaction to higher temperatures. Thus, care was taken to prevent atmospheric exposure by storing the sample in a glovebox until just prior to measurement. Still this was not always successful, and several measurements were not included in the enthalpy analysis due to severe peak broadening and splitting.

The measured enthalpy values were observed to have very high variation (standard deviations $\sim 10\%$ of the measured value) even when peaks with extreme broadening were excluded. This variability can be explained by the inconsistent energetics of the initial microstructure across samples. Measurements in various superprotonic solid acid systems have revealed that the initial microstructure and strain of a sample can greatly influence the superprotonic transition enthalpy measured in the first heating cycle. Consequently, the first recorded enthalpy is frequently several standard deviations away from the mean measured in subsequent heating cycles. Far more precise results are obtained if only the subsequent heating cycles are averaged. Unfortunately, the extreme metastability of the $\text{Cs}_7(\text{H}_4\text{PO}_4)(\text{H}_2\text{PO}_4)_8$ phase prevented us from pursuing this approach, as the material was not observed to undergo the reverse superprotonic reaction even after 3 hrs at 25°C (Figure 2.S-4). Therefore, the recorded enthalpies were all measured on different samples during the first heating cycle.

Figure 2.S-5. DSC signal from a measurement in which the sample was heated to 130 °C, cooled to 25 °C, held for 3 hrs, and then heated to 130 °C again. The DSC signal illustrates that the superprotonic reaction forming $\text{Cs}_7(\text{H}_4\text{PO}_4)(\text{H}_2\text{PO}_4)_8$ occurs in the first heating cycle, but no reverse reaction is observed and no reaction is observed to occur in the second heating.

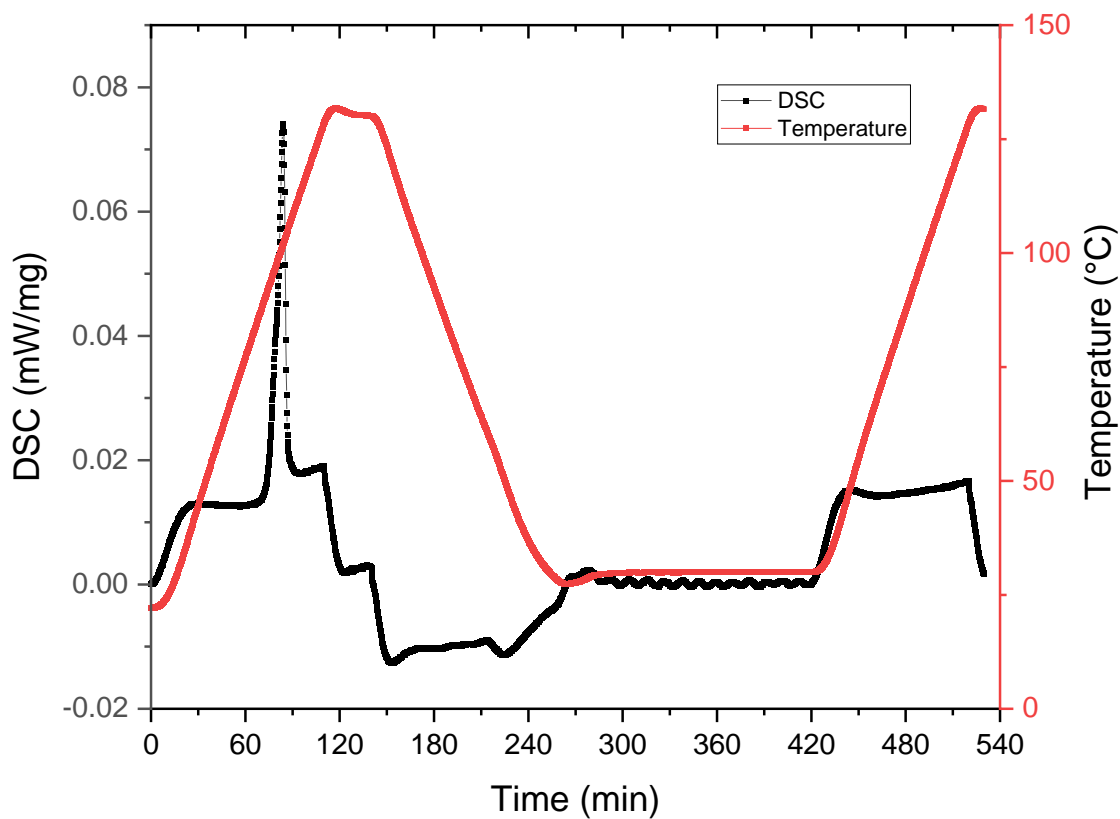
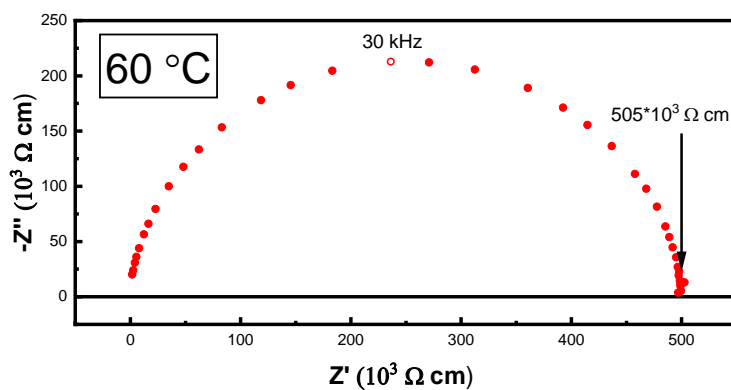


Figure 2.S-6. Representative impedance spectra for the (a) low temperature and (b) high temperature responses of $\text{Cs}_7(\text{H}_4\text{PO}_4)(\text{H}_2\text{PO}_4)_8$. Impedance values have been normalized to the thickness and area of the pellet. Note the 3 order-of-magnitude difference in the scale between the low and high temperature responses. Low temperature spectra with semi-circular arcs were fit using RQ circuits. High temperature spectra were fit using a Warburg diffusion element.

a.



b.

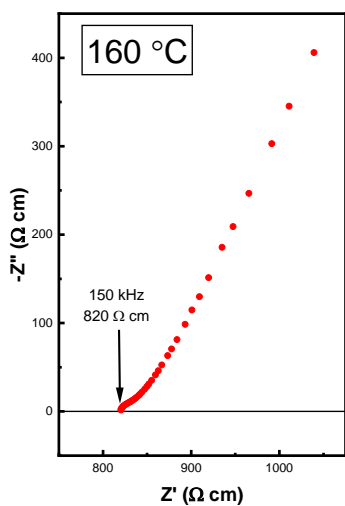


Figure 2.S-7. TGA/DSC measurements on $\text{CsH}_5(\text{PO}_4)_2$ sample with a ramp rate of $1\text{ }^\circ\text{C}/\text{min}$ under both dry and humidified Ar atmospheres. The dry Ar atmosphere was achieved with 20 sscm Ar. The humidified Ar atmosphere was achieved with the gas and water flow conditions listed in Table 2.S-5 for 0.4 atm pH_2O .

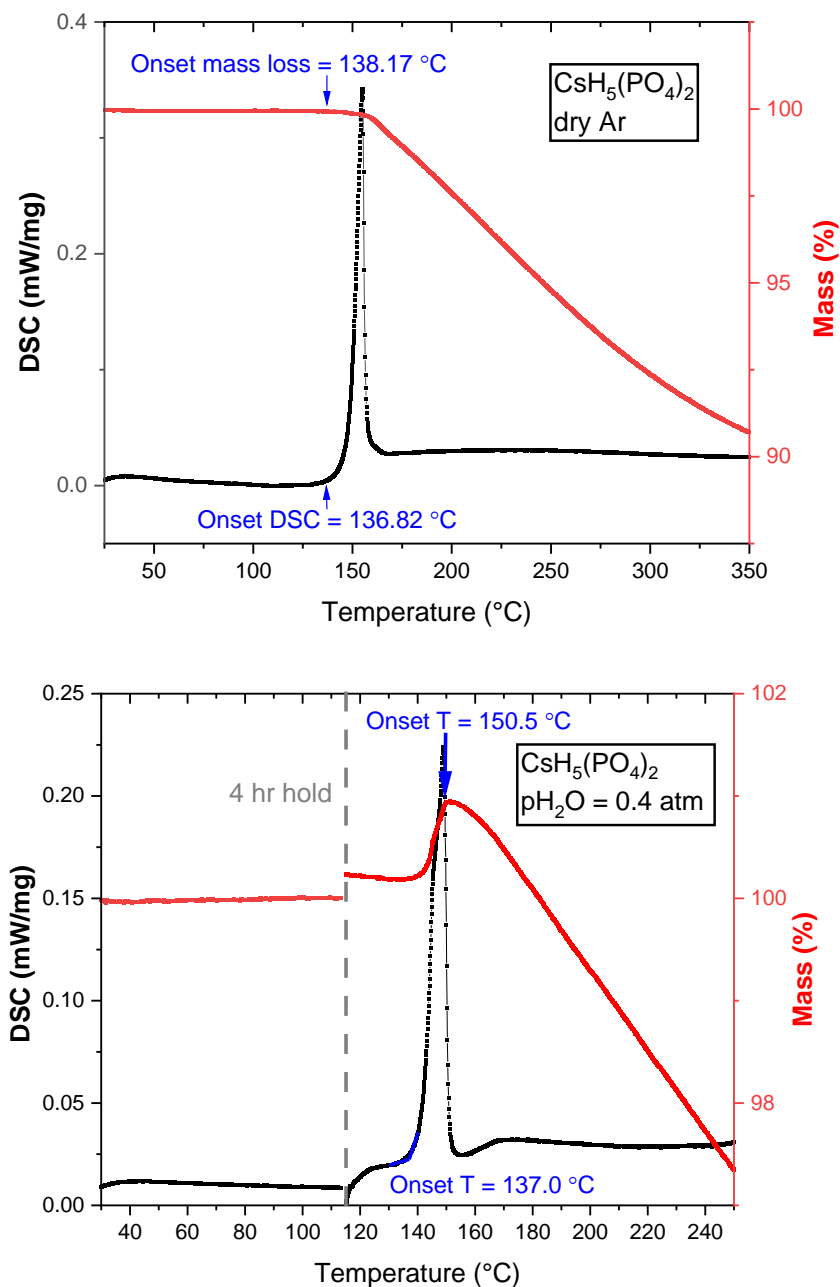
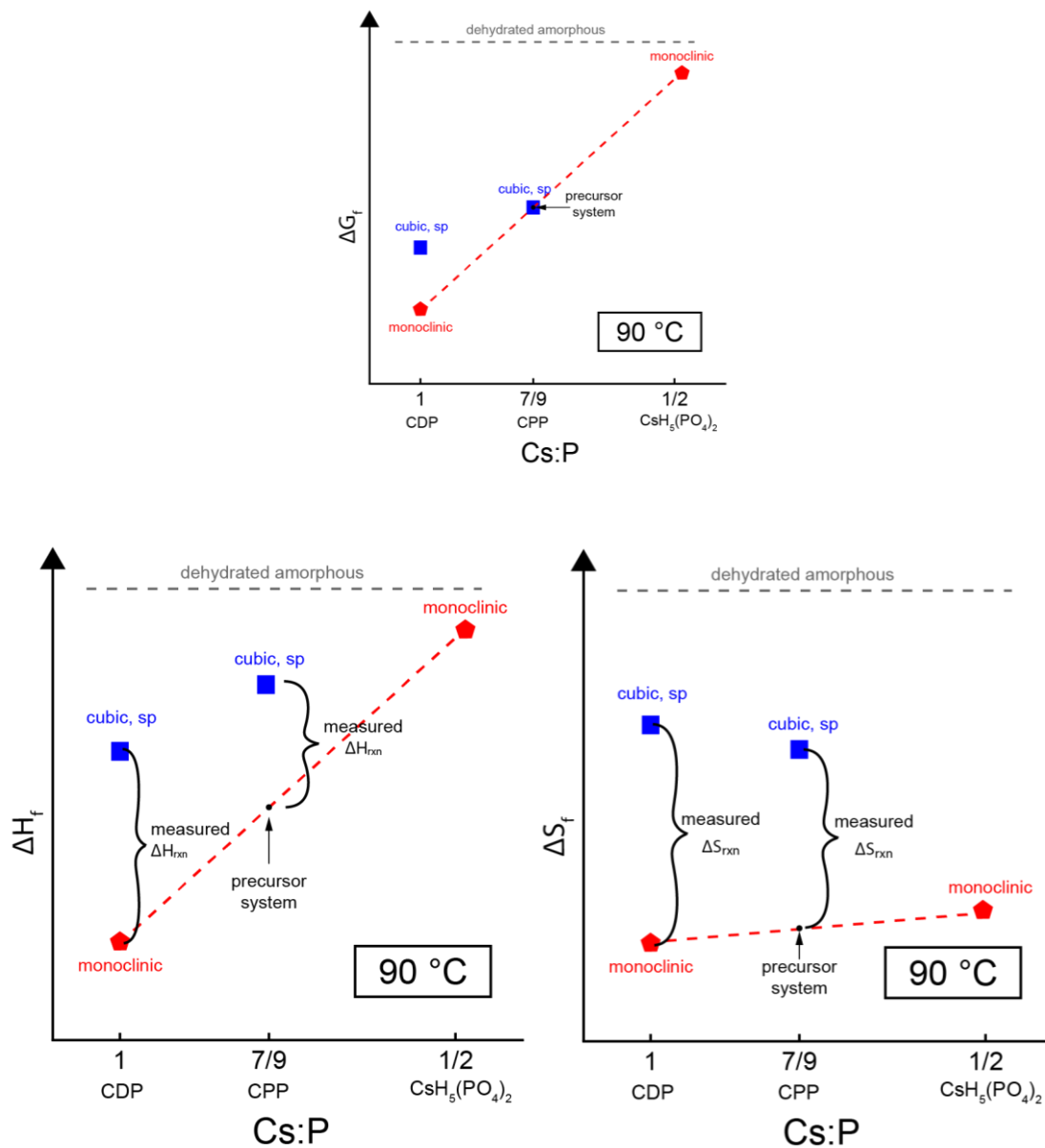


Figure 2.S-8. Schematic of proposed formation (a) Gibbs free energies, ΔG_f , (b) enthalpies, ΔH_f , and (c) entropies, ΔS_f , for the $\text{CsH}_2\text{PO}_4 - \text{CsH}_5(\text{PO}_4)_2$ phase space at 100 °C.



The proposed thermodynamic framework assumes that the liquid phase of each composition, produced either by melting or dehydration, has the same thermodynamic values of formation. In the Gibbs free energy diagram, the ΔG_f of CPP is depicted below that of the precursor mixture, reflecting the experimental stability of CPP at 100 °C. The depicted ΔH and

ΔS values for the reaction forming CPP had to be consistent with the experimental observation that these values in CPP were lower than the transition ΔH and ΔS for CDP respectively. The lower value of the ΔH of the superprotonic reaction/transition in CPP vs CDP was unexpected as it is reasonable to assume that the H_4PO_4^+ cation is highly energetically unfavorable and results in a high ΔH_f . However the anticipated high ΔH_f for CPP can be reconciled with the low measured ΔH of reaction by considering the instability of the $\text{CsH}_5(\text{PO}_4)_2$ reactant. As shown in Figure 2.S-7, the $\text{CsH}_5(\text{PO}_4)_2$ compound melts at around 130 °C, and thus its ΔH_f is likely comparable to its liquid phase at 100 °C. Thus the ΔH_f of the reactant mixture is significantly higher than the ΔH_f of monoclinic CDP alone.

From the ΔS of reaction forming CPP we postulate that the ΔS_f of CPP is less than that of cubic CDP. Although the ΔS_f of the $\text{CsH}_5(\text{PO}_4)_2$ has not been characterized, it is likely comparable to that of monoclinic CDP as the two phases are both ordered solid acids of similar chemistry and bonding. Furthermore, the instability of the $\text{CsH}_5(\text{PO}_4)_2$ compound suggests that it is unlikely that the monoclinic phase has significant entropy. As such, it is unlikely that a difference in precursor entropy produces the discrepancy in the ΔS of reactions for CPP and CDP. As stated in the main text, the reduced ΔS_f of CPP in comparison to cubic CDP is likely the result of the lower number of in anion-site phosphate orientations in CPP (3) compared to CDP (6).

Chapter 3: Phase Behavior and Superprotonic Conductivity in the System (1-x)CsH₂PO₄ – xH₃PO₄: Discovery of Off-stoichiometric α -[Cs_{1-x}H_x]H₂PO₄

Adapted with permission from: Wang, L.W., Patel, S.V., Truong, E., Hu Y-Y, Haile, S.M. Phase Behavior and Superprotonic Conductivity in the System (1-x)CsH₂PO₄-xH₃PO₄: Discovery of Off-stoichiometric α -[Cs_{1-x}H_x]H₂PO₄. *Chem. Mater.* 2022, 34, 1809-1820.

3.1 Introduction

Solid acid materials with dynamically disordered hydrogen bond networks^{72,73} have garnered interest as electrolytes due to their exceptional proton conductivities at intermediate temperatures (in the approximate range of 100 - 300 °C). These superprotonic compounds are composed of metal cations, typically alkali metals (Cs, Rb, K), and acidic oxyanions, typically protonated PO₄, SeO₄, and SO₄. At slightly elevated temperatures, the materials adopt disordered crystalline arrangements characterized by rapid oxyanion reorientation and highly mobile disordered protons. These superprotonic phases can exhibit conductivities that exceed 10⁻² S cm⁻¹.^{12,74}

Amongst the known superprotonic solid acid materials, only CsH₂PO₄ (CDP) has been employed to any significant extent in technologically relevant device demonstration and deployment. This is primarily because only the phosphate anion displays the requisite chemical stability in both oxidizing and reducing environments for device operability.^{12,49,75} Solid acids incorporating SO₄ and SeO₄ groups generally react with hydrogen to generate H₂S and H₂Se byproducts, respectively.⁷⁶ The superprotonic transition in CDP occurs at 228 °C and results in a transformation from a low temperature monoclinic phase to a superprotonic cubic phase with a CsCl-like structure with orientationally-disordered H₂PO₄⁻ anions.^{12,77,78} At 250 °C the proton conductivity is 2.5 × 10⁻² S cm⁻¹.^{12,77} While the transport properties and redox stability of CDP are well-suited for a range of electrochemical applications, there has been some interest in extending the range of superprotonic conductivity to below 228 °C and/or increasing the

conductivity of the low temperature phase so as to minimize possible challenges with the three orders of magnitude increase in conductivity at the superprotonic phase transition. Approaches to achieving these goals include preparation of composites,^{30,79-83} homogeneous doping^{84,85} (via substitutional elements in the CDP structure), and heterogeneous doping^{57,86,87} (via introduction of secondary components, which can be considered a form of composite preparation).

Of the strategies employed to improve the overall properties of CDP, recent work of Ponomareva and coworkers is intriguing for its use of additives such as $\text{CsH}_5(\text{PO}_4)_2$ and H_3PO_4 ⁵⁷, and $\text{Cs}_2\text{HPO}_4 \cdot \text{H}_2\text{O}$ and $\text{Cs}_3(\text{H}_{1.5}\text{PO}_4)_2$ ⁸⁶ to CDP, described by those authors to be heterogeneous dopants. In all cases, the additives increased the conductivity at temperatures below the superprotonic transition with minimal impact on the high temperature conductivity, and in some cases, also improved stability against dehydration. In parallel with this work, we recently showed the existence of the new compound $\text{Cs}_7(\text{H}_4\text{PO}_4)(\text{H}_2\text{PO}_4)_8$ or CPP, which forms at 90 °C through stoichiometric reaction of CDP and $\text{CsH}_5(\text{PO}_4)_2$.⁸⁸ This compound is structurally similar to CDP with rotationally disordered phosphate anions arranged in an approximately simple cubic arrangement. It differs from CDP in that one in eight cations is the unusual polycation group H_4PO_4^+ , and the ordered arrangement of these species generates a cell that has a $4 \times 4 \times 4$ superstructure relative to conventional superprotonic CDP. The compound exhibits a moderate conductivity of $5.8 \times 10^{-4} \text{ S cm}^{-1}$ at 140 °C, and was found to be thermally stable under nominally dry Ar up to ≈ 150 °C.

The existence of CPP indicates that the phase behavior of mixtures of CDP and $\text{CsH}_5(\text{PO}_4)_2$ must be more complex than suggested by the concept of heterogeneous doping. Accordingly, we undertake here a systematic study of the $(1-x)\text{CsH}_2\text{PO}_4 - x\text{H}_3\text{PO}_4$ system from $x = 0$ (CDP) to $x =$

2/9 (CPP). We find at temperatures above 90 °C a two-phase region composed of stoichiometric monoclinic CDP and stoichiometric CPP. At further elevated temperatures, we observe solution behavior and find that cubic CDP, previously considered to be a compound of fixed stoichiometry in the $\text{Cs}_3\text{PO}_4 - \text{H}_3\text{PO}_4$ phase space, in fact, exists over a wide composition range. We show that the structural chemistry in the solid solution region is described macroscopically according to $[\text{Cs}_{1-x}\text{H}_x]\text{H}_2\text{PO}_4$ and explore the impact of Cs deficiency on the proton transport properties. The insights presented here open up a new approach to modifying the physical and chemical properties of superprotonic solid acids.

3.2 Methods

Crystals of CDP and $\text{CsH}_5(\text{PO}_4)_2$ were independently grown from stoichiometric aqueous solutions of CsCO_3 and phosphoric acid by evaporation. Samples of various compositions were created from these crystals, which were ground together and homogenized in a mortar and pestle. Dense compacts of each sample were obtained by uniaxial pressing, and the samples were subsequently annealed at elevated temperature for several (1-3) days with introduction of humidity as required to prevent dehydration. In the case of compositions $x = 2/9$ and 0.18, this step was carried out at 130 °C under dry N_2 , whereas for compositions $0 < x < 0.18$, the temperature was 230 °C and the atmosphere humidified N_2 (steam partial pressure, $p_{\text{H}_2\text{O}} = 0.4$ atm). X-ray diffraction of the annealed samples, collected after exposure to ambient temperature for several (3-14) days, revealed the original precursor phases in the anticipated relative quantities (as shown for example for the $x = 0.07$ material, Figure 3.S-1), despite the sluggishness of the reverse transition returning the high temperature phase(s) to a mixture of CDP(m) and $\text{CsH}_5(\text{PO}_4)_2$. Here, the combination of the extended period of time at ambient

temperature and additional grinding prior to XRD are presumed to have facilitated the reverse reaction. The annealing step was found to improve kinetics for the various phase transitions during heating, likely due to enhanced contact between particles of different phases, and thus all measurements reported here are from annealed, reground samples.

3.2.1 Thermal Analysis

The thermodynamics of various processes (phase transitions, phase formation reactions, dehydration reactions) were measured by simultaneous thermogravimetric analysis (TGA) and differential scanning calorimetry (DSC) using a Netzsch STA F3 equipped with a water vapor generator. Just prior to measurement, annealed compacts were ground and powder samples (~60 mg) were lightly pressed into platinum pans. Measurements were conducted with Ar protective and carrier gas streams, and a 1 °C/min heating rate was used in all ramp steps. Steam was produced by the water vapor generator and introduced during 2 h isothermal holds at 130 °C to create highly humidified atmospheres ($p_{\text{H}_2\text{O}} = 0.4 - 0.6 \text{ atm}$). The humidified atmosphere was maintained at all temperatures above 130 °C.

3.2.2 X-ray Diffraction

High temperature X-ray diffraction (HTXRD) measurements were conducted on a Rigaku Ultima diffractometer with an in-house constructed stage that allowed for active humidification of the sample atmosphere. A N_2 gas stream was passed through a temperature-controlled bubbler to create various levels of humidification ($p_{\text{H}_2\text{O}} = 0.4 - 0.7 \text{ atm}$) prior to entering the sample chamber. Humidified gas flow was supplied only at sample temperatures above 130 °C. Samples were prepared by pressing dense compacts from the annealed, reground powders. This was done to create intimate contact between precursor phases which was crucial to achieving complete reaction of the reactants. Samples were heated at a ramp rate of 1 °C/min and held at each

temperature for 20 minutes before measurement. Diffraction patterns were collected with a 5° $2\theta/\text{min}$ scan rate and a 0.3° step size. Rietveld refinement against the diffraction patterns to obtain lattice parameters and phase fractions was performed using the software GSAS-II and the established structures of the relevant phases (monoclinic CDP, monoclinic $\text{CsH}_5(\text{PO}_4)_2$, cubic CDP, and cubic CPP).

3.2.3 NMR

Further structural characterization was achieved through high-temperature solid-state ^1H and ^{31}P magic angle spinning (MAS) nuclear magnetic resonance (NMR) spectroscopy. All NMR spectra were collected on a Bruker spectrometer at a Larmor frequency of 500 MHz for ^1H and 202 MHz for ^{31}P , using a laser MAS probe at a spin rate of 4 kHz. Powder samples were packed into a 4-mm insert which was loaded into a 7-mm rotor and placed into the probe. Variable-temperature ^1H and ^{31}P NMR spectra were collected between room temperature and 200°C . For lower-temperature ^1H NMR measurements below 160°C , a spin echo pulse sequence with a $\pi/2$ -pulse of $4.40\ \mu\text{s}$ was applied with a recycle delay of 500 s. At 160°C , the recycle delays were optimized and a 10 s delay was used for all subsequent higher temperature measurements. For ^{31}P NMR measurements, a single $\pi/2$ -pulse of $5.00\ \mu\text{s}$ was applied with a recycle delay of 1000 s for low temperatures, which was then changed to 30 s for measurements at 160°C and above. An inversion recovery pulse sequence was used to determine the T_1 relaxation times for ^1H and ^{31}P at temperatures between $160 - 200^\circ\text{C}$. In all measurements, 10 min of temperature equilibration was allowed at each step prior to data acquisition. The ^{31}P NMR shifts were calibrated using $(\text{NH}_4)_2\text{HPO}_4$ with a ^{31}P resonance at 1.34 ppm. The ^1H NMR shifts were calibrated using adamantane with a ^1H resonance at 1.83 ppm. Sample heating was achieved using a diode laser, and temperature values were calibrated using ^{79}Br NMR of dry KBr.

3.2.4 Impedance Spectroscopy

Dense compacts for conductivity measurements, roughly 1 mm thick, were prepared by pressing powder samples at 280 MPa for 5 minutes and then at 390 MPa for 5 min, achieving >92 % theoretical density. Silver electrodes, ~100 nm in thickness, were sputtered on each side. AC impedance spectra were collected at temperatures ranging from 60 - 250 °C in a flowing N₂ atmosphere (40 sccm). At temperatures of 130 °C and above, the N₂ gas was humidified to either 0.69 atm of steam (for samples $x = 0.18, 0.15,$ and 0.07) or 0.47 atm of steam (for samples $x = 0.05,$ and 0.02). Humidification was achieved by passing the gas stream through a bubbler maintained at either 90 or 80 °C, respectively. The samples were held at each measurement temperature for 30 min prior to recording impedance, with a heating rate of 2 °C/min applied between steps. Data were collected using an Agilent 4284A LCR analyzer over the frequency range 20 - 10⁵ Hz with a 20 mV amplitude. Impedance data were analyzed using the commercial software package Zview.

3.3 Results and Discussion

The phase diagram of the $(1-x)\text{CsH}_2\text{PO}_4-x\text{H}_3\text{PO}_4$ system in the CsH_2PO_4 -rich region, as deduced from the thermal, XRD, and NMR studies described in detail below, is shown in Figure 1. The compounds CDP, CPP and $\text{CsH}_5(\text{PO}_4)_2$ all occur in this system. A remarkable finding here is that the cubic superprotonic phase of CDP can accommodate a high level of Cs deficiency by forming vacancies on the cation site which are charge-balanced by excess protons. The resulting composition is $[\text{Cs}_{1-x}\text{H}_x]\text{H}_2\text{PO}_4$ and, recognizing the compositional variability, the cubic phase is hereafter designated α -CDP(ss), where ss = solid solution. This compound exhibits

eutectoid behavior with a eutectoid composition and temperature of $x = 0.18$ and $T = 155\text{ }^\circ\text{C}$, respectively.

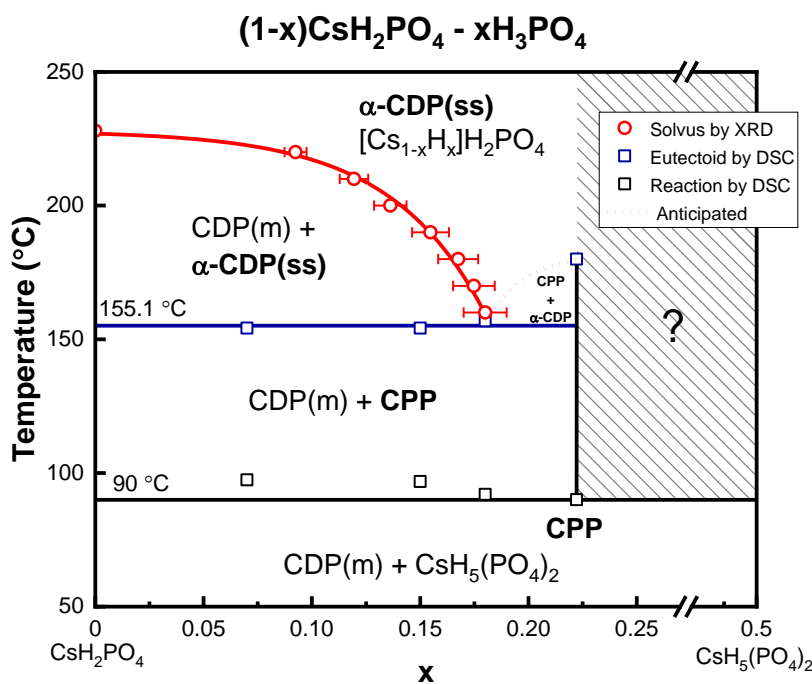


Figure 3.1. Phase diagram of the $(1-x)\text{CsH}_2\text{PO}_4 - x\text{H}_3\text{PO}_4$ system in the Cs-rich region.

3.3.1 Direct Characterization of Phase Behavior

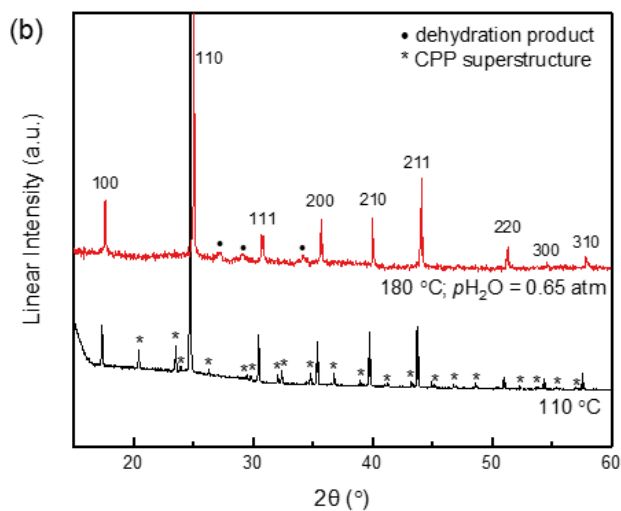
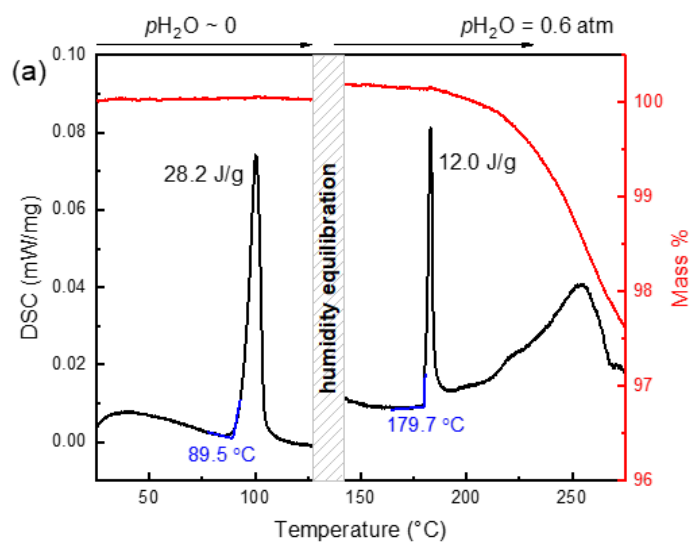
The phase transformation behavior of three compositions in the $(1-x)\text{CsH}_2\text{PO}_4 - x\text{H}_3\text{PO}_4$ system are summarized in Figures 2 – 6. The examples selected correspond to (i) CPP, $x = 2/9$ (Figure 3.2), with selected data taken from our previous work,⁸⁸ (ii) the eutectoid composition, $x = 0.18$ (Figure 3.3 –Figure 3.5), and (iii) a representative composition rich in Cs relative to the eutectoid, $x = 0.07$ (Figure 6). The data reported are the simultaneous DSC/TGA profiles (with corresponding dTG profiles in Figure 3.S-2) and in situ diffraction patterns for all three

compositions, along with variable temperature NMR spectra for the eutectic composition.

Thermal analysis data for an additional composition in the Cs rich region ($x = 0.15$) are provided in the supplementary information (Figure 3.S-3).

For all samples, the ambient temperature diffraction patterns (example shown in Figure 3.S-1) revealed a mixture of monoclinic CDP [hereafter CDP(m)] and $\text{CsH}_5(\text{PO}_4)_2$ phases. For the material of global composition $x = 2/9$, the mixture of CDP(m) and $\text{CsH}_5(\text{PO}_4)_2$ reacted at 90 °C to form stoichiometric CPP, a result that is consistent with what we have reported previously⁸⁸. This reaction is revealed by an endothermic event that occurs without mass loss at 90 °C (Figure 3.2a) and in the diffraction pattern collected at 110 °C (Figure 3.2). In highly humidified atmospheres ($p_{\text{H}_2\text{O}} = 0.6$ atm), further heating produced a second sharp thermal anomaly at 180 °C. While mass loss quickly followed this thermal event, the event itself was independent of mass loss. This transition was noted in our previous work, however, we had not fully established its nature.⁸⁸ Here we find the transition to correspond to the complete transformation of CPP to a simple cubic phase, Figure 3.2b ($T = 180$ °C). The lattice constant of this new phase, $a = 5.0445(7)$ Å, is substantially smaller than the subcell lattice parameter of CPP, $5.0577(7)$ Å at 175 °C, indicating a contraction in molar volume at the transition, Figure 3.2c. Rietveld refinement (Figure 3.S-4) showed the 180 °C pattern to be consistent with the structure of cubic superprotonic CDP (CsCl-type, space group $Pm\bar{3}m$), with the exception of a difference in cell parameter. Stoichiometric cubic CDP, which exists only at temperatures of 228 °C and higher, has a cell parameter of $4.970(3)$ Å at 250 °C,⁶ significantly smaller than that of the material encountered here. Recognizing this new material to share the phase space of stoichiometric, CsH_2PO_4 , it is designated α -CDP(ss), where ss = solid solution. Except for the

unusual subcell contraction at the transition from CPP to α -CDP(ss), the thermal expansion behavior of α -CDP(ss) encountered at this composition is rather standard, Figure 3.2c.



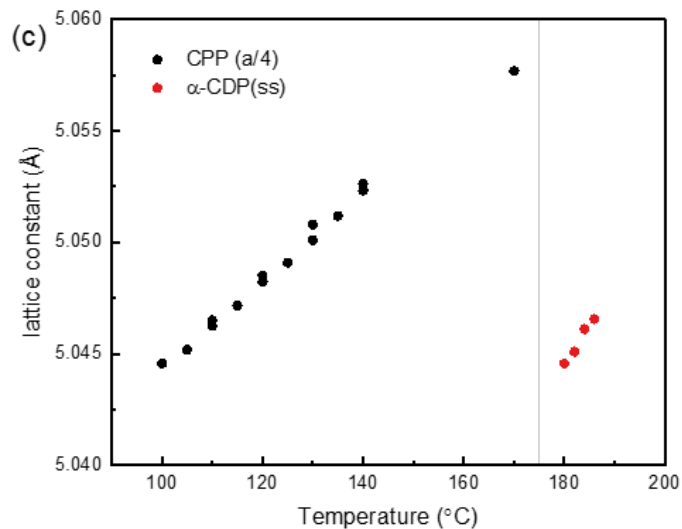


Figure 3.2. Phase transformation behavior of $(1-x)\text{CsH}_2\text{PO}_4 - x\text{H}_3\text{PO}_4$ at $x = 2/9$, the composition corresponding to the compound $\text{Cs}_7(\text{H}_4\text{PO}_4)(\text{H}_2\text{PO}_4)_8$ or CPP: (a) simultaneously measured TGA/DSC profiles at a heating rate of $1\text{ }^\circ\text{C}/\text{min}$ (data after ref⁸⁸ with permission from the American Chemical Society); (b) XRD patterns measured at the temperatures and $p\text{H}_2\text{O}$ values indicated ($T = 110\text{ }^\circ\text{C}$, pattern after ref⁸⁸ with permission from the American Chemical Society); and (c) lattice constant as a function of temperature (uncertainties in the refined values fall within the span of the datapoint symbols, Figure 3.S-4). In (a), $p\text{H}_2\text{O} = 0.6\text{ atm}$ (balance Ar) was introduced at $130\text{ }^\circ\text{C}$ as part of the heating protocol, and data reflecting system equilibration to the high humidity condition are omitted. The results reveal the transitions: $\text{CDP(m)} + \text{CsH}_5(\text{PO}_4)_2 \rightarrow \text{CPP}$ @ $90\text{ }^\circ\text{C}$ and $\text{CPP} \rightarrow \alpha\text{-CDP(ss)}$ @ $180\text{ }^\circ\text{C}$.

The eutectoid composition sample ($x = 0.18$) similarly revealed reaction between CDP(m) and $\text{CsH}_5(\text{PO}_4)_2$ at $90\text{ }^\circ\text{C}$ to form CPP, as indicated by a sharp endothermic peak at this temperature (Figure 3.3a). In this case, however, the CPP product appeared in equilibrium with excess CDP(m) (Figure 3.3b, $T = 140\text{ }^\circ\text{C}$ pattern). This two-phase mixture was stable up to $157\text{ }^\circ\text{C}$, at which temperature CDP(m) and CPP underwent further reaction, as indicated by a second large, binodal and extended endothermic feature in the DSC profile (Figure 3.3a). The diffraction pattern collected at $160\text{ }^\circ\text{C}$ revealed the reaction to correspond to the complete transformation to a simple cubic phase with lattice constant $5.0277(3)\text{ \AA}$ and hence the formation of $\alpha\text{-CDP(ss)}$. As was the case for the $x = 2/9$ sample, the absence of mass loss upon the formation of $\alpha\text{-CDP(ss)}$

implies that the composition of the cubic phase is equal to that of the global sample. The overall shape of the DSC signal associated with the eutectoid reaction, bi-nodal peak followed by a long tail, is somewhat unusual. This behavior, which was not observed for $x = 2/9$, is tentatively ascribed to the timescale of interdiffusion between CDP(m) and CPP required to form the α -CDP(ss) phase. That is, under the 1 °C/min heating rate used in the thermal analysis studies the eutectoid reaction evidently does not reach completion until 180 °C. In contrast, equilibration at 160 °C in the diffraction experiment was apparently possible due to the slower effective heating rate, in which data were acquired after a 20 min hold at the measurement temperature. Rietveld analysis (Figure 3.S-5) showed this pattern, as in the $x = 2/9$ case, to be consistent with the structure of cubic superprotonic CDP, with the exception of having a distinctly larger lattice constant. However, the cell volume of the α -CDP(ss) obtained at $x = 0.18$ was substantially smaller than that obtained from the $x = 2/9$ material, a phenomenon discussed further below. The thermal expansion behavior of α -CDP(ss) at the eutectoid composition, now captured over the temperature range from 160 to 178 °C, was again unremarkable (Figure 3.3c).

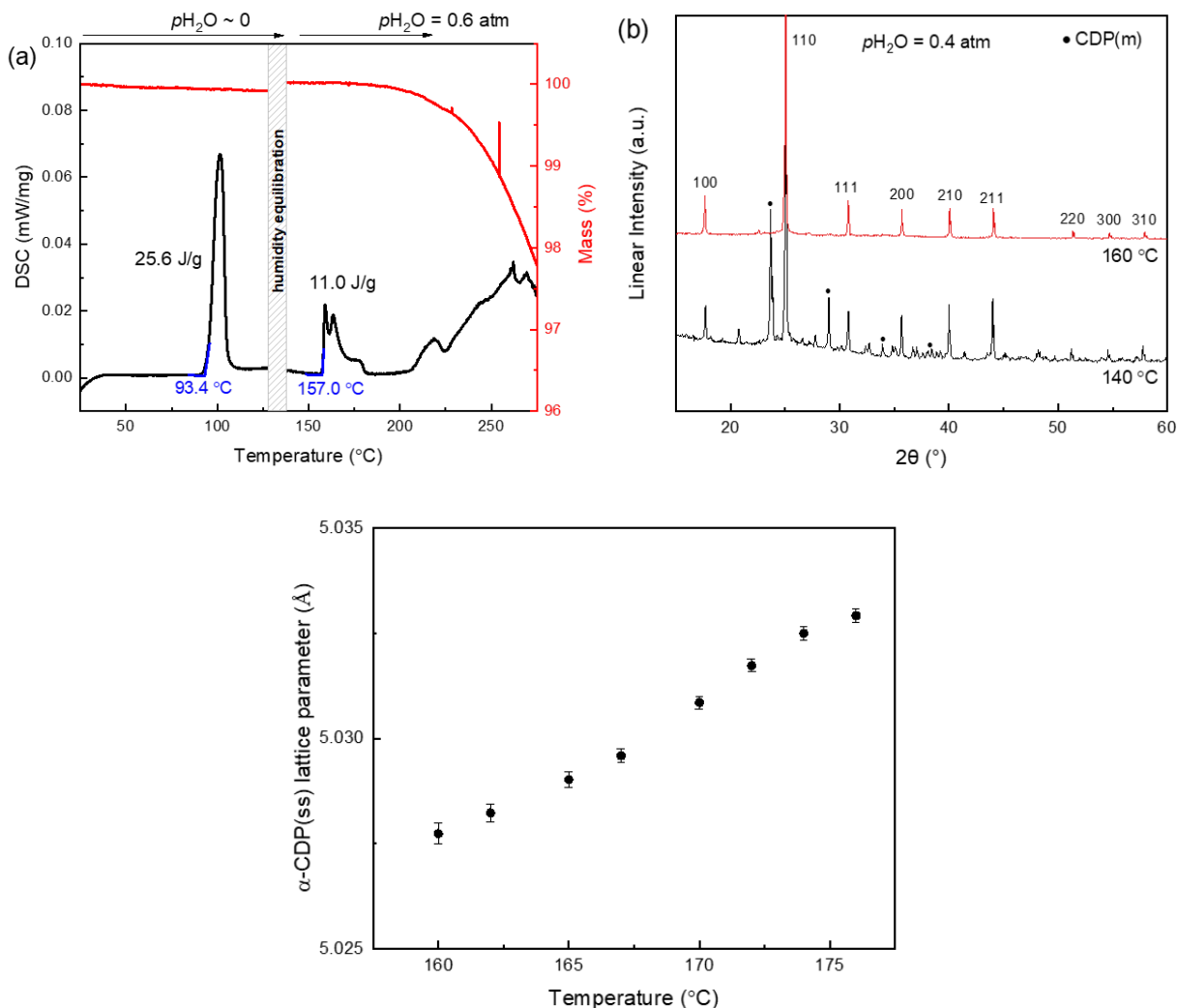


Figure 3.3 Phase transformation behavior of $(1-x)\text{CsH}_2\text{PO}_4 - x\text{H}_3\text{PO}_4$ at $x = 0.18$, the eutectoid composition: (a) XRD patterns measured at the temperatures indicated with inset showing cubic lattice parameter; (b) simultaneously measured TGA/DSC profiles at a heating rate of $1^\circ\text{C}/\text{min}$; and (c) lattice constant obtained from Rietveld refinement as a function of temperature. Data in (a) at temperatures of 130°C and above were collected with the sample chamber atmosphere maintained at $p_{\text{H}_2\text{O}} = 0.4 \text{ atm}$ (balance N_2), whereas those in (b) were collected with sample chamber atmosphere maintained at $p_{\text{H}_2\text{O}} = 0.6 \text{ atm}$ (balance Ar). Data reflecting system equilibration to the high humidity condition at 130°C are omitted from (a). The results reveal the transitions: $\text{CDP(m)} + \text{CsH}_5(\text{PO}_4)_2 \rightarrow \text{CDP(m)} + \text{CPP}$ @ 90°C and $\text{CDP(m)} + \text{CPP} \rightarrow \alpha\text{-CDP(ss)}$ @ 160°C .

The ^{31}P and ^1H NMR results for the $x = 0.18$ material, Figure 3.4 and Figure 3.5, respectively, generally agree with the XRD and DSC findings. The spectra collected at $140\text{ }^\circ\text{C}$ show the sample existed as a two-phase mixture of CDP(m) and CPP. CPP is represented in the ^{31}P spectrum at this temperature by the two cation-site phosphorus resonances (4.6 and 3.7 ppm) as well as the anion-site phosphorus resonance (0.3 ppm)¹², whereas in the ^1H spectra it is represented by the sharp resonance at 13.2 ppm (at $120\text{ }^\circ\text{C}$). The presence of CDP(m) is more difficult to discern given its relatively low molar fraction of the sample ($< 20\%$) and the broader resonances characteristic of this phase. Nevertheless, its presence can be observed in the ^{31}P spectra as a broad resonance at -4.5 ppm and in the ^1H spectra as a broad feature at ~ 11.6 ppm (Figure 3.S-6, too small for Figure 3.4a and Figure 3.5a). These resonances are consistent with previous reports for CDP(m),^{14,15} though it is noted that the expected proton resonance of CDP(m) at ~ 14 ppm is obscured by the larger CPP resonance. Heating induces changes in the spectra that reflect the formation of single phase α -CDP(ss). In the ^1H spectra (Figure 3.5) a new resonance emerges at $165\text{ }^\circ\text{C}$ at a shift of 12.6 ppm and grows with temperature at the expense of the CPP resonance now at 12.9 ppm, until the latter is no longer observed at $185\text{ }^\circ\text{C}$. The coexistence of signals from the two phases from 165 to $180\text{ }^\circ\text{C}$ is attributed to the sluggish kinetics of the reaction, as discussed in the context of the thermal behavior, along with a likely thermal gradient in the rotor, rather than thermodynamic equilibrium between the two compounds. Close examination of the high-temperature spectra indicates a splitting of the new ^1H peak (Figure 3.S-7a), potentially due to ^{31}P - ^1H J-coupling, but the effect was not further explored. In the ^{31}P spectra (Figure 3.4), the consumption of CPP is evident by the loss of intensity from the cation-site resonances, an effect which initiates at $160\text{ }^\circ\text{C}$ and appears

complete by 175 °C. Simultaneously, the resonance associated with the anion-site phosphorous, at -0.4 ppm at 160 °C, broadens and is resolvable into two peaks over the temperature range 165 to 175 °C (Figure 3.S-7b). The emergent, slightly upfield peak within this pair is attributed to α -CDP(ss). Its position, after accounting for the obvious temperature dependence evident in Figure 3.4b, is similar to that of the phosphorus resonance in superprotonic stoichiometric CDP, which occurs at a shift of -1.8 ppm⁸⁹ at 250 °C. Distinct T_1 relaxation times were measured for the two anion-site resonances, Figure 3.4c, with faster dynamics indicated in α -CDP(ss) ($T_1 \approx 2$ s) than CPP (T_1 falling with temperature from ≈ 8 s to ≈ 5 s). At 180 °C and above, only the anion-site phosphorus resonance remains, indicating that this is the sole phosphorus environment in α -CDP(ss).

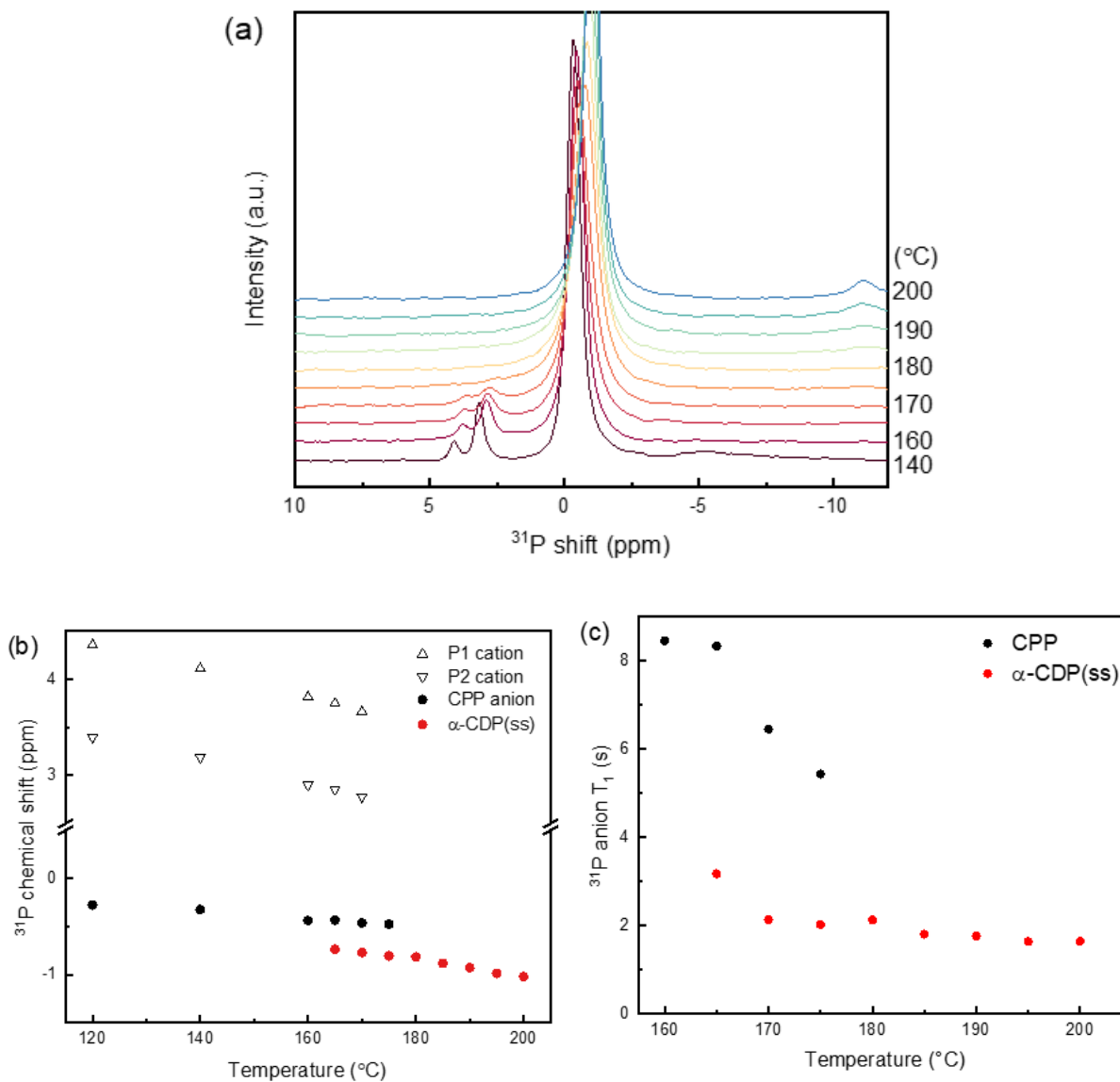


Figure 3.4. Variable temperature ^{31}P NMR measurements of $(1-x)\text{CsH}_2\text{PO}_4 - x\text{H}_3\text{PO}_4$ at $x = 0.18$, the eutectoid composition: (a) spectra collected at indicated temperatures; (b) chemical shifts as a function of temperature; (c) and T_1 relaxation time of the ~ 0 ppm resonance as a function of temperature.

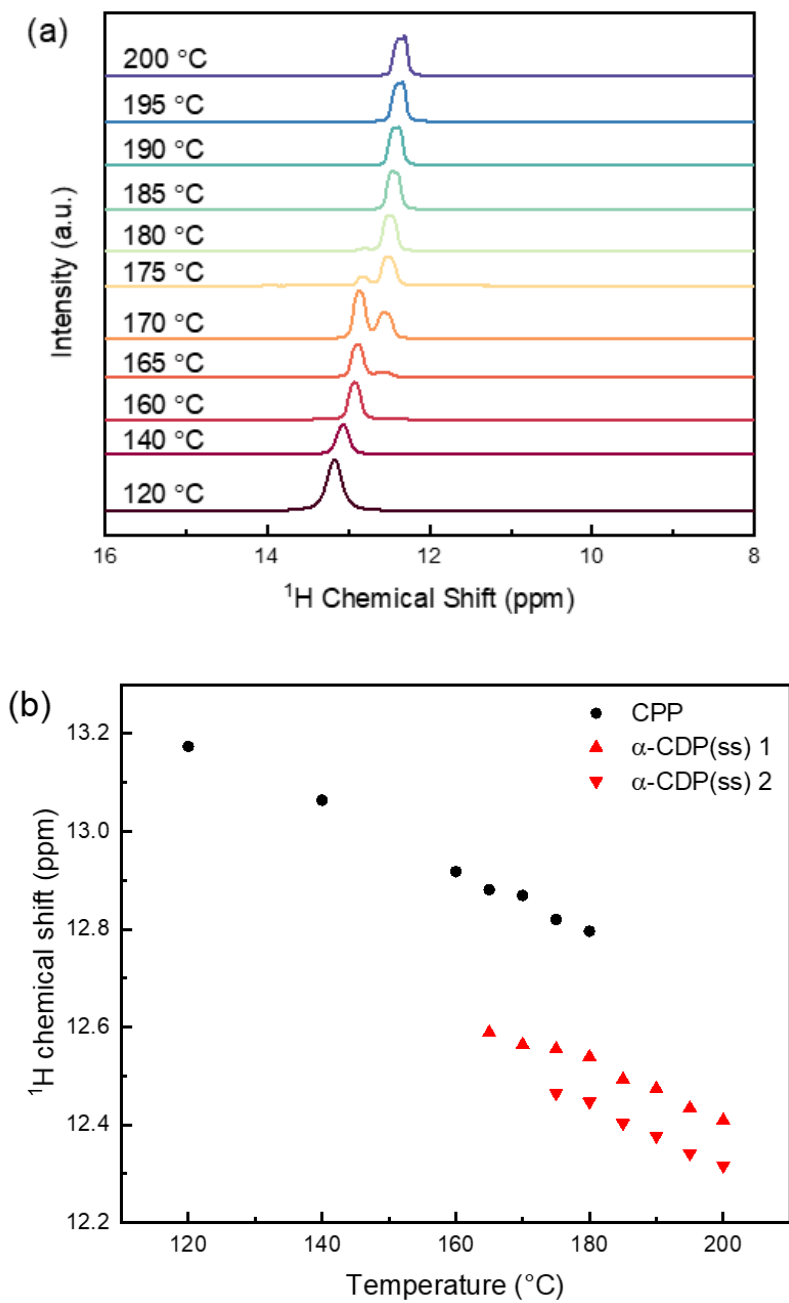


Figure 3.5. Variable temperature ^1H NMR measurements of $(1-x)\text{CsH}_2\text{PO}_4 - x\text{H}_3\text{PO}_4$ at $x = 0.18$, the eutectoid composition: (a) spectra collected at indicated temperatures; and (b) chemical shifts as a function of temperature.

Turning to the behavior in the Cs-rich region of the phase diagram ($x = 0.07$), Figure 3.6, the two-phase mixture of CDP(m) and $\text{CsH}_5(\text{PO}_4)_2$ present at ambient temperature reacted on heating to form CPP in equilibrium with excess CDP(m). Similar to the other compositions, the endothermic formation of CPP occurred, without mass loss, Figure 3.6a, but in this case the reaction kinetics were slightly retarded, and the thermal signal was detected with an onset at 97 °C. The diffraction pattern collected at 150 °C revealed stoichiometric quantities of the two phases (CPP and CDP(m)), Figure 3.6b. On further heating, the mixture underwent a second reaction at 154 °C to yield eutectoid α -CDP(ss), now in equilibrium with excess CDP(m). The thermal signature reveals a binodal peak that initiates at this temperature, similar to what was observed for the eutectic composition (Figure 3.6a). The formation of α -CDP(ss) can be clearly seen in the diffraction pattern collected at 160 °C from the presence of the (110) peak of this phase at $25.1^\circ 2\theta$ (Figure 3.6b, see also Figure 3.S-8). The lattice parameter of α -CDP(ss) at 160 °C was 5.028(5) Å, essentially identical to that found for the sample with the eutectoid composition (5.0277(3) Å). The diffraction data further revealed the presence of residual CPP at 160 °C, even though, in principle, this phase is not expected to coexist with α -CDP(ss) under such conditions ($T = 160$ °C, $x = 0.07$); this is likely due to a small thermal gradient across the sample stage. Increasing the temperature to 170 °C induced the reaction of the remaining CPP, leaving a two-phase mixture of α -CDP(ss) and CDP(m). Further heating between 170 – 230 °C resulted in a gradual consumption of CDP(m) by dissolution into the α -CDP(ss) phase as evidenced in the diffraction data by a decrease in the CDP(m) peak intensities and an increase in the intensities of the peaks due to α -CDP(ss). The dissolution was detected in the thermal data by a long and substantial endothermic event which peaked at 216.5 °C. This process was moreover

accompanied by a *decrease* in the cell parameter of α -CDP(ss) (Figure 3.6c), which terminated only with the complete consumption of CDP(m) at 230 °C. Positive linear thermal expansion of α -CDP(ss) was observed at temperatures above 230 °C. Thus, the lattice contraction of α -CDP(ss) with heating is concluded to be a result of CDP(m) incorporation and the accompanying change in composition. In contrast, CDP(m) underwent conventional thermal expansion, consistent with previous characterizations of this phase⁹⁰ (Figure 3.S-9a).

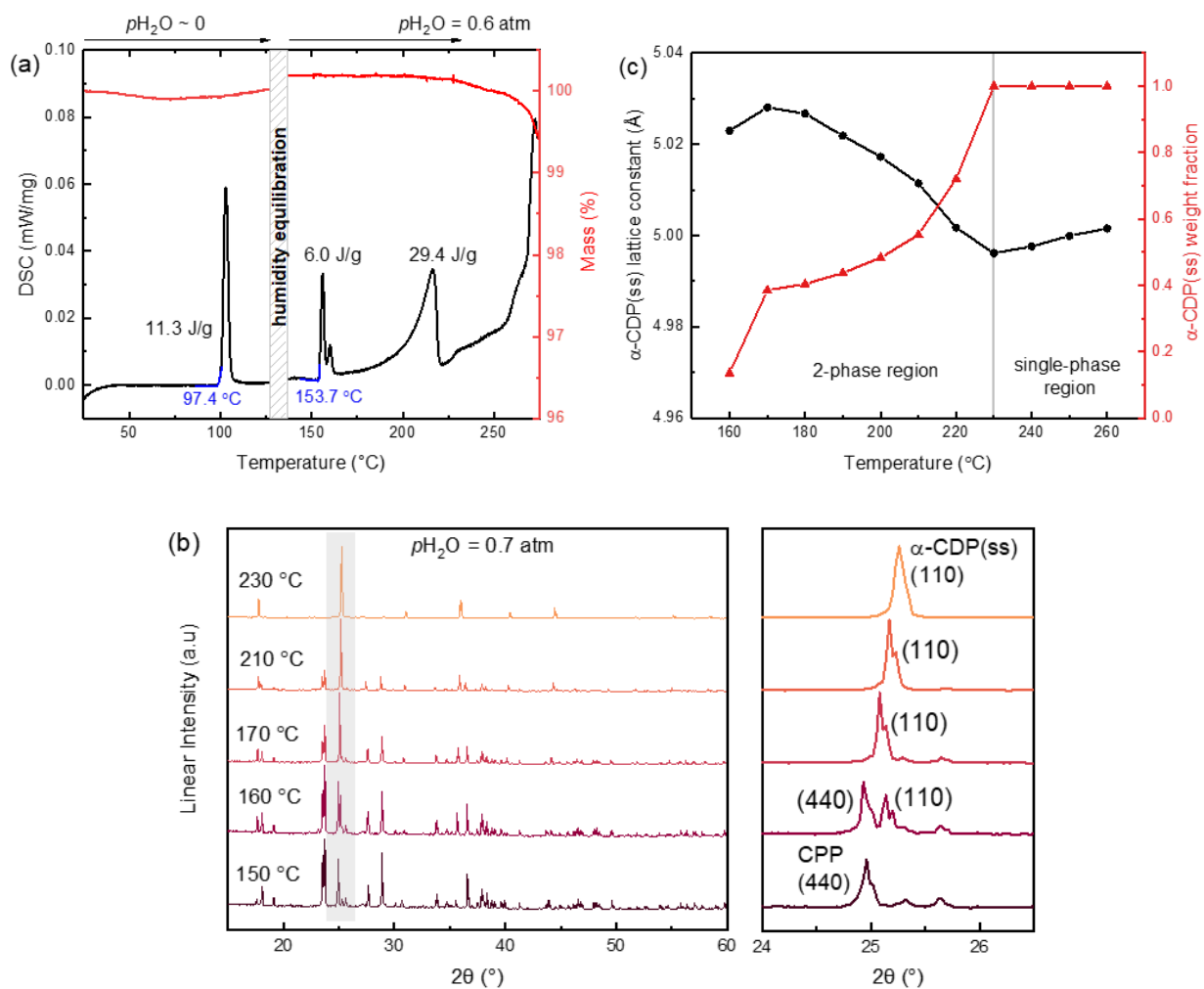


Figure 3.6. Phase transformation behavior of $(1-x)\text{CsH}_2\text{PO}_4 - x\text{H}_3\text{PO}_4$ at $x = 0.07$: (a) Simultaneously measured TGA/DSC profiles at a heating rate of $1^{\circ}\text{C}/\text{min}$; (b) XRD patterns measured at the temperatures indicated; and (c) lattice constant and weight fraction as functions of temperature (uncertainties in the refined values fall within the span of the datapoint symbols). In (a) $p\text{H}_2\text{O} = 0.6 \text{ atm}$ (balance Ar) was introduced at 130°C as part of the heating protocol, and data reflecting system equilibration to the high humidity condition are omitted. In (b) were collected with the sample chamber atmosphere maintained at $p\text{H}_2\text{O} = 0.7 \text{ atm}$ (balance N_2). In (c) the lines between points serve only to guide the eye and do not reflect sample behavior between points. The results reveal the transitions: $\text{CDP(m)} + \text{CsH}_5(\text{PO}_4)_2 \rightarrow \text{CDP(m)} + \text{CPP}$ @ 90°C and $\text{CDP(m)} + \text{CPP} \rightarrow \text{CDP(m)} + \alpha\text{-CDP(ss)}$ @ 160°C .

It is to be emphasized that all of the phase transitions discussed above occurred in the absence of mass loss, as shown unequivocally by the differential thermal gravimetric (dTG) profiles (Figure 3.S-2) derived from TGA profiles reported in Figure 3.2a, Figure 3.3a, and Figure 3.6a. The dTG analysis reveals a decreasing stability limit with increasing x . Specifically, with 0.6 atm partial pressure of steam CDP ($x = 0$) is known to dehydrate at $T_d = 284$ °C.⁹¹ Here, mass loss was observed to initiate under $p_{\text{H}_2\text{O}} = 0.6$ atm at $T_d = 225$ °C, 184 °C, and 180 °C, respectively, when $x = 0.07$, 0.18 and 2/9. At the composition of CPP, the α -CDP(ss) phase is thus barely captured under $p_{\text{H}_2\text{O}} = 0.6$ atm before decomposition occurs. A widening of the stability window under higher $p_{\text{H}_2\text{O}}$ (as expected thermodynamically) has been shown elsewhere.⁸⁸ Here, the decomposition of the other compositions has not been studied as systematically, and the quoted temperatures for the onset of mass loss reflect the lower bounds for material stability. The decrease in unit cell constant beyond the eutectoid temperature for the α -CDP(ss) phase observed in the $x = 0.07$ sample (Figure 3.6c) was attributed in the discussion above to changes in composition arising from the dissolution of stoichiometric CDP(m), CsH_2PO_4 , into the non-stoichiometric α - $[\text{Cs}_{1-x}\text{H}_x]\text{H}_2\text{PO}_4$ (ss) phase. Examining the temperature dependence of the lattice parameters for all compositions studied (Figure 3.7, $x = 0, 0.02, 0.05, 0.07, 0.15, 0.18, 2/9$), it is evident that chemically induced contraction on heating is largely obeyed for all samples that exist as a two-phase mixture of α -CDP(ss) and CDP(m). Upon the complete consumption of CDP(m), α -CDP(ss), now isolated as a single phase, displays in all cases, conventional linear thermal expansion. (Figure 3.S-10 shows the coincidence of the single-phase regions with the positive thermal expansion behavior.) The single-phase data moreover reveal a strong compositional dependence of the cell volume, with larger x values resulting in larger lattice

constants. After accounting for the influence of thermal expansion by extrapolating the measured lattice parameters to a common temperature of 170 °C, it is further evident that the lattice parameter depends linearly on composition x in α -[Cs_{1-x}H_x]H₂PO₄(ss) (Figure 3.7b), in accord with Vegard's Law and with a slope of 0.46(3) Å/ x . The smooth linear behavior indicates that the manner by which excess H₃PO₄ is incorporated into this phase is the same across the entire composition range examined. This expansion with x is entirely consistent with the observed contraction on heating in the two-phase region. Furthermore, the consistency of the chemical contraction in the two-phase region across samples obviously indicates a shared composition trend, or solvus line, that exists between the eutectoid point and the superprotonic transition of CDP. At lower temperatures, 160 - 170 °C, α -CDP(ss) undergoes expansion rather than contraction (Figure 3.7a). This implies that the composition change just above the eutectoid temperature must be small, allowing thermal expansion effects to dominate the behavior, which in turn implies that the solvus line must be relatively steep from 155 to 170 °C.

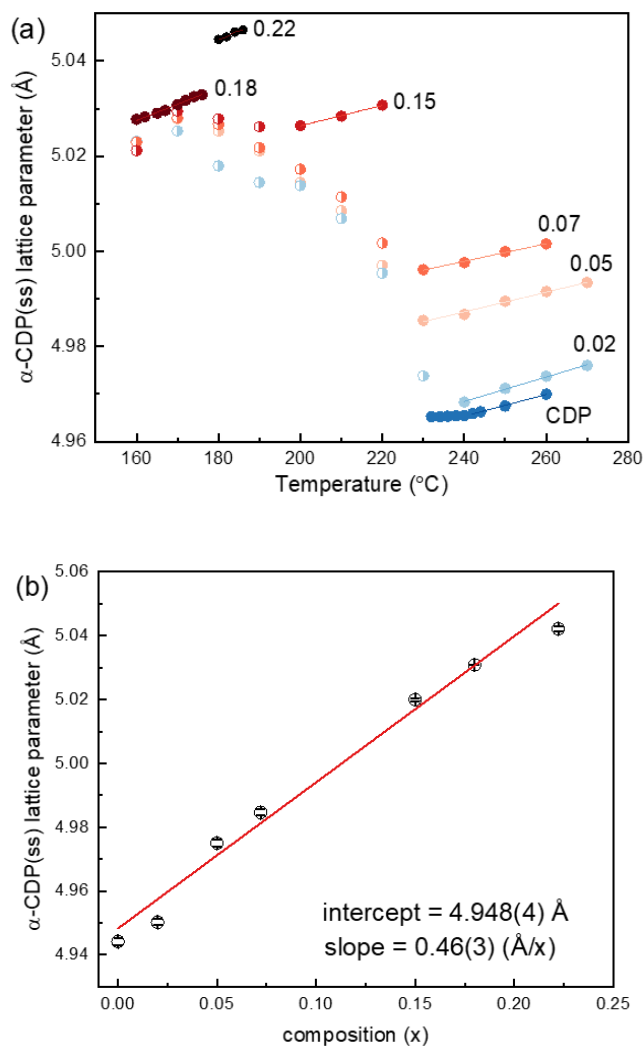


Figure 3.7. Lattice parameters of the α -CDP(ss) phase of various sample compositions, x : (a) thermal evolution of the lattice parameter, with x as indicated, at $p_{\text{H}_2\text{O}}$ between 0.4 and 0.7 atm, as required for suppressing dehydration; and (b) lattice parameters of single phase α -CDP(ss) as a function of composition, upon extrapolation to 170 °C. In (a), filled symbols indicate the presence of only α -CDP(ss) in the diffraction pattern, whereas half-filled symbols indicate the coexistence with CDP(m). The linear trend of lattice parameter with composition is consistent with the empirical Vegard's law. In (a), uncertainties in the refined values fall within the span of the datapoint symbols, as they do in (b), and are omitted for visual clarity. The refinement results for each sample are provided in Figure 3.S-10.

In contrast to α -CDP(ss), the cell volumes of the CDP(m) and CPP phases did not significantly deviate from those of the stoichiometric phases at any of the temperatures at which these phases were observed (Figure 3.S-9). Thus, CDP(m) and CPP exhibit little-to-no non-stoichiometry in the phase space characterized here, and they are accurately represented as line compounds on the phase diagram. Observed in this study was also an unusual reversible mass loss arising from the α -CDP(ss) phase in response to changes in temperature and steam partial pressure, which was accompanied by a slight change in cell volume (Figure 3.S-11). In the two-phase region, however, there was no impact on cell volume, implying no impact on the chemically induced thermal contraction (Figure 3.S-11c).

3.3.2 Solvus Line Determination

Most commonly, determination of the solvus line (where the term is used here to refer to the boundary between the two-phase α -CDP(ss) + CDP(m) region and the single phase α -CDP(ss) region) in a phase diagram such as that in Figure 1 is achieved by quantifying the molar fractions of components in equilibrated mixtures within the two phase region or establishing the temperature at which the low-temperature phase is no longer detected. The requisite data are typically obtained by diffraction studies. The former approach requires reliable detection of the minority phase in the diffraction data, ideally at multiple global compositions, whereas the latter requires measurements in small temperature steps to accurately reveal the boundary, particularly if the boundary is shallow. Applying these standard approaches to the data collected here at five compositions within the two-phase region using 10 °C temperature steps produced reasonable datapoints for the solvus boundary, but with large scatter, Figure S11. The uncertainty in the solvus position was particularly high at low x , where for example, phase analysis suggested possible retention of CDP(m) in the $x = 0.02$ sample at a temperature as high as 230 °C. In light

of the transition temperature in stoichiometric CDP of 228 °C,⁹¹ such behavior is thermodynamically forbidden in a eutectoid system.

An alternative and more accurate approach is pursued here by recognizing that at each diffraction measurement in the two-phase region, the composition and hence lattice parameter of α -CDP(ss) depends only on temperature and is independent of the global composition. Thus, embedded in the lattice parameter data in Figure 3.7 is the composition of the phase boundary at each measurement temperature. If one considers a temperature of 210 °C, for example, each of the measurements of samples with global compositions $x = 0.07, 0.05$ and 0.02 , reflect the lattice parameter of α -CDP(ss) at the phase boundary at 210 °C. In principle, the three datapoints, with an average lattice parameter value of 5.009 Å, should fully overlap, but they are slightly distinct due to experimental uncertainties. In the case of the $x = 0.02$ composition, the quantity of α -CDP(ss) in the two-phase mixtures is small, particularly at temperatures just above the eutectoid temperature, and hence the uncertainty in the cell parameter for measurements in this region is high. Nevertheless, accuracy is gained from this approach because determination of the lattice parameter of a cubic material is generally more reliable than determination of phase fractions. In this system in particular, peak intensities in the high-temperature diffraction patterns were found to be impacted by grain coarsening induced by the solid-state reactions; the transformation to a smaller number of large-sized crystallites removed the randomness generally required for interpreting peak intensities in terms of phase fractions. From an average of the reliable cell parameters of α -CDP(ss) in the two-phase measurements, we generate the lattice parameter of the composition at the phase boundary (a_b) as a function of temperature, Figure 3.8. In turn, the

lattice parameter of the α phase, a_α , can be treated, to a first approximation, as the sum of the thermal expansion and the chemical expansion terms:

$$a_\alpha(x_c, T) = a_{\alpha,0} + B \cdot x_c + D \cdot T; \quad a_{\alpha,0} = 4.948(4) \text{ \AA}, \quad B = 0.46(3) \text{ \AA}/x_c, \quad \text{and} \quad D = 2.2(1) \times 10^{-4} \text{ \AA}/^\circ\text{C}$$

where x_c is the composition of α -CDP(ss) and T is temperature. The term D is determined by averaging over the thermal expansion behavior of all compositions of $x \leq 0.15$ (Figure 3.S-10).

Inverting the above with a_α set to a_b , we solve for the composition at the phase boundary at each temperature between 160 – 220 °C. This result is also shown in Figure 3.8, as well as in Figure 3.1. The scatter is much smaller than in the case of the direct determination of the phase boundary (Figure 3.S-12).

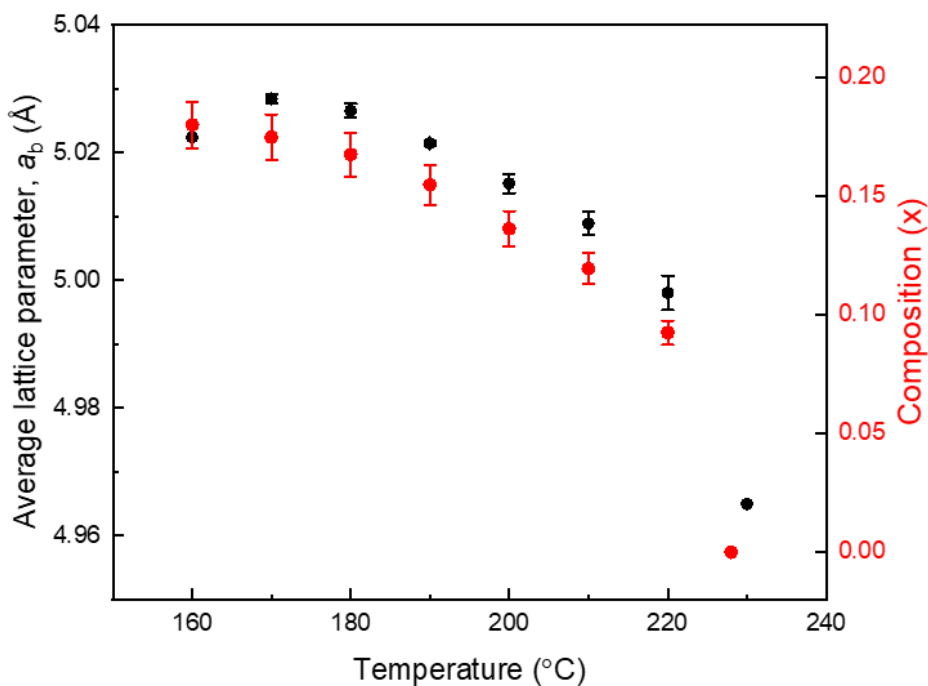


Figure 3.8. Determination of the solvus boundary: temperature dependence of the cell parameter of α -CDP(ss) at the boundary between the α -CDP(ss)+CDP(m) and α -CDP(ss) regions and inferred composition of α -CDP(ss) at the boundary.

3.3.3 Structure and Chemistry of α -CDP(ss)

The crystal structure of stoichiometric, superprotonic CDP is well-known. In this state, the material adopts the CsCl structure-type with H_2PO_4 anions residing on the Cl site and displaying nearly free rotational disorder. The observation in the present study of a material with stoichiometry $[\text{Cs}_{1-x}\text{H}_x]\text{H}_2\text{PO}_4$ in the same phase space as cubic CsH_2PO_4 implies that the superprotonic structure can accommodate unusual types of point defects. In particular, the Cs: PO_4 ratio of less than 1 requires either (i) the presence of Cs vacancies (charge balanced by proton interstitials, which would presumably form neutral H_3PO_4 groups), (ii) the presence of H_3PO_4 interstitials, a highly unlikely scenario given the density of packing in the CsCl structure-type, or (iii) similar to CPP, the occurrence of anti-site defects in which H_4PO_4^+ cations replace Cs species. The experimental data strongly point towards the first of these scenarios, the occurrence of Cs vacancies. The proposed structure is shown schematically in Figure 3.9 where the partial occupancy of the Cs site denotes the disordered vacancies. A key indicator of Cs vacancy formation is the significant contraction of the subcell volume at the CPP to α -CDP(ss) transition, Figure 3.2c. Prior to the transition, the subcell volume of CPP is substantially larger than that of stoichiometric, superprotonic CDP. This expansion occurs because the H_4PO_4^+ ions are larger than the Cs^+ cations which they replace. A CPP \rightarrow α -CDP(ss) transition involving only a disordering of the Cs^+ and H_4PO_4^+ cations, and hence the creation of anti-site defects in the latter, would be expected to have very little impact on the subcell volume. In contrast, elimination of the large polycations from the cation sites would very plausibly decrease the subcell volume, as observed. Attempts to confirm the presence of Cs vacancies by Rietveld refinement of the Cs site occupancy were, however, unsuccessful. This is attributed to the inherent challenge of high correlation between displacement parameter and occupancy factor in

any structure analysis and the specific challenge here of the coarsening of the microstructure through the high temperature reactions that form CPP and especially α -CDP(ss). The coarsening was observed to modify peak intensities due to the loss of randomness in the crystallite orientations as a consequence of the transformation to a smaller number of large-sized crystallites.

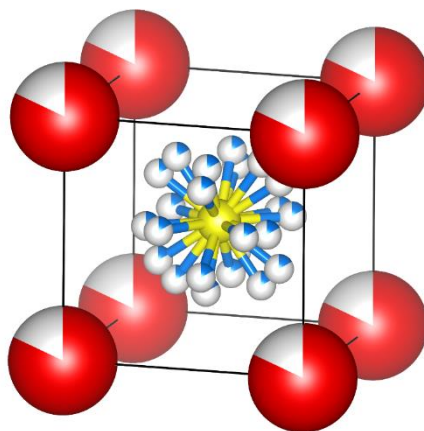


Figure 3.9. Schematic of the α -CDP(ss) structure. The multiple orientations of the phosphate anion represent the rotational disorder characteristic to superprotonic phases. The Cs site is partially occupied with a random distribution of vacancies. Protons are omitted from the figure.

Further evidence of the absence of anti-site defects (H_4PO_4^+ species residing on the cation sites in α -CDP(ss)) is provided by the NMR data discussed above. The ^{31}P NMR spectra, Figure 3.4, revealed that the disordered anion phosphate is the only phosphorus resonance associated with the α -CDP(ss) phase. In the ^1H NMR spectra, Figure 3.5, the very slight splitting of the high temperature resonance appears too small to be a consequence of anti-site defects. The overall position of the peak suggests that the excess protons in α -CDP(ss) are largely indistinguishable in both position and motion from the protons in conventional cubic CDP.

Accepting that Cs deficiency in α -[Cs_{1-x}H_x]H₂PO₄ is accommodated by the presence of Cs vacancies, it is at first glance surprising that the lattice constant increases with x . The result suggests that in the absence of a Cs cation, unmitigated electrostatic repulsion of the eight nearest neighbor phosphate groups causes expansion, despite the likelihood that, for reasons of overall charge balance, some of the phosphate groups are neutral H₃PO₄ species. In the case of Rb and K substituted CDP ([Cs_{1-x}Rb_x]H₂PO₄ and [Cs_{1-x}K_x]H₂PO₄) contraction occurs,⁸⁴ consistent with the presence of a smaller isovalent species on the Cs site.

3.3.4 Conductivity

The conductivity of the materials studied here (in the heating cycle) are summarized in Figure 3.10. The behavior of CDP fully agrees with prior reports,¹² with a sharp, 3-order of magnitude increase in conductivity at the monoclinic-to-cubic transition that initiates at 228 °C. For the samples with $x = 2/9$ (equivalent to CPP) and 0.18, the formation of CPP is evident from the moderate jump in conductivity that initiates at ≈ 100 °C, reasonably close to the CPP formation temperature of ≈ 90 °C detected by thermal analysis. At 125 °C, at which all compositions (except the end-members) exist as a two-phase mixture of CDP(m) and CPP, the conductivity generally increases with x . This reflects the higher conductivity of CPP than CDP(m) and the simple two-phase mixing behavior. For all two-phase samples except $x = 0.02$, a further moderate jump in conductivity that initiates at ≈ 150 °C is evident, reflecting the formation of α -CDP(ss). At the eutectoid composition ($x = 0.18$), the transition produces single-phase α -CDP(ss), which has a slightly higher conductivity than that of single-phase CPP ($2.61(8) \times 10^{-3}$ vs $1.19(3) \times 10^{-3}$ S cm⁻¹ @ 158 °C). The slightly lower conductivity of CPP than CDP, despite the crystallographic similarities of the two structures, was noted in our previous study.⁸⁸

Here, because of ready dehydration of the $x = 2/9$ composition at high temperature, the impact of the 180 °C phase transformation of CPP to α -CDP(ss) could not be observed. Within the two-phase region of CDP(m) and α -CDP(ss) (observed in samples with $x < 0.18$ above 155 °C), the conductivity generally increases with x , again reflecting the fact that the superprotonic α -CDP(ss) phase accounts for a greater proportion of the material. In contrast to the behavior below the eutectoid temperature, however, the low x compositions show upward concavity in the $\sigma(T)$ profiles, a feature taken to reflect the increasing α -CDP(ss) content with temperature. The non-monotonic trend with composition at low temperature, below the CPP formation, likely reflects differing levels of H₂O adsorption by the highly deliquescent CsH₅(PO₄)₂ compound.

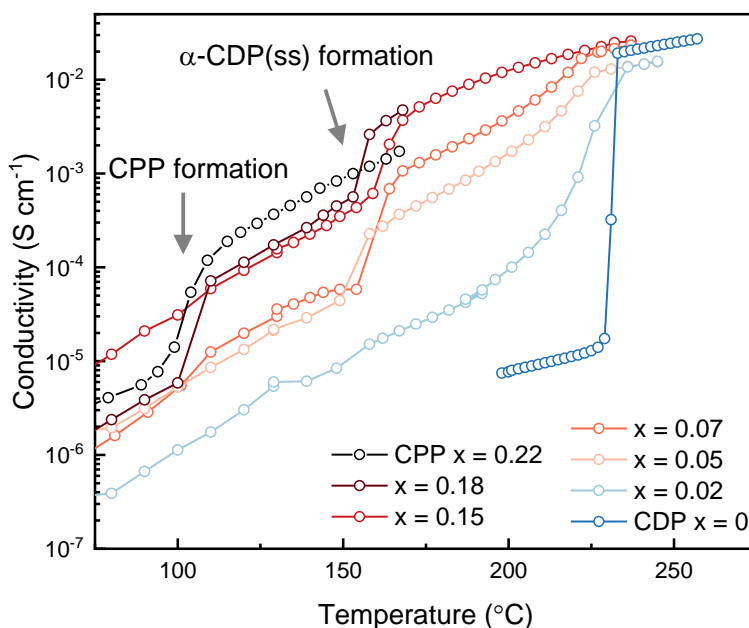


Figure 3.10. Conductivity of materials in the $(1-x)\text{CsH}_2\text{PO}_4 - x\text{H}_3\text{PO}_4$ system as a function of temperature on heating with compositions as indicated (conductivity of $x = 0.22$ composition after ref ⁸⁸ with permission from the American Chemical Society). Data above 130 °C are

collected under high $p_{\text{H}_2\text{O}}$: 0.69 atm for $x = 0.18, 0.15$ and 0.07 , and 0.47 atm for $x = 0.05$ and 0.02 . The phase transition corresponding to the formation of CPP from CDP(m) and $\text{CsH}_5(\text{PO}_4)_2$ at ≈ 90 °C is evident in the behavior of the compositions with large x (0.22 and 0.18), and the formation of α -CDP(ss) at ≈ 150 °C, approximately the eutectic temperature, is evident in compositions with moderate to large x (0.05, 0.07, 0.15 and 0.18). In the single-phase region, the conductivity is largely insensitive to composition.

The conductivities measured upon cooling through the solvus boundary were largely consistent with those obtained on heating, and only slight hysteresis was detected at the eutectoid temperature for those samples investigated in this regards (Figure 3.S-12). Notably, however, elevated conductivity was generally retained at temperatures below that corresponding to CPP decomposition into CDP(m) and $\text{CsH}_5(\text{PO}_4)_2$. This reflects the tendency of CPP to be retained as a metastable state outside of its stability limits, to as low as 80 °C.⁸⁸

An important feature of the conductivity of α -CDP(ss) is its weak sensitivity to composition x (in its stoichiometry $[\text{Cs}_{1-x}\text{H}_x]\text{H}_2\text{PO}_4$) both in terms of absolute conductivity and activation energy in the single phase region. While a small systematic trend may have been obscured as a result of experimental uncertainty, the absence of a detectable impact is somewhat surprising given the significant influence of composition on both proton concentration and unit cell dimensions, Figure 3.7b. It is of some value to compare this behavior to that of Rb- and K-substituted CDP. Both these dopants reduced conductivity and induced lattice contraction, but the detrimental impact of K on proton transport at equivalent lattice contraction was far more pronounced than that of Rb.⁸⁴ Thus, the impact of cation chemistry on proton transport extends beyond structural influences – a conclusion again found in the present study where no clear correlation between lattice expansion and conductivity is observed. In the CsHSO_4 - CsH_2PO_4 system, which forms a solid solution in the cubic superprotonic phase at high temperature, the

conductivity decreases with increasing CsH_2PO_4 and correspondingly proton content.⁹² This result implies that the proton concentration similarly plays a secondary role in establishing the conductivity.

Regardless of the subtlety of the role of material stoichiometry, the overall high conductivity of α -CDP(ss) indicates that the proton transport mechanism is analogous to that in stoichiometric CDP, *i.e.*, it involves rapid phosphate group reorientation and proton transfer between neighboring polyanionic groups. Rapid anion reorientation is indeed evident from the sharpness of the ^{31}P NMR peak at -1.2 ppm, Figure 3.4a. The high conductivity of α - $[\text{Cs}_{1-x}\text{H}_x]\text{H}_2\text{PO}_4$ at temperatures well below the superprotonic transition of stoichiometric CsH_2PO_4 has potential implications for electrochemical devices. In particular, a decrease in operating temperature may decrease the energy costs of generating high levels of $p\text{H}_2\text{O}$ at high temperature as required to stabilize CsH_2PO_4 against dehydration.⁹¹ The material of composition $x = 0.15$, with conductivity exceeding $5 \times 10^{-3} \text{ S cm}^{-1}$ over the temperature range 160 to 235 °C, appears especially attractive in this regards.

3.4 Summary and Conclusions

This work reveals that cubic CDP accommodates chemical off-stoichiometry with a formula described as $[\text{Cs}_{1-x}\text{H}_x]\text{H}_2\text{PO}_4$ for x at least as large as $2/9$. Excess H_3PO_4 units are incorporated into the cubic structure via the creation of vacancies on the cation site which are charge balanced by the excess protons. The $(1-x)\text{CsH}_2\text{PO}_4 - x\text{H}_3\text{PO}_4$ phase diagram in the $0 \leq x \leq 2/9$ range obeys eutectoid behavior, anchored, at temperatures above 90 °C, by stoichiometric, monoclinic CDP at $x = 0$ and stoichiometric $\text{Cs}_7(\text{H}_4\text{PO}_4)(\text{H}_2\text{PO}_4)_8$ at $x = 2/9$. The eutectoid reaction at which α -CDP(ss) forms from these two precursors occurs at 155 °C and $x = 0.18$. A surprising feature

of α -CDP(ss) is the increase in cell volume with increasing chemical replacement of Cs^+ by H^+ . The behavior is proposed to reflect the formation of cation site vacancies, with protons becoming associated with phosphate groups, as opposed to occupation of cation sites by protons. The expansive effect of Cs deficiency in α -CDP(ss) manifests as a chemically induced unit cell contraction when the phase is heated under equilibrium conditions alongside monoclinic CDP; heating in this two-phase region induces gradual dissolution of the stoichiometric monoclinic phase into α -CDP(ss) thereby reducing the Cs deficiency in the latter. This behavior was exploited to establish the position of the solvus line boundary between α -CDP(ss) and the two-phase region comprised of monoclinic CDP and α -CDP(ss). The concept of cation off-stoichiometry, in which protons replace large cations chemically but not structurally, presents a new approach in the design of superprotonic solid acid electrolytes and specifically the formation of superprotonic phases.

The conductivity of α -CDP(ss) is surprisingly insensitive to the compositional off-stoichiometry. Furthermore, the eutectoid reaction temperature of α -CDP(ss), 155 °C, is substantially lower than the superprotonic transition temperature of stoichiometric CDP, 228 °C, and the solvus boundary between α -CDP(ss) and the two-phase, monoclinic CDP and α -CDP(ss) region is relatively steep near the eutectoid composition. Combined, these effects result in high conductivity in compositions slightly rich in CDP relative to the eutectoid composition at temperatures well below the superprotonic transition of stoichiometric CDP. The excellent proton conductivities exhibited by these α -CDP(ss) phases present an opportunity to extend the low-temperature operating limit of devices based on superprotonic solid acid electrolytes.

Supplemental Information

Figure 3.S-1. Comparison of X-ray diffraction patterns and refinement results obtained from the $(1-x)\text{CsH}_2\text{PO}_4-x\text{H}_3\text{PO}_4$ material of global composition $x = 0.07$, before and after annealing at $230\text{ }^\circ\text{C}$ (under $p\text{H}_2\text{O} = 0.4\text{ atm}$) for 3 days. Post-annealing data collected after 6 days at ambient temperature, and both measurements are obtained from well-ground samples. The refined phase weight fractions of CDP(m) and $\text{CsH}_5(\text{PO}_4)_2$ are within error of the input values of 0.893 and 0.107 weight fractions, respectively. All structure parameters of CDP(m) (space group $P2_1/m$), except lattice parameters, were fixed to those reported by Matsunaga *et al.*⁹³ (including anisotropic displacement parameters and hydrogen positions), whereas the model for $\text{CsH}_5(\text{PO}_4)_2$ (space group $P2_1/c$) was taken from that reported by Efremov *et al.*⁹⁴ (including hydrogen positions). For the latter phase, displacement parameters for all atoms were set to 0.01 \AA^{-2} . All structure parameters except lattice parameters were fixed during refinement. Default GSAS-II peak profiles were employed (*i.e.*, the peaks were modeled as pseudo-Voigt functions), and the broadening was entirely attributed to the instrument. The 5 profile parameters and their Θ -dependences were established from a measurement using a LaB_6 standard (NIST SRM 660c) and were fixed during refinement. Each background was treated with a (unique) Chebyshev polynomial with 10 coefficients. In the final analysis cycle, lattice parameters and sample displacement parameter were refined. The results show that under conditions promoting equilibration, the phase transitions on heating that yield α -CDP are fully reversible.

Pre-anneal, $R_{\text{wp}} = 8.78\%$	a (Å)	b (Å)	c (Å)	β (°)	wt. frac.	expected
CDP(m)	7.902(2)	6.3813(2)	4.8735(8)	107.697(3)	0.887(2)	0.893
$\text{CsH}_5(\text{PO}_4)_2$	10.871(4)	7.761(2)	9.524(4)	96.67(2)	0.115(4)	0.107
Post-anneal, $R_{\text{wp}} = 7.50\%$	a (Å)	b (Å)	c (Å)	β (°)	wt. frac.	expected
CDP(m)	7.904(2)	6.3832(2)	4.8753(6)	107.702(3)	0.903(2)	0.893
$\text{CsH}_5(\text{PO}_4)_2$	10.874(4)	7.764(2)	9.519(4)	96.62(3)	0.097(4)	0.107

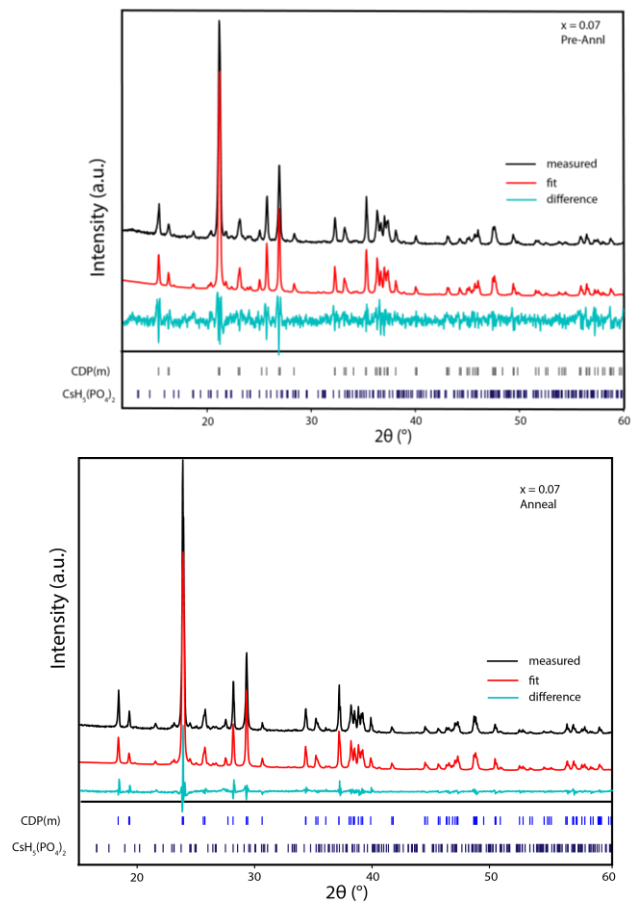
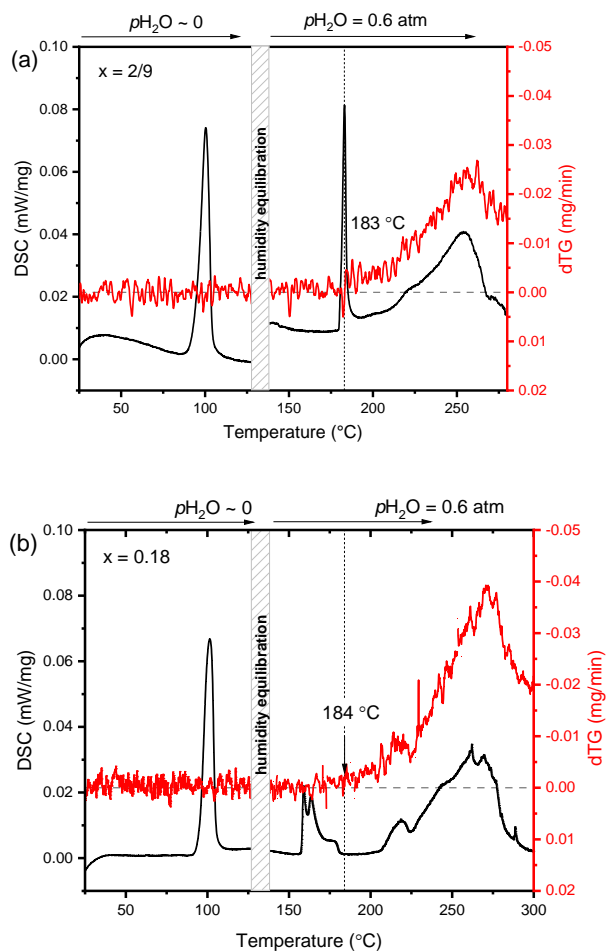


Figure 3.S-2. Comparison of differential scanning calorimetry and differential thermogravimetric profiles for samples in the $(1-x)\text{CsH}_2\text{PO}_4-x\text{H}_3\text{PO}_4$ system with global composition as indicated. In all cases, mass loss occurs at temperatures beyond the phase transitions of CPP formation and α -CDP(ss) formation detected by calorimetry.



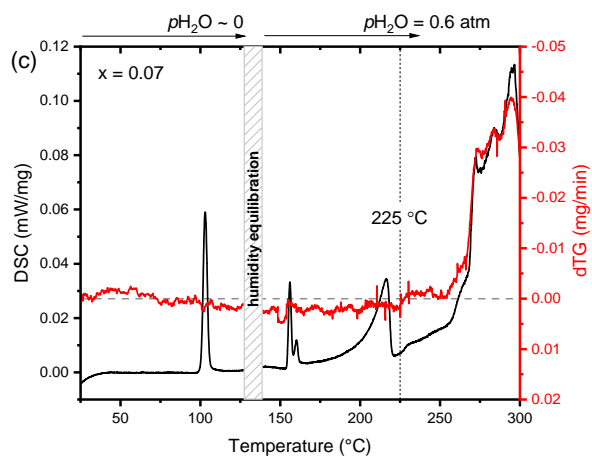


Figure 3.S-3. Thermal analysis of the $(1-x)\text{CsH}_2\text{PO}_4-x\text{H}_3\text{PO}_4$ material of global composition $x = 0.15$: (a) DSC and TG profiles; and (b) DSC and dTG profiles. Formation of CPP initiates at 96.5°C , whereas formation of $\alpha\text{-CDP(ss)}$ initiates at 154.6°C . Dehydration under these conditions of $p\text{H}_2\text{O} = 0.4\text{ atm}$ initiates at 178°C , well past the temperatures at which CPP and $\alpha\text{-CDP(ss)}$ form.

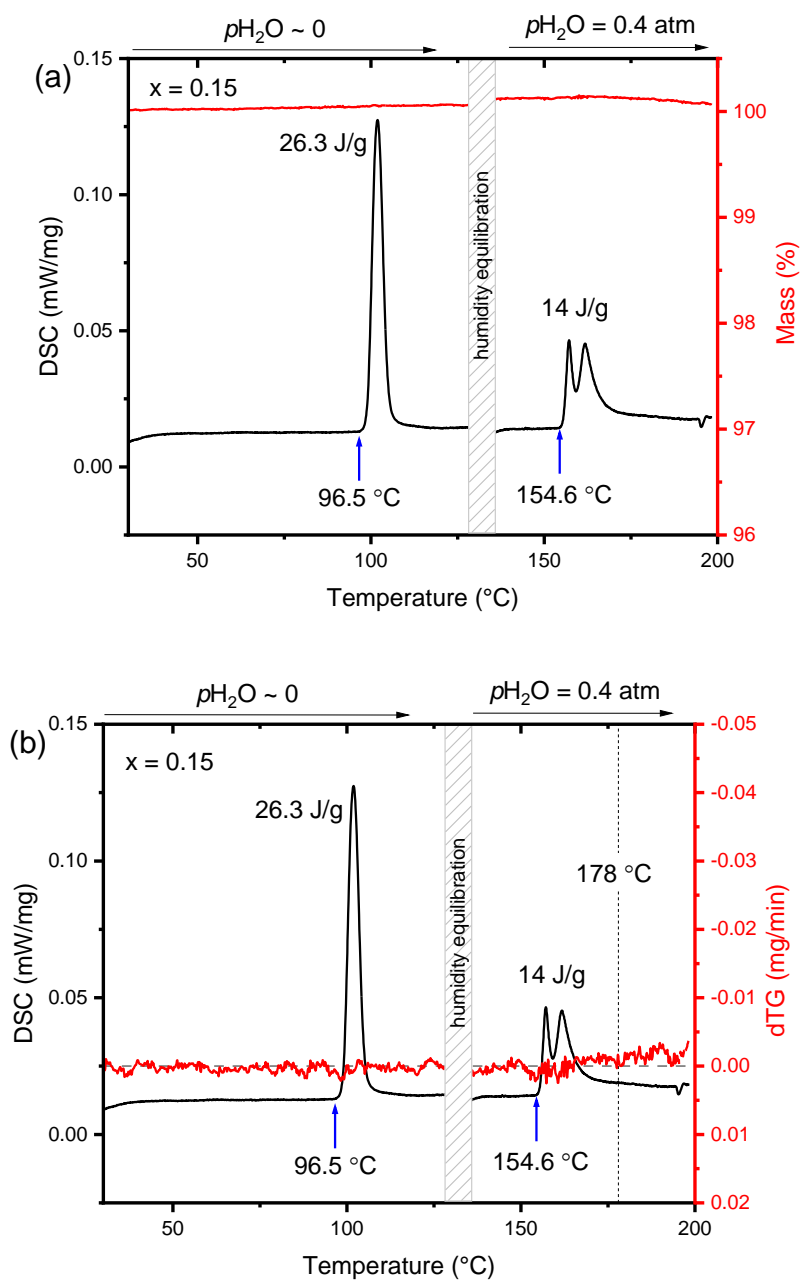


Figure 3.S-4. Example results of Rietveld refinement against diffraction data from the $(1-x)\text{CsH}_2\text{PO}_4-x\text{H}_3\text{PO}_4$ material of global composition $x = 2/9$ for selected temperatures (110 °C, CPP phase; and 180 °C, α -CDP(ss) phase), and accompanying listing of lattice parameter at each measurement/refinement temperature. Patterns shown correspond to those of main text Figure 2b. In the temperature range 110-170 °C, all structure parameters of CPP except lattice parameter and hydrogen positions were fixed to those reported in Wang *et al.*⁸⁸ (including anisotropic displacement parameters). The structure (space group $Pm-3n$) has 29 non-hydrogen atom positions in the asymmetric unit with all oxygen atoms sitting on sites of one-third occupancy. In the temperature range 180-186 °C, all non-hydrogen atomic positions were fixed to those reported by Yamada *et al.*⁹⁵ for the structure of cubic CDP (space group $Pm-3m$) and displacement factors treated as isotropic, with a fixed U_{iso} of 0.01 \AA^{-2} . The structure has 3 non-hydrogen atom positions in the asymmetric unit with the single, crystallographically distinct oxygen atom sitting on a site of one-sixth occupancy. Although, as shown in this work, Cs vacancies occur in α -CDP this feature was not modeled in the refinement. Hydrogen atoms were omitted from both structure models. Default GSAS-II peak profiles were employed (*i.e.*, the peaks were modeled as pseudo-Voigt functions), and the broadening was entirely attributed to the instrument. The 5 profile parameters and their Θ -dependences were established from a measurement using a LaB_6 standard (NIST SRM 660c), which were then held fixed during refinement. Each background was treated with a (unique) Chebyshev polynomial with 10 coefficients. The sample displacement was treated in the following way. At the measurement temperature of 100 °C, at which CPP was fully formed, lattice parameter and sample displacement were simultaneously refined. Sample displacement was then held fixed for subsequent refinements involving the CPP structure. Similarly, the lattice parameter of α -CDP and the sample displacement were simultaneously refined at 180 °C, and the latter held fixed at this new value for all higher temperature refinements. Preferred orientation in α -CDP was treated (though not adequately captured) using an 8th order spherical harmonic model. In the final analysis cycle for each measurement temperature, only the lattice parameter was refined.

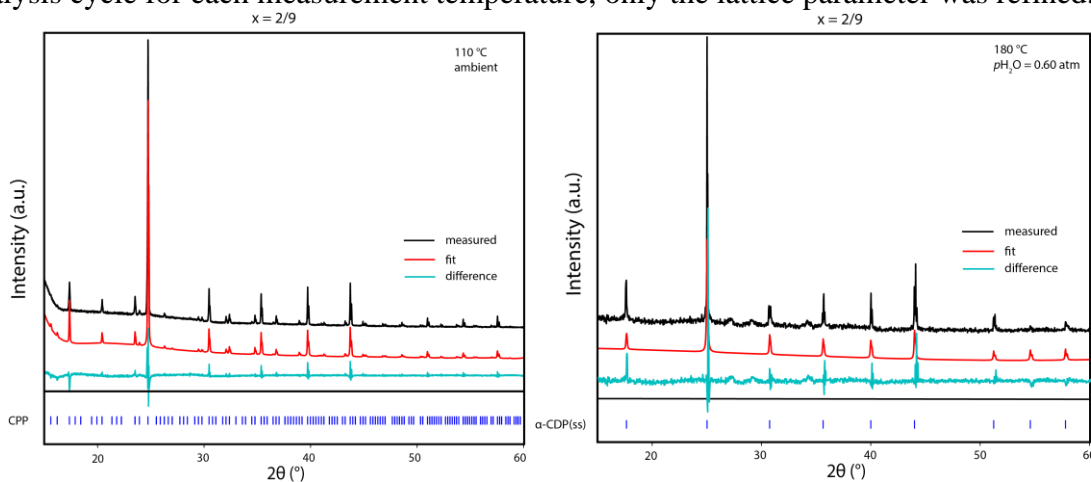


Figure 3.S-4 continued.

Temperature (°C)	CPP <i>a</i> , (Å)	<i>R</i> _{wp} , %
100	20.1783(3)	8.63
105	20.1807(3)	8.56
110	20.1850(2)	8.14
110	20.1860(3)	8.54
115	20.1886(3)	8.34
115	20.1886(3)	8.34
120	20.1929(2)	7.78
120	20.1940(3)	8.36
125	20.1963(3)	8.31
130	20.2032(2)	7.60
130	20.2004(3)	8.19
135	20.2047(3)	8.14
140	20.2105(2)	7.69
140	20.2093(3)	7.92
170	20.231(3)	12.66

Temperature (°C)	α -CDP <i>a</i> , (Å)	<i>R</i> _{wp} , %
180	5.0457(3)	15.72
180	5.0446(7)	10.33
182	5.0451(9)	11.40
184	5.0461(9)	11.09
186	5.0466(8)	10.71

Figure 3.S-5. Example results of Rietveld refinement against diffraction data from the $(1-x)\text{CsH}_2\text{PO}_4-x\text{H}_3\text{PO}_4$ material of global composition $x = 0.18$ at 140 and 160 °C, and accompanying listing of lattice parameter at each measurement/refinement temperature. Patterns shown correspond to main text Figure 3.3b. At 140 °C the phases CDP(m) and CPP are present. All structure parameters of CDP(m), except lattice parameters, were fixed to those reported by Matsunaga *et al.*⁹³ (including anisotropic displacement parameters and hydrogen positions), whereas all structure parameters of CPP, except lattice parameter, were fixed to those reported in Wang *et al.*⁸⁸ (including anisotropic displacement parameters). The structure of CDP(m) has 5 non-hydrogen atoms in the asymmetric unit, with all (non-hydrogen) sites fully occupied. The structure of CPP has 29 atom positions in the asymmetric unit with all oxygen atoms sitting on sites of one-third occupancy. At 160 °C and higher, only α -CDP is present. The atomic positions in this phase were fixed to those reported by Yamada *et al.*³ for the structure of cubic CDP and displacement factors treated as isotropic, with a fixed U_{iso} of 0.01 \AA^{-2} . The structure has 3 non-hydrogen atom positions in the asymmetric unit with the single, crystallographically distinct oxygen atom sitting on a site of one-sixth occupancy. Although, as shown in this work, Cs vacancies occur in α -CDP this feature was not modeled in the refinement. Hydrogen atoms were omitted from structure models of CPP and α -CDP. Default GSAS-II peak profiles were employed (*i.e.*, the peaks were modeled as pseudo-Voigt functions), and the broadening was entirely attributed to the instrument. The 5 profile parameters and their Θ -dependences were established from a measurement using a LaB_6 standard (NIST SRM 660c), which were then held fixed during refinement. Each background was treated with a (unique) Chebyshev polynomial with 10 coefficients. The sample displacement was treated in the following way. At 140 °C, at which CPP is the dominant phase, sample displacement and CPP lattice parameter were refined simultaneously. Displacement was then fixed, and lattice parameters of both CDP(m) and CPP refined, along with phase fraction. At 160 °C, at which α -CDP was fully formed, lattice parameter and sample displacement were simultaneously refined. Sample displacement was then held fixed for subsequent refinements involving the α -CDP structure. Preferred orientation in α -CDP was treated (though not adequately captured) using an 8th order spherical harmonic model.

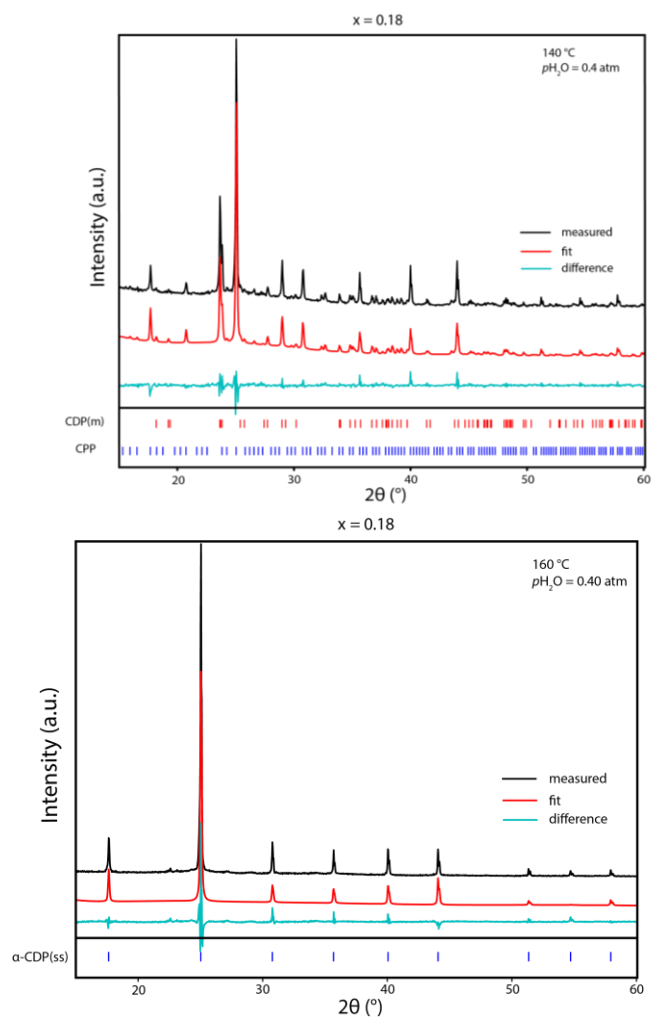


Figure 3.S-5 continued.

T (°C)	Monoclinic CDP lattice parameters				CPP <i>a</i> , (Å)	Wt. Frac. CPP	<i>R</i> _{wp}
	<i>a</i> (Å)	<i>b</i> (Å)	<i>c</i> (Å)	β (°)	<i>a</i> (Å)		
140	7.916(6)	6.463(1)	4.863(2)	107.12(1)	20.2153(8)	0.781(5)	8.24

Temperature (°C)	α-CDP <i>a</i> , (Å)	<i>R</i> _{wp} %
160	5.0298(4)	14.67
162	5.0282(2)	14.93
165	5.0290(2)	14.45
167	5.0296(2)	13.69
170	5.0309(2)	13.45
172	5.0317(2)	13.56
174	5.0325(2)	13.32
176	5.0329(2)	13.30

Figure 3.S-6. Zoomed in presentations of the (a) ^{31}P and (b) ^1H NMR spectra collected from the $(1-x)\text{CsH}_2\text{PO}_4-x\text{H}_3\text{PO}_4$ material of global composition $x = 0.18$ (eutectoid composition) at the indicated temperatures, which lie below the eutectoid reaction temperature. Highlighted regions show the signal from the CDP(m) phase.

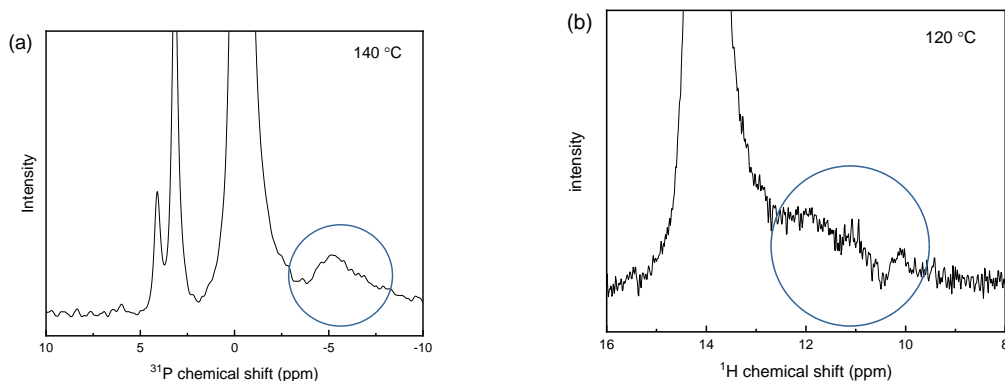


Figure 3.S-7. Deconvolution of the (a) ^1H and (b) ^{31}P NMR resonances collected from the $(1-x)\text{CsH}_2\text{PO}_4-x\text{H}_3\text{PO}_4$ material of global composition $x = 0.18$ (eutectoid composition) at the indicated temperatures.

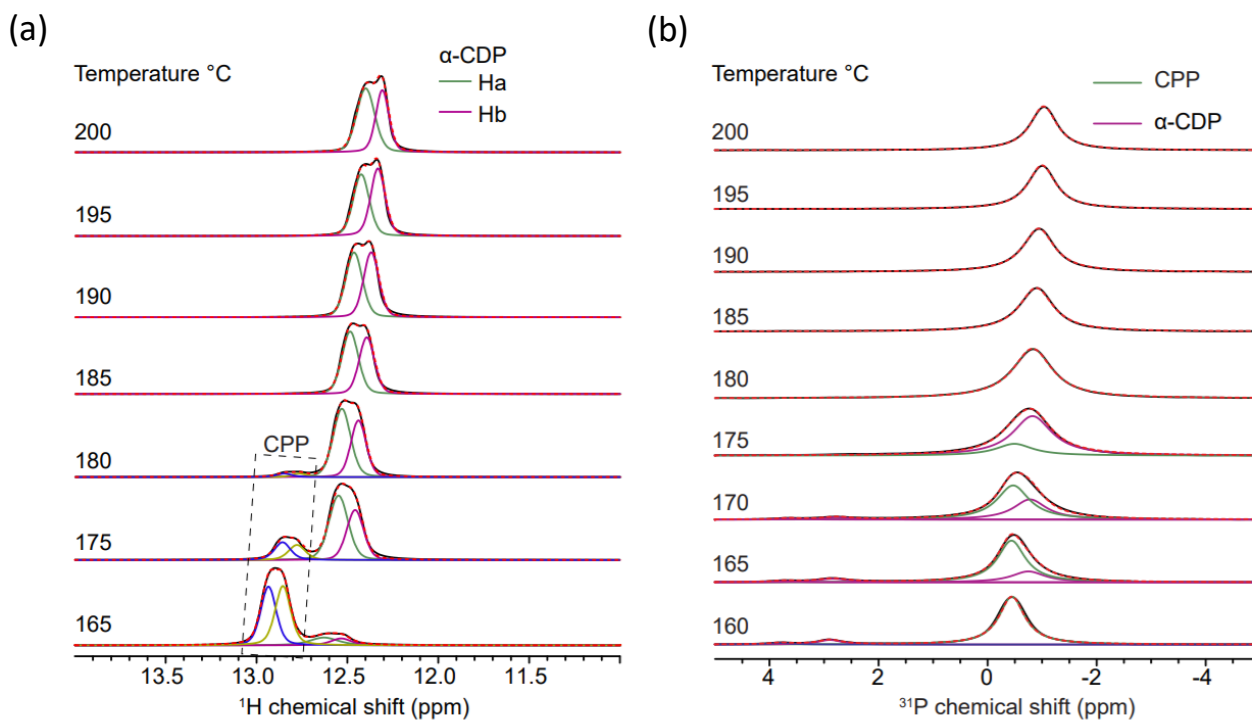
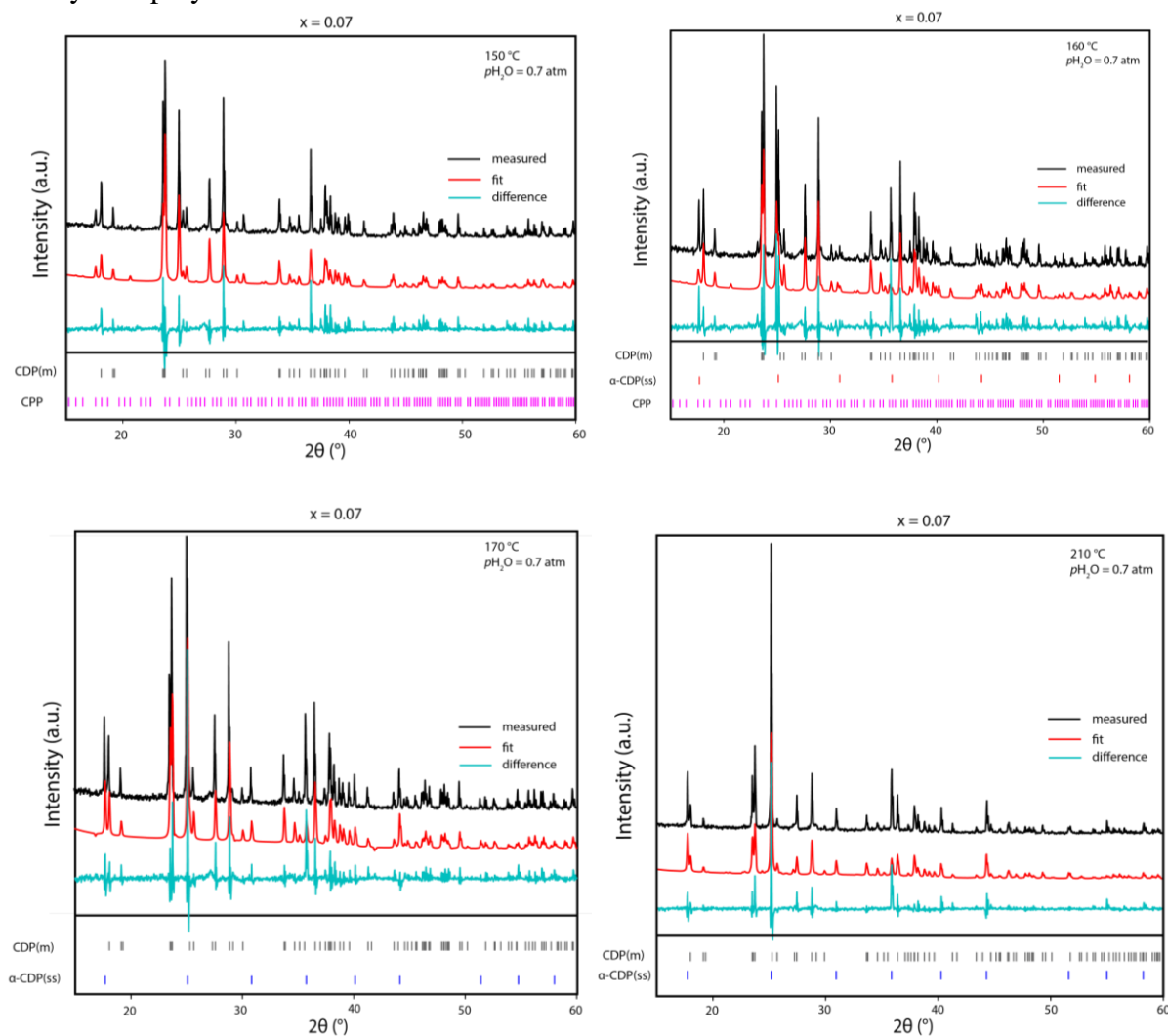
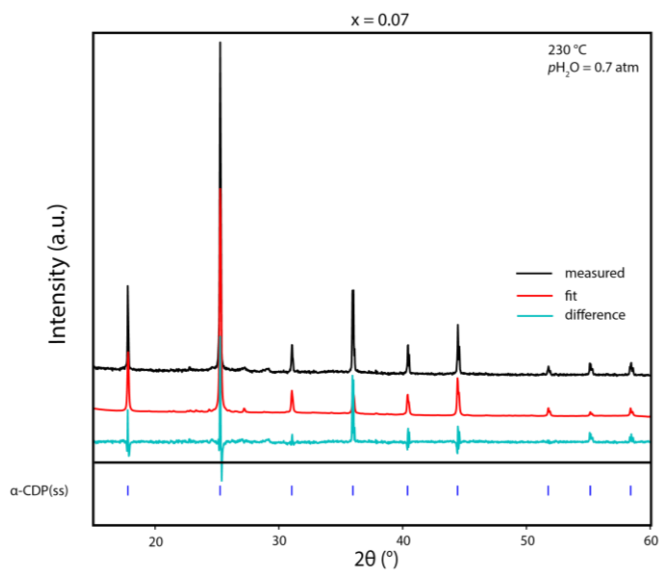


Figure 3.S-8. Example results of Rietveld refinement against diffraction data from the $(1-x)\text{CsH}_2\text{PO}_4-x\text{H}_3\text{PO}_4$ material of global composition $x = 0.07$ (data correspond to main text Figure 3.6b). Refinement procedures followed the methodology described above in the descriptions of Figure 3.S-1, Figure 3.S-4, and Figure 3.S-5. With the exception of lattice parameters, the structure of CDP(m) was fixed to that reported by Matsunaga *et al.*⁹³ and the structure of CPP to that reported by Wang *et al.*⁸⁸ The structure of α -CDP was modeled according to that reported by Yamada *et al.*⁹⁵ for cubic CDP. Although, as shown in this work, Cs vacancies occur in α -CDP, Cs site occupancy was fixed at 1. In addition to lattice parameter, isotropic displacement parameters were refined for α -CDP. At temperatures at which more than one phase appeared in the pattern, phase fractions were also refined. Peak profiles were modeled with pseudo-Voigt functions using fixed parameters determined from a separate measurement using a LaB_6 standard (NIST SRM 660c). Each background was treated with a (unique) Chebyshev polynomial with 10 coefficients.





(°C)	Monoclinic CDP				CPP	α-CDP	R _w p, %
	<i>a</i> (Å)	<i>b</i> (Å)	<i>c</i> (Å)	β (°)	<i>a</i> (Å)	<i>a</i> (Å)	
150	7.924(5)	6.4621(8)	4.866(2)	107.179(9)	20.217(4)	N/A	18.47
160	7.921(4)	6.4681(5)	4.864(1)	107.128(8)	20.220(4)	5.0206(8)	20.10
170	7.924(4)	6.4755(6)	4.863(2)	107.082(9)	N/A	5.0281(4)	18.63
210	7.927(5)	6.5115(9)	4.856(2)	106.82(1)	N/A	5.0114(4)	18.55
230	N/A	N/A	N/A	N/A	N/A	4.9961(3)	19.62

Figure 3.S-9. Cell volumes of (a) CCP and (b) CDP(m) as functions of temperature. Equivalence of values from single phase and mixed phase materials reveals the fixed stoichiometric nature of these compounds. Results obtained from Rietveld refinement as described in the heading to Figure S10.

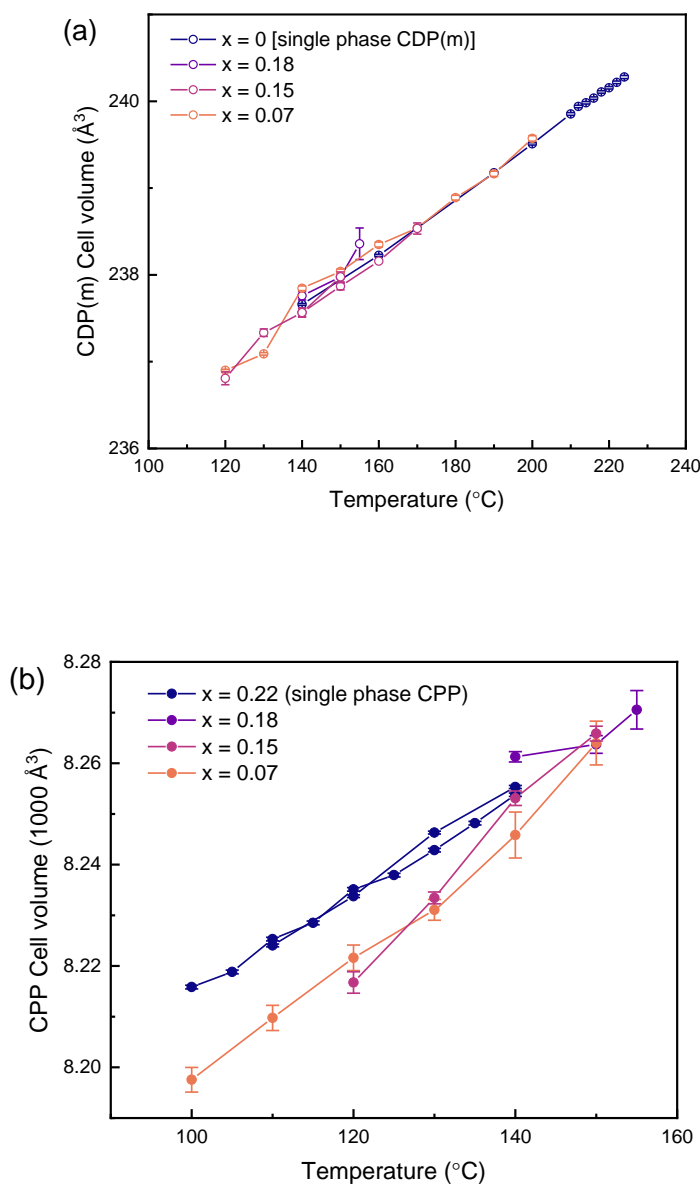
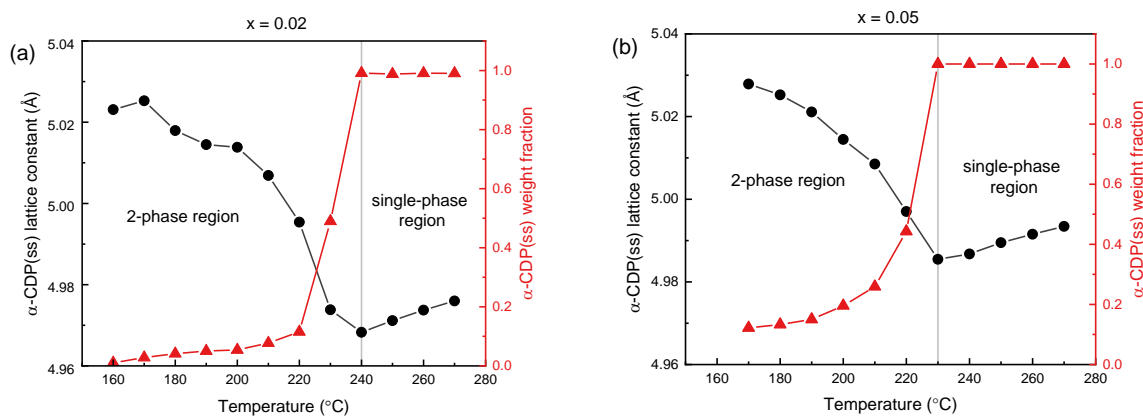
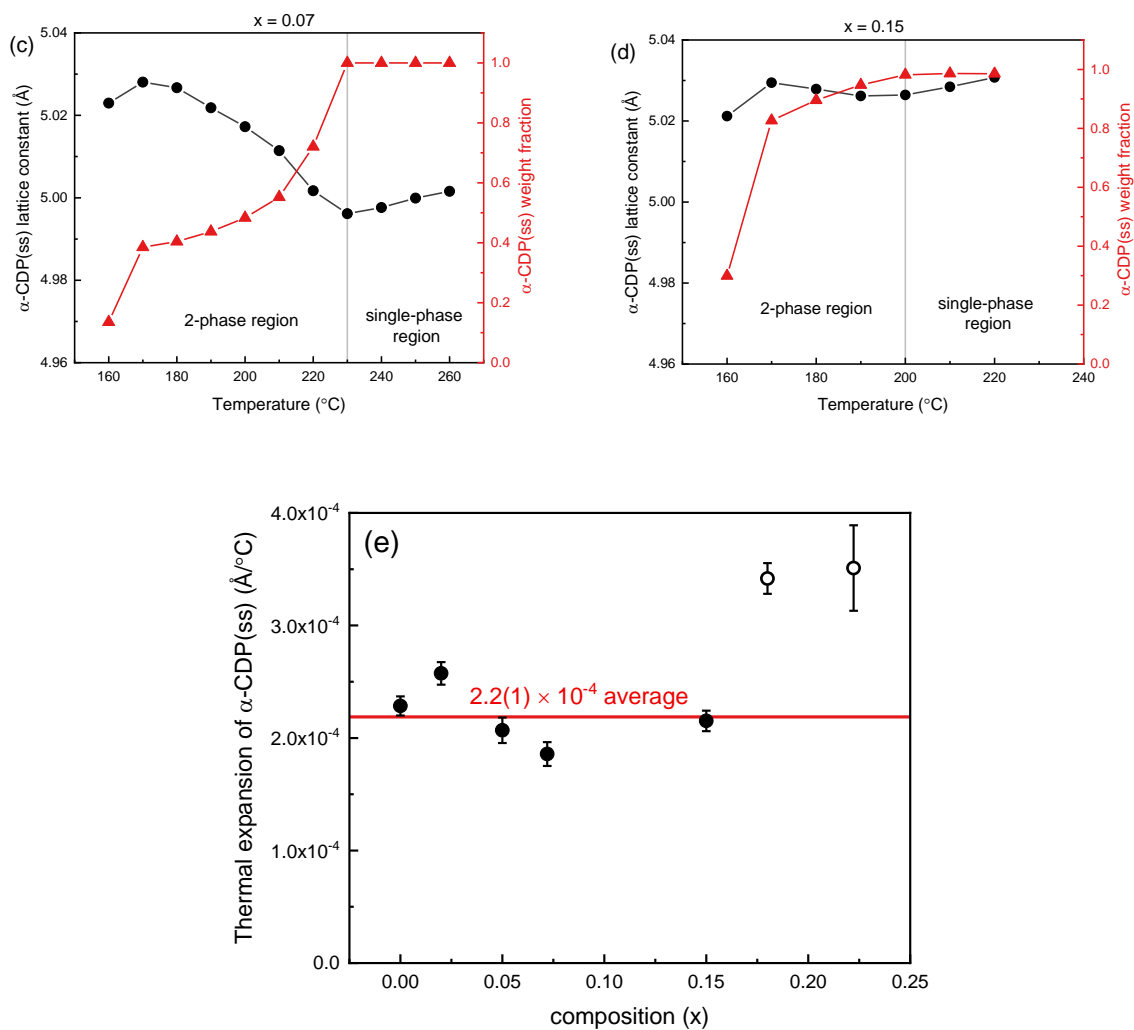


Figure 3.S-10. Temperature dependence of lattice constant and phase fraction of α -CDP(ss) component in samples of various compositions (as indicated) in the $(1-x)\text{CsH}_2\text{PO}_4\text{-}x\text{H}_3\text{PO}_4$ system (a-d), and (e) lattice expansion behavior in the single phase region. The average expansion of $2.2(1) \times 10^{-4} \text{ \AA/ } ^\circ\text{C}$ was used in the evaluation of the solvus phase boundary. Complete listing of results obtained by Rietveld analysis of the corresponding diffraction patterns is also provided. Uncertainties in lattice parameters and phase fractions fall within the span of the symbols used to plot the data. Refinement procedures followed the methodology reported above in the description of Figure S8. In the two-phase regions, the structure of CDP(m) was fixed, with the exception of lattice parameters, to that reported by Matsunaga *et al.*⁹³ The structure of α -CDP was modeled according to the report by Yamada *et al.*⁹⁵ for cubic CDP. Although, as shown in this work, Cs vacancies occur in α -CDP, Cs site occupancy was fixed at 1. In addition to lattice parameter, isotropic displacement parameters were refined for α -CDP. At temperatures at which more than one phase appeared in the pattern, phase fractions were also refined. Peak profiles were modeled with pseudo-Voigt functions using fixed parameters determined from a separate measurement using a LaB_6 standard (NIST SRM 660c). Each background was treated with a (unique) Chebyshev polynomial with 10 coefficients. The sample displacement was treated in the following way. At 160°C , at which CPP is the dominant phase, sample displacement and CPP lattice parameter were refined simultaneously. Displacement was then fixed, and lattice parameters of both CDP(m) and CPP refined, along with phase ratio. At 160°C , at which CDP(m) was the dominant phase, the lattice parameters of this structure and the sample displacement were simultaneously refined. Sample displacement was then held fixed for subsequent refinements for a global given composition.





$x = 0$ (CsH_2PO_4) [See Figure 3.7a, main text for accompanying figure]

Temperature ($^\circ\text{C}$)	α -CDP a (\AA)	R_{wp}
232	4.9653(2)	11.96036
234	4.9652(2)	12.96135
236	4.9653(2)	14.13596
238	4.9654(1)	14.97225
240	4.9655(1)	15.75314
242	4.9659(1)	16.0244
244	4.9662(1)	15.96522
250	4.9675(2)	16.05989
260	4.9700(1)	15.5905

$x = 0.02$

Temperature (°C)	α -CDP a (Å)	Phase wt. fraction	R_{wp} , %
160	5.023(9)	0.010(5)	19.24
170	5.025(4)	0.028(3)	19.46
180	5.018(3)	0.041(4)	20.57
190	5.014(2)	0.050(5)	20.55
200	5.014(3)	0.054(5)	20.35
210	5.007(2)	0.077(5)	20.32
220	4.995(1)	0.115(6)	19.57
230	4.9738(4)	0.490(8)	19.36
240	4.9683(2)	0.992(5)	15.83
250	4.9712(2)	0.988(5)	15.99
260	4.9737(2)	0.991(5)	15.54
270	4.9760(2)	0.990(5)	15.21

 $x = 0.05$

Temperature (°C)	α -CDP a (Å)	Phase wt. fraction	R_{wp}
170	5.0279(4)	0.121(4)	15.05
180	5.0252(4)	0.133(3)	15.54
190	5.0211(4)	0.150(3)	15.92
200	5.0145(3)	0.196(4)	15.83
210	5.0085(3)	0.259(4)	16.76
220	4.9970(3)	0.443(5)	17.12
230	4.9855(2)	1	19.40
240	4.9868(2)	1	19.54
250	4.9895(2)	1	19.92
260	4.9915(1)	1	14.89
270	4.9934(1)	1	13.78

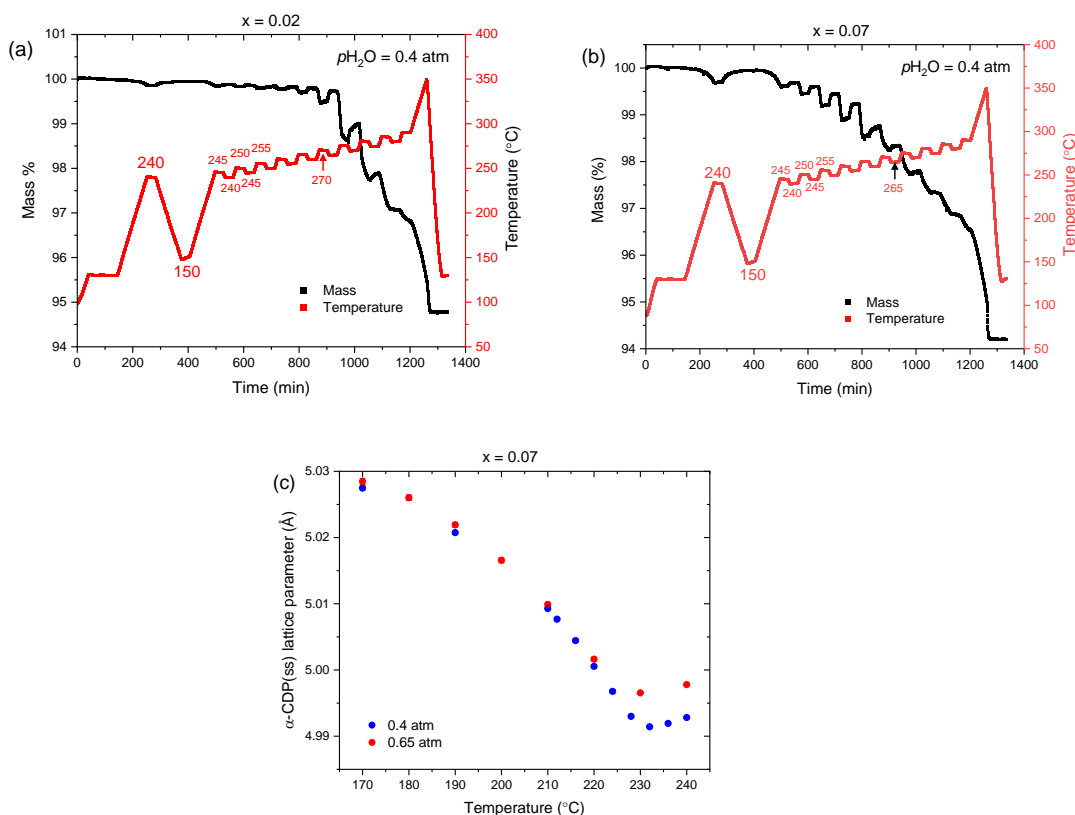
 $x = 0.07$

Temperature (°C)	α -CDP a (Å)	Phase wt. fraction	R_{wp}
160	5.023(1)	0.14(1)	20.46
170	5.0281(4)	0.385(8)	18.63
180	5.0267(4)	0.40(2)	18.02
190	5.0218(4)	0.437(7)	18.27
200	5.0172(4)	0.483(7)	17.92
210	5.0114(4)	0.552(8)	18.55
220	5.0017(4)	0.721(8)	20.63
230	4.9961(3)	1	19.62
240	4.9976(3)	1	19.63
250	4.9999(3)	1	20.24
260	5.0016(3)	1	19.90

$x = 0.15$

Temperature (°C)	α -CDP a (Å)	Phase wt. fraction	R_{wp}
160	5.0212	0.30(1)	14.67
170	5.0295(2)	0.83(1)	13.16
180	5.0279(2)	0.896(4)	12.49
190	5.0262(2)	0.947(4)	12.03
200	5.0264(2)	0.982(4)	12.21
210	5.0284(2)	0.986(4)	13.57
220	5.0307(3)	0.986(6)	16.65

Figure 3.S-11. Physical characteristics of samples of various compositions in the $(1-x)\text{CsH}_2\text{PO}_4-x\text{H}_3\text{PO}_4$ system, as indicated, as a function of temperature and steam partial pressure: (a), (b) mass and (c) lattice parameter of α -CDP(ss) for global compositions indicated. Despite mass sensitivity to steam partial pressure, the cell parameters of the α -CDP(ss) phase are unchanged in the two-phase regime of composition-induced thermal contraction. Lattice parameters in (c) were obtained by Rietveld refinement following the methodology reported above in the description of Figure S10 and full details of the refinement results under $p\text{H}_2\text{O} = 0.65$ atm are also reported with that figure. Details for $p\text{H}_2\text{O} = 0.4$ atm are reported here.



$x = 0.07, p\text{H}_2\text{O} = 0.4$ atm.

Temperature (°C)	α -CDP a (Å)	R_{wp} , %
170	5.0275(3)	12.58
190	5.0207(3)	12.29
210	5.0093(3)	10.98
212	5.0077(3)	11.07
216	5.0044(3)	11.62
220	5.0006(3)	11.36
224	4.9968(3)	11.90
228	4.9930(2)	11.29
232	4.9914(1)	11.66
236	4.9919(1)	12.25
240	4.9928(2)	12.55

Figure 3.S-12. Evaluation of the solvus phase boundary by diffraction analysis: (a) determination of the phase fraction of α -CDP(ss) as a function of composition, used for establishing the boundary by the Lever Rule, and (b) comparison of boundary determination by Vegard's Law (main text), the Lever Rule from part (a), and observation of the temperature at which CDP(m) is no longer detected in the diffraction data. As would be expected, the three approaches are in general agreement. The uncertainty is smaller from the Vegard's Law analysis than the Lever Rule analysis as a result of the difficulty of accurately establishing phase fractions from the diffraction data. Data plotted in (a) correspond to tabular listed provided in Figure S10.

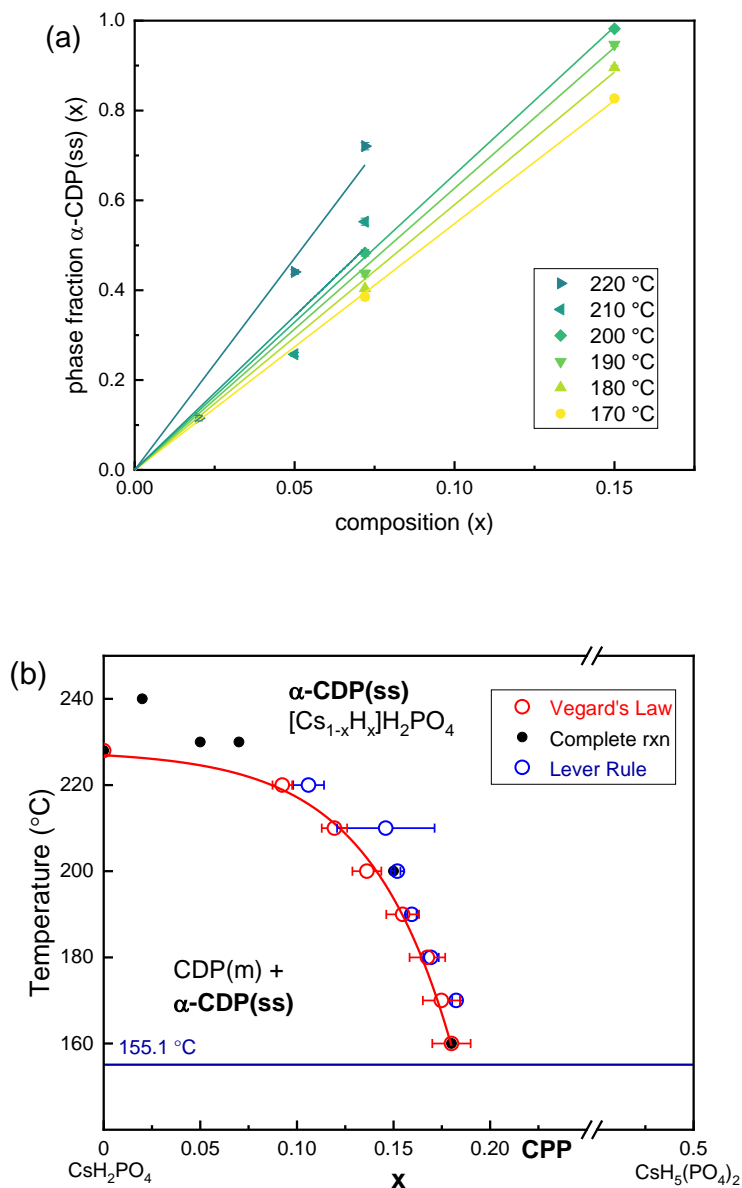
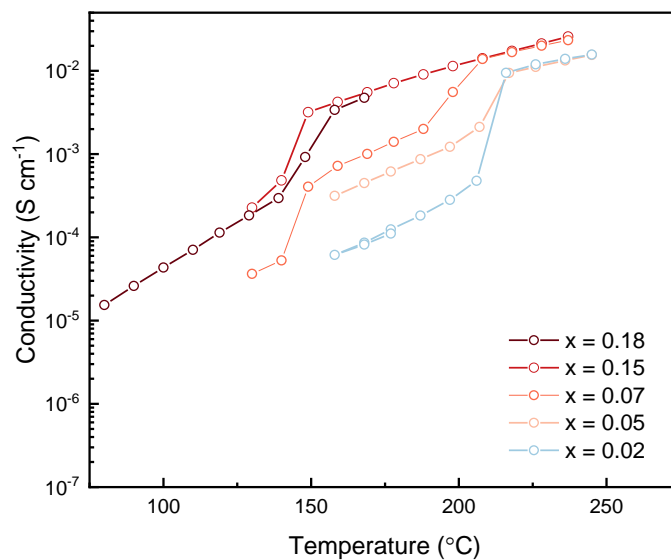


Figure 3.S-13. Conductivity of materials in the $(1-x)\text{CsH}_2\text{PO}_4 - x\text{H}_3\text{PO}_4$ system as a function of temperature on cooling with compositions as indicated. The data are consistent with that measured on heating with a slight hysteresis observed in the temperature of the reverse eutectoid reaction ($\alpha\text{-CDP(ss)} \rightarrow \text{CDP(m)} + \text{CPP}$).



Chapter 4: Review of Solid Acid Devices

In order to achieve a net zero emissions society and avoid the most catastrophic outcomes of a climate crisis, a diverse range of electrochemical devices must be developed not only for energy conversion and storage but also emerging applications such as ammonia synthesis and CO₂ reduction. Electrochemical devices based on superprotonic solid acid electrolytes may be well suited to play a significant role in this new economy as these devices feature unique advantages over nearby technologies such as polymer electrolyte membrane (PEM) cells and solid oxide cells. Within this chapter, the development of solid acid devices (SADs) is reviewed. Focus is first directed towards the current prevailing application as fuel cells, and the foundational principles for fuel cell operation and characterization are presented. Attention is then turned towards prospective electrolytic applications for which the opportunities and challenges are discussed.

4.1 Basic Principles of Fuel Cells and Electrochemical Devices

Application of solid acid electrolytes has primarily been explored for fuel cells, and thus it is helpful to start with an overview of the fundamental principles underlying fuel cell operation. A fuel cell is a device that electrochemically captures the Gibbs free energy of a fuel oxidation reaction – in essence converting fuel to electricity. The device is characterized by three active components: an anode at which the fuel is oxidized, a dense electrolyte layer that is responsible for transporting the ions across the device, and a cathode at which oxygen is reduced. In fuel cells that employ a proton conducting electrolyte, such as solid acid fuel cells (SAFCs) or polymer electrolyte membrane fuel cells (PEMFCs), the protons that are produced at the anode are transported through the electrolyte layer and then react with electrons and oxygen at the

cathode to form steam or water (Figure 4.1) . The electrons that are produced at the anode instead travel through an external circuit, doing electrical work, and then recombine and react with the protons at the cathode. For the common fuel cell operated on hydrogen fuel, the device operates by performing the hydrogen oxidation reaction (HOR), Eq. (1, at the anode and the oxygen reduction reaction (ORR), Eq. (2, at the cathode.

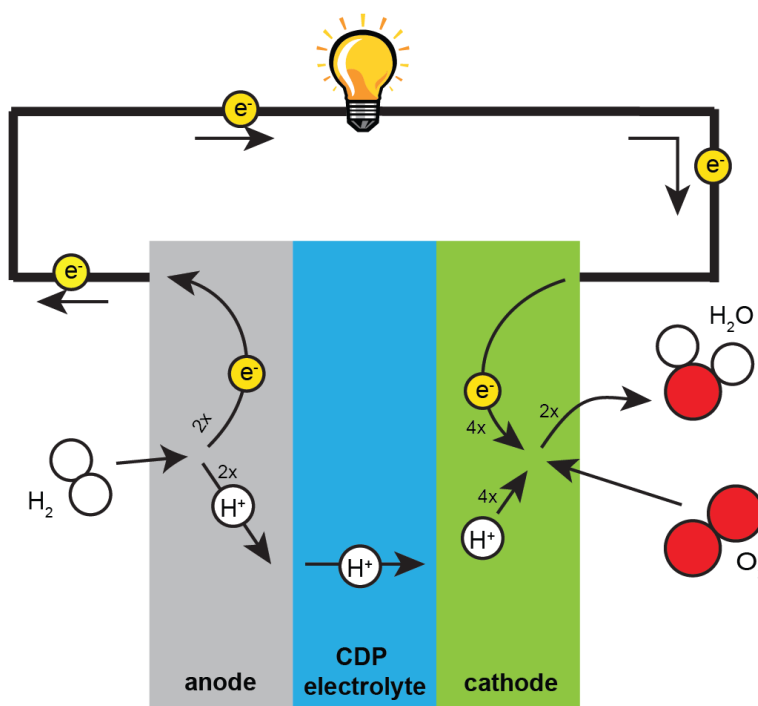
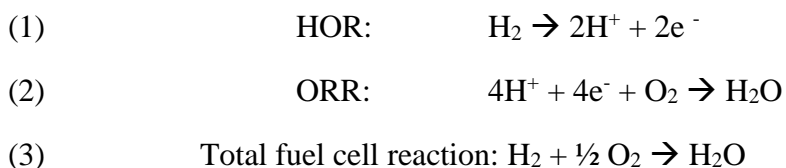


Figure 4.1. Schematic of the charge transport mechanisms and electrochemical reactions in a standard hydrogen SAFC.

The Gibbs free energy of the fuel cell reaction or hydrogen combustion reaction defines the maximum energy the fuel cell is capable of producing per fuel molecule and dictates the

potential across the cell when no current is drawn. This potential is called theoretical open circuit voltage (OCV) and is calculated from the Gibbs free energy of reaction, ΔG , by:

$$(4) \quad E_{Nernst}^{OCV} = \frac{-\Delta G}{nF}$$

where ΔG is expressed in J/mol, n is the number of electrons transferred in the fuel cell reaction (for the hydrogen fuel cell reaction as written in Eq(3), $n = 2$), and F is Faraday's constant or the charge per mol of electrons, 96485 C/mol.

This equation can be rearranged to a more useful form known as the Nernst equation by recognizing that the Gibbs free energy of each reactant and product can be broken down to their standard state Gibbs free energies and their activity or concentration dependent terms.

$$(5) \quad E_{Nernst}^{OCV} = E^0 - \frac{RT}{nF} \ln \left[\frac{\prod a_{products}^{v_i}}{\prod a_{reactants}^{v_i}} \right]$$

where E^0 is the standard state potential, a refers to the activity of a species, and v is the stoichiometric coefficient of the species in the fuel cell reaction. E^0 is calculated from the standard state Gibbs free energy of reaction ΔG^0 using:

$$(6) \quad E^0 = \frac{-\Delta G^0}{nF}$$

It should be noted that the standard state Gibbs free energy is determined at 1 atm and at a *specified temperature*. Therefore ΔG^0 should be determined at the specified operating temperature. Standard state thermodynamic values for most relevant gases are available as a function of temperature on the NIST database.

The activity of a gaseous species can be taken to be its partial pressure if an activity coefficient of 1 is assumed, as it typically is. The simplified Nernst equation for the hydrogen fuel cell reaction is then:

$$(7) \quad E_{Nernst}^{OCV} = E^0 - \frac{RT}{nF} \ln \left[\frac{p_{H_2O}}{p_{H_2} * p_{O_2}^{1/2}} \right]$$

Again, the Nernst potential serves to dictate the theoretical potential across the cell when no current is drawn from the cell. However, when current is drawn, various resistive processes within the cell result in voltage loss, reducing the cell potential from OCV and reducing the energy supplied by each electron. These resistive processes include the electrochemical reaction kinetics and charge transport of ions and electrons through the electrodes and the electrolyte.

Plotting the voltage across the cell as a function of the current density results in the polarization curve. The power density can then be produced by multiplying the voltage and current density at each point. High performance fuel cells minimize polarization losses to achieve high current densities at high operating voltages. Minimizing polarization losses results in both higher power densities and efficiencies, which will be discussed in the next section.

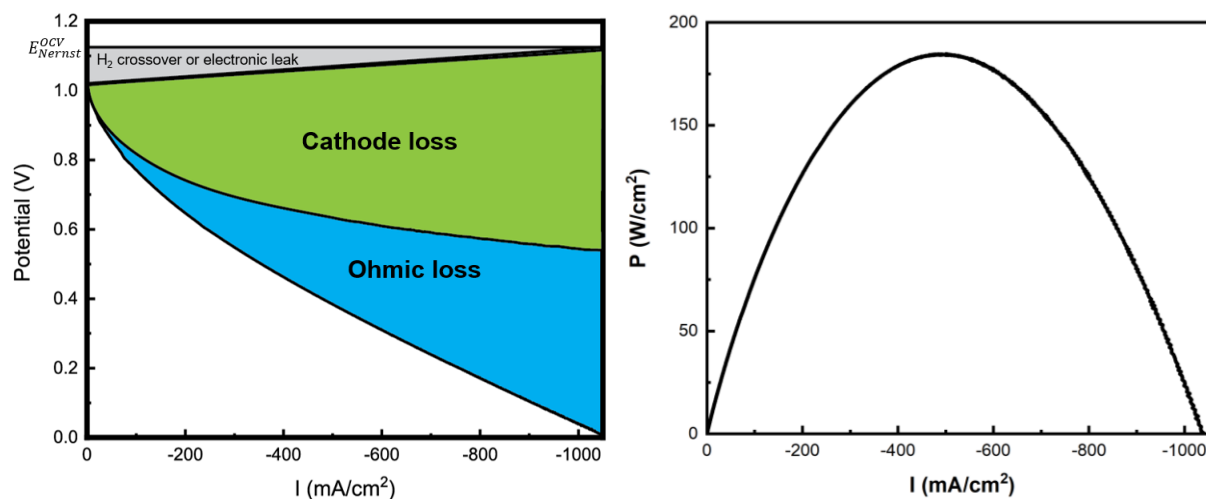


Figure 4.2. Polarization curve of a SAFC with delineated voltage loss contributions.

4.1.1 Fuel Cell Efficiency

The efficiency of a fuel cell is defined as the ratio of the electrical energy produced by the fuel cell reaction and the theoretical enthalpy of the reaction. The maximum electrical energy the fuel cell can produce is defined by the Gibbs free energy of the reaction and can only be achieved at the Nernst OCV. Therefore, the maximum efficiency of a fuel cell is defined as:⁹⁶

$$(8) \quad \varepsilon_{max} = \frac{\Delta G}{\Delta H}$$

Interest in fuel cells is in part derived from the ability of these devices to achieve efficiencies higher than the Carnot efficiency. However, in contrast to the Carnot efficiency, the maximum

fuel cell efficiency decreases with temperature. This fact can be simply arrived at by substituting $\Delta G = \Delta H - T\Delta S$ into Eq. (8) which produces the expression $\varepsilon = 1 - T\Delta S/\Delta H$. ΔS and ΔH are relatively constant (and both negative) and thus the maximum fuel cell efficiency decreases linearly with increasing temperature by the ratio $\Delta S/\Delta H$. It should also be noted that there is a distinction between calculated efficiency values that presume liquid water or steam as a reaction product in determining ΔH . If liquid water is assumed to be the product, ΔH will include the exothermic heat of condensation and will therefore be greater in magnitude than if steam is the product. Therefore, ΔH values calculated based on a liquid water product are termed the higher heating value or ΔH_{HHV} , whereas those based on steam are called the lower heating value or ΔH_{LHV} . It should also be noted that regardless of the choice of ΔH_{HHV} or ΔH_{LHV} , the calculation of ΔG should always reflect the actual phase of the reaction product. A SAFC operating at 250 °C has a $\varepsilon_{max,HHV}$ of 75% and a $\varepsilon_{max,LHV}$ of 89 % (these efficiencies are not specific to SAFCs, but rather a true for any fuel cell operating at 250 °C).

While ε_{max} defines the theoretical maximum efficiency of the fuel cell, it is not achievable in practice as current can only be drawn by reducing the cell potential from OCV. The energy of each electron is defined by the operating voltage, and thus the change in efficiency based on voltage can be easily calculated as:

$$(9) \quad \varepsilon_{voltage} = \frac{V}{E_{Nernst}^{OCV}}$$

Thus it is clear that in order to maintain high efficiencies, a fuel cell must operate at high voltages. However, operating at high voltages restricts the current densities that the cell can produce. Therefore, it is critical that polarization losses are minimized to allow for high current densities to be achieved with minimal sacrifices in efficiency.

The total efficiency of the fuel cell in operation is then calculated as the product of the two terms:

$$(10) \quad \epsilon_{total} = \epsilon_{max} * \epsilon_{voltage}$$

This calculation assumes that no fuel is lost, either left unreacted or consumed by a side reaction.

4.1.2 Polarization Losses

4.1.2.1 Experimental OCV and Leak currents

The experimental open circuit voltage (OCV) is the voltage across the device at which no net current is drawn. The experimental OCV is frequently observed at voltages significantly lower than the theoretical Nernst potential. These observations are attributed not to an error in the thermodynamic calculations for the fuel cell, but rather sources of leak current that flow opposite to the direction of fuel cell current. Remember the experimental OCV only measures the potential at which the net current is zero with no knowledge of the underlying mechanisms that may contribute to the current. Thus if an opposing leak current exists within the cell, the experimental OCV is recorded at the potential at which the fuel cell reaction produces a current that cancels out the leak current.⁹⁷

Two common examples of leak current are those produced by hydrogen crossover and electronic leakage currents. The case of electronic leakage is simpler and thus treatment of electronic leakage first is appropriate. If there is a small amount of electronic conductivity through the fuel cell, whether by an imperfection in the cell fabrication or the inherent electronic conductivity of the electrolyte, there will be an internal flow of electrons from the low electric potential at the anode to the high potential at the cathode, or equivalently an electronic current

from the cathode to the anode. In order to achieve net zero current, a fuel cell current must be generated equal in magnitude to the leak current, which can only be produced by reducing the cell potential from the theoretical Nernst OCV. At the low current densities required to negate the electronic leak, the fuel cell current is controlled by the kinetics of the ORR which increase exponentially as the cell potential is decreased, ie. $I \propto \exp(E_{Nernst}^{OCV} - V)$. In contrast, the electronic leakage current increases linearly with the cell potential according to Ohm's Law, ie. $I_{leak} = V/R$ where R is the electronic resistance across the cell. The experimental OCV can be calculated as the potential where the equations for the ORR current and leak current are equal.

The other frequently observed leak current is attributed to hydrogen crossover from the anode to the cathode, which can occur due to leakage through the electrolyte layer or poor sealing around the cell. When hydrogen is present at the cathode, it is exposed to a potential that is most likely much higher than the hydrogen equilibrium potential for HOR. To validate this statement, consider that the experimental OCV of a properly fabricated cell should be > 0.95 V, whereas in order for the equilibrium potential calculated from the hydrogen concentration gradient to be ≈ 1 V, the cathodic atmosphere would have to be as low as 10^{-20} atm. If the hydrogen concentration were to be so low as to approach such a value, there would essentially be no leaks through the cell and any hydrogen oxidation current that could be produced would be so small as to be incapable of meaningfully impacting the OCV. Rather, any meaningful leak of hydrogen would result in a much lower hydrogen concentration potential; for example, even 10^{-5} atm of hydrogen at the cathode would produce an equilibrium potential for HOR of 0.5 V. Therefore, for a meaningful hydrogen leak, there exists a significant overpotential for the HOR at the cathode. Given the facility of the HOR, it can be assumed that the hydrogen at the cathode is

instantly oxidized at a rate equivalent to the hydrogen leak rate. As the hydrogen leak rate is constant, the hydrogen oxidation current can also be assumed to be constant at higher potentials. Analogous to the case prior, the experimental OCV occurs at the potential where the exponential ORR rate is equal to the hydrogen oxidation rate.

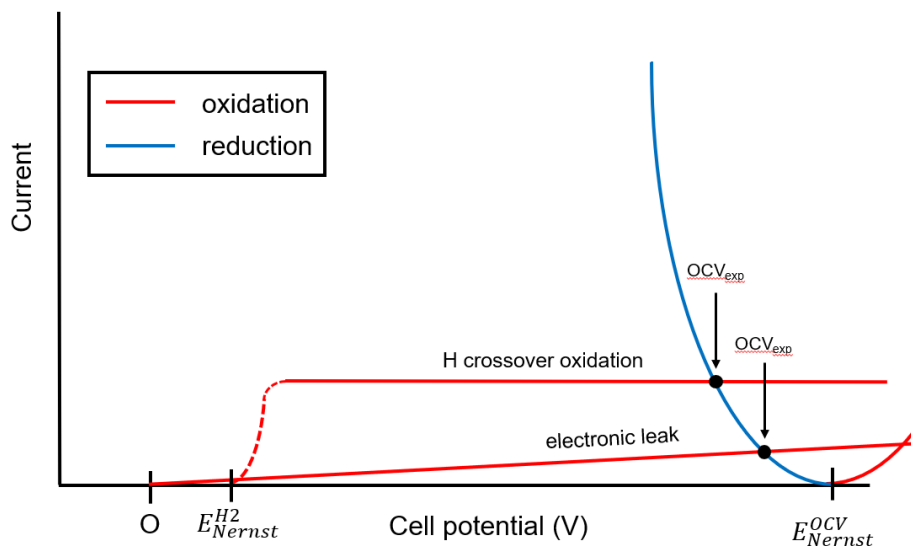


Figure 4.3. Schematic of the balance of leak and fuel cell currents at the cathode. The experimental OCV is observed at the potential at which the reducing ORR current at the cathode negates the oxidizing leak currents.

While hydrogen crossover and electronic leakage are the most commonly cited examples of leak currents, other sources are certainly possible. Two examples which are particularly relevant in SAFCs are the oxidation of the catalyst and the oxidation of the carbon paper current collector at the cathode. Unfortunately, the kinetics of these reactions have not been well studied in SAFCs.

4.1.2.2 Ohmic Losses

The electrolyte layer acts as a simple resistor for the proton current and the ohmic losses can be directly calculated by multiplying the current and the ohmic resistance. The ohmic resistance is typically measured by electrochemical impedance spectroscopy or by current interrupt measurements.

4.1.2.3 Charge Transfer Kinetics losses

In a standard hydrogen fuel cell, the kinetics of the ORR are typically several orders of magnitude slower than kinetics of the HOR. The effect is so extreme that often in accounting for the fuel cell performance, the losses due to the HOR are neglected altogether, and the charge transfer resistances are attributed entirely to the ORR.

Although the ORR is a multi-electron transfer reaction composed of several elementary steps, it is helpful to first understand the electrokinetics of a single electron transfer reaction. The reaction kinetics of a single electron transfer reaction have traditionally been described using a Marcus Theory framework as shown in Figure 4.4. The Gibbs free energies of the product and reactants are plotted for the hypothetical electron transfer reaction: $OH^* + e^- + H^+ \leftrightarrow H_2O$. Because the electron and proton are charged species, their electrochemical potentials are linearly dependent on the electric potentials in their respective phases according to $\bar{\mu}_i = \mu_i + zF\phi_i$. In a fuel cell the source of the electrons and protons are described as experiencing two different electric potentials, that of the electronic conductor/catalyst phase and that of the electrolyte phase respectively. At equilibrium, where there is net zero reaction, the potentials of the two phases are such that the energies of the reactants and product are equal, and the activation energy of

reaction is $\Delta G_c^{*,0}$. At equilibrium, the equivalent and opposite rates of the forward and backward reaction is termed the exchange current density, i_0 , which is related to the activation energy through an Arrhenius relationship: $i_0 \propto \exp\left(\frac{-\Delta G_c^{*,0}}{RT}\right)$.

When the potential of either phase is changed from their equilibrium value, the energy of the reactants responds accordingly, and the reaction is no longer in equilibrium. In practice, we only have direct influence on the potential of the electronic phase as measured by the potentiostat. It is helpful to make the analogy to the fuel cell reaction, despite this hypothetical scenario being only one elementary step in the ORR. At OCV, the potential of the Pt phase is the OCV and the reaction below is in equilibrium. However, as the fuel cell potential and correspondingly the Pt phase potential is reduced from OCV, the energy of the reactants increases and the reaction has a net rate in the forward direction. The potential of the electrolyte phase also responds to the change in the fuel cell potential, an effect that will be explored in Chapter 5, however for now the potential of the electrolyte phase will be taken to be constant. When the energy of the reactants is increased, the new activation energy of the forward reaction, ΔG_c^* , is calculated as:

$$(11) \quad \Delta G_c^* = \Delta G_c^{*,0} - \beta F(\Delta\varphi_e - \Delta\varphi_H)$$

where $\Delta\varphi_e$ and $\Delta\varphi_H$ are the change in potential of the electron and proton phases respectively from their equilibrium values, and β is the symmetry parameter that describes the symmetry of the intersection of the energy profiles at the reaction barrier. More plainly, β describes the efficiency with which applied bias is transferred to reducing the activation energy, and for most reactions β has a value around 0.5, meaning 50% efficiency of energy transfer. For a single electron transfer reaction β is also equal to the cathodic charge transfer coefficient α . Notably,

the expression for the activation energy derived here for a coupled proton and electron transfer reaction includes potential terms for both charged species, which is a deviation from the equation most often presented for a single electron transfer where only the electron potential term exists.

The reduced activation energy results in an increased forward cathodic reaction rate which can be calculated as $i_c = i_0 \frac{C_O}{C_O^*} \exp\left(\frac{\beta F(\Delta\varphi_H - \Delta\varphi_e)}{RT}\right)$. The $\frac{C_O}{C_O^*}$ term reflects the dependence of the reaction rate on the reactant concentration normalized to the reference concentration that i_0 was measured at. Along the same line of reasoning, the backward anodic reaction rate decreases to reflect the increased activation energy: $i_a = i_0 \frac{C_R}{C_R^*} \exp\left(\frac{-(1-\beta)F(\Delta\varphi_H - \Delta\varphi_e)}{RT}\right)$. The total reaction rate is then the sum of the anodic and cathodic currents:

$$(12) \quad i = i_0 \left\{ \frac{C_O}{C_O^*} \exp\left(\frac{\beta F(\Delta\varphi_H - \Delta\varphi_e)}{RT}\right) - \frac{C_R}{C_R^*} \exp\left(\frac{-(1-\beta)F(\Delta\varphi_H - \Delta\varphi_e)}{RT}\right) \right\}$$

This equation is the famous Butler-Volmer equation adjusted for a coupled proton and electron transfer. At high applied biases, where $\Delta\varphi_H - \Delta\varphi_e$ reaches significant positive values, the anodic current term becomes negligible and the Butler-Volmer equation can be simplified to the Tafel form:

$$(13) \quad i = i_0 \frac{C_O}{C_O^*} \exp\left(\frac{\beta F(\Delta\varphi_H - \Delta\varphi_e)}{RT}\right)$$

In the standard formalization, $\Delta\varphi_e$ is termed the overpotential, η , but in this derivation $\eta = \Delta\varphi_H - \Delta\varphi_e$ is more appropriate.

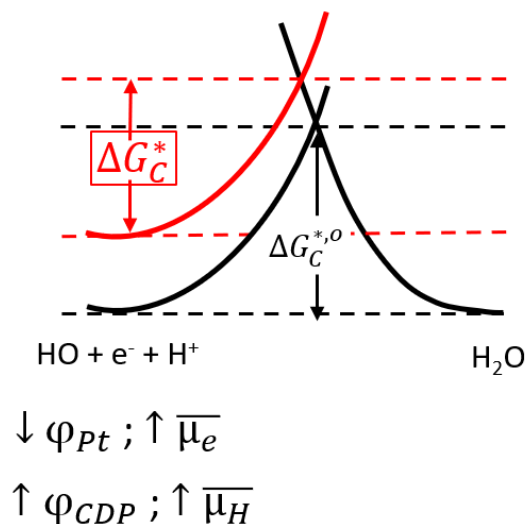


Figure 4.4. Marcus theory description of the kinetics of a single electron transfer reaction

4.1.3 Regions of the Polarization Curve

As shown in **Error! Reference source not found.**, at low current densities the polarization losses in the cell are dominated by charge transfer kinetics, specifically those associated with the ORR at the cathode. At low current densities, ohmic losses are minor and similarly the overpotential loss through the cathode is relatively limited, implying relatively uniform activation of the cathode. Therefore, at low current densities one can expect the polarization curve to roughly follow Butler-Volmer behavior. This region of the polarization curve is termed the activation region, as the majority of the bias is spent to activate the kinetics of the charge transfer reactions.

At higher biases, the reaction kinetics are described by the Tafel equation. The exponential form of the Tafel equation means that, on the typical linear scale of the polarization curve, increases in the ORR rate appear to be “for free”, with negligible bias being spent towards

further activating the ORR (Figure 4.2). At high current densities, while the increase in the ORR rate might appear as “free”, the ohmic losses are increasingly more costly, linearly scaling with the current. Therefore, in this region of the polarization curve, traditionally termed the “ohmic” region, the slope of the polarization curve is roughly the ohmic resistance of the electrolyte. It should also be noted, that in contrast to the activation region where the cathode is roughly uniformly active, in the ohmic region the high current densities result in significant overpotential losses through the cathode and the reaction becomes highly concentrated at the electrolyte-cathode interface, a result which will be explored in Chapter 5.

Finally at very high current densities, the polarization curve is often observed to turn downwards, such that further decreasing the potential of the cell produces very little increase in current density. This effect is due to mass transport limitations of reactant species to active sites in the electrodes and is called the “diffusion limited” region. Notably, no such region is observed in SAFCs, due to not enough current being drawn even at the limiting current density to induce significant diffusion limitations. The limiting current density is defined as the current density achieved when the cell is held at 0 V and the entire thermodynamic potential of the fuel cell reaction is spent.

4.2 Solid Acid Fuel Cells

A typical solid acid membrane electrode assembly (MEA) is built upon a thick stainless steel gas diffusion layer (GDL) and is comprised of a microporous layer (MPL), an anode layer, a dense CDP electrolyte layer, a cathode layer, carbon paper, and a stainless-steel mesh. The GDL, carbon paper, and stainless-steel mesh serve as gas-permeable electronic current carriers.

The active layers of the MEA are fabricated by successively uniaxially pressing powders onto the GDL and are shown in Figure 4.5.

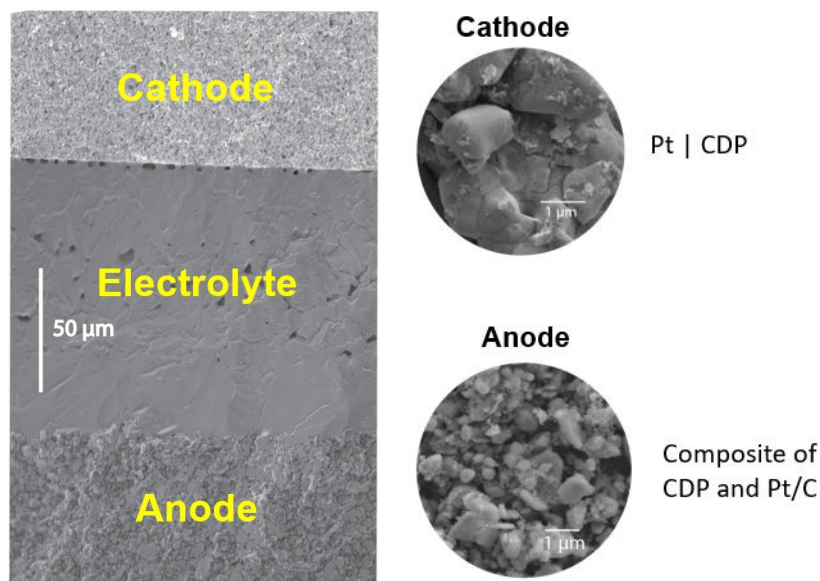


Figure 4.5. Cross sectional SEM image of a SAFC where the active components are shown. SEM images of the cathode and anode powders are shown in the insets.

The basic mechanisms of charge and mass transport in SAFCs are largely identical to other fuel cells based on proton conducting electrolytes as shown in Figure 4.1. High performance SAFC electrodes are capable of producing high current densities by transporting protons, electrons, and gas phase reactants to a high density of catalytic sites distributed throughout a porous electrode. In solid acid fuel cells, these electrodes are a porous composite of CDP particles, an electronically conductive material, and catalyst nanoparticles.

Despite the nominal advantages of solid acid electrolytes, the performance of SAFCs thus far is significantly worse than that of PEMFCs. In fact, the highest stable power densities that have been demonstrated are around 0.2 W/cm^2 , with a current density at 0.8 V of $\sim 50 \text{ mA/cm}^2$.⁵⁰

Both of these values are far from the 2020 DOE performance targets for PEMFCs which are a peak power density of 1 W/cm^2 (at 150 kPA pressure) and 300 mA/cm^2 at 0.8 V. The underperformance of SAFC is observed in spite of the exceedingly high Pt loading in these devices, which is often several mg Pt/cm^2 . In contrast, the DOE targets were recently met by a PEMFC with an ultralow platinum group metal (PGM) loading of 0.07 mg/cm^2 which demonstrated $>400 \text{ mA/cm}^2$ at 0.8 V and 1.01 W/cm^2 .⁹⁸

The limitations of SAFCs are attributed to challenges arising in the cathode, which is responsible for a majority of the polarization losses and accounts for the vast majority of the Pt loading in the cell ($\sim 2 \text{ mg/cm}^2$) (Figure 4.2). Comparison of impedance spectra taken under symmetric H_2 conditions (HOR/HER) with those taken under fuel cell measurement illustrates the overwhelming dominance of the cathodic charge transfer resistance; the spectra captured under symmetric H_2 has a charge transfer resistance of $0.05 \Omega \text{ cm}^2$ at OCV, while that taken under fuel cell measurement has an arc diameter of $\sim 2 \Omega \text{ cm}^2$ at 0.8 V (a bias of over 300 mV).^{48,99} While the challenge of sluggish ORR kinetics is faced in all fuel cells, the cathodic activation losses are particularly pronounced in SAFCs, which is clearly reflected in the current densities at 0.8 V. At 0.8 V, the performance of both SAFCs and PEMFCs is dictated by the kinetics of the ORR and yet PEMFCs produce nearly 8 times the current density of SAFCs at this potential ($400 \text{ vs } 50 \text{ mA/cm}^2$) with less than a tenth of the Pt loading ($1.75 \text{ vs } 0.07 \text{ mg Pt/cm}^2$).⁹⁸ The unusual inactivity of SAFC cathodes is the critical factor hindering cell performance, and it is prudent to target efforts to improve SAFCs at the cathode.

4.2.1 SAFC Cathodes

Unfortunately, the poor performance of SAFC cathodes was not well understood until the work conducted in Chapter 5. The higher operating temperatures of SAFCs compared to PEMFCs should in theory result in enhanced thermal activation of the ORR on active Pt sites, increasing the exchange current density. The fact that such an effect has not manifested in higher performance cathodes might lead one to believe that microstructural limitations of charge and mass transport are responsible. In Chapter 5, I will show that this assumption is not true, but it is worthy nonetheless to examine the microstructure of the SAFC cathode. State-of-the-art SAFC cathodes are composed of Pt-CDP composite particles, in which a thin layer of Pt nanoparticles coats sub-micron CDP particles, that are pressed to form the porous cathode. This microstructure is notably devoid of a C based support, in contrast to the SAFC anode or PEMFC electrodes, due to the instability of most such materials in the oxidizing cathodic SAFC environment.^{100,101} Instead the electronic current is carried through the cathode solely in the Pt film. A certain threshold of Pt loading is required to achieve sufficient electronic connectivity, but exceeding this threshold does not yield higher current densities as the density of catalytic active sites does not increase as the Pt film is made thicker.^{50,51} While a substantial portion of the cathode is comprised of Pt (~20 wt%), this mass fraction is on par with those in PEMFC cathodes and is not the origin of the exceedingly high Pt loading in SAFCs.^{50,102} Rather the high Pt loading arises from the much thicker cathode layer in SAFCs vs PEM: 25 - 100 μm in SAFCs vs $\sim 5 \mu\text{m}$ in PEMFCs. Prior to the work conducted in Chapter 5, the microstructural influence on charge and mass transport in SAFC cathodes had not been well studied, with the single study modelling these behaviors being deemed to be significantly flawed.¹⁰³

Thin films of Pt have been deposited on CDP particles for porous cathodes by two methods: metal organic chemical vapor deposition (MOCVD)⁵⁰, which results in a film of nanoparticles, and atomic layer deposition (ALD)⁵¹, which results in a smooth continuous film. Both approaches yielded similar performances, peak power densities of $\sim 200 \text{ mW/cm}^2$. Additionally, both studies observed that inadequate Pt loading on CDP resulted in films that were susceptible to coarsening, which reduced the electrochemically active surface area (ECSA) both due to particle size growth and due to electronic disconnection of Pt islands. Reducing the CDP particle size, and thus increasing the area for Pt loading, was shown to proportionally increase the current density and reduce the polarization resistance ($R_p^{-4} \propto SA_{\text{CDP}}$).¹⁰⁴ However, increasing the CDP surface area linearly increases the required Pt loading to maintain electronic connectivity. Additionally, it will be shown in Chapter 5 that relying solely on reducing the CDP particle size to achieve the DOE performance target of $300 \text{ mA/cm}^2 @ 0.8\text{V}$ would require CDP particles of 50 nm diameter, which is likely too small to be maintained against coarsening without additional supports.

Surprisingly little has been done in the exploration of catalyst chemistry in SAFC cathodes, despite the opportunity for significant improvements in catalytic activity and reduction of the platinum group metal (PGM) loading. Nevertheless, it has been shown that Pt-Pd catalysts are significantly more active than Pt alone.^{99,104,105} In fact the highest activity Pt-Pd catalyst, $\text{Pd}_{0.84}\text{Pt}_{0.16}$, demonstrated current densities that exceeded the DOE current density target, albeit briefly – exhibiting $>300 \text{ mA/cm}^2 @ 0.8 \text{ V}$.⁹⁹ The origin of the superior activity of Pd rich catalysts is not well understood. While Pd core - Pt shell nanoparticles have shown superior ORR activity compared to Pt in acidic aqueous solutions,^{106,107} the spontaneous formation of such

nanostructures would seem unrealistically fortuitous and is not claimed by the authors of the study. The possibility that the O binding energy of this Pd-Pt alloy is nearer to the Sabatier optimum than Pt alone cannot be ruled out, although the opposite was observed in aqueous rotating disk electrode measurements at room temperature.¹⁰⁷ Another possibility is that the introduction of Pd increases the diffusivity of protons through the catalyst film to active sites on the surface, an effect which has been observed in studies of Pd-Pt bilayers at the anode.¹⁰⁸ Unfortunately, the enhanced activity of Pd rich alloys is unstable, as Pd is reactive with CDP, forming Pd phosphates in oxidizing conditions. However, stabilizing Pd against CDP could yield significant improvement of SAFC performance and attempts to do so with a thin film oxide barrier layer will be discussed in the Appendix. Another obvious candidate for exploration is PtCo, which has demonstrated activity superior to that of Pt in PEMFCs.

While most carbon based supports are unsuitable for SAFC cathodes, a boron doped graphene support was shown to have enhanced stability against oxidation in SAFC cathodic conditions and when mixed to form a composite cathode delivered stable performance over 40 hrs.¹⁰⁹ While the authors did not demonstrate performance on the timescale of thousands of hours required for commercial application, the approach of chemical modification to stabilize carbon based supports appears promising and could significantly reduce the Pt loading in the cathode. Utilizing a B doped graphene support, Pt loadings of 1.3 g/cm^2 were demonstrated to have stable performance,¹⁰⁹ a slight improvement over what was demonstrated prior with cathodes in which Pt was deposited by MOCVD (1.7 mg/cm^2).⁵⁰

SAFC degradation is also a chief concern, as lifetimes currently stand around 1000-2000 hrs due to microstructural-evolution induced failure of the cathode. The degradation primarily

occurs at the electrolyte layer – cathode layer interface where the CDP electrolyte is observed to infiltrate the porous cathode resulting in densification and loss of active sites.¹⁰⁴ This effect has been attributed to local overheating due to current constriction and focusing and heat evolved from the resistive ORR.¹⁰⁴ Local heating is suspected to cause temperature increases that induce the dehydration of CDP, causing the material to form a liquid phase, which upon re-solidification, results in a densification of the once porous cathode.¹¹⁰ It has been further suggested that the liquid dehydrate phase can be reduced onto active Pt sites, resulting in catalyst poisoning.¹¹¹ These effects are not observed at the anode where the fine microstructure appears unchanged after hundreds of hours of operation – further evidence that it is the resistive ORR responsible for local overheating.¹⁰⁴

4.2.2 Anode

In contrast to the cathodic ORR, HOR at the anode is extremely facile. Symmetric cells employing standard SAFC anodes as both electrodes operated in a symmetric hydrogen atmosphere for HER/HOR exhibit combined electrode resistances as low as $0.05 \Omega \text{ cm}^2$ with no bias.⁹⁹ The charge transfer resistance attributed to the anode is thus negligible in comparison to that of the cathode, and accordingly the development of the anode has primarily focused on reducing the Pt loading while maintaining performance. The current standard anode is a composite of Pt on C black and CDP with a Pt loading of $\sim 1 \text{ mg/cm}^2$ (our own unpublished advances of the anode mixture place this value at 0.3 mg/cm^2).¹⁰⁹ Achieving high Pt utilization in composite SAFC anodes is more challenging than in PEMFC anodes due to the inability of the

solid CDP electrolyte particles to permeate and envelop Pt/C particles as the ionomer does in PEMFCs.

Progress in reducing the Pt loading at the anode has focused on nanostructuring the anode to increase the Pt utilization and ECSA. One such approach has been the introduction of nanostructured C supports, specifically carbon nanotubes (CNTs).¹¹²⁻¹¹⁴ Notably, incorporation of Pt/CNT into porous composite anodes resulted in electrodes with significantly lower Pt loadings (0.2 mg/cm^2 per electrode) that achieved charge transfer resistances ($0.05 \Omega \text{ cm}^2$) in line with those demonstrated by previous standard anodes.¹¹³ Additionally, deposition of nanostructured anodes has been demonstrated using spray techniques, such as electrospray and spray drying, and resulted in not only higher Pt utilization but also significantly lower Pt loading at the anode.^{112,114-116} A combined approach of electrospray deposition of a mixture of CDP and Pt/CNT produced an anode with ultra-low Pt loading (0.01 mg/cm^2) and high Pt utilization.¹¹² Unfortunately, the ultra-low loading also resulted in higher ASR's – $1.2 \Omega \text{ cm}^2$ at zero bias. However, such a value is still dwarfed by the cathodic charge transfer arc, and the trade-off of minor activity losses for reduced Pt loading may be favorable.

A fundamental study of the HOR kinetics in SAFC anodes surprisingly revealed that activity is not dictated by triple phase boundaries, as conventionally assumed for composite electrodes, but rather by double phase boundaries between Pt and the gas phase.¹¹⁷ The activity of the entire Pt-gas interface is made possible by the diffusion of H atoms through the Pt catalyst, presumably through the grain boundaries.¹¹⁷ Additionally it has been shown that both the surface reaction resistance and the H diffusion resistance are significantly reduced by introducing a Pd

overlayer on top of the Pt catalyst.¹⁰⁸ However, the reactivity of Pd with CDP is again observed at the anode, where Pd phosphides are formed by the reaction.

4.3 Alternative Fuels

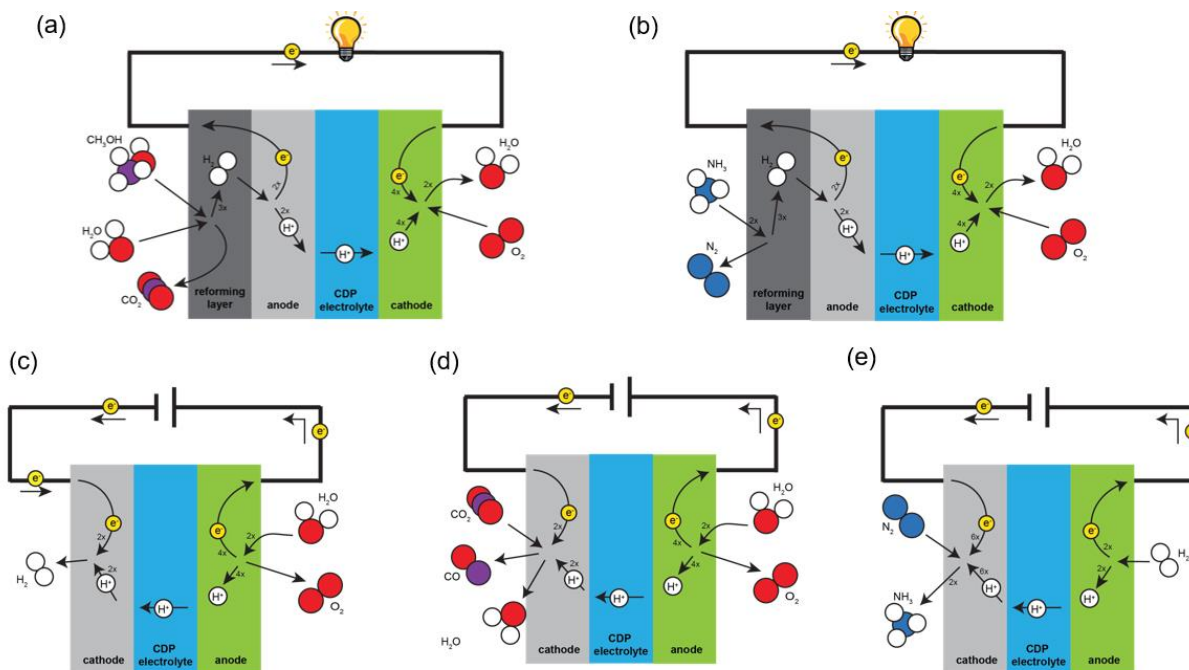


Figure 4.6. Schematics representing various solid acid devices. (a) methanol fuel cell. (b) ammonia fuel cell. (c) steam electrolysis cell. (d) CO₂ reduction electrolysis cell. (e) ammonia synthesis electrolysis cell.

While the gravimetric energy density of hydrogen is exceptionally high, the volumetric energy density of hydrogen even at 700 bar ($33.33 \text{ Wh/g LHV} \times 39.6 \text{ g/L} = 4.75 \text{ MJ/L}$) is less than a fifth of that of gasoline (32.00 MJ/L). Additionally, the infrastructure for hydrogen transport and storage is extremely limited. Therefore in applications where volumetric energy density or ease of fuel transport are crucial, a liquid hydrogen carrier is more sensible. One of the chief advantages of SAFCs is the ability to contend with alternative liquid hydrogen carriers and

impurities that would either result in dissolution and crossover or act to poison the catalyst in PEMFCs. The anhydrous solid electrolyte and intermediate operating temperatures in SAFCs means that these molecules are impermeable to the membrane and are rapidly desorbed from the catalyst.

Alcohols, such as methanol which features a volumetric energy density of 15.74 MJ/L, are highly attractive hydrogen carriers for SAFCs as these fuels are relatively safe – both with regard to toxicity and flammability - have well-established transportation infrastructure, and are already currently produced in high volumes. As previously noted, while alcohol fuels present major challenges to PEMFCs due to fuel solubility/crossover and CO poisoning, these issues are avoided in SAFCs due to the solid anhydrous electrolyte and the higher operating temperatures. The consumption of an alcohol fuel necessarily involves CO₂ as a product (ex: global fuel cell reaction for methanol $\text{CH}_3\text{OH} + 3/2\text{O}_2 \rightarrow \text{CO}_2 + 2\text{H}_2\text{O}$). However, these fuels can, in principle, be produced electrochemically from captured CO₂ or as biofuels, in which case the process is carbon neutral. SAFCs have been demonstrated to operate very effectively using alcohol fuels with peak power densities exceeding 200 mW/cm².^{45,47,104} A few modifications to the cell architecture must be made to allow for alcohol fuels. The first is the introduction of a reforming layer on the anode side of the cell which produces hydrogen by thermally reforming the alcohol with steam (ex: $\text{CH}_3\text{OH} + \text{H}_2\text{O} \rightarrow 3\text{H}_2 + \text{CO}_2$). Secondly, the anode catalyst composition must be adjusted to tend with the high amounts of CO produced either by incomplete reforming or as an intermediate of direct oxidation of the alcohol on the anode catalyst. A SAFC with a reforming layer composed of Cu-ZnO supported on Al₂O₃ in conjunction with a Pt-Ru anode catalyst was shown to be highly active with methanol, exhibiting a peak power density of 226

mW/cm² which was nearly comparable to the power density of a pure hydrogen fuel (270 mW/cm²). The slight loss in peak power density associated with the methanol fuel is due to the reformer being unable to keep up with the rate of hydrogen oxidation at high current densities. At lower current densities, even up to 0.5 A/cm², performances with methanol or hydrogen fuels are essentially identical. The outstanding performance of SAFCs utilizing alcohol fuels positions these devices to stand out in markets where volumetric energy density is crucial.

Ammonia is also an attractive alternative fuel. Like alcohols, ammonia, which is already extensively produced and delivered as fertilizer, can be stored and transported using extensive existing infrastructure, but unlike organic fuels, ammonia produces no pollutant gases when utilized in a fuel cell, only nitrogen and steam. In PEMFCs, ammonia is extremely deleterious, with even ppm levels of the molecule resulting in catastrophic failure of the device.^{118,119} Thus if ammonia is to serve as a hydrogen carrier for PEMFCs, point-of-use conversion of ammonia to high purity hydrogen is critical. In contrast, SA devices are well poised to serve not only as ammonia-to-hydrogen converters, but even direct ammonia fuel cells as ammonia is neither detrimental to the solid acid electrolyte nor poisoning to the catalysts at the elevated operating temperatures. Similar to the alcohol SAFC, a SA device operating on ammonia features a thermal cracking layer on the anode side of the cell, splitting ammonia to produce nitrogen and hydrogen which in turn is consumed by the HOR reaction at the anode, shifting the thermal decomposition equilibrium towards further hydrogen production. Using this approach, the rates of ammonia cracking can be significantly enhanced, and the thermodynamic limitations of equilibrium can be overcome.

An impressive SA ammonia-to-hydrogen device was demonstrated with a thermal cracking layer composed of Ru/CNT and standard composite electrodes (Pt/C black and CDP) as both the anode and cathode, performing HOR and HER respectively.¹²⁰ The device exhibited remarkable hydrogen production rates with 100% Faradaic efficiency at exceptionally low overpotentials. The catalyst-mass-normalized hydrogen production rates were competitive with the best rates from thermal ammonia decomposition, which were conducted at much higher temperatures (350 – 500 °C). Although the device demonstrated current densities as high as 480 mA/cm² with 0.402 V of bias, sluggish ammonia decomposition rates began to limit performance at current values greater than 200 mA/cm². There are no current reports of an SAFC operating on ammonia, but such a device is easily conceivable given that the cathode is indifferent to the fuel source so long as protons are readily supplied. Thus swapping the cathode on the ammonia-to-hydrogen device for a standard SAFC cathode performing ORR would create a direct ammonia SAFC. However, such a device would face the aforementioned limitations of the ammonia cracking rate as well as the charge transfer losses associated with ORR at the cathode. Thus advancement of ammonia based SAFC relies on both improvements to the thermal cracking layer and the ORR kinetics at the cathode.

4.4 Prospective Electrolytic Applications

There are several electrolytic applications in which solid acid devices may present significant advantages over existing technologies, for example in the production of carbon neutral fuels or critical chemical feedstocks. Unfortunately, little has been done in the development of electrolytic solid acid devices. In order to encourage the development of

electrolytic SADs, here I briefly highlight the most notable opportunities and challenges for solid acid devices in the applications of hydrogen production from steam electrolysis, CO₂ reduction, and ammonia synthesis.

The production of green hydrogen is essential to achieving a sustainable hydrogen economy. Current green hydrogen production relies heavily on PEM electrolyzers which utilize incredibly scarce and expensive Ir catalysts for the oxygen evolution reaction (OER). The reliance on Ir is necessitated by the oxidizing and acidic environment at the PEM electrolyzer anode which dissolves non-noble, and even some noble, metals. In contrast, the anhydrous nature of the solid acid system does not allow for catalyst dissolution and thus the chemical constraints can be relaxed to include less noble metals and even non-PGM catalysts which have been observed to exhibit exceptional OER activity in alkaline aqueous solutions.¹²¹ However, as previously noted, CDP presents stability challenges of its own and thus stability of any catalyst must first be assessed with CDP. RuO₂ is a particularly exciting OER catalyst candidate as it has been shown to exhibit higher OER activity than even IrO₂ in PEMECs, but rapidly dissolves in the anodic environment.¹²² There are some encouraging signs for Ru stability with CDP as a PtRu catalyst was demonstrated to be stable in the anode of a direct methanol SAFC.⁴⁷

The electroreduction of CO₂ to form useful reagents and products such as carbon monoxide, alcohols or hydrocarbons can improve the economic value of captured CO₂ and provides a sustainable pathway to form critical carbon-containing compounds which have become ubiquitous as polymers, adhesives, solvents, lubricants, and fuels. CO₂ electroreduction has been primarily explored in low temperature aqueous systems; although solid oxide CO₂ electrolyzers have also been shown to be effective, these systems are limited to producing solid

carbon and CO due to the high operating temperatures. The principal challenges identified in low temperature aqueous CO₂RR are low catalytic activity, product selectivity, and catalyst stability. The CO₂RR is in competition with the typically very facile HER, and thus in order to achieve high Faradaic efficiencies for CO₂RR, selection of catalysts that are poor at HER is essential. A variety of catalysts have been demonstrated to be capable of the CO₂RR including Cu, Au, Ag, Zn, Pd, and Pt.¹²³ While the best of these catalysts have demonstrated >90% Faradaic efficiencies, the activity of these catalysts are still far from commercial requirements, with current densities of only ~10 mA/cm² produced at hundreds of mV of bias.¹²⁴ Additionally, the solubility of CO₂ in aqueous solutions can be a debilitating factor; in thin membrane electrode assemblies, CO₂ crossover due to carbonate formation can result in CO₂ losses of 75%.¹²⁵ Solid acid devices are poised to make substantial advances in CO₂RR due to the kinetic benefits of elevated temperatures and the impermeability of solid acid membranes. However, the challenge of selectivity for CO₂RR is likely to be a significant hurdle in solid acid devices as in aqueous electrolyzers, and the identification and design of selective catalysts is crucial. Gold may be a promising candidate as it has shown to be an ineffective catalyst for HOR,¹¹⁷ stable with CDP, and, in aqueous solutions, an active and CO₂RR selective catalyst.¹²⁴ Another factor to contend with is the reverse water gas shift reaction ($\text{CO} + \text{H}_2\text{O} \rightarrow \text{CO}_2 + \text{H}_2$) which is thermodynamically spontaneous under the cathodic solid acid electrolyzer condition and capable of reverting CO back to CO₂. A solid acid based CO₂ – H₂O co-electrolysis device was demonstrated by Bjerrum et al. which utilized a composite CDP-SiC electrolyte with a Ni CO₂RR catalyst at the cathode and an IrO₂ OER catalyst at the anode.¹²⁶ The device, which operated at 300 °C and 8 atm, demonstrated Faradaic efficiencies > 90 % for methane formation at 14 mA/cm².

In many regards, ammonia is the perfect hydrogen carrier: easily liquifiable and transportable, and when consumed as a fuel, produces only nitrogen and steam. However, the synthesis of ammonia has long been a difficult problem of balancing conflicting thermodynamic and kinetic requirements. In order to overcome this challenge, traditional Haber Bosch ammonia synthesis reactors operate at high temperatures (~ 500 °C), which favor fast kinetics but low equilibrium ammonia concentrations, and high pressures (20 MPa), which help to slightly improve the equilibrium concentrations. These Haber Bosch plants are prohibitive at small scales making it difficult to build a network of reactors tied to alternative energy production sites. Electrochemical ammonia synthesis could be the key in decoupling the kinetics, which can be controlled by the bias, from the thermodynamics of ammonia production. Additionally electrochemical reactors offer the benefits of smaller modular systems. However, once again catalyst reaction selectivity is the critical challenge as the ornery nitrogen reduction reaction (NRR) is in competition with the facile HER. To date, attempts at electrochemical ammonia synthesis have focused on low temperature aqueous systems and only achieved ammonia concentrations in the ppm range, with current densities of $\mu\text{A}/\text{cm}^2$, and Faradaic efficiencies $<10\%$.¹²⁷ Plainly, monumental improvements in NRR activity and selectivity are required in order for this process to be considered for commercial applications. Solid acid systems may facilitate the breaking of the notoriously stable N-N triple bond and improve the kinetics of NRR.

4.5 Electrochemical Characterization of SAFCs

4.5.1 Open Circuit Voltage

The experimental open circuit voltage represents the cell voltage at which no current is produced and can provide a means of assessing the isolation of the electrodes both electrically and with respect to gas atmosphere. In general, observation of the OCV closer to the theoretical Nernst potential represents better integrity of the electrolyte layer and sealants in isolating the electrodes. OCV should be tracked while the cell is heated to operating temperatures, however it is critical that during this heating stage, the combination of hydrogen and air/oxygen are not introduced until the cell has undergone the superprotonic transition. Below the superprotonic transition temperature, the electrolyte layer of the cell is somewhat porous, and gas leaks are prevalent across the cell. The mixing of hydrogen and oxygen across the cell can cause combustion within the electrodes especially in the presence of Pt catalysts, resulting in cell damage prior to reaching operating temperatures.

It is therefore recommended that the cell be brought up from 150 °C under humidified hydrogen at the anode and humidified nitrogen at the cathode. While the thermodynamic potential is poorly defined for this condition, in practice the unavoidable hydrogen leak across the porous electrolyte layer establishes a hydrogen concentration potential. In our experience a well-sealed cell should have an OCV between 0.6 – 0.7 V under humidified hydrogen and nitrogen at 250 °C. If this criteria is met, it is then considered safe to introduce air or oxygen to the cathode.

4.5.2 Potential Sweep Methods

Potential sweep methods such as linear sweep voltammetry or cyclic voltammetry are powerful tools for the characterization of electrochemical reaction kinetics or the characterization of a transient response, such as the evolution of a diffusion gradient or the oxidation of a catalyst. In linear sweep voltammetry, the voltage between the electrodes is linearly varied at a controlled sweep rate (mV/s) between two voltages which are termed the upper and lower vertex potentials. In cyclic voltammetry, the potential is cycled between these two potentials, often several times until a stable consistent response is produced.

Cyclic voltammetry (CV) is most frequently employed in liquid electrochemistry, where the technique is used to study the reversible reduction and oxidation of species in solution. Although this application is quite distinct from the technique's use in fuel cells, a basic understanding of the more common liquid application is helpful in establishing a broader perspective of the technique and the field of electrochemistry in general. In liquid electrochemistry, the voltammograms frequently take the form of the "duck curve", in which opposing reduction and oxidation peaks frame the standard potential for the reaction of interest. The observation of the reduction and oxidation peaks is a product of a lag in formation of the diffusion layer compared to the potential sweep rate. Were the voltage swept slow enough such that the diffusion concentration profiles of the reactants and products were in equilibrium with the bias and surface reaction rate, the current would monotonically increase with increasing voltage, eventually plateauing at the diffusion limited current. However, because the potential is swept at a rate faster than the diffusional kinetics, the reaction rate is able to momentarily reach a maximum. The faster the voltage is swept, the more out of equilibrium the diffusion profiles will be and the higher the peak current observed. This relationship is described by the Randles-Sevcik

equation. For further understanding, the reader is directed to read Dempsey et al. which does a fantastic job describing the application and principles of cyclic voltammetry in liquid electrochemistry in simple clear terms.¹²⁸ In fuel cells, however, the duck curve is not observed because reactant gas diffusion is very rapid in comparison to liquid diffusion and thus the current response measured in fuel cells reflects the kinetics of the electrochemical reactions rather than the diffusion kinetics. In other words, in fuel cells, the equilibrium diffusion profile is instantaneously established at each potential, and as a result, out-of-equilibrium peaks in the current response are not observed.

In the work presented here, CV measurements are primarily used as a method to repeatedly probe the kinetics of a reaction to assess stability and increase statistical representation. However, CV measurements are commonly used in fuel cell literature as well to characterize the active surface area in the cell. For example, CV measurements are commonly employed in PEMFCs to characterize the electrochemically active surface area (ECSA) of an electrode using hydrogen underpotential deposition.^{129,130,131} In this method, the electrode is deposited on a glassy carbon disk and submerged in an acidic solution. CV measurements are then taken over a voltage window of typically 0.1 - 0.8 V vs RHE. The lower vertex potential is specifically selected to avoid the hydrogen evolution reaction but include the adsorption and desorption of proton, ie. $H^+ + e^- \leftrightarrow H^*$. The adsorption and desorption peaks can then be integrated to determine the total charge of adsorb/desorbed protons, which can then be correlated to the active surface area using a correlation factor. These measurements can also be conducted in operando, ie. on a full MEA in a fuel cell test station, by flushing the electrode of interest with an inert gas.^{40,132}

Unfortunately, hydrogen UPD peaks have not been observed in SAFCs. However, a method was demonstrated for determining the ECSA by integrating the Pt oxide reduction peaks in CV sweeps.¹³³ In determining the Pt ECSA, it is not appropriate to simply integrate the Pt oxide reduction peak because the extent of oxide formation and reduction may not correspond to a single monolayer of Pt oxide at the surface of the catalyst. Therefore, it is both possible to under and overestimate the ECSA by directly interpreting the Pt oxide reduction peak. If the upper vertex potential is not high enough to induce total surface oxidation, the reduction peaks will only account for a fraction of the true ECSA. Conversely if the upper vertex potential is too high, the interior bulk of the Pt catalyst will be oxidized and reduced. The approach presented by Varga et al.¹³³ accounts for these trends by taking a series of CV measurements at increasing upper vertex potentials. The Pt oxide reduction peaks are then analyzed as a function of the upper vertex potential. The authors posit that two distinct regimes will emerge – one in which increasing the UVP increases the Pt surface oxidation/reduction and another in which increasing bulk Pt oxidation/reduction is induced– and that the intersection of these two regimes represents the complete Pt surface oxidation and reduction.¹³³

4.5.3 Impedance Spectroscopy

The basic principles of impedance spectroscopy were reviewed in Chapter 1 section 1.5.3, however the impedance response of porous electrodes is far more complex than those of electrolyte samples and therefore worthy of its own treatment. In a porous composite electrode composed of ion-conducting electrolyte particles, electronic conductor particles, and catalyst particles, ionic and electronic currents are both carried throughout the entire thickness of the

electrode and converted from one to the other by the electrochemical reactions taking place on the catalyst. As the catalyst particles are distributed throughout the electrode, the conversion from one current to the other occurs gradually through the electrode. In modelling the impedance of this complex system, a 1-dimensional framework called a transmission line model (TLM) is frequently implemented.^{134,135} In the TLM, parallel ionic and electronic rails run the length (or thickness) of the porous electrode, however only the ionic rail extends through the electrode – electrolyte interface and conversely only the electronic rail extends beyond the thickness of the electrode (Figure 4.7). Along each current rail the transport of the charge is subject to the effective resistivity of the conducting phase. The rails are connected within the electrode by “rungs” representing the electrochemical reaction impedance that allows for the conversion of current in one rail to the other. The electrochemical reaction impedance is modeled by a circuit element with the charge transfer resistance in parallel with a constant phase element (CPE), representing the double layer capacitance at the electrolyte-catalyst interface.

The impedance of the TLM is described by the following equation:¹³⁴⁻¹³⁶

$$Z_{TLM}(\omega) = \frac{\chi_1 \chi_2}{\chi_1 + \chi_2} \left(L + \frac{2\kappa}{\sinh(L/\kappa)} \right) + \kappa \frac{\chi_1^2 + \chi_2^2}{\chi_1 + \chi_2} \coth(L/\kappa)$$

Where $\kappa = \sqrt{\frac{\zeta}{\chi_1 + \chi_2}}$; $\zeta(\omega) = \frac{r_{ct}}{1 + (i\omega\tau_{ct})^n}$ where r_{ct} is the differential charge transfer resistance,

τ_{ct} is the time constant of the CPE representing the double layer capacitance and n is the standard CPE exponent; L is the thickness of the porous electrode. χ_1 and χ_2 are the area-normalized effective resistivities of the ionic and electronic conductors ($\Omega \text{ m}^{-1}$), calculated by dividing the effective resistivities ($\Omega \text{ m}$) by the geometric area of the electrode. The differential charge transfer resistance, r_{ct} ($\Omega \text{ m}$) can be calculated from the Pt specific charge transfer

resistance R_{ct} ($\Omega \text{ m}^2_{\text{Pt}}$), the volumetric active area density A_r ($\text{m}^2_{\text{Pt}}/\text{m}^3$), and the geometric area of the electrode A (m^2):

$$r_{ct} = \frac{R_{ct}}{A_r * A}$$

The Pt specific charge transfer resistance, R_{ct} ($\Omega \text{ m}^2_{\text{Pt}}$) is related back to the exchange current density, i_0 ($\text{A}/\text{m}^2_{\text{Pt}}$), measured on flat cathodes by the equation:

$$R_{ct} = \frac{RT}{nFi_0(C_{O_2}/C_{O_2}^*)^\gamma}$$

Where n is the number of electrons involved in the rate determining step or the value of n in the Butler-Volmer exponential. It has been argued that this term can only take a value of 1.

If the electronic conductivity is sufficiently high, such that the potential loss along the electronic rail is negligible in comparison to the loss along the ionic rail, then the impedance $Z_{TLM}(\omega)$ can be further simplified to:

$$Z_{TLM}(\omega) = \kappa * \chi_1 * \coth(L/\kappa)$$

The impedance spectra of a transmission line model often takes the shape of a half tear drop.

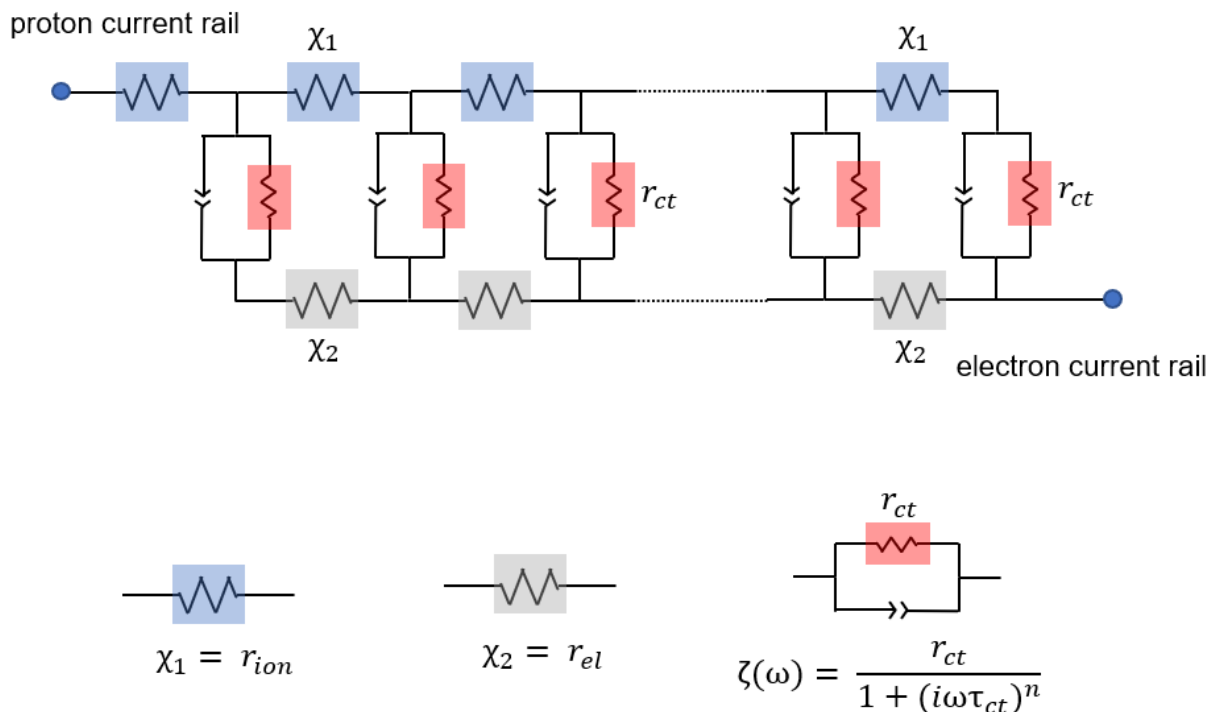


Figure 4.7. Transmission line model for a porous electrode with a proton conducting electrolyte.

4.5.4 Chronoamperometry/Chronopotentiometry

Chronoamperometry and chronopotentiometry are means of measuring the evolution of cell performance. Chronoamperometry is the measure of the cell potential over time at a fixed current, and conversely chronopotentiometry is the measure of the cell current over time at a specified potential. In well-behaved SAFCs, it is not unusual to observe the cell performance improve over the first few hours of measurement as the microstructure evolves to provide more intimate contact between the electrolyte particles, especially those at the electrolyte – electrode interface.

In flat cathode samples performing ORR, care should be taken not to hold the cell at high current densities which have been shown to result in the local overheating and dehydration of the CDP. The resultant amorphous CDP dehydrate then penetrates the catalyst layer and acts to smother catalyst sites.¹¹⁰ It is recommended that a flat cathode be held at less than 1 mA/cm² to ensure stability at the cathode interface. For a Pt catalyst electrode this condition typically produces a cell potential of 0.7 V, which is low enough to prevent the oxidation of Pt.

Chapter 5: Understanding SAFC Cathode Limitations through Experimentally Informed 1-D Modeling

5.1 Background

The unique properties of solid acid electrolytes are in many ways ideal for fuel cell operation and confer significant advantages to solid acid fuel cells (SAFCs) over other fuel cell technologies. The solid acid electrolyte of choice is almost exclusively cesium dihydrogen phosphate (CDP), CsH_2PO_4 – an anhydrous solid state electrolyte that exhibits excellent proton conductivity ($\sim 2 \times 10^{-2}$ S/cm) at intermediate temperatures (228 – 300 °C) with no observable electronic conductivity. With regard to these properties, CDP compares quite favorably against other ionic conductors. Operating within the intermediate temperature range allows SAFCs to tolerate high levels of impurities that are deleterious to low temperature polymer electrolyte membrane (PEM) devices while not being so hot as to be onerous for thermal cycling or to create challenges for materials design of auxiliary components, as is the case in high temperature solid oxide devices. The elevated operating temperature of SAFCs in comparison to PEMFCs should in theory correspond to more rapid reaction kinetics and thus reduced electrode polarization losses. Reduced polarization losses should in turn yield higher current and power densities which ideally could be achieved even with reduced catalyst loading. However, in reality the superior performance anticipated from elevated operating temperatures has not been realized, as the most advanced SAFCs reported have only produced peak power densities of ~ 200 mW/cm² and current densities @0.8 V of ~ 50 mA/cm² with Pt loadings of 1.75 mg/cm².⁵⁰ In comparison, a recent report of a PEMFC demonstrated a peak power density >1 W/cm² and a current density at 0.8 V of 0.5 A/cm² while utilizing a Pt loading of only 0.1 mg/cm².⁹⁸ The question haunting the

field of SAFCs is thus: why has operating at higher temperatures not yielded superior performance? Furthermore, without a clear understanding of the limiting factors inhibiting SAFC performance, efforts to improve SAFCs are left in the dark about which properties to target.

As is the case in most fuel cells, the principal polarization loss in SAFCs is attributed to the cathode and the sluggish ORR kinetics. In comparison the losses arising from the anode are essentially negligible, which can be demonstrated by comparing the charge transfer resistances produced by a standard SAFC, typically several $\Omega \text{ cm}^2$, and a solid acid hydrogen pump, performing HOR/HER in a symmetric hydrogen environment, which is $0.05 \Omega \text{ cm}^2$.⁹⁹ The poor performance of the SAFC cathode in comparison to those of PEMFCs is particularly surprising given the anticipated enhancement of the ORR kinetics at higher temperatures. The contradiction of the expected relative performance implies that microstructural factors have stunted the cathodic activity, and therefore an understanding of the cathode must capture not only the ORR kinetics but also the microstructural influences on active area and charge and mass transport. State-of-the-art SAFC cathodes are comprised of submicron CDP particles coated with a thin film of Pt nanoparticles.⁵⁰ The Pt coated CDP particles are pressed together to form a porous cathode typically 50 - 100 microns thick. In this architecture, the CDP particles are responsible for proton transport to active Pt sites, whereas the film of Pt nanoparticles is responsible for both electronic transport and ORR catalysis. The cathode is typically operated at 250 °C in humidified air with 0.38 atm of steam; the high partial pressure of steam is required to stabilize CDP against dehydration. Carbon supports that are utilized in PEMFCs for electronic conductivity and to reduce the Pt loading are typically not stable in the operating temperature and oxidizing atmosphere of the SAFC cathode.^{100,101}

In this work, we aim to establish an understanding of the SAFC cathode by constructing a one-dimensional (1-D) model that relies on input parameters describing the cathode microstructure, reaction kinetics, and operating conditions and utilizes these parameters to calculate the interconnected local reaction rates, charge and mass transport fluxes, and potential profiles within the cathode. Each of the input parameters that informed the model was experimentally measured or independently calculated here, with extensive effort taken to characterize the ORR kinetics on Pt catalysts in SAFCs. A membrane electrode assembly (MEA) geometry featuring a flat cathode was developed to evaluate catalyst specific ORR kinetics without the complications of charge and mass transport present in a porous cathode.

5.2 Methods

5.2.1 Description of 1-D Cathode Model

A one-dimensional model of the cathode was written largely following the framework originally constructed by Springer et al^{137,138} in 1991 which has since been extensively utilized and expanded to characterize both PEMFC and SOFC cathodes.^{132,139-141} The model calculates the fluxes of protons, electrons, and gaseous products and reactants, the potential profiles in both the CDP electrolyte phase and the platinum phase, and the consumption or production of these species by the oxygen reduction reaction through a porous cathode. The fluxes of the various relevant species and the potential profiles are related by a series of coupled differential equations with boundary conditions at either the cathode – electrolyte interface or the cathode – gas interface. Together these differential equations and boundary conditions constitute a classic

boundary value problem. A complete summary of the equations and boundary conditions is provided in where z is the stoichiometric coefficient of the species in the ORR reaction, ie -1 for O_2 and 2 for H_2O .

Assuming no gas leaks through the electrolyte layer, the fluxes of gas species must be zero at the electrolyte – cathode interface, ie. $\mathbf{N}_i(\mathbf{x} = \mathbf{0}) = \mathbf{0}$.

The model is constructed such that the electrolyte – cathode interface is assigned as $x = 0$ and the cathode – gas interface is $x = L$, where L is the thickness of the cathode. In this formulation, fluxes of species outward from the electrolyte – cathode interface are positive.

Eq (14) and (15) describe the consumption of protons and electrons respectively from the local ORR rate, Q (A/m^3). The protonic current, j_p , is depleted as protons move further from the electrolyte – cathode interface, increasing x , whereas the electronic current, j_e , is depleted as electrons travel inward from the current collector at the gas-cathode interface, decreasing x . Assuming no electronic leakage in the cell, the electronic current must be zero at the electrolyte – cathode interface due to the electrically insulating nature of the CDP electrolyte layer. Similarly the protonic current is zero at the gas-cathode interface due to the proton impermeable current collector. These requirements establish the boundary conditions $j_p(x = L) = j_e(x = 0) = 0$ and additionally stipulate that the proton and electron currents are equivalent at their respective interfaces of origin, $j_p(x = 0) = j_e(x = L)$.

$$(14) \quad \frac{dj_p}{dx} = -Q$$

$$(15) \quad \frac{dj_e}{dx} = Q$$

The local ORR rate, Q , is calculated using the Butler-Volmer framework in which the forward and reverse reaction rates scale exponentially with the local overpotential, η . The overpotential is defined here as the thermodynamic driving force for a rate-limiting step of the ORR involving both proton and electron transfer. The overpotential is calculated from the

electrochemical potentials of the protons, electrons, and gas phase reactants and products to produce the following equation:

$$(16) \quad \eta = \varphi_{CDP} - \varphi_{Pt} + E^0 - \frac{RT}{nF} \ln \left(\frac{p_{H_2O}}{p_{H_2} \cdot p_{O_2}^{\frac{1}{2}}} \right)$$

where φ_{CDP} and φ_{Pt} are the local potentials of the CDP and Pt phases respectively; E^0 is the standard state potential of the fuel cell reaction; and p_{H_2O} , p_{H_2} , and p_{O_2} are the local partial pressures of steam at the cathode, hydrogen at the anode, and oxygen at the cathode respectively. The standard state potential, E^0 , was calculated from the Gibbs free energy of the fuel cell reaction ($E^0 = \Delta G^0/zF$) at 250 °C using thermodynamic values from the NIST database. The platinum phase potential at the cathode – gas interface, $\varphi_{Pt}(x = L)$, is defined by the user as a boundary condition and corresponds to the experimentally measured potential of the cathode. While the absolute value of φ_{CDP} is unknown, it is only the change in φ_{CDP} from its value at equilibrium that is relevant for the calculation of overpotential. For convenience the equilibrium reference value of φ_{CDP} is assigned as 0 V here, which is reflected in the expression for overpotential (Eq (16)). The last two terms in Eq (16) are equivalent to the Nernst potential of the cell, E_{OCV}^{Nernst} , when evaluated at the cathode-gas interface. E_{OCV}^{Nernst} directly reflects the Gibbs free energy of the fuel cell reaction at the temperature and pressure of the supplied gasses and defines the theoretical fuel cell potential at open circuit voltage (OCV). While the last two terms in Eq (16) are always defined as E_{OCV}^{Nernst} at $x = L$, when current is drawn the partial pressures of steam and oxygen change in the cathode ($x < L$) and these terms then reflect the decrease in the local Nernst potential. For the purposes of this model, the hydrogen partial pressure at the anode is assumed to remain constant at the supplied value.

$$(17) \quad E_{OCV}^{Nernst} = E^0 - \frac{RT}{nF} \ln \left(\frac{p_{H_2} O^L}{p_{H_2} * p_{O_2}^{L, \frac{1}{2}}} \right)$$

where the superscript L denotes the pressure supplied at the cathode-gas interface, $x = L$.

In order to simplify the presentation of the overpotential profiles, we redefine the CDP potential with a reference value at the fuel cell Nernst potential, ie.

$$\varphi'_{CDP} = \varphi_{CDP} + E_{OCV}^{Nernst}$$

where φ'_{CDP} satisfies the boundary condition $\varphi'_{CDP}(x = 0) = E_{OCV}^{Nernst}$. The expression for overpotential can thus be redefined as:

$$(18) \quad \eta = \varphi'_{CDP} - \varphi_{Pt} - \frac{RT}{nF} \left[\frac{1}{2} \ln \left(\frac{c_{O_2}}{c_{O_2}^L} \right) + \ln \left(\frac{c_{H_2O}^L}{c_{H_2O}} \right) \right]$$

The local ORR rate, Q , is calculated from the local overpotential using the following expression of the Butler-Volmer equation:

$$(19) \quad Q = A_r i_0 \left[\left(\frac{c_{O_2}}{c_{O_2}^*} \right)^\gamma \exp \left(\frac{\alpha F \eta}{RT} \right) - \left(\frac{c_{O_2}}{c_{O_2}^*} \right)^\gamma \exp \left(\frac{-(1-\alpha) F \eta}{RT} \right) \right]$$

The exchange current density, i_0 , describes that rate of forward and reverse reaction at net zero current density (ie. when the cell is held at E_{OCV}^{Nernst}). The exchange current density is normalized to the Pt surface area and has units A/m^2_{Pt} . A_r describes the volumetric density of active Pt surface area in the cathode and has units m^{-1} (m^2_{Pt}/m^3). The term $\left(\frac{c_{O_2}}{c_{O_2}^*} \right)^\gamma$ describes the dependence of ORR rate on the oxygen reactant concentration, C_{O_2} (mol/m^3), where γ is the experimentally measured reaction order and $C_{O_2}^*$ is the reference concentration of 1 atm of oxygen at the operating temperature. α is the cathodic charge transfer coefficient and characterizes the effectiveness of the overpotential at driving forward the ORR.

The overpotential profile evolves throughout the cathode not only due to the changes in the oxygen and steam compositions, but also – in fact primarily – due to changes in the CDP and Pt phase potentials. The potential of each of these phases changes in proportion to the local current density in what is an effective Ohm's law relationship (Eqs (20) and (21)).

$$(20) \quad \frac{d\phi'_{CDP}}{dx} = \frac{-j_p}{\sigma_{CDP}^*}$$

$$(21) \quad \frac{d\phi_{Pt}}{dx} = \frac{j_e}{\sigma_{Pt}^*}$$

where σ_{CDP}^* and σ_{Pt}^* are the effective conductivities of protons and electrons respectively in the porous cathode. Effective conductivities are volumetrically averaged across the cathode accounting for the insulating porous space and secondary phase.

Gas phase diffusion is modeled using a modified Stefan-Maxwell model assuming no pressure gradient exists in the cathode.

$$(22) \quad \frac{-dC_i}{dx} = \sum_{j \neq i}^n \frac{y_j N_i - y_i N_j}{D_{ij}^{B,eff}} + \frac{N_i}{D_i^{K,eff}}$$

where C_i is the local concentration of species i (mol/m³), y_i is the local mole fraction of the species, N_i is the local molar flux of the species (mol/m² s), $D_{ij}^{B,eff}$ is the effective binary diffusion coefficient of species i and j , and $D_i^{K,eff}$ is the effective Knudsen diffusion coefficient of species i .

Strictly speaking neglecting the pressure gradient term is not technically correct, however this simplification can be made here without introducing significant error as the pressure gradient produced within the cathode is relatively small, as will be shown by the results of the model. The concentration of each gas species at the cathode-gas interface is simply that of the supplied

cathode gas stream. The change in the flux of each gas species is dictated by the amount consumed or produced by the ORR locally.

$$(23) \quad \frac{dN_i}{dx} = \frac{zQ}{nF}$$

where z is the stoichiometric coefficient of the species in the ORR reaction, ie -1 for O_2 and 2 for H_2O .

Assuming no gas leaks through the electrolyte layer, the fluxes of gas species must be zero at the electrolyte – cathode interface, ie. $N_i(x = 0) = 0$.

Table 5.1. Coupled differential equations and boundary conditions constituting the boundary value problem that describes the cathode.

Variable	Differential equation	Boundary Condition
j_p proton current (A/m ²)	(14) $\frac{dj_p}{dx} = -Q$	$j_p(L) = 0$
j_e electronic current (A/m ²)	(15) $\frac{dj_e}{dx} = Q$	$j_e(0) = 0$
φ'_{CDP} CDP potential (V)	(20) $\frac{d\varphi'_{CDP}}{dx} = \frac{-j_p}{\sigma_{CDP}^*}$	$\varphi'_{CDP}(0) = E_{OCV}^{Nernst}$
φ_{Pt} Pt potential (V)	(21) $\frac{d\varphi_{Pt}}{dx} = \frac{j_e}{\sigma_{Pt}^*}$	$\varphi_{Pt}(L) = E_{OCV}^{Nernst}$ - applied bias
C_{O_2} O ₂ concentration (mol/m ³)	(22) $\frac{-dC_{O_2}}{dx} = \sum_{j \neq i}^n \frac{y_j N_i - y_i N_j}{D_{ij}^{B,eff}} + \frac{N_i}{D_i^{K,eff}}$	$C_{O_2}(L) = C_{O_2}(\text{supplied})$
N_{O_2} O ₂ flux (mol/m ² s)	(23) $\frac{dN_{O_2}}{dx} = -\frac{Q}{nF}$	$N_{O_2}(0) = 0$
C_{H_2O} H ₂ O (mol/m ³)	(22) $\frac{-dC_{H_2O}}{dx} = \sum_{j \neq i}^n \frac{y_j N_i - y_i N_j}{D_{ij}^{B,eff}} + \frac{N_i}{D_i^{K,eff}}$	$C_{H_2O}(L) = C_{H_2O}(\text{supplied})$
N_{H_2O} H ₂ O flux (mol/m ² s)	(23) $\frac{dN_{H_2O}}{dx} = \frac{2Q}{nF}$	$N_{H_2O}(0) = 0$
C_{N_2} N ₂ (mol/m ³)	(22) $\frac{-dC_{N_2}}{dx} = \sum_{j \neq i}^n \frac{y_j N_i - y_i N_j}{D_{ij}^{B,eff}} + \frac{N_i}{D_i^{K,eff}}$	$C_{N_2}(L) = C_{N_2}(\text{supplied})$
N_{N_2} N ₂ flux (mol/m ² s)	(23) $\frac{dN_{N_2}}{dx} = 0$	$N_{N_2}(0) = 0$

where Q is the local reaction rate calculated from the Tafel equation:

$$(19) \quad Q = A_r i_0 \left[\left(\frac{C_{O_2}}{C_{O_2}^*} \right)^{\gamma} \exp\left(\frac{\alpha F \eta}{RT}\right) - \left(\frac{C_{O_2}}{C_{O_2}^*} \right)^{\gamma} \exp\left(\frac{-(1-\alpha) F \eta}{RT}\right) \right]$$

$$(18) \quad \eta = \varphi'_{CDP} - \varphi_{Pt} - \frac{RT}{nF} \left[\frac{1}{2} \ln\left(\frac{C_{O_2}}{C_{O_2}^L}\right) + \ln\left(\frac{C_{H_2O}^L}{C_{H_2O}}\right) \right]$$

5.2.1.1 Strategies for Interpreting Model Results

The boundary value problem defined in Table 5.1 was solved using the python function “solve_bvp” in the “scipy” package with 500 points between the cathode-electrolyte interface and the cathode-gas interface. The solution of the boundary value problem produces profiles for each of the variables in Table 5.1. An example set of solution profiles is shown in Figure 5.1. When changes in the local gas composition are minor, as will later be shown to be the case here, the overpotential can be approximated as the difference between the potential of the CDP phase, φ'_{CDP} , and the Pt phase, φ_{Pt} , ($\eta \approx \varphi'_{CDP} - \varphi_{Pt}$), allowing the overpotential to be easily interpreted as the window between the two potential profiles. The overpotential window shrinks with increasing x because of ohmic losses in φ'_{CDP} and φ_{Pt} that are proportional to the local proton and electron currents respectively. Because the ionic conductivity in a porous cathode is almost always lower than the electronic conductivity, often by orders of magnitude, a majority of the overpotential loss arises from the loss in the electrolyte potential, φ'_{CDP} , and thus the overpotential profile will have a maximum at $x = 0$. The narrowing overpotential profile in turn results in a local reaction rate profile that is more sharply concentrated at $x = 0$ due to the exponential relationship of the Butler-Volmer equation.

Modeled polarization curves were produced by evaluating the model at various biases at intervals of 0.05 V and recording the Pt potential and total electronic current density at $x = L$.

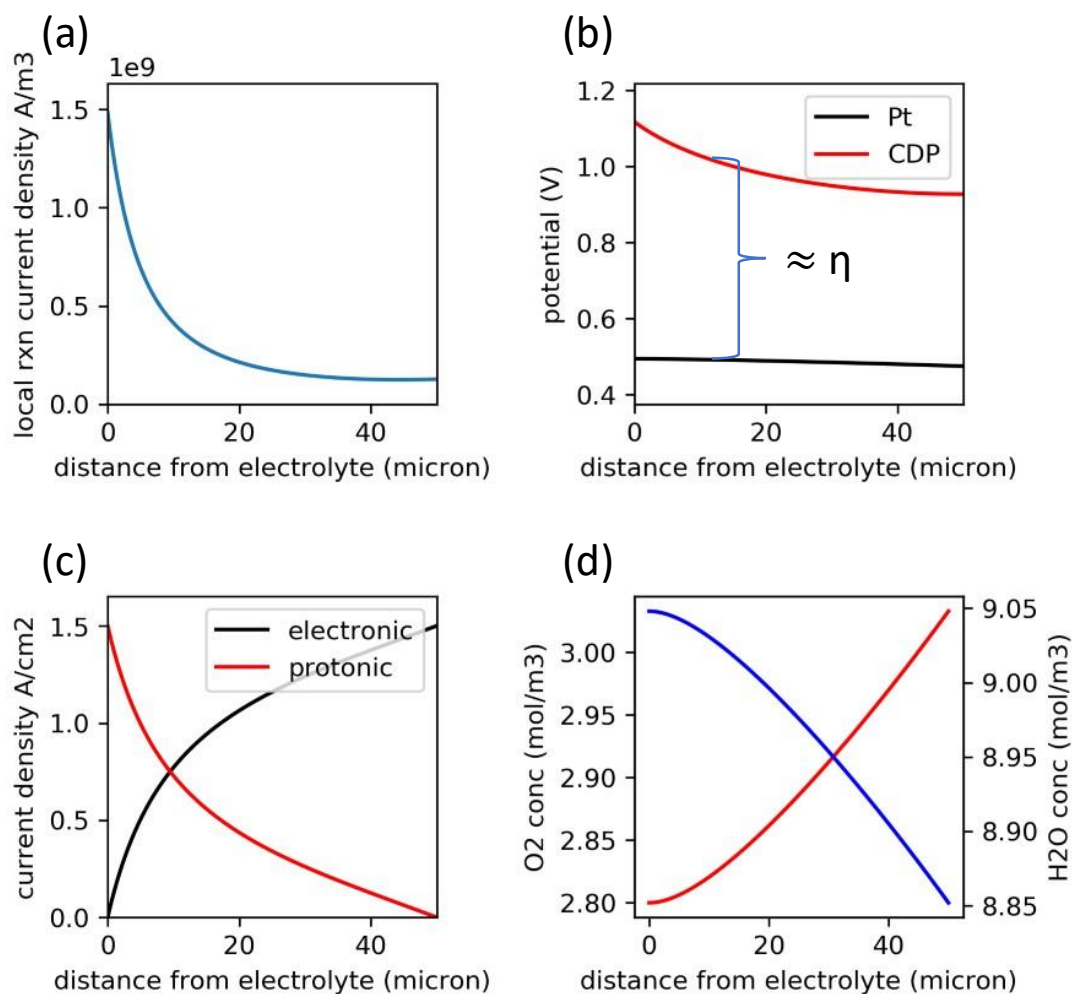


Figure 5.1. Example solution to the model boundary value problem. (a) profile of the local ORR rate. (b) profiles for the potential of the CDP phase, φ'_{CDP} , and the Pt phase, φ_{Pt} . (c) electron and proton current density profiles. (d) oxygen and steam concentration profiles.

5.2.2 Measuring and Calculating Model Parameters

Validation of fuel cell models is often done by comparing the experimental and modeled polarization curves. However, due to the overparameterized nature of the model, agreement with the experimental curve alone cannot be relied upon to ensure that the internal behavior in the fuel

cell (local reaction rates, fluxes, etc) has been accurately captured by the model. This is especially the case when a large number of model parameters are refined to fit the experimental polarization curve. Therefore, in this work we experimentally measured or independently calculated each of the model parameters. Table 5.2 summarizes values of the model parameters we collected and the method of measurement or calculation.

Table 5.2. Summary of the model parameters, the values determined, and the method of measurement or calculation.

Parameter	Value	Method of determination
Cathode Microstructure		
ϵ porosity	0.31	Porous cathode density.
r_{pore} pore radius (m)	$5 \cdot 10^{-7}$	Cross-sectional SEM.
t cathode layer thickness (m)	$83 \cdot 10^{-6}$	Cross-sectional SEM
A_r volumetric active area density ($m^2 Pt/m^3$)	$21.8 \cdot 10^6$	BET and porous cathode density
Electrochemistry – Tafel parameters		
i_0 exchange current density (A/m^2_{Pt})	0.026 - 0.039	Fit to flat cathode measurements
$\Delta G_c^{*,0}$ equilibrium activation energy (kJ/mol)	106 – 118	Fit to flat cathode measurements
α Tafel asymmetry parameter	0.54 - 0.69	Fit to flat cathode measurements
γ O_2 activity power law exponent	0.75 - 0.84	Fit to flat cathode measurements
Charge Transport		

σ_{CDP}^* effective proton conductivity (S/m)	1.15	$\sim(1 - \varepsilon)\sigma_{CDP}$. Literature on conductivity of overlapping spheres.
σ_{Pt}^* effective electronic conductivity (S/m)	27.6	Van der Pauw measurement of porous cathode at ambient conditions
Gas Diffusion		
$D_{c,d}^B$ binary diffusion coefficient of c in d (m^2/s)	$D_{c,d}(T_o, P_o) \left(\frac{P_o}{P_i}\right) \left(\frac{T_i}{T_o}\right)^{3/2} \frac{\Omega_{D,T_o}}{\Omega_{D,T_i}}$	Hirschfelder correlation. Reference binary diffusion coefficients ($D_{c,d}(T_o, P_o)$) and collision integrals, ($\Omega_{D,T}$) from Fundamentals of Momentum, Heat and Mass Transfer. ¹⁴²
$D_{c,d}^{B,eff}$ effective binary diffusion coefficient in porous cathode (m^2/s)	$\varepsilon^{3/2} D_{c,d}^B$	Bruggeman correction
D_i^K Knudsen diffusion	$r_{pore} \sqrt{\frac{8RT}{\pi M_i}}$ where M_i is the molar mass of the gas molecule i	

5.2.2.1 Measuring ORR kinetics of Pt Nanoparticles

Tafel parameters were measured on membrane electrode assemblies (MEAs) with flat cathodes in order to achieve precise and uniform control of the electric potential and gas atmosphere at the active Pt surface. A flat cathode was fabricated by first pressing a dense CDP pellet, $\frac{3}{4}$ " in diameter and roughly 1 mm thick, and then polishing the cathodic face of the pellet to a reflective finish using 1200 grit polishing paper. AFM conducted on the polished surface showed low surface roughness with polishing scratches of roughly 0.5 μm in depth. Pt nanoparticles were then deposited on the polished surface by metal organic chemical vapor

deposition (MOCVD) in a procedure similar to that reported by Papandrew et al.⁵⁰ A powder mixture of Pt(acac)₂ and CDP, with a gravimetric surface area of 3.5 m²/g, was created using the same ratio of components as in the porous cathode of this study (60.6 mg Pt(acac)₂ and 100 mg CDP). The pellet was placed at the bottom of a 20 mL borosilicate vial with the polished surface facing up and the powder mixture was then distributed across the face of the pellet. By utilizing the same deposition method as implemented in porous cathodes we ensure that the Pt nanoparticulate film perfectly mimics those on the porous cathode powders. The small amount of additional surface area introduced by the pellet face (2.85 cm²) is dwarfed by the surface area of the CDP in the powder bed (0.35 m²) and thus it is safe to assume that the deposition is not perturbed by the addition of the pellet. The deposition was then conducted following the procedures reported by Papandrew et al.⁵⁰ In short, the sample vial was placed in a vacuum oven along with another vial filled with a small amount of water to produce ~0.3 atm of steam in the chamber at 215 °C. The oven was then deoxygenated by pumping and back filling with N₂ several times and then brought to 215 °C and left to rest for 15 hrs. Following the deposition, the oven was cooled to 150 °C and evacuated and backfilled with N₂ several times to remove the steam and any unreacted precursors. After removing the vial from the oven, the powder was shaken off the pellet and the pellet face was then blown with a nitrogen stream to remove residual powders. The resulting pellet surface exhibited a reflective silverish finish. SEM images of the cathodic pellet face showed that Pt nanoparticles had deposited on the surface in a morphology and distribution identical to that of the porous cathode powders.

The anodic face of the pellet was then brought together with a porous anode supported on a stainless steel gas diffusion layer (GDL), fabricated in a similar fashion to that reported in Uda

et al.⁴⁶ The two components, CDP pellet and anode supported on GDL, were wrapped together in 12 cm of Teflon tape and sealed using an isostatic press at 3 MPa for 5 s. The exposed cathode area, or geometric surface area, was calculated using ImageJ software. The active CDP surface area was calculated by multiplying the geometric surface area by the roughness measured from AFM. A disk of carbon paper with a microporous layer and another stainless steel GDL were added to the cathode as current collectors and the MEA was wrapped again with 15 cm of Teflon tape to seal the entire cell.

Measurement of Tafel parameters were conducted at three temperatures – 235, 240, and 250 °C – and with two different cathodic gas conditions at each temperature – humidified air and O₂. The anodic gas stream was humidified 10% H₂ in Ar throughout and humidification was achieved by passing the gas streams through bubblers held at 75 °C to achieve 0.38 atm of H₂O. The MEAs were held at 0.5 mA/cm²_{geometric} at 235 °C until the voltage stabilized, typically a period of 5-10 hrs. Cyclic voltammetry measurements with 3 cycles were conducted at each measurement condition with a sweep rate of 2 mV/s and a lower vertex potential of 0.6 - 0.65 V. In between cyclic voltammetry measurements, the cell was held at a current density of 0.5 mA/cm²_{geometric}, and the voltage response was monitored to ensure equilibration to each new condition, typically around 20 minutes. The measurement conditions were designed to ensure the cathode was not exposed to high current densities which have been observed to result in local overheating and liquification of CDP at the electrolyte cathode interface.¹¹⁰

The measured current values were renormalized to the Pt surface area using the following equation:

$$i(A/m_{Pt}^2) = \frac{I(A)}{SA_{geo} * r_{AFM} * r_{Pt-CDP}}$$

where SA_{geo} is the geometric surface area of the MEA, r_{AFM} is the roughness factor of the polished CDP pellet as measured by AFM, and r_{Pt-CDP} is the CDP-to-Pt surface area conversion factor that was determined by BET using methods described in the subsequent section.

The linear Tafel region of the polarization curves were fit to the Tafel equation to determine values of the exchange current density i_0 (A/m_{Pt}^2), the cathodic charge transfer coefficient α , the O_2 concentration exponent γ , and the activation energy of the ORR $\Delta G_C^{*,0}$ (kJ/mol):

$$(24) \quad \ln(i) = \ln \left[i_0 \left(\frac{c_{O_2}}{c_{O_2}^*} \right)^\gamma \right] + \frac{\alpha F \eta}{RT}$$

5.2.2.2 Microstructural Properties

Two freestanding cathode films of different mass loadings were uniaxially pressed by spreading cathode powders over a 3/4" diameter die coated in Kapton tape and pressing at 1 ton for 3 seconds. Comparing the thickness of the cathode films, determined by cross-sectional SEM, with the geometric-area mass loading revealed that both films had a density of 2.78 g/cm³. This density was 69% of the theoretical density of the cathode powders (4.048 g/cm³) and thus the porosity was taken to be 0.31. The thickness of the experimental cell cathode was also determined post-measurement using cross-sectional SEM.

The gravimetric surface area of the cathode CDP powders before and after Pt MOCVD were measured using BET on a Micromeritics 3Flex instrument with Krypton as the adsorbent

gas. The CDP powders were found to have a surface area of 3.5 m²/g whereas the Pt coated powders had a surface area of 7.74 m²/g. The volumetric active area density, A_r , was calculated from multiplying the porous cathode density ($\rho_{\text{cathode}}/\text{m}^3$) and the gravimetric surface area of the Pt deposited cathode powders ($A_r = SA_{\text{gravimetric}} \times \rho_{\text{cathode}}$). A CDP-to-Pt surface area conversion factor was calculated by taking the ratio of the surface areas of the CDP powders before and after Pt deposition, each normalized to the mass of CDP, i.e. $r_{\text{Pt-CDP}} = SA_{\text{Pt|CDP}} / (m_{\text{CDP}} * SA_{\text{CDP}}) = 2.87$, where m_{CDP} is the mass fraction of CDP in the post deposition powders (0.77).

5.2.2.3 Charge Transport

The effective electronic conductivity of the cathode at room temperature was measured using the Van der Pauw method.¹⁴³ Conducting the measurement at room temperature ensured that charge transport in the CDP phase was negligible. A porous cathode was formed by uniaxially pressing cathode powders onto a CDP pellet. The Van der Pauw method was conducted by pressing down silver wires to four points (A, B, C, D) that were spaced at approximately even intervals around the perimeter of the cathode. Details about the Van der Pauw method and calculation can be found in the supplemental information (Figure 5S.-7). The resistivity at room temperature was then thermally corrected to 250 °C using the following linear correction:

$$\rho = \rho(T_0)(1 + \alpha\Delta T)$$

with a resistivity correction factor α for Pt of $3.93 * 10^{-3} \text{ }^\circ\text{C}^{-1}$. The temperature corrected conductivity of the porous cathode was 27.6 S m⁻¹.

The effective proton conductivity of the porous cathode was estimated by referencing literature in which the conductivity of a porous media was modelled using randomly distributed overlapping spheres.¹⁴⁴ Various methods of calculation for a media with 30 % porosity provided a range of effective conductivities that were 40 – 60 % of the pure material's conductivity. A value of 50 % of CDP's conductivity was selected for this analysis, resulting in an effective conductivity of 1.15 S m⁻¹ at 250 °C. The temperature-dependent conductivity of CDP was calculated using an Arrhenius equation where the activation energy and log of pre-exponential factor were referenced from Ayako et al to be 38.4 kJ/mol and 11.32 Ω⁻¹ cm⁻¹ K respectively.¹⁷

5.2.2.4 Gas Diffusion

Gas diffusion coefficients were extracted from data provided in Fundamentals of Momentum, Heat and Mass Transfer, 5th edition, by Welty, Wicks, Wilson, and Rorrer¹⁴² and Diffusion: Mass Transfer in Fluid Systems by Cussler¹⁴⁵. Binary diffusion coefficients were collected for oxygen, nitrogen, and steam at reference temperature and pressure, T₀ and P₀ respectively, which were in most cases standard temperature and pressure. The Hirschfelder correlation was then applied to correct these diffusion coefficients to operating temperature and pressure, 250 °C and 1 atm.

$$D_{c,d}(T_i, P_i) = D_{c,d}(T_o, P_o) \left(\frac{P_o}{P_i} \right) \left(\frac{T_i}{T_o} \right)^{3/2} \frac{\Omega_{D,T_o}}{\Omega_{D,T_i}}$$

where $\Omega_{D,T}$ is the collision integral of the gas as determined from Fundamentals of Momentum, Heat and Mass Transfer.¹⁴² A full accounting of the calculation of the binary diffusion coefficients is provided in **Error! Reference source not found.**

Table 5.3. Binary diffusion coefficients.

$D_{c,d}(250\text{ }^{\circ}\text{C}, 1\text{ atm})$ (cm ² /s)	Oxygen	Steam	Nitrogen
Oxygen	-	0.8416	0.5093
Steam		-	0.8190
Nitrogen		-	-

Knudsen diffusion coefficients were calculated to account the gas molecule interactions with the walls of the pores in the cathode. The Knudsen diffusion coefficient can be simply calculated using:

$$D_i^K = r_{pore} \sqrt{\frac{8RT}{\pi M_i}}$$

where r_{pore} is the radius of the pore, and M_i is the molecular weight of the gaseous species. The resulting Knudsen diffusion coefficients are listed in Table 5.4.

Table 5.4. Knudsen diffusion coefficients.

D_i^K (cm ² /s)	Oxygen	Steam	Nitrogen
	2.942	3.922	3.145

Comparing the relative magnitude of the binary and Knudsen diffusion coefficients, it is clear that Knudsen diffusion is the dominant mode of transport in SAFC cathodes. Effective

binary and Knudsen diffusion coefficients were calculated by applying the Bruggemann correction:

$$D^{eff} = \varepsilon^{3/2} D$$

5.2.3 Experimental Measurements of a SAFC

CDP particles with a gravimetric surface area of 3.5 m²/g were coated with Pt nanoparticles using the MOCVD method described by Papandrew et al.⁵⁰ A Pt loading of 23 wt% was achieved by adding 120 mg of Pt(acac)₂ to a vial with 200 mg of the CDP powder. The morphology and nanoparticle size of the Pt film were consistent with those reported by Papandrew et al. The Pt coated CDP powders were then pressed onto an anode supported half-cell, fabricated using methods similar to those described in Uda et al.⁴⁶ In short, a microporous layer (MPL), anode layer, and electrolyte layer were pressed onto a stainless steel gas diffusion layer (GDL). The MPL layer consisted of CDP, carbon black, and naphthalene as a fugitive pore former. The anode layer consisted of CDP and 20wt% Pt on C black in a 6:1 weight ratio.

Polarization curves were collected from the cell at 250 °C with humidified (pH₂O = 0.38 atm) air or oxygen supplied to the cathode and humidified hydrogen to the anode.

Electrochemical impedance spectra were collected with a Biologic 2 spectrometer at various biases (OCV (1.02 V), 0.8, 0.7, 0.6, and 0.4 V) with a 10 mV amplitude. The ohmic resistance was determined from the high-frequency intercept of the spectra, and the ohmic losses were subtracted from the polarization curve in comparing modeled and experimental results. In Appendix A, the spectra are fit using a transmission line model to extract charge transport and transfer parameters, and the results are compared to the values independently determined here.

5.3 ORR Kinetics of Pt Nanoparticles: Results and Discussion

Polarization curves were collected from three flat-cathode MEAs (A, B, and C) at 235, 240, and 250 °C with both humidified air and oxygen supplied to the cathode. The polarization curves exhibited Tafel behavior as well as the anticipated trends with increasing temperature and partial pressure of oxygen (Figure 5.2). The linear region of the polarization curves, when plotted as $\ln(i)$ vs η , was fit using the Tafel equation to extract α from the slope and the reactant concentration modified exchange current density, $i_0 \left(\frac{c_O}{c_O^*}\right)^\gamma$, from the intercept.

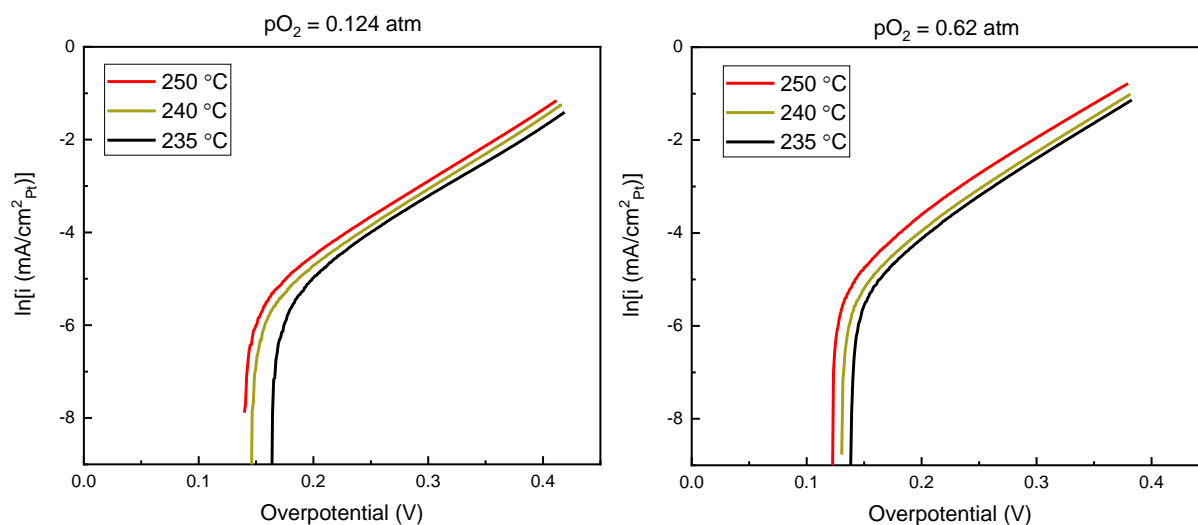


Figure 5.2. Polarization curves collected from MEA A under (a) humidified air and (b) humidified oxygen at the listed temperatures.

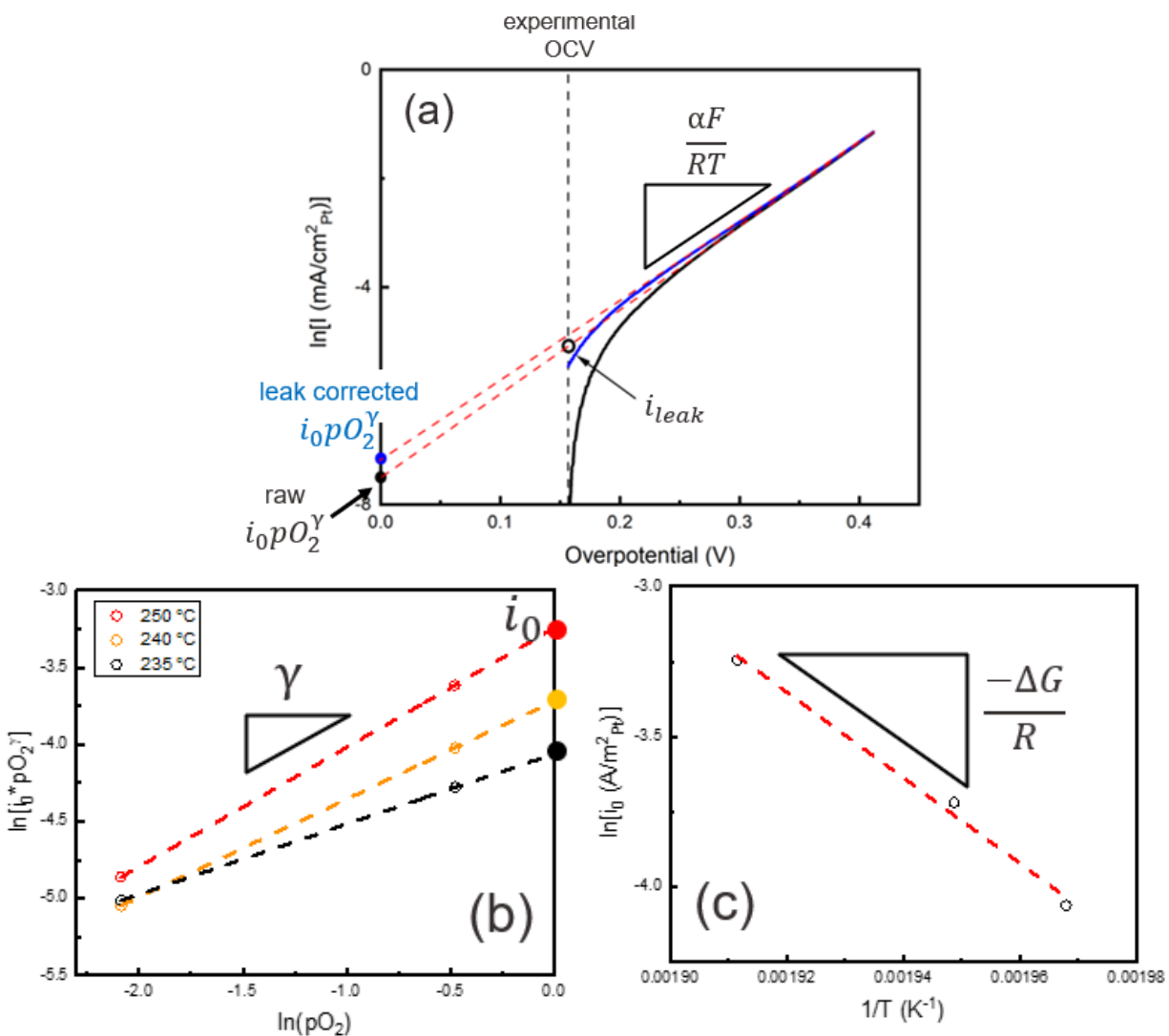
A notable feature in the data is the disparity between the theoretical Nernst potential and the experimental OCV, which is approximately 150 mV lower.^{97,130} Similar discrepancies in

OCV values are well documented in PEMFC literature and have been attributed to the presence of an anodic side reaction at the cathode. When both ORR and an anodic reaction are present at the cathode, the experimental OCV reflects the potential where these two currents neutralize each other.⁹⁷ Potential anodic side reactions at the cathode include hydrogen oxidation of hydrogen leaking across from the anode, platinum oxidation, and carbon oxidation. Although it is unknown the extent to which each of these anodic side reactions are present, we attempt to correct for the anodic current using an approach developed in PEMFC literature.^{97,130} In this approach, the linear Tafel behavior is extrapolated to the experimental OCV and the current density at this potential is taken to be the anodic leak current, i_{leak} . It is assumed that this anodic leak current is present at roughly the same magnitude across the entire polarization curve, and a leak corrected polarization curve is produced by adding the leak current to the raw current data, i.e. $i_{\text{leak corrected}} = i + i_{\text{leak}}$. This correction is valid if the anodic current is due to hydrogen crossover; the hydrogen oxidation current is assumed to be equivalent to the hydrogen crossover rate because of the large overpotentials that exist between the standard hydrogen oxidation potential, $E^0 = 0 \text{ V}$, and the potential of the cathode during these measurements (0.6 – 1 V) as well as the relative facility of hydrogen oxidation. The rate of hydrogen crossover can be taken as constant across the timescale of the measurement and thus a constant hydrogen oxidation current can be anticipated.

The leak corrected current densities were then fit to the Tafel equation (Eq. (24)) producing leak corrected values for α and $i_0 \cdot p\text{O}_2^\gamma$ (Figure 5.3a). The leak correction resulted in α values that were approximately 0.03 lower than those derived from raw polarization data and $i_0 \cdot p\text{O}_2^\gamma$ values that were approximately 0.01 $\text{A}/\text{m}^2_{\text{Pt}}$ higher than those from raw data. The

$\ln[i_0(pO_2)^\gamma]$ values determined for humidified air and oxygen were plotted against $\ln(pO_2)$ and for each temperature series the data was fit with a line to extract the i_0 and γ values (Figure 5.3b). $\ln(i_0)$ was then plotted against $1/T$ and fit with the relationship $\ln(i_0) \propto -\Delta G_C^{*,0}/RT$ (Figure 5.3c).

Figure 5.3. Data analysis used to extract Tafel parameters from experimental polarization curves. (a) Leak corrected current densities (blue) were produced by adding a constant leak current, i_{leak} , to the raw experimental current densities (black). The slope of the fit line was used to determine α and the extrapolated value at zero overpotential was used to determine $i_0 \cdot pO_2^\gamma$. (b) Fitting of the $i_0 \cdot pO_2^\gamma$ values from data collected under air and O_2 . γ was determined from the slope of the fit line and extrapolation of the fit line to 1 atm O_2 ($\ln(pO_2) = 0$) produced the exchange current density i_0 . (c) Fitting of the temperature dependence of the exchange current densities to determine the activation energy $\Delta G_C^{*,o}$.



The results of the Tafel fitting for MEAs A, B, and C are summarized in Table 5.5 and the complete Tafel fitting results for each MEA are provided in the Figure 5S.-3Figure 5S.-4, and Figure 5S.-5.

Table 5.5. Summary of the Tafel parameters from MEAs A, B, and C. The reported i_0 , α and γ values correspond to those collected at 250 °C, and α values are reported for both humidified air and oxygen. The α , γ , and $\Delta G_C^{*,0}$ values were determined from leak corrected data.

MEA	i_0 raw (A/m ² Pt)	i_0 leak corrected (A/m ² Pt)	α air	α O ₂	γ	$\Delta G_C^{*,0}$ (kJ/mol)
A	0.026	0.039	0.66	0.62	0.77	118
B	0.030	0.038	0.59	0.54	0.75	114
C	0.015	0.026	0.69	0.64	0.84	106
avg	0.024	0.034	0.64	0.60	0.79	112

Relatively good agreement is found in the Tafel parameters from MEAs A, B, and C, with the slight variations attributed to gas leaks and small inconsistencies in sample prep.

Comparison of the Tafel parameters measured here and those found in the PEMFC literature reveal key insights into the relative reaction kinetics in these two systems (

Table 5.6). The exchange current density i_0 determined here is roughly two orders of magnitude greater than those from PEMFCs, which is evidence of the thermal enhancement of the ORR kinetics. However, the i_0 values here are an order of magnitude lower than that would be predicted if the thermal activation trend observed in PEMFCs was extended to the operating temperature of SAFCs.¹⁴⁶ The deviation is indicative of differences in the ORR mechanism in these two systems, a conclusion which is reinforced by the significant differences in the α and $\Delta G_C^{*,0}$ values. The disparity in the cathodic charge transfer coefficient α has devastating implications for the relative performance of SAFCs. The lower α value in SAFCs combined with the higher operating temperature means that the Tafel slope is more than double that of PEMFCs; in practical terms, the difference in Tafel slopes means that more than twice as much overpotential must be supplied to produce an order of magnitude increase in reaction rate in SAFCs compared to PEMFCs. This effect more than negates the higher exchange current densities in SAFCs – a fact which can be painfully visualized by plotting the local reaction rate functions of the two systems using Eq (19) (Figure 5.4).

$$(19) \quad Q = A_r i_0 \left[\left(\frac{c_{O_2}}{c_{O_2}^*} \right)^\gamma \exp \left(\frac{\alpha F \eta}{RT} \right) - \left(\frac{c_{O_2}}{c_{O_2}^*} \right)^\gamma \exp \left(\frac{-(1-\alpha) F \eta}{RT} \right) \right]$$

While the SAFC reaction rate is significantly higher at low overpotentials, reflecting the higher i_0 , at realistic operating potentials, $\eta > 0.3$ V, the PEMFC reaction rate grows to be orders of magnitude greater. Based on this result alone, one can conclude that the performance of SAFCs is significantly hindered by the low cathodic charge transfer coefficient α or the high Tafel slope compared to that of PEMFCs.

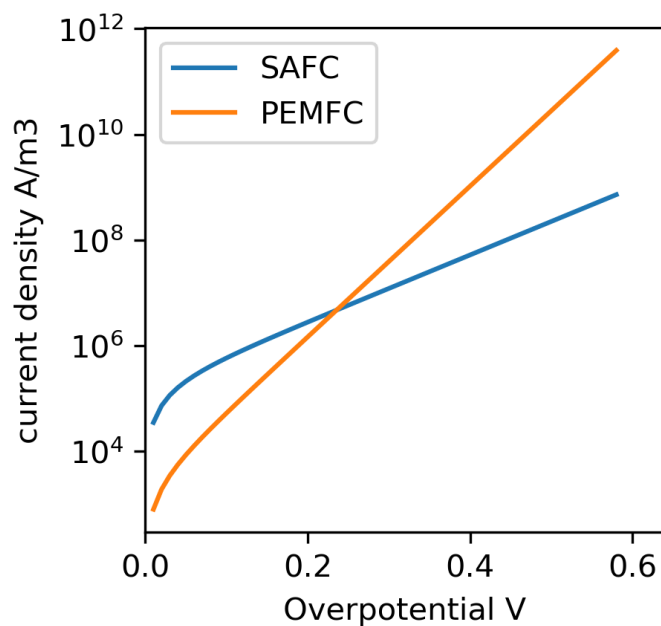
The vastly different Tafel behavior of Pt catalysts in SAFCs and PEMFCs is perhaps not surprising considering the differences in the local Pt environments and the nature of the

electrolyte phase. In SAFCs, the Pt catalyst is deposited on the surface of the CDP electrolyte particle where the active sites are directly exposed to the gas phase. In contrast in PEMFCs, the Pt catalyst is loaded onto a C particle which is then enveloped in a layer of the hydrated ionomer, such that the reaction occurs in a semi-aqueous environment.

Table 5.6. Comparison of the Tafel parameters on Pt catalysts collected here for SAFCs with those reported for PEMFCs.

	SAFC	PEMFC	PEMFC ref
i_0 (A/m ² Pt)	0.026 - 0.039	$1 - 4 * 10^{-4}$	130,141,146
A_R (m ² Pt/m ³)	$21.8 * 10^6$	$1-3 * 10^7$	130,132,141
$A_R i_0$ (A/m ³)	$5.7 - 8.5 * 10^5$	$5 * 10^3$	130
α	0.59 - 0.69	1	130,132,141,146,147
b Tafel slope (mV/decade)	150 - 176	70	130,132,141,146,147
γ	0.75 - 0.84	0.54 - 1	132,146,147
$\Delta G_C^{*,o}$	106 - 118	67	146

Figure 5.4. Plot of the local reaction rate functions, Eq. (19), for SAFCs vs PEMFCs. The parameters for the SAFC function were taken from MEA A; $i_0 = 0.034 \text{ A/m}^2_{\text{Pt}}$; $A_R = 21.8 \cdot 10^6 \text{ m}^2_{\text{Pt/m}^3}$; $\alpha = 0.66$; $\gamma = 0.77$; $C_{O_2} = 3.03 \text{ mol/m}^3$; $T = 250 \text{ }^\circ\text{C}$. The parameters for the PEMFC function were taken from Gasteiger et al.^{130,146}; $i_0 = 0.00025 \text{ A/m}^2_{\text{Pt}}$; $A_R = 3 \cdot 10^7 \text{ m}^2_{\text{Pt/m}^3}$; $\alpha = 1$; $\gamma = 0.7$; $C_{O_2} = 3.67 \text{ mol/m}^3$.



5.4 Modelling SAFC behavior

5.4.1 Validation of the Model

The validity of the 1-D cathode model and the experimental parameters was evaluated by comparing the model-predicted polarization curves to the experimental SAFC polarization curves (Figure 5.5). Modeled and experimental results were compared for cathodic gas environments of humidified air ($p_{\text{O}_2} = 0.124$ atm, $p_{\text{H}_2\text{O}} = 0.38$ atm) and oxygen ($p_{\text{O}_2} = 0.62$ atm, $p_{\text{H}_2\text{O}} = 0.38$ atm). The model was evaluated for the leak corrected Tafel parameters from each MEA (Table 5.5), with α values selected to correspond to the relevant modeled gas condition, ie. when modelling humidified air, the α measured under humidified air was used.

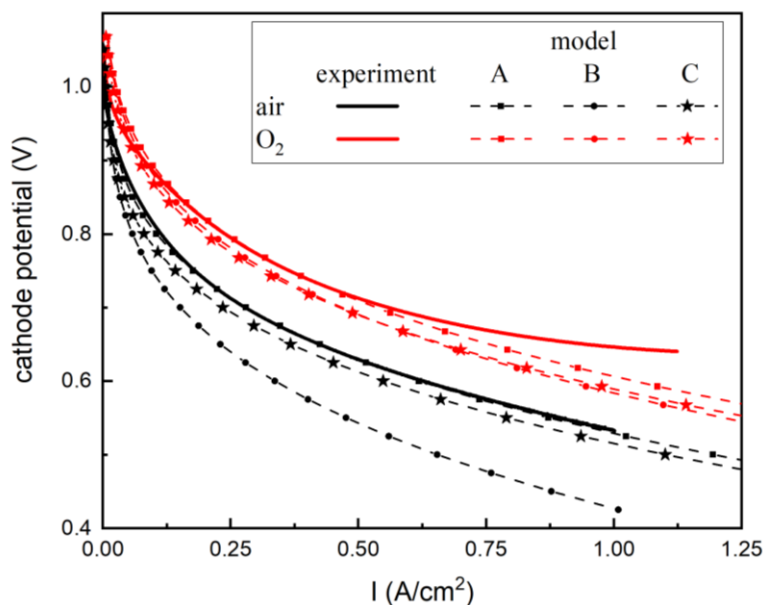


Figure 5.5. Comparison of the modeled polarization curves using Tafel parameters from MEAs A, B, and C (Table 5.5) with polarization curves collected on an experimental fuel cell.

Relatively good agreement between the modeled and experimental curves for humidified air is achieved from the Tafel parameters of MEAs A and C – in fact near perfect agreement is produced from the Tafel parameters of A. The polarization curve produced from MEA B however significantly underpredicts the current densities, despite having a higher $i_0 \left(\frac{c_{O_2}}{c_{O_2}^*} \right)^{\gamma}$ value than MEA C. The underpredicted current densities from MEA B reflect instead the smaller α value that is more than 0.06 smaller than those from A and C, highlighting the outsized impact even a small change in α can produce.

The humidified oxygen results again reveal that the curve produced from Tafel parameters of MEA A most closely matches the experimental data. The predicted curves from MEAs B and C slightly underpredict the current densities. Examining the results from MEA A, strong agreement between model and experiment is observed at cathodic potentials between 0.9 – 0.7 V; however at cathodic potentials above 0.9 V the modelled current density exceeds the experimental, whereas below 0.7 V the experimental current density exceeds the modelled. Above 0.9 V, we believe the overprediction to be attributed to either hydrogen crossover or platinum oxidation effects at the cathode that result in diminished experimental OCVs. Below 0.7 V however, the experimental data exhibits an increase in the slope of the $\log(i)$ vs V, that is not predicted by the model. We posit that this behavior is attributed to a decrease in the ORR Tafel slope at higher overpotentials. Evidence of this behavior was observed in the polarization curves collected on MEA C in which two linear Tafel trends were observed such that at low overpotentials the current density followed a higher Tafel slope (~ 160 mV/decade), but then adopted a lower Tafel slope (~ 130 mV/decade) at higher overpotentials. Given the critical importance of the Tafel slope, the observation of a lower slope motivates studies to elucidate the

mechanistic origins of the double slope behavior and the influence of oxygen partial pressure and overpotential.

The general agreement of the modeled and experimental polarization curves is a massive achievement considering that each of the model parameters was measured or calculated independently. While the Tafel parameters from each of the MEAs does an adequate job at capturing the experimental behavior (apart from MEA B with air), the results from A stand out as exceptional, and thus Tafel parameters from A were utilized in the subsequent sections to study the behavior of modified SAFC cathodes.

Having established a robust model of the cathode, it is now instructive to examine the internal mechanisms at play within the cathode at various levels of bias. Consistent with established fuel cell theory, at low current densities SAFCs operate within what is known as the activation regime or region of the polarization curve. The activation regime is characterized by the applied bias being almost entirely spent towards activating the ORR kinetics, with minimal losses due to ohmic resistance in both the electrolyte and cathode and minimal gas diffusional losses. As shown in Figure 5.6b, when operating in the activation regime at a cathodic potential of 0.8 V, the overpotential is roughly constant through the cathode. In turn, the local reaction rate is also relatively flat, and the proton and electron current profiles are nearly linear. Because of the relatively low reaction rates in the activation regime, changes in gas composition are minimal; in Figure 5.6b there is a less than a 1% difference in the O₂ concentration at the cathode-electrolyte interface and at the cathode-gas interface. At higher current densities, the cell enters into a new regime in which reaction kinetics, charge transport through the cathode, and ohmic resistance from the electrolyte layer each play significant roles in defining the cell

performance. We term this regime the mixed-control regime and in SAFCs this regime defines the remainder of the polarization curve – from the activation region to the limiting current density. In the mixed-control regime, substantial overpotential losses are incurred in the cathode due almost entirely to the decline in φ'_{CDP} , which reflects the lower effective proton conductivity compared to electronic conductivity. The decline in φ'_{CDP} produces a narrowing overpotential window that in turn results in a local reaction rate profile that is sharply concentrated at the cathode-electrolyte interface. Consequently, the proton and electron current profiles are also steeper at this interface. Notably, in SAFCs the gas diffusional losses remain minimal throughout the polarization curve; near the peak power density at a cathodic potential of 0.58 V, the O₂ concentration loss is only 6% and even at the limiting current density the loss is 15%. Absent from the SAFC polarization curve is a diffusion limited regime, which is observed in both PEMFCs and SOFCs. The relatively minor changes in gas composition observed in SAFC cathodes justify the simplified Stefan-Maxwell diffusion model implemented here, in which the total pressure gradient term is ignored. Additionally, the minor changes in gas composition validate the approximation of overpotential as simply the difference between φ'_{CDP} and φ_{Pt} .

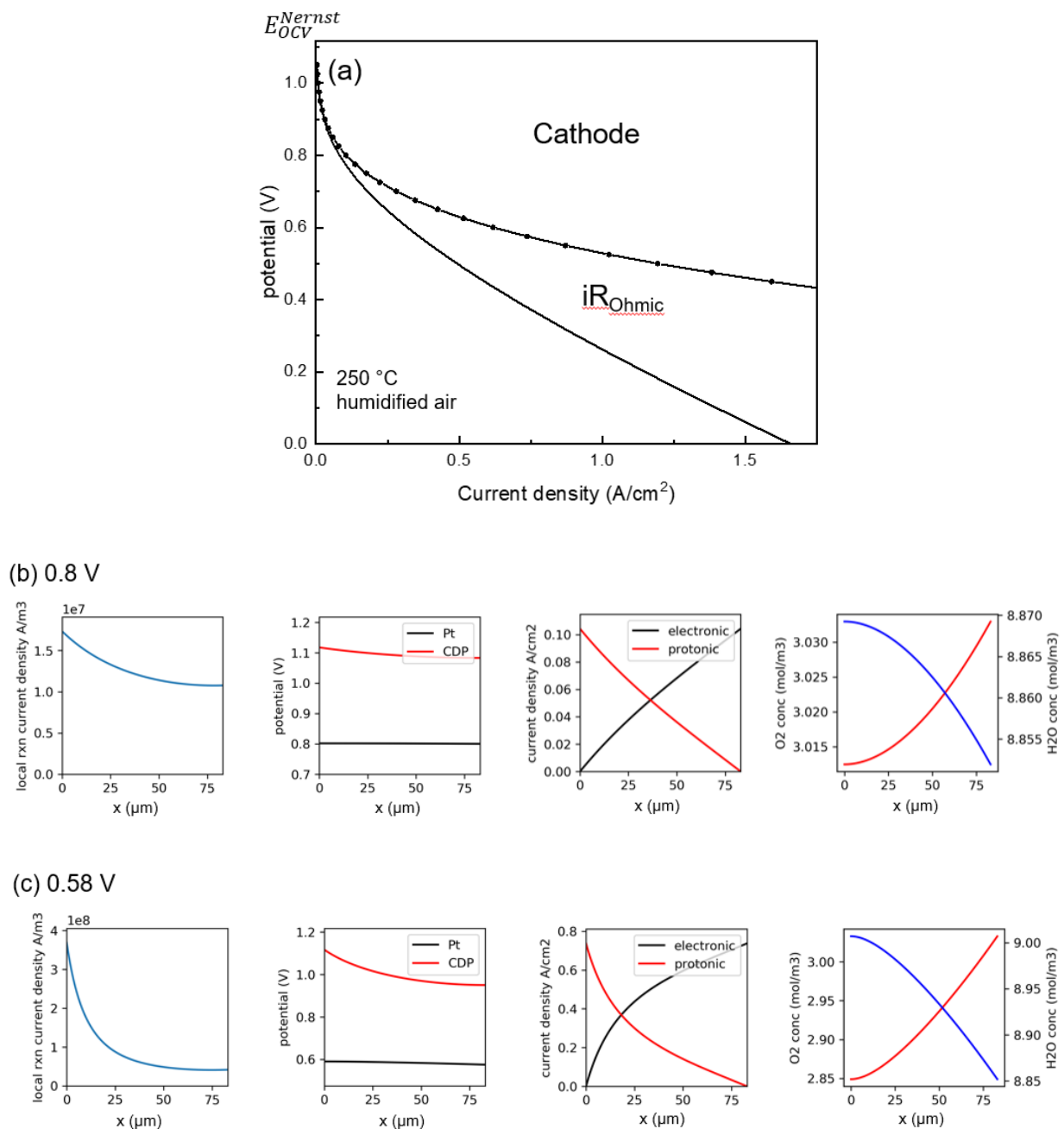


Figure 5.6. (a) Modeled polarization curve at 250 °C with humidified air using Tafel parameters from MEA A. The cathodic polarization response is denoted with circles. The full cell polarization curve with added ohmic losses from the electrolyte layer is represented by the lower solid line. The internal mechanisms at cathodic potentials of (b) 0.8 V and (c) 0.58 V. From left to right the panels in (b) and (c) illustrate the profiles for local reaction rate, the ϕ'_{CDP} and ϕ_{Pt} potentials, the proton and electron currents, and the oxygen and steam concentrations.

5.4.2 Case Studies of SAFC Cathode Performance

It is now useful to interrogate the model to study the influence of changing various parameters. This serves both to determine which improvements in materials properties would be most impactful on cell performance as well as to identify the optimal microstructural design and operating conditions. The studied parameters include charge transfer coefficient, conductivity of the electrolyte phase, humidification, operating temperature, cathode thickness, and CDP particle size. The study of each of the parameters was done by holding the other parameters at the experimentally measured or calculated values, and unless otherwise noted, each case study was conducted for a 50 μm cathode operating at 250 $^{\circ}\text{C}$ under humidified air ($p_{\text{H}_2\text{O}} = 0.38 \text{ atm}$). The modeled cathode polarization curves were adjusted to include ohmic losses from the electrolyte layer.

Attention is focused on improving two key performance metrics – peak power density (PPD) and current density at 0.8 V ($I@0.8\text{V}$). We compare our $I@0.8\text{V}$ results to the 2020 DOE PEMFC technical target of 300 $\text{mA}/\text{cm}^2_{\text{geo}}$ at 0.8V.

5.4.2.1 Cathodic Charge Transfer Coefficient α

As previously stated, the cathodic charge transfer coefficient α is a critically important parameter that defines the Tafel slope or the impact of bias on the reaction rate. The low value of α measured here in comparison to that observed in PEMFCs is principally responsible for the low ORR rates in SAFCs. As expected, increasing the value of α results in significant improvements to the polarization curve, as shown in Figure 5.7. Increasing the α value from 0.658, measured here, to 1.0, as reported for PEMFCs, has the effect of more than tripling the

I@0.8V and increasing the PPD from 281 to 454 mW/cm² (Figure 5.7). These improvements were the most pronounced across all of the case studies examined here, and as such we deem the charge transfer coefficient the most impactful parameter to target for the advancement of SAFCs. As impressive as these improvements are, notably they still fall short of the DOE targets. However, it is likely the case that higher α values would warrant a reevaluation of microstructural parameters, such as cathode thickness, that would result in further improvements.

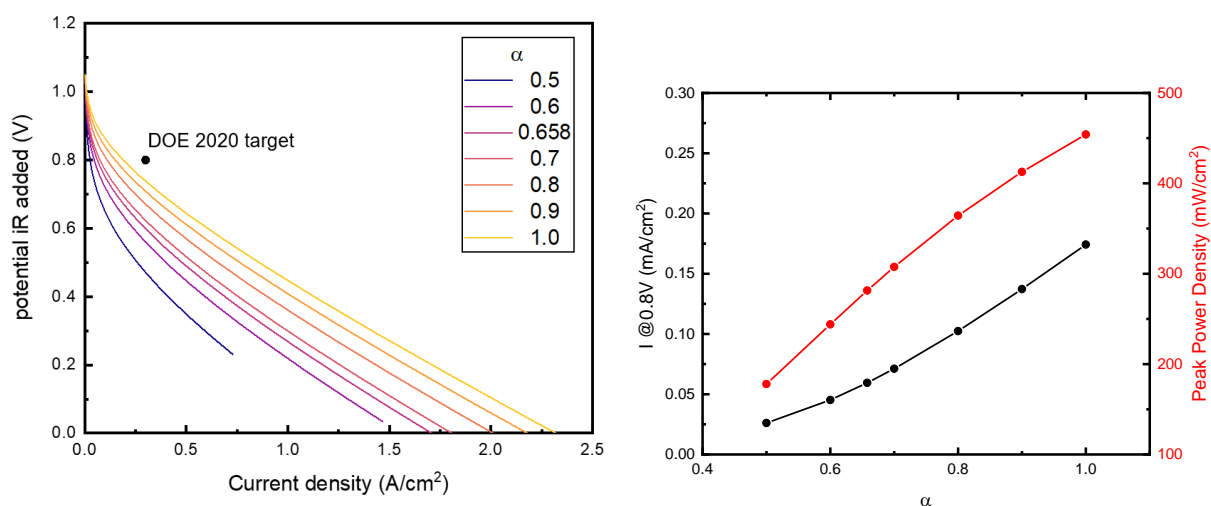


Figure 5.7. (a) Comparison of modeled fuel cell polarization curves with various values of α . (b) $I_{@0.8V}$ and PPD as a function of the α parameter.

While it is clear that achieving higher α values is extremely beneficial, a rational pathway to do so is unclear. The mechanistic role of the α parameter in a multistep electron transfer function is more complicated than may initially be conceived from a transition state theory framework for a single electron transfer reaction, as was laid out in the IUPAC technical report on the subject.¹⁴⁸ In a traditional transition state theory framework, α takes the role of the

asymmetry parameter, here termed β , that describes the efficiency with which applied bias reduces the reaction activation energy barrier and typically takes a value around 0.5. However, in the case of a multielectron transfer reaction, such as the ORR, the impact of the applied bias must be considered for each of the elementary reactions involved. Assuming a single rate determining elementary step and that all of the other steps are in quasi-equilibrium, the α value can be defined as:¹⁴⁸

$$\alpha = \frac{n_f}{\nu} + n_r \beta$$

where n_f is the number of electrons involved prior to the rate determining step, ν is the number of times the rate determining step occurs in the multielectron transfer reaction, and n_r is the number of electrons involved in the rate determining step, which the authors of the IUPAC report state can only be 1 or 0. Considering that the measured α values here are around 0.5, it is sensible to assume that the rate determining step for ORR in SAFCs is the first electron transfer reaction and that α is equal to the asymmetry parameter β of that electron transfer reaction. Drawing mechanistic conclusions about the ORR in PEMFCs based on $\alpha = 1$ is more dubious as multiple proposed mechanisms are capable of producing a value of 1. Perhaps the only mechanistic conclusion that can be drawn from an α value of 1 is that the first electron transfer reaction is not the rate determining step. Efforts to increase the value of α must then seek changes to the ORR mechanism such that a later step in the reaction mechanism is the rate determining step.

5.4.2.2 Proton Conductivity of the Electrolyte

As previously stated, proton transport is principally responsible for the overpotential loss through the porous cathode. Therefore, it is valuable to consider the potential impact of discovering an electrolyte with increased proton conductivity. Evaluation of the model for proton conductivities that range from the experimental conductivity to twice that value are shown in Figure 5.8, where the enhanced proton conductivity has been accounted for not only in the porous cathode but also in the electrolyte layer.

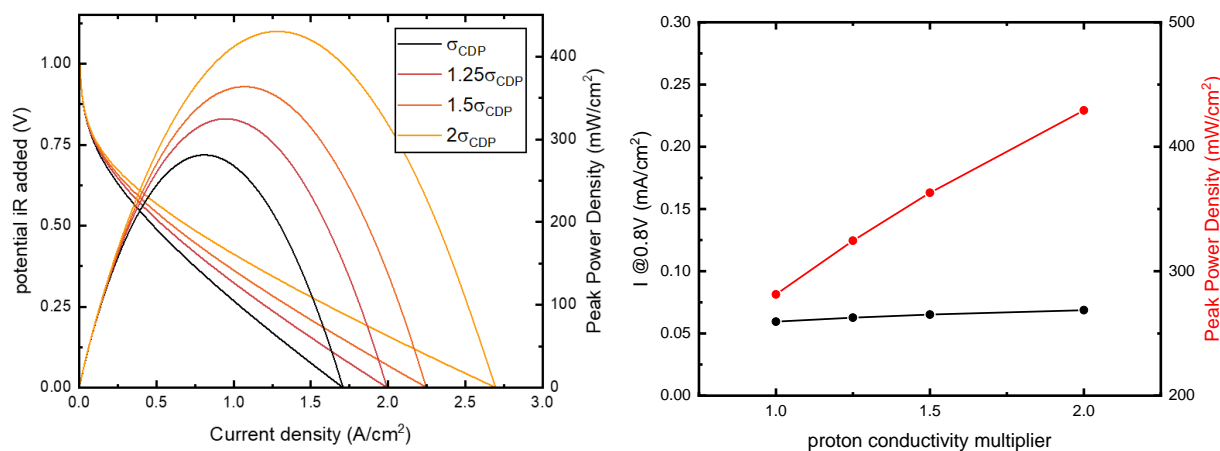


Figure 5.8. (a) Analysis of the effect of increasing the proton conductivity of the electrolyte phase by multiples of 1.25, 1.5, and 2. (b) $I @ 0.8V$ and PPD values from 6a.

As shown in Figure 5.8, increasing the proton conductivity has almost no effect on the current density at 0.8 V. This is to be expected because at 0.8 V the cathode operates in the activation regime where relatively minor overpotential losses are incurred, and thus further reducing the overpotential loss by increasing conductivity has very limited effect. However, the benefit of the increased proton conductivity becomes apparent at higher current densities where

overpotential losses in the cathode and ohmic losses from the electrolyte become significant. This is reflected in the near linear increase of the PPD with increasing proton conductivity.

5.4.2.3 Required Humidification

One of the principal constraints in operating a SAFC is supplying a sufficiently humidified atmosphere to prevent the degradation/dehydration of the CDP electrolyte. In commercial devices, a steam partial pressure of 0.38 atm is supplied at 250 °C to provide a comfortable 18 °C buffer against dehydration. This level of humidification is similar to those supplied in PEMFCs to maintain the hydration of the ionomer. While the humidification requirement is not unique to SAFCs it nonetheless acts to reduce the performance of the fuel cell by diluting the oxygen reactant concentration and reducing the thermodynamic potential of the cell. However, in contrast to hydrated ionomer electrolytes, solid acids do not rely on water/steam for proton transport, and thus it is conceivable that a solid acid electrolyte could be discovered that exhibits reduced or nonexistent humidification requirements. In fact, a solid acid phase derived from CDP was reported in 2020 by the authors here which had superprotonic conductivity over a wide thermal stability window without humidification.⁹ Unfortunately, the proton conductivity of that phase was roughly an order of magnitude lower than that of CDP. Nevertheless, it is interesting to consider what effect reduced humidification would have on fuel cell performance.

In Figure 5.9, the effect of reduced humidification on cell performance is examined for operation with humidified H₂ – air. Included for reference are the data produced from humidified oxygen at the cathode with the experimental partial pressure of steam ($p_{\text{H}_2\text{O}} = 0.38$ atm). The

partial pressure of steam was found to have a surprisingly strong impact on the performance of the cell; in fact, the performance that would be achieved under air humidified with 0.05 atm steam is essentially equivalent to that which is achieved under oxygen with the current humidification. This result is surprising given that the humidified air has a partial pressure of oxygen that is significantly lower than that of the oxygen case (0.20 vs 0.62 atm oxygen). The unusual congruence of the two results, despite the disparity in reactant concentrations, is achieved because of the difference in the Nernst potentials. The Nernst potential of the humidified air case was 1.18 V, roughly 50 mV higher than that of the humidified oxygen case. In fact, the change in Nernst potential is itself largely capable of predicting the observed trend with humidification (Figure 5.9c); reducing the humidity by-in-large vertically translates the polarization curve by the change in the Nernst potential. This is apparent if one plots the voltage required to achieve 0.3 A/cm^2 against the Nernst OCV for the various humidified air studies. The nearly 1-to-1 relationship between the two potentials implies that the change in Nernst potential has far more influence than the increase in the ORR rate associated with increased oxygen reactant concentration.

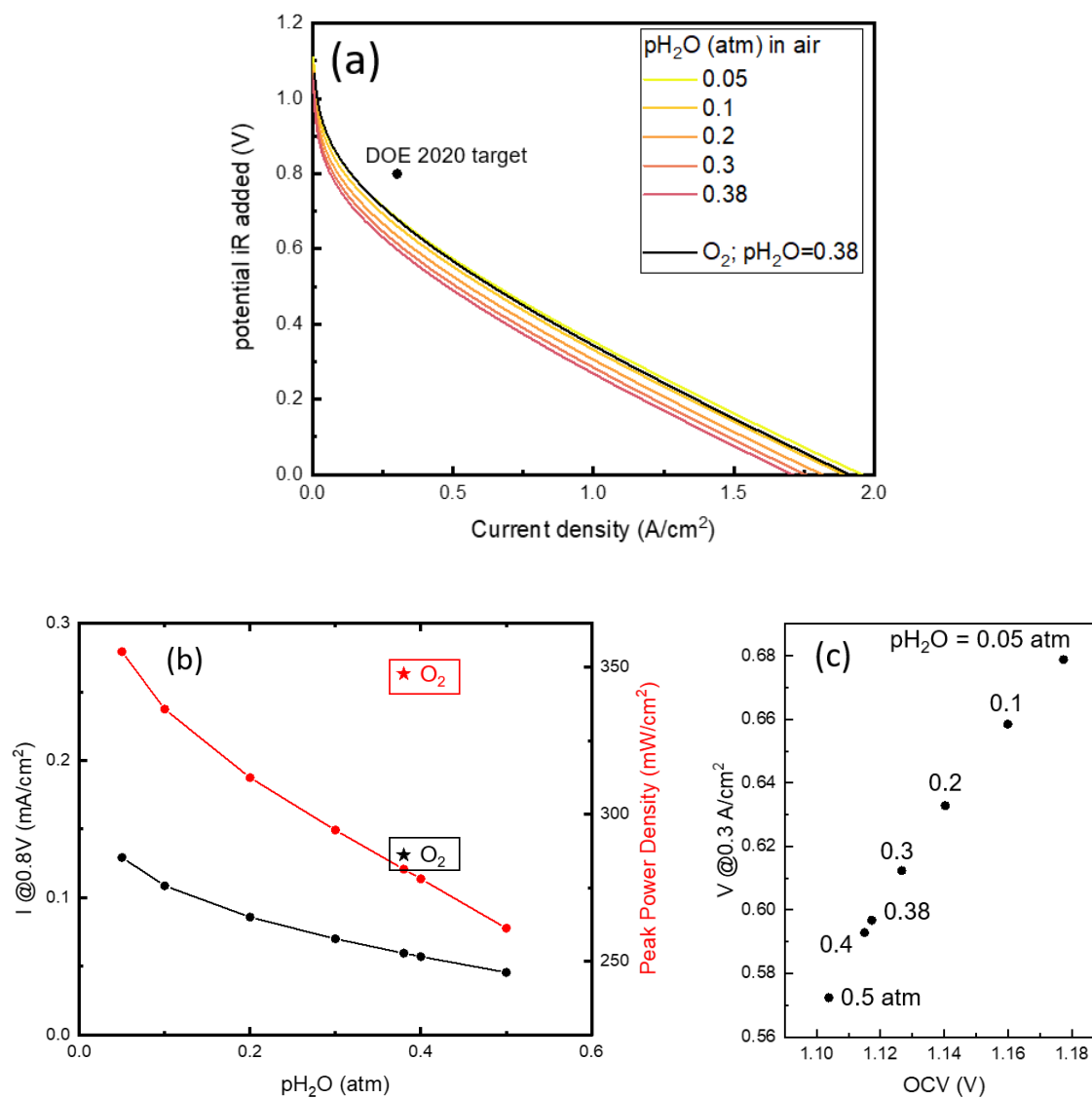


Figure 5.9. (a) Modeled polarization curves for various levels of humidification for a H_2 – air fuel cell. For comparison, the modeled polarization curve for oxygen at the current experimental level of humidified ($\text{pH}_2\text{O} = 0.38 \text{ atm}$) is plotted in black. (b) I @ 0.8 V and PPD values from the polarization curves in 7a. The stars represent the values from humidified O_2 . (c) voltage at $0.3 \text{ A}/\text{cm}^2$ vs OCV for the modeled curves from humidified H_2 – air.

5.4.2.4 Operating Temperature

Given the thermal activation of the ORR kinetics, the optimization of operating temperature might on the surface appear to be a simple problem with a simple answer: operate as hot as you can. However, in reality there are several competing effects produced by increasing temperature. Increasing the operating temperature results in the following effects:

- (1) The exchange current density increases according to the relationship: $\ln(i_0) \propto -\Delta G_C^{*,0}/RT$, where $\Delta G_C^{*,0}$ was experimentally determined to be 118 kJ/mol.
- (2) The Tafel slope increases according to the equation: $\frac{RT}{\log(e)\alpha F}$
- (3) The proton conductivity of the CDP phase increases according to the equation:

$$\sigma = \frac{A}{T} \exp\left(\frac{-E_A}{RT}\right)$$

Where $\log(A)$ and E_A were taken to be 38.4 kJ/mol and 11.32 $\Omega^{-1} \text{ cm}^{-1} \text{ K}$ respectively.¹⁷ The conductivity of CDP influences proton transport in both the porous electrode and the electrolyte layer.

- (4) Finally, and most critically, the required amount of humidification to prevent dehydration increases. In this case study of temperature, the partial pressure of steam was chosen such that an 18 °C buffer existed between the operating and dehydration temperatures. The dehydration temperature for each partial pressure of steam was calculated using the following relationships determined in Ayako et al.¹⁶:

$$\text{For } T_{\text{dehydration}} < 267 \text{ }^\circ\text{C: } \log(\text{pH}_2\text{O}) = 5.66 - 3290/T_{\text{dehydration}}$$

$$\text{For } T_{\text{dehydration}} > 267 \text{ }^\circ\text{C: } \log(\text{pH}_2\text{O}) = 7.90 - 4500/T_{\text{dehydration}}$$

The effects of temperature on gas diffusivity and electronic conductivity were ignored in this case study as the gas diffusion losses and electronic ohmic losses were relatively inconsequential.

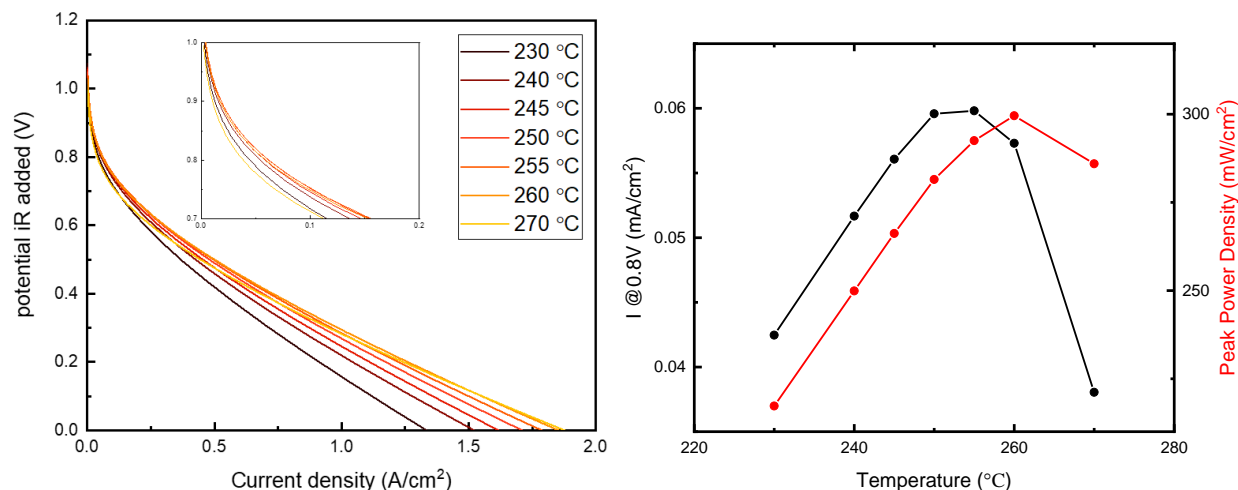


Figure 5.10. (a) Modeled polarization curves for various operating temperatures with humidified air. (b) $I@0.8V$ and PPD values from the polarization curves in (a).

The polarization curves and performance metrics for a range of operating temperatures are shown in Figure 5.10. The optimal operating temperature range, as determined by the $I@0.8V$ and PPD values, is between 250 – 260 °C. It is difficult to draw causal relationships between the thermally dependent effects listed above and the performance trends in Figure 5.10b given the complexity and interdependence of the effects. However, it is likely the case that the reduction in the $I@0.8V$ and PPD from 260 to 270 °C is due to the increase in humidification from 0.54 to 0.76 atm of steam and the resultant decrease in OCV and oxygen concentration.

5.4.2.5 Exchange Current Density and Active Pt Surface Area

It is of course possible to increase cell performance by increasing either the exchange current density i_0 or the volumetric density of active Pt area, A_r . In terms of impact on the modeled performance, the effect of a percent increase in either of these terms is equivalent, as the two only appear in the expression for the local reaction rate Q and are grouped together as a product. Increasing A_r with the present SAFC cathode microstructure necessitates that the CDP particle size is reduced and that the Pt loading is increased to cover the additional surface area. Figure 5.11 shows the effect of increasing either i_0 or A_r by various multipliers, and it is observed that increasing either parameter is highly effective at improving both $I@0.8V$ and peak power density. In fact, nearly linear improvement in these metrics were produced by increasing i_0 or A_r up to 3-fold, and with a multiplier of 10, the predicted performance is close to achieving the DOE $I@0.8V$ target. However, the microstructural changes required to increase A_r are both costly and experimentally difficult to produce and maintain. Figure 5.11c shows the Pt mass normalized performance metrics, and it is clear that the performance gains with increasing A_r are outpaced by the increase in Pt loading. Additionally, 50 nm CDP particles are required to produce a 10x increase in A_r and particles that small have not yet been achieved. The smallest demonstrated CDP particle size is 100 nm, which was produced using an electrospray deposition method, and while measurements of the electrodes derived from those particles showed stability over 24 hrs under hydrogen, stability is required over significantly longer timescales under the much more deleterious ORR reaction.¹¹⁵ Thus it is my present view that decreasing the CDP particle size to increase the active surface area is not a sufficient strategy to improving SAFC performance. Pursuing increases in i_0 however does appear to be worthwhile. The plausibility of

achieving a 10-fold increase in i_0 is encouraged by the fact that if the thermal enhancement trend of i_0 observed in PEMFCs were extended to SAFC operating temperatures the predicted value is $0.41 \text{ A/m}^2_{\text{Pt}}$, more than 10 times the i_0 value measured here.¹⁴⁶

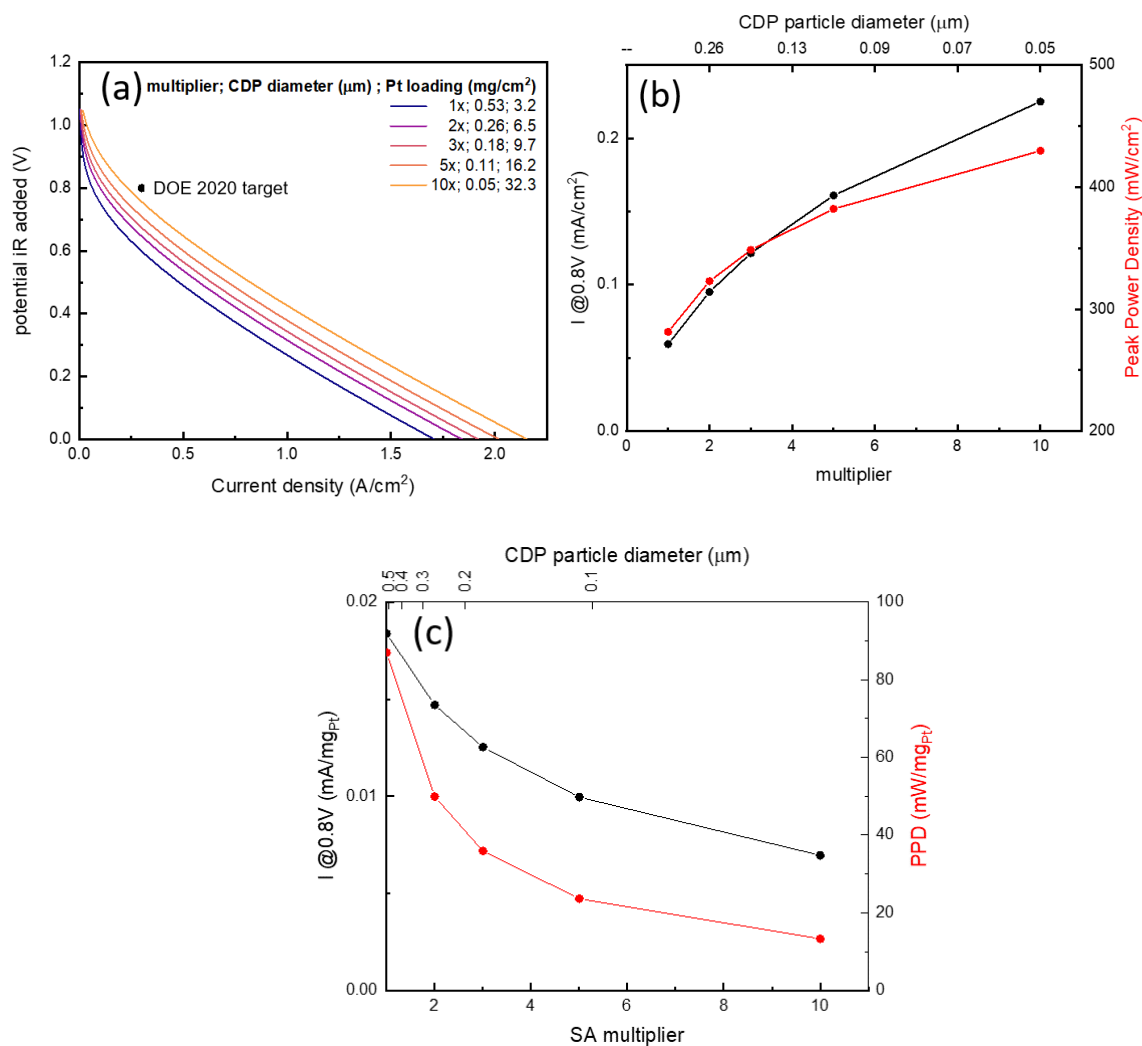


Figure 5.11. (a) Modeled polarization curves for increases in i_0 or A_r by the indicated multipliers. Included in the legend are the CDP particle diameter and Pt loading that correspond to the A_r . (b) $I @ 0.8\text{V}$ and PPD values from the polarization curves in (a) with CDP particle diameters corresponding to the A_r values shown on the upper x axes. (c) Pt utilization, as evaluated by the Pt loading normalized $I @ 0.8\text{V}$ (mA/mg_{Pt}) and peak power density (mW/mg_{Pt}), plotted as a function of the A_r multiplier.

5.4.2.6 Cathode Thickness

A peculiarity of the SAFC is the extreme thickness of the cathode. While PEM and SOFCs have electrodes around 10 μm thick, the cathode of SAFCs is between 50 – 100 μm . The thickness of the cathode linearly increases the Pt loading, a key barrier to commercialization of SAFCs. In order to achieve platinum loadings reasonably close to the DOE 2020 target for PEMFCs of 0.125 mg/cm^2 , the cathode thickness must be decreased. Figure 5.12 illustrates the impact of cathode thickness over a range of values from 10 – 100 μm . Reducing the cathode thickness below 50 μm results in a near linear decrease in the $I@0.8\text{ V}$. This effect is observed because the cathode experiences relatively minimal overpotential losses at 0.8 V, and thus reducing the cathode thickness below 50 μm simply results in less Pt to catalyze the ORR. However, at higher cathode thicknesses the increase in current density with thickness begins to diminish, as overpotential and gas transport losses begin to play a larger role. While thicker cathodes produced higher $I@0.8\text{V}$ values over the range of thicknesses explored here, the thinnest cathodes achieve the highest Pt utilization by minimizing overpotential and gas transport losses. Thus an economic optimization should be conducted to determine the optimal cathode thickness, taking into the account the price per unit performance ($\$/\text{mA}$ or $\$/\text{mW}$) and the price of Pt ($\$/\text{mg}$). In contrast to the $I@0.8\text{V}$ trend, the peak power densities achieved a peak at 50 μm . The peak power density occurs at much higher current densities than those recorded at 0.8V and thus is much more sensitive to the charge and gas transport losses of thicker cathodes.

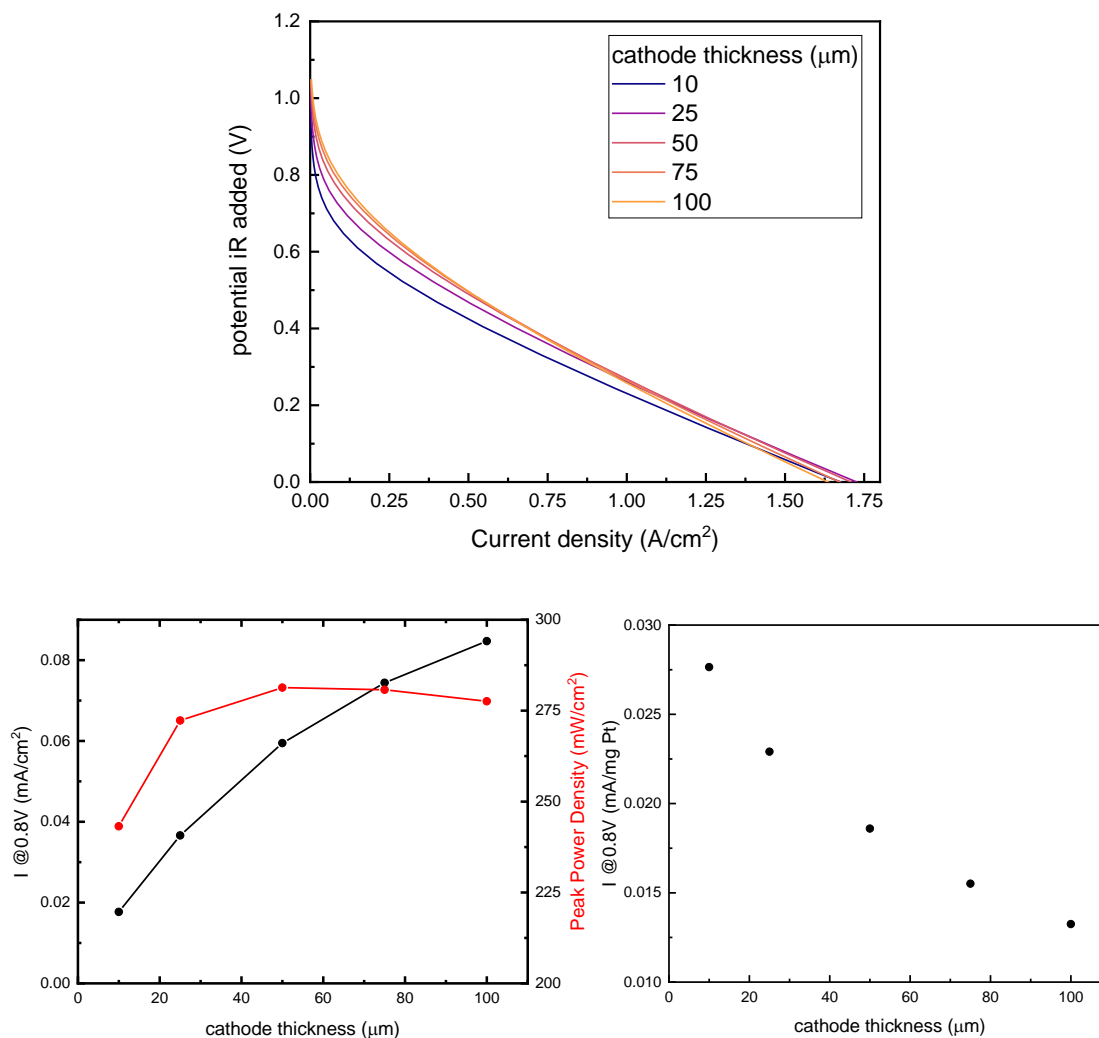


Figure 5.12. (a) Modeled polarization curves for various thicknesses of the cathode. (b) $I @ 0.8V$ and PPD values from the polarization curves in (a). (c) Platinum utilization as defined as the current density produced at 0.8V normalized by the total Pt loading. The platinum utilization is calculated using a volumetric Pt loading of $0.64 \text{ mg Pt}/\text{cm}^3$.

5.4.2.7 Cell Pressure

Increasing the overall pressure of the cell improves the performance by increasing the concentration of oxygen reactant which also increases the Nernst potential. In the case study here, we examine the effect of increasing the total cell pressure while holding the partial pressure

of steam at 0.38 atm, with the remaining pressure being composed of hydrogen or air at the anode or cathode respectively. Figure 5.13 shows that increasing the pressure significantly improves the cell performance, both in terms of the $I@0.8V$ and the PPD. However, the performance falls far short of the DOE 2020 PEMFC target of 1 W/cm^2 at 1.5 atm. Additionally, pressurization of the cell requires an energy penalty that is not captured here in this data.

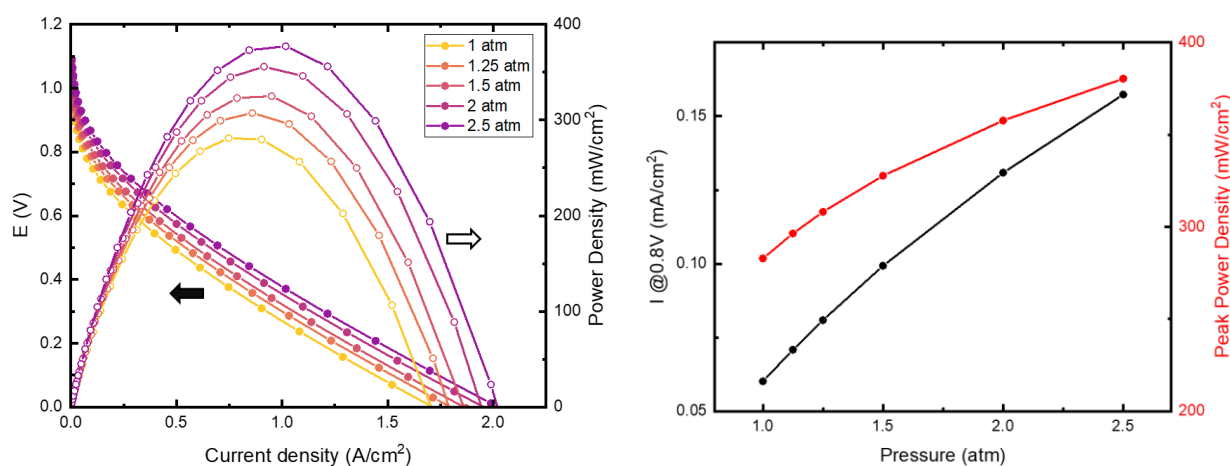


Figure 5.13. (a) Modeled polarization curves for various cell pressures. (b) $I@0.8V$ and PPD values from the polarization curves in (a).

5.5 Conclusions

In this work, we have utilized a 1-D modeling approach to achieve a comprehensive understanding of the factors limiting SAFC cathode performance. Based on this understanding, efforts to develop SAFCs can be targeted towards improving the parameters and materials properties that are most impactful on SAFC performance.

Key to the development of this model was characterization of the electrochemical kinetics of the ORR on the Pt nanoparticle catalysts employed in the cathode. As the first to characterize these kinetics, we developed a new MEA geometry that allowed for precise control

of the active surface area while eliminating charge and mass transport effects. Beyond the measurements conducted here, the methodology developed provides a platform for the screening of alternative catalyst candidates in search of those with favorable kinetic parameters.

Characterization of the ORR kinetic parameters on Pt revealed that although the effect of thermal activation was tangible in the increased value of the exchange current density, the lower cathodic charge transfer coefficient in SAFCs compared to PEMFC (0.65 vs 1) had devastating implications for the relative performance of SAFCs. It was shown through the 1-D model that if the charge transfer coefficient were to be increased to a value of 1 the performance of SAFCs would substantially improve, exhibiting a roughly 3-fold increase in the current density at 0.8 V and a 50% increase in the peak power density. We strongly advise that future research efforts be focused on achieving this improvement in the transfer coefficient.

Additionally, the model developed here was entirely informed by experimentally measured or independently calculated parameters, including those for mass and charge transport. It was then no small feat that the model produced a near perfect account of the experimental polarization curve. The trends in internal reaction rates and charge and mass transport phenomena were studied at different regions of the polarization curve. Furthermore, the model was utilized to evaluate the impact of changes to various cathode properties that included: cathodic charge transfer coefficient, proton conductivity of the electrolyte phase, humidity, operating temperature, exchange current density, active surface area, cathode thickness, and cell pressure. In addition to the critical importance of the charge transfer coefficient, it was found that significant improvements to cell performance could be achieved by discovering a solid acid electrolyte with reduced humidification requirements.

Supplemental Information

Figure 5S.-1. Procedure for the fabrication of flat cathode MEAs.

CDP pellet preparation

CDP crystals were first ground in a glovebox by mortar and pestle. Roughly 1g of the powders were then carefully chopped into a $\frac{3}{4}$ " diameter die, where the ends of both die caps were coated with Kapton tape. The filled die, with both Kapton-coated die caps inserted, was then stored in a 130 °C oven for at least 3 hours. The pellet was then removed from the oven and pressed at 4 tons for 10 minutes, after which the die was removed from the press and allowed to naturally cool (~15 minutes). I term this procedure "hobo hot pressing". The resulting CDP pellets attained roughly 95% theoretical density.

The pellets were then polished to a mirror finish on what was to be the cathode face. To do so, the pellet was first polished using a 2000 grit sandpaper. The thickness of the pellet was checked across its area to ensure a nonuniformity of less than 0.03 mm. The mirror finish was then achieved by polishing with the fine 1200 grit sandpaper, cutting small squares of the paper out and rubbing the sandpaper over the cathodic face of the pellet. This final step was done very meticulously and could take up to 40 minutes to remove all of the scratches. When held to the light, the center of the pellet should be nearly free of any visual imperfections and highly reflective. AFM images of the polished surface show relatively low surface roughness, although polishing scratches of ~0.5 μm depth were omnipresent.

Pt deposition

Pt nanoparticles were deposited on the pellet using the powder bed MOCVD approach described in the text (Section 5.2.2.1). SEM images of the surface post deposition confirmed that the Pt nanoparticle film was identical to that on cathode powders.

MEA Fabrication

Following the MOCVD, the powders were dumped from the pellet and the pellet was vigorously blown with an air stream to remove residual powders. The anode face and edges of the pellet was polished to remove deposited Pt in order to prevent electrical shorts. An anode supported on a GDL was fabricated with a diameter that was slightly smaller than the pellet. The anode on GDL was then held against the anodic face of the CDP pellet and the two were wrapped with 12 cm of PTFE along the edges. The PTFE was gently flattened by hand onto the faces of pellet and GDL. A circular piece of Kapton film was taped to the back of the GDL and a piece of MPL C paper was placed on top of the exposed cathode face of the pellet. The assembly was then wrapped in 20 cm of military grade PTFE and vacuum sealed inside of a Trojan condom. The sealed sample was then isostatically pressed at 3 MPa for 5s. The sample was then removed from the press and the condom, and the military grade PTFE and protective Kapton film were removed from the sample. A stainless steel GDL was then added to the cathodic face, in contact with the carbon paper, and the assembly was then finished by wrapping in 15 cm PTFE.

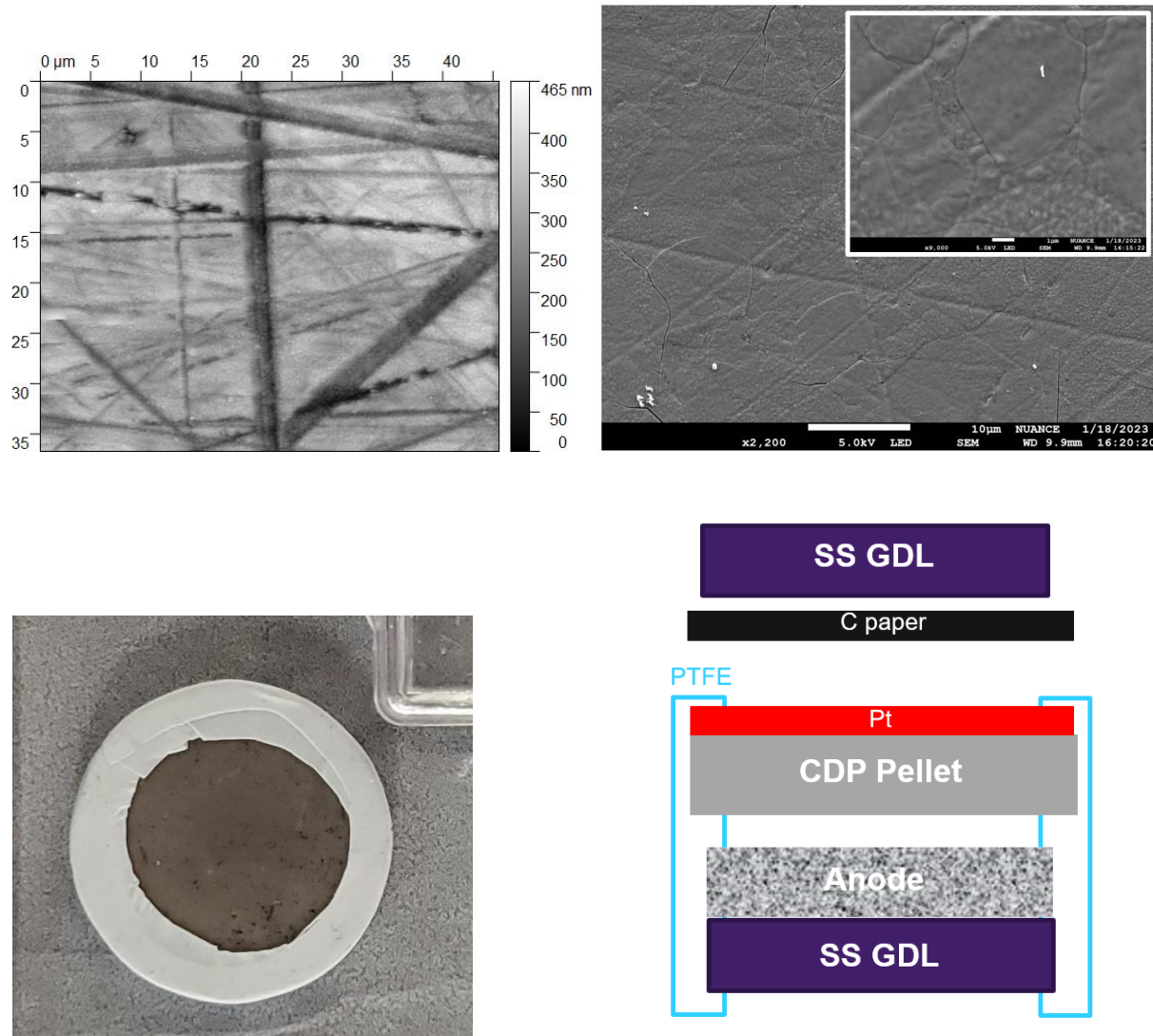
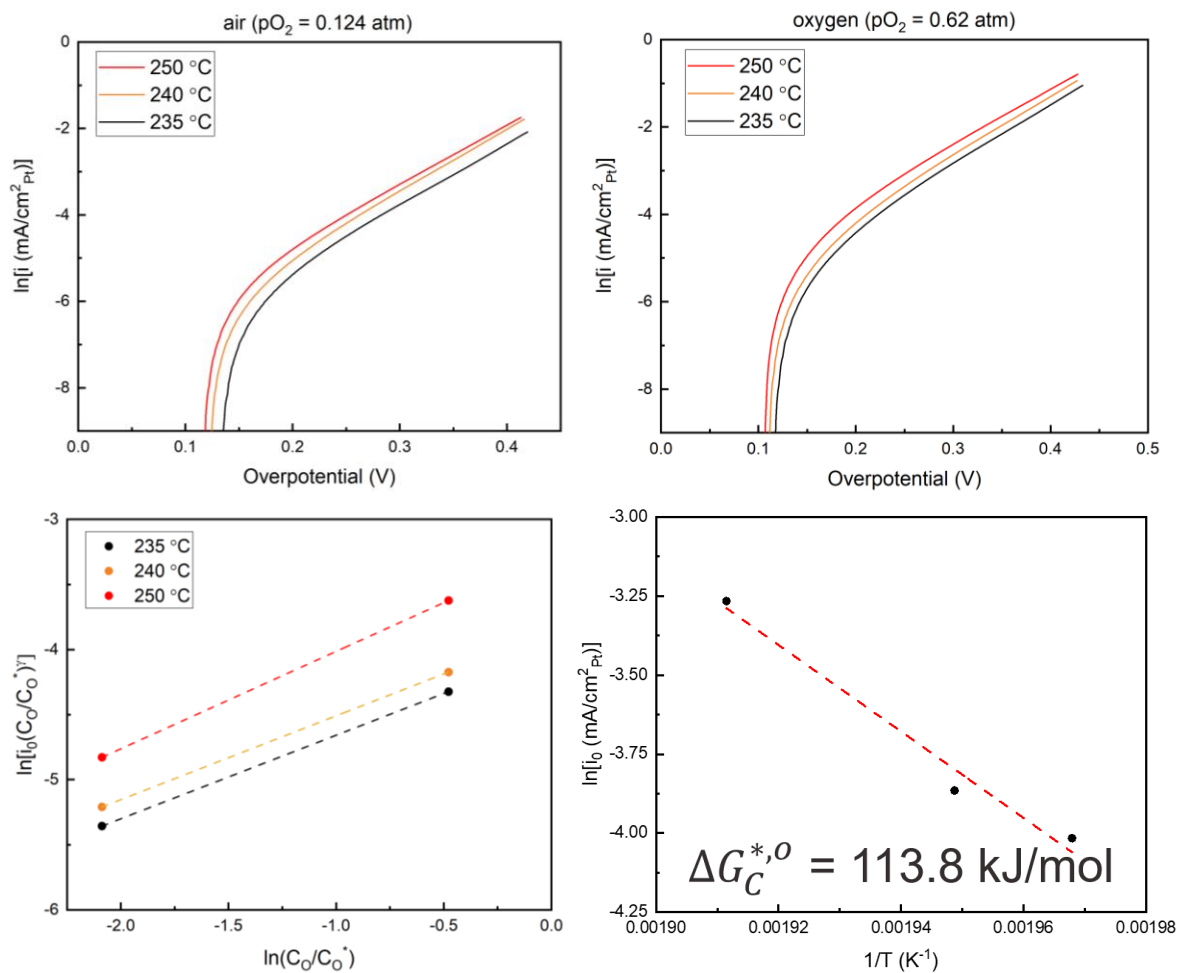


Figure 5S.-2. (a) AFM images of the polished CDP pellet. (b) SEM images of the cathodic face of the CDP pellet after the Pt nanoparticle deposition. (c) The MEA after wrapping the CDP pellet and anode on GDL together in PTFE prior to pressing. (d) Schematic of the assembled MEA. The outermost layer of PTFE has been omitted for clarity.

Figure 5S.-3. Tafel fitting data for MEA A.

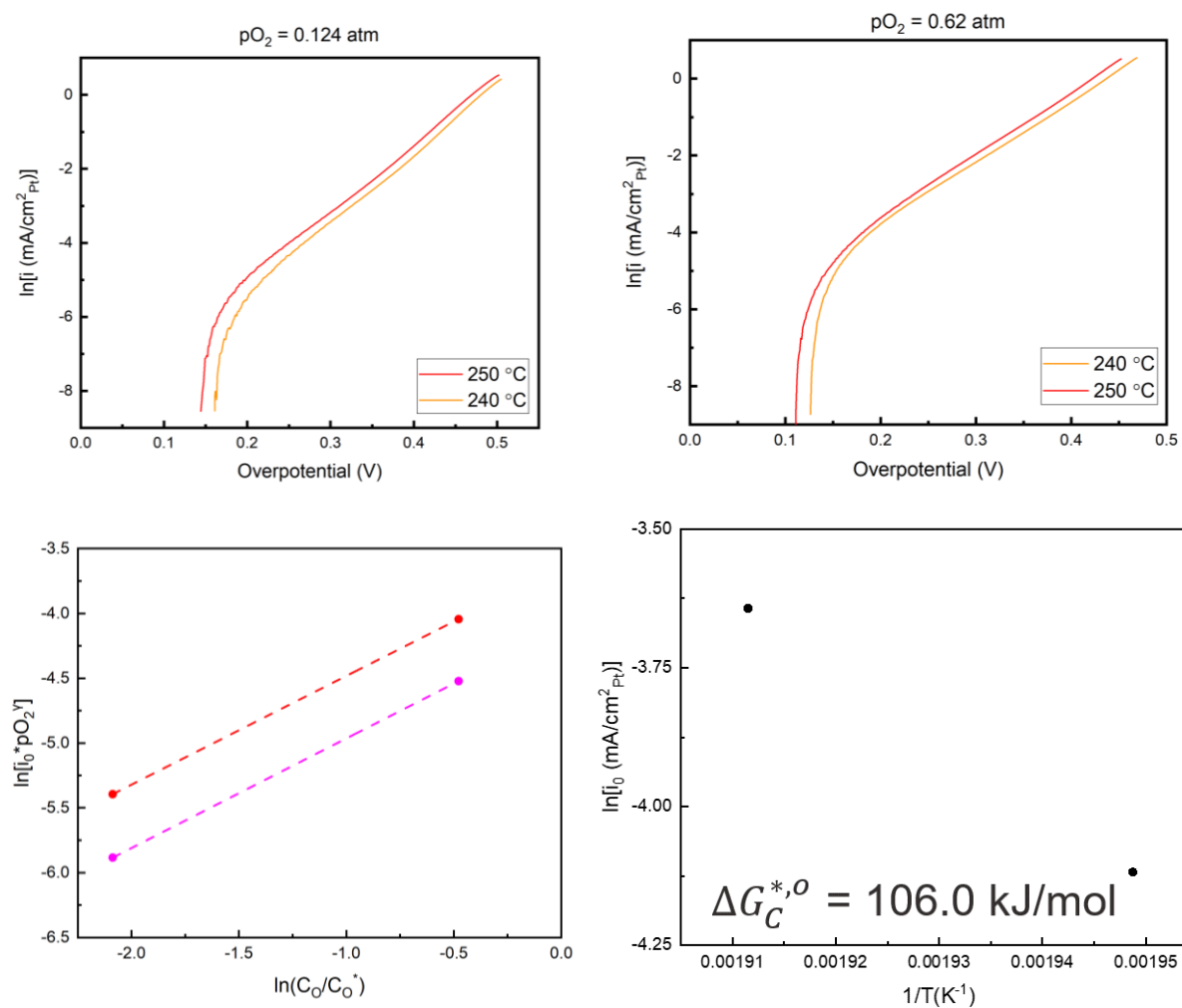
	Air (pO₂ = 0.124 atm)		O₂ (pO₂ = 0.62 atm)		Calculated pO₂ = 1 atm	
T (°C)	i _o (pO ₂) ^γ	α	i _o (pO ₂) ^γ	α	i _o (A/m ²)	γ
235	0.00664	0.61741	0.01385	0.62736	0.04942	0.45621
240	0.00642	0.64666	0.01789	0.62056	0.06962	0.63667
250	0.00774	0.65781	0.0269	0.61862	0.11177	0.77429

Figure 5S.-4. Tafel Fitting for MEA B.



T (°C)	Air ($pO_2 = 0.124$ atm)		O ₂ ($pO_2 = 0.62$ atm)		Calculated $pO_2 = 1$ atm	
	$i_0(pO_2)^\gamma$	α	$i_0(pO_2)^\gamma$	α	$i_0 (A/m^2)$	γ
235	0.00472	0.58405	0.01325	0.56516	0.01801	0.64183
240	0.00546	0.6102	0.0154	0.57463	0.02096	0.64405
250	0.008	0.58892	0.02669	0.54332	0.03818	0.74842

Figure 5S.-5. Tafel Fitting for MEA C.



	Air (pO ₂ = 0.124 atm)		O ₂ (pO ₂ = 0.62 atm)		Calculated pO ₂ = 1 atm	
T (°C)	i _o (pO ₂) ^γ	α	i _o (pO ₂) ^γ	α	i _o (A/m ² Pt)	γ
240	0.00278	0.7127	0.01086	0.66494	0.01628	0.846
250	0.01304	0.68672	0.0503	0.6376	0.02617	0.83879

Figure 5S.-6. The density of porous SAFC cathodes was measured by comparing the thickness of freestanding cathode films and their geometric surface area.

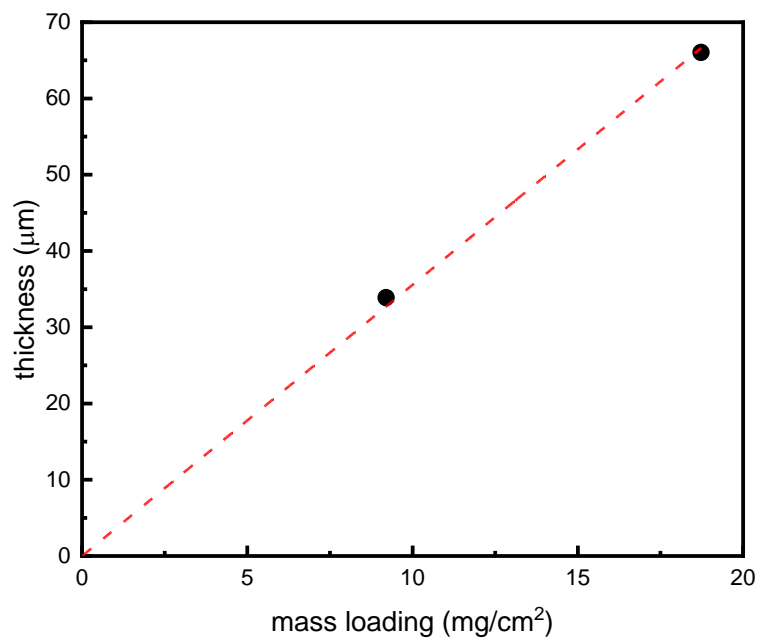
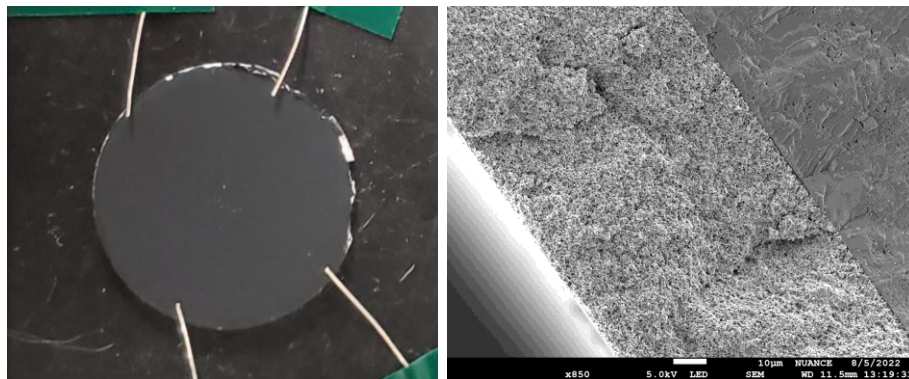


Figure 5S.-7. Measurement of electronic conductivity in porous SAFC cathode through the Van der Pauw method.



Van der Pauw resistance measurements were collected using a Keithley Potentiostat. Four silver wires were placed along the perimeter of the porous cathode as shown in Figure 5S.-2a. The wires were contacted to the porous cathode by pressing down firmly using a glass slide until the resistance value reached a minimum. Bias was applied between two of the wires and a current response was measured between the other two. The resistance produced by taking the ratio of the bias applied between wires C and D and the current measured between wires A and B is termed $R_{AB,CD}$. A subsequent measurement was taken by switching the role of each wire without moving the placement of the wires on the cathode such that the new resistance is $R_{BC,DA}$. The resistivity of the porous cathode can then be calculated using these two resistances and the thickness of the cathode t , as determined by cross-sectional SEM, from the following equations:

$$\rho = \frac{\pi t}{\ln 2} \frac{R_{AB,CD} + R_{BC,DA}}{2} f$$

where f is a value that satisfies the equation

$$\cosh \left\{ \frac{\ln 2 \frac{R_{AB,CD} - 1}{R_{BC,DA}}}{f \frac{R_{AB,CD} + 1}{R_{BC,DA}}} \right\} = \frac{1}{2} e^{\ln 2 / f}$$

The resistance values collected at room temperature were 32.6 and 88.57 Ω and the measured cathode thickness was 76 μm . f was solved to have a value of 0.9212, which then produced a resistivity of 1.92 $\Omega \text{ cm}$ at room temperature.

The resistivity at room temperature was then thermally corrected to 250 $^{\circ}\text{C}$ using the following linear correction:

$$\rho = \rho(T_0)(1 + \alpha\Delta T)$$

With a resistivity correction factor α for Pt of $3.93 * 10^{-3} \text{ }^{\circ}\text{C}^{-1}$. The temperature corrected conductivity of the porous cathode was 27.6 S m^{-1} .

Table 5S.-1. Calculation methods for gas diffusion coefficients.

Gas diffusion coefficients were extracted from data provided in Fundamentals of Momentum, Heat and Mass Transfer, 5th edition, by Welty, Wicks, Wilson, and Rorrer¹⁴² and Diffusion: Mass Transfer in Fluid Systems by Cussler¹⁴⁵. Binary diffusion coefficients were collected for oxygen, nitrogen, and steam at reference temperature and pressure, T_0 and P_0 respectively, which were in most cases standard temperature and pressure. The Hirschfelder correlation was then applied to correct these diffusion coefficients to operating temperature and pressure, 250 °C and 1 atm.

$$D_{c,d}(T_i, P_i) = D_{c,d}(T_o, P_o) \left(\frac{P_o}{P_i} \right) \left(\frac{T_i}{T_o} \right)^{3/2} \frac{\Omega_{D,T_o}}{\Omega_{D,T_i}}$$

These reference binary diffusion coefficients, $D_{c,d}(T_o, P_o)$, were taken from Table J.1 in Fundamentals of Momentum, Heat and Mass Transfer and are listed below. All values are provided in units of cm^2/s and correspond to a reference pressure of 1 atm, and reference temperatures as listed.

$D_{c,d}(T_o, P_o = 1 \text{ atm})$	Oxygen	Steam	Nitrogen
Oxygen	-	0.260 (298 K) H ₂ O in air ¹⁴² 0.282 (308.1 K) ¹⁴⁵	0.181 (273 K)
Steam		-	0.260 (298 K) H ₂ O in air ¹⁴² 0.293 (298.2 K) ¹⁴⁵
Nitrogen			-

The Hirschfelder correlation was then applied to correct these diffusion coefficients to operating temperature and pressure, 250 °C and 1 atm.

$$D_{c,d}(T_i, P_i) = D_{c,d}(T_o, P_o) \left(\frac{P_o}{P_i}\right) \left(\frac{T_i}{T_o}\right)^{3/2} \frac{\Omega_{D,T_o}}{\Omega_{D,T_i}}$$

Where $T_i = 250$ °C, $P_i = 1$ atm, and $\Omega_{D,T}$ is the collision integral of the gas. The collision integral is obtained from Table K.1 and is dependent on the Lenard-Jones potential of the binary mixture, kT/ε_{cd} . The Lenard-Jones parameter of the binary mixture, ε_{cd} , is calculated from the Lenard-Jones force constants of each species, ε_c and ε_d , using the following equation.

$$\varepsilon_{cd}/k = \sqrt{\left(\frac{\varepsilon_c}{k}\right)\left(\frac{\varepsilon_d}{k}\right)}$$

The individual Lenard-Jones force constants were extracted from Table K.2.¹⁴²

ε_{cd}/k (K)	Oxygen	Steam	Nitrogen
Oxygen	113	200.6	101.7
Steam		356	180.5
Nitrogen			91.5

$\frac{\Omega_{D,T_o}}{\Omega_{D,T_i}}$	Oxygen	Steam	Nitrogen
Oxygen		1.2048/0.9870 =1.2207	0.97916/0.922616 =1.0613
Steam			1.1527/0.95784 = 1.2035
Nitrogen			

$D_{c,d}$ ($T_i = 250$ °C, $P_i = 1$ atm) (cm ² /s)	Oxygen	Steam	Nitrogen
Oxygen	-	0.8416 0.7609 ¹⁴⁵	0.5093
Steam		-	0.8297 0.8190 ¹⁴⁵
Nitrogen		-	-

Appendix A: Transmission Line Modeling of Impedance from SAFC Cathodes

Impedance spectra of the SAFC studied in Chapter 5 were collected at various cell potentials (OCV, 0.8, 0.7, 0.6, 0.4 V) as shown in Figure A.1. The spectra take the shape characteristic of porous electrodes in which a near 45° slope is observed at high frequencies and a bias-dependent charge transfer arc is observed at low frequencies. The charge transfer contribution is observed to shrink drastically with applied bias.

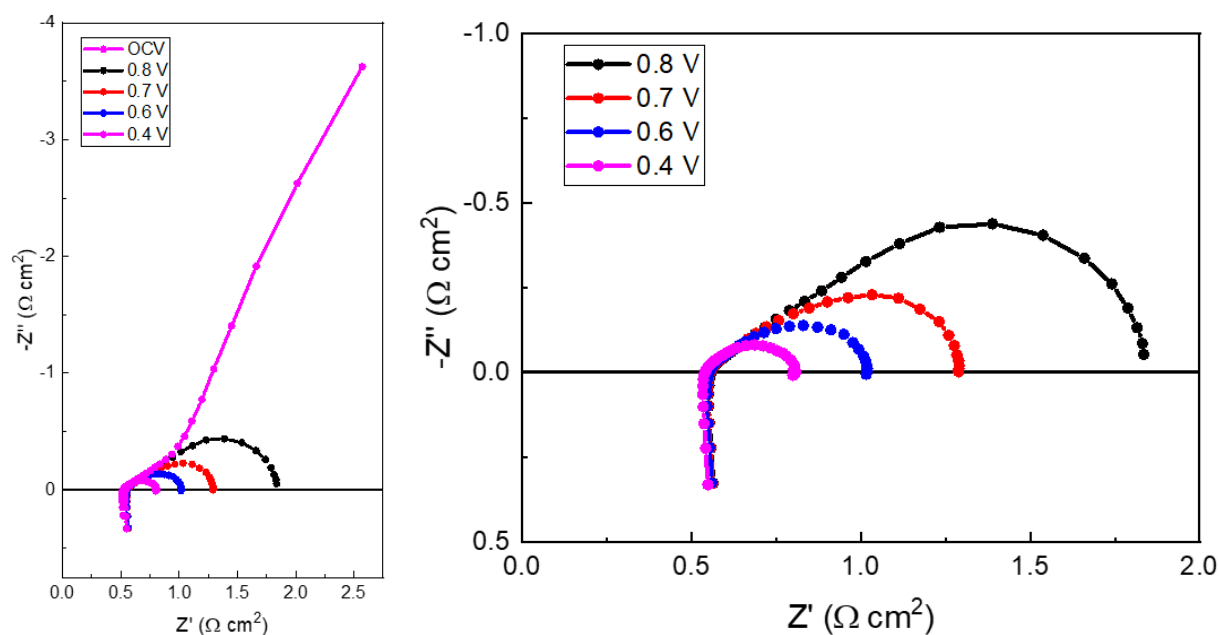


Figure A.1. EIS spectra collected from the SAFC studied in Chapter 5 at various cell potentials. The spectra were collected under humidified air- H_2 ($p_{H_2O} = 0.38$ atm) supplied to the cathode and anode respectively.

The impedance response of porous electrodes is frequently modeled using a transmission line model (TLM) described by two parallel rails carrying protonic and electronic current

connected by charge transfer “rungs”. The model is described in more detail in Chapter 4.5.3 but is summarized here in Figure A.2 and below:¹³⁴⁻¹³⁶

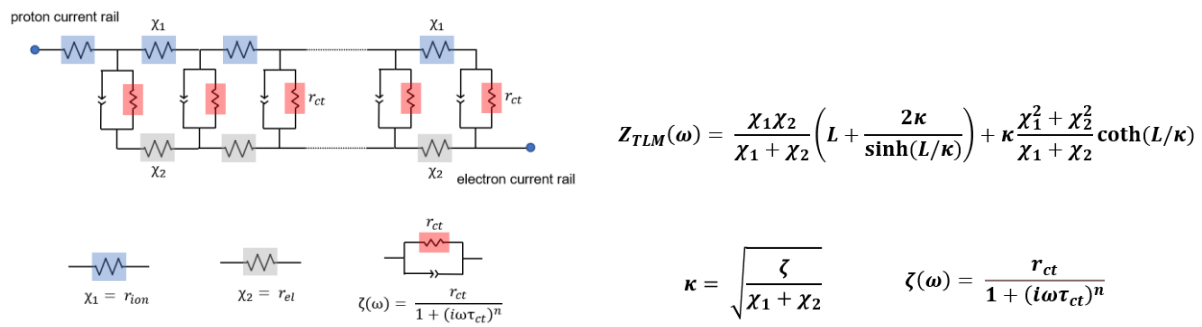


Figure A.2. Summary of the transmission line impedance model.

- r_{ct} is the differential charge transfer resistance ($\Omega \text{ m}$). It can be calculated from the values measured here in this study using:

$$r_{ct} = \frac{R_{ct}}{A_r * A}$$

Where A is the geometric area of the electrode (m^2) and R_{ct} is the Pt specific charge transfer resistance ($\Omega \text{ m}^2_{\text{Pt}}$) calculated as

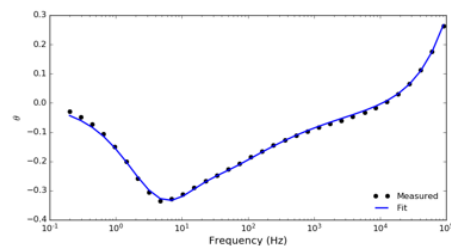
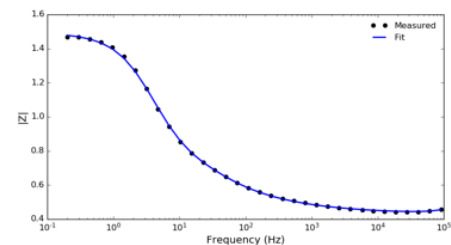
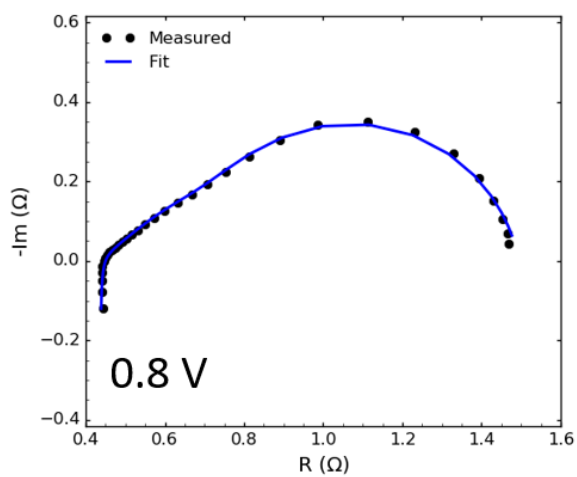
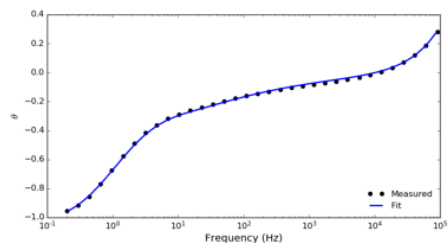
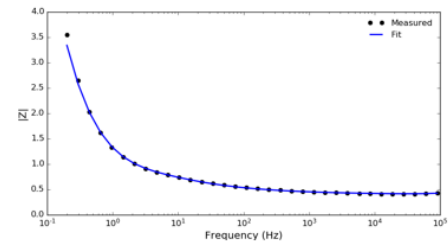
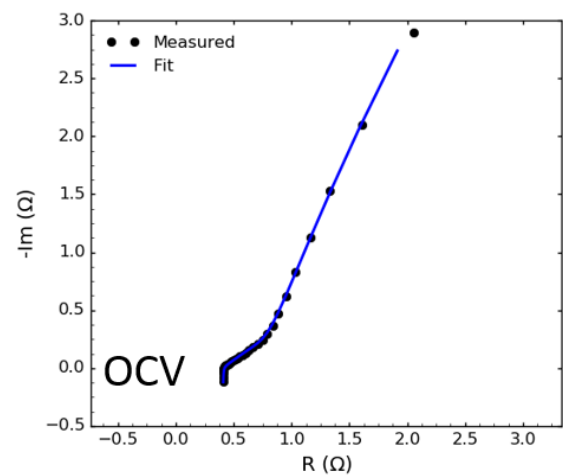
$$R_{ct} = \frac{RT}{F i_0 (C_{O_2}/C_{O_2}^*)^\gamma}$$

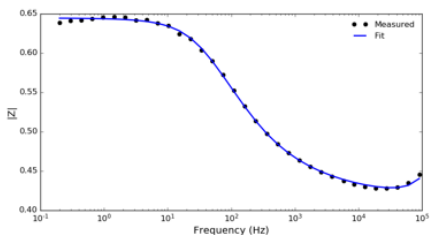
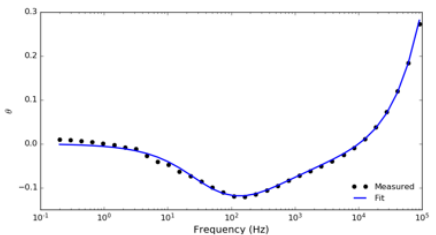
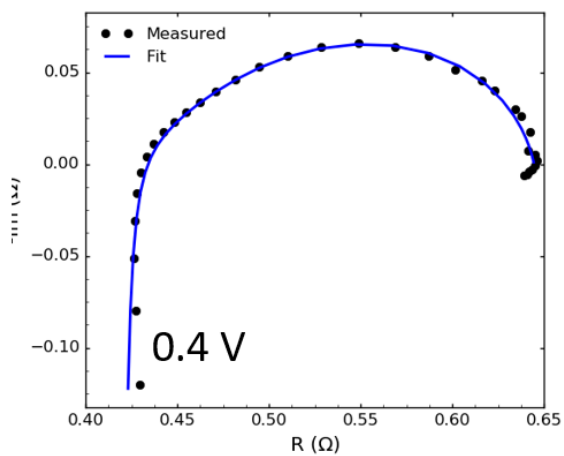
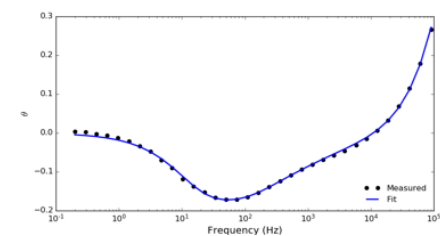
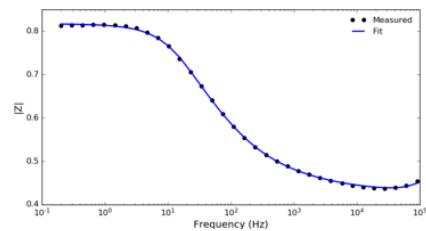
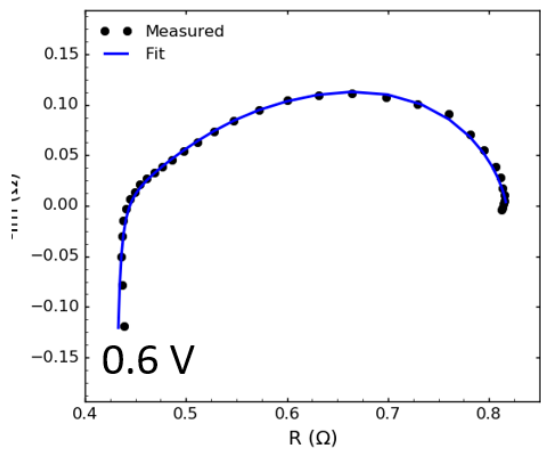
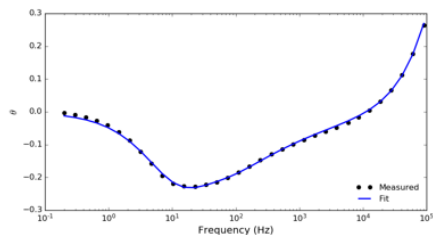
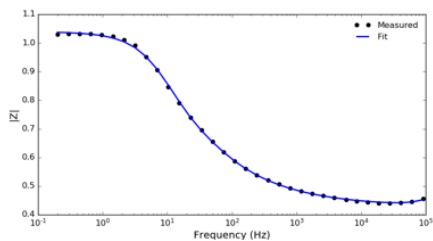
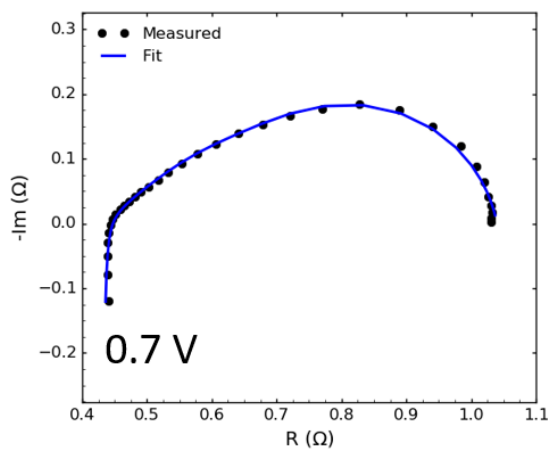
- τ_{ct} is the time constant of the CPE representing the double layer capacitance and n is the standard CPE exponent.
- L is the thickness of the porous cathode.
- χ_1 and χ_2 are the area-normalized effective resistivities of the ionic and electronic conductors ($\Omega \text{ m}^{-1}$). The values are calculated by dividing the effective resistivities ($\Omega \text{ m}$) by the geometric area of the electrode.

$$\chi_i = 1/(\sigma_i^* * A)$$

An equivalent circuit model for the SAFC was created by joining the TLM in series with a resistor and an inductor. The model was used to fit the impedance spectra in Figure A.1 and the results are shown in Figure A.3.

Figure A.3. Impedance spectra collected at various cell potentials fit using a transmission line model (TLM) in series with an inductor and a resistor. For the spectra collected at each potential, the Nyquist and Bode plots are shown.





The spectra are remarkably well fit by the model especially considering the approximations taken to represent the electrochemical kinetics. In each fit spectra, the reduced Chi square error is less than 10^{-4} . The fit TLM parameters are summarized in Table A.1 and compared to the parameter values implemented in the 1D SAFC modeling (Chapter 5). While the ability of the TLM to fit the experimental data is impressive, interpretation of the physical meaning of the fit parameters should be done with caution. A critical limitation of the TLM is the modeling of the electrochemical reaction using a consistent RQ circuit throughout the length of the electrode. This method of modeling is justifiable at OCV because the Taylor series expansion of the Butler-Volmer equation around $\eta = 0$ produces a linear I-V response that can be approximately modeled using a RQ circuit. However, the validity of this approach quickly breaks down away from OCV, where the electrochemical kinetics are exponential in relation to overpotential. The approximation of a constant RQ element fails to capture the evolving local reaction rate behavior through the electrode. Additionally, the TLM model implemented makes no consideration for gas diffusion or the impact of oxygen concentration on reaction kinetics. In theory, interpretation of the TLM fit parameters from spectra at OCV should be valid. However, the measurements at OCV are the most impacted by experimental errors and complications. Firstly, the spectra at OCV are the least complete as the charge transfer arc is only partly captured. Secondly, leak currents are more dominant of the current response at OCV. Thirdly, at OCV the platinum catalyst is likely oxidized, altering the catalytic effect. These errors can obfuscate the assessment of reaction kinetics but should still allow for measurement of the effective conductivities.

There are several notable trends in the fit parameters. r_{ct} is clearly observed to decrease with lower cell potentials as expected from the activation of the charge transfer kinetics. χ_1 and χ_2 also display monotonic trends with cell potential, decreasing and increasing with lower potential respectively. However, these values would ideally be constant across the fit spectra as the charge transport properties do not evolve as a function of potential. The proton conductivity implemented in the 1D model lies within the range determined by the EIS fitting here but appears to be on the high end. Conversely, the electron conductivity appears to be too low in comparison to the fit values, but given that this value is significantly higher than the proton conductivity in any case the potential impact of an error here is negligible. The conductivity values determined from the fitting of the spectra at OCV and 0.8 V were evaluated using the 1-D model where all other model parameters were maintained at the values determined in Chapter 5. The 1-D modeling illustrates that the reduced proton conductivity values suggested by the TLM fitting act to slightly decreased the predict cell performance.

Table A.1. Fit TLM parameters from the impedance spectra measured at the specified cell potentials. The fit values are compared to parameter values used in the 1D modeling.

	1D model	OCV (1.02 V)	0.8 V	0.7 V	0.6 V	0.4 V
χ_1 ($\Omega \text{ m}^{-1}$)	6860	12600	10500	9200	8200	5900
σ_{CDP}^* (S m)	1.15	0.633	0.763	0.874	0.98	1.4
χ_2 ($\Omega \text{ m}^{-1}$)	290	$4 \cdot 10^{-10}$	140	100	100	0.05
σ_{Pt}^* (S m)	27.6	$2 \cdot 10^{13}$	56	70	70	10^5
r_{ct} ($\Omega \text{ m}$)	$2.1 \cdot 10^{-3}$	$3.5 \cdot 10^{-3}$	$6.63 \cdot 10^{-5}$	$3.24 \cdot 10^{-5}$	$1.72 \cdot 10^{-5}$	$8.4 \cdot 10^{-6}$
$A_r i_0 (pO_2)^y$ (A/m^3)	$1.7 \cdot 10^5$	$1.0 \cdot 10^5$	$5.43 \cdot 10^6$	$1.11 \cdot 10^7$	$2.09 \cdot 10^7$	$4.3 \cdot 10^7$
τ_{ct} (s)	-	140	0.29	0.0991	0.0458	0.0186
n	-	0.786	0.876	0.879	0.874	0.87

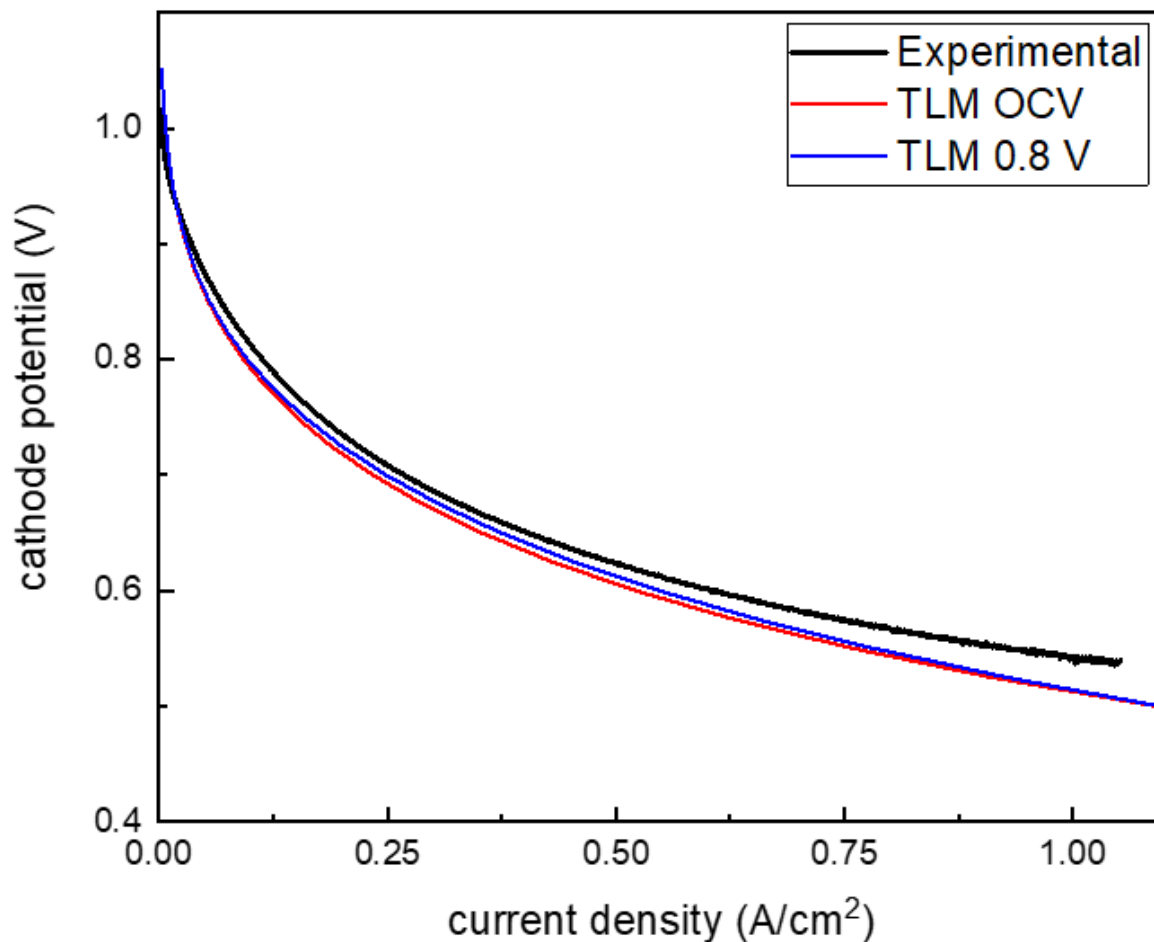


Figure A.4. Comparison of the modeled polarization curves using proton and electron conductivity values determined from the TLM fitting of EIS spectra at OCV and 0.8 V. The model reflects predicted behavior under humidified air-H₂ (pH₂O = 0.38 atm), and the corresponding experimental SAFC measurement is shown for reference.

Appendix B: Stabilizing Pd catalysts with Oxide Barrier Layers

B.1 Background

Since as early as 2009, it has been known that PdPt alloy ORR catalysts exhibit superior but fleeting performance compared to Pt catalysts.^{99,104,105} Fuel cells employing PdPt alloys at the cathode demonstrated remarkable performance over the first few hours of operation, ~400 mA/cm² @0.6 V vs 200 mA/cm² with Pt, however the performance rapidly decayed over the course of 12 hrs to be significantly worse than that of Pt. The rapid degradation is attributed to the reaction of Pd with CDP forming water soluble Pd phosphates which were characterized using both solid state ³¹P MAS NMR and solution NMR.¹⁰⁵ Nevertheless, the results are encouraging as they demonstrate that higher catalyst activity and fuel cell performance can be achieved with PdPt catalysts; the challenge is now to stabilize these catalysts with CDP to maintain the initial performance.

In this work, we aimed to stabilize PdPt catalysts with CDP by introducing a thin film oxide barrier layer between the two phases. In this approach, a thin film oxide coating would be applied to CDP powders using atomic layer deposition (ALD) prior to catalyst deposition in order to prevent contact between the catalyst and CDP. In using ALD, a very thin film of oxide can be conformally coated onto the CDP powders such that proton transport resistance can be minimized through the film while ensuring encapsulation. In this work, TiO₂ and Ta₂O₅ were selected as barrier layers because of the ease with which these oxide can be deposited by ALD and the stability of these oxides with CDP. Ultimately it was found that while TiO₂ was capable of preventing the degradative reaction, whereas Ta₂O₅ was not, the introduction of the barrier

layer significantly reduced the performance of the cathode. The methods developed here are still instructive for the characterization and fabrication of SAFCs.

B.2 Stabilizing Pd

In order to create cathode particles with the target dual layer nanostructure, an oxide barrier was first deposited onto CDP particles using ALD and then an exterior layer of catalyst nanoparticles was deposited atop the oxide coating using MOCVD (Figure B.1).

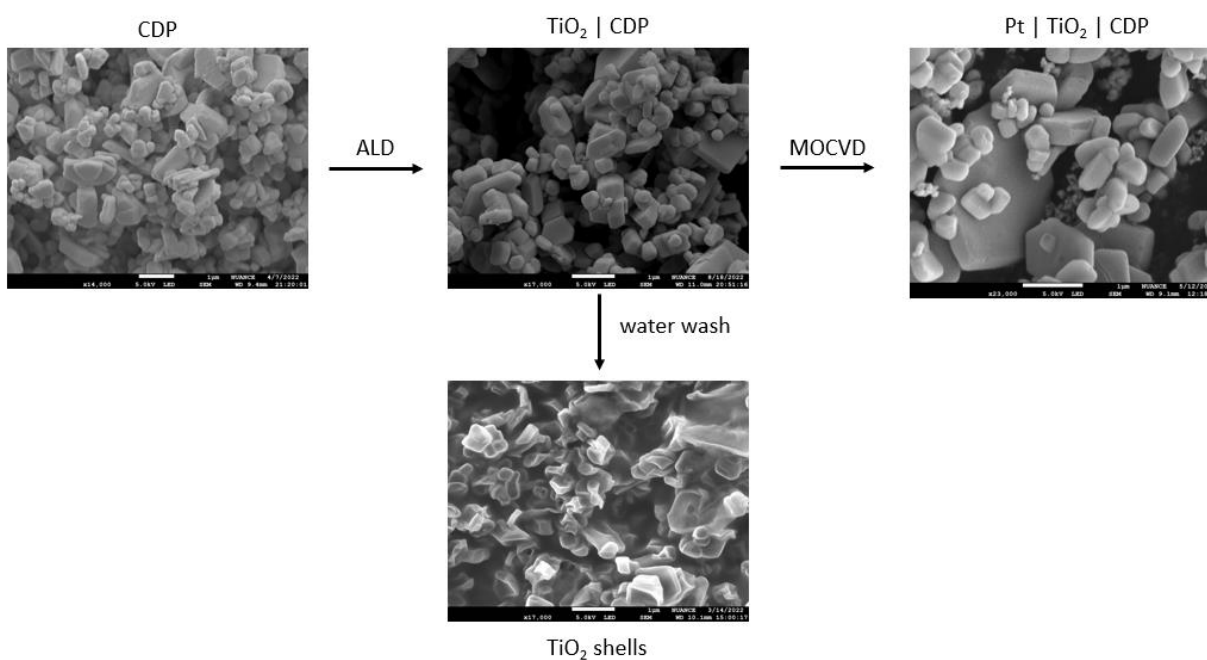


Figure B.1. SEM images of powders after each stage of the process to create catalyst | oxide | CDP particles. In each of the images, aside from the post-MOCVD image, the samples were treated with 25 nm of Ag by sputtering to reduce charging effects in the SEM. The base particles of CDP are shown on the left. Particles coated with 7.5 nm of TiO₂ by ALD are shown in the top center image. The bottom center image shows the TiO₂ coated particles after washing with water. The CDP has been dissolved, but the TiO₂ coating remains visible. The rightmost image shows TiO₂ | CDP particles coated with Pt nanoparticles using MOCVD, which creates a fuzzy white film on the surface of the particles.

Atomic layer deposition (ALD) of TiO_2 and Ta_2O_5 was conducted using an Arradiance GEMStar XT-P instrument equipped with a powder tumbler. 200 mg of fine CDP were loaded into a powder tumbler that was then attached to the Arradiance instrument. In the deposition of both oxides, the stage and door temperatures were set to 150 °C. In order to achieve complete surface coverage of the powders the tumbler was rotated throughout the deposition and a pseudo exposure mode deposition procedure was implemented. The pseudo exposure mode deposition involved momentarily closing the vacuum valve during precursor pulses and repeatedly pulsing each precursor several times before introducing the next precursor. The metal precursors for TiO_2 and Ta_2O_5 deposition were tetrakis(dimethylamino)titanium (TDMAT), heated to 65 °C, and tris(diethylamido)(tert-butylimido)tantalum (TBTDET), heated to 115 °C, respectively. The oxidant in both cases was steam. The pulse sequences for each oxide deposition are shown in Figure B.2 below. The ALD growth rates were calibrated using XRR on films deposited on standard Si substrates and found to be 0.59 Å/cycle and 0.87 Å/cycle for TiO_2 and Ta_2O_5 respectively.

The microstructure of the oxide coated CDP particles and of the oxide films themselves were visualized using SEM. Oxide coated particles were dispersed on carbon tape on an SEM stub. The oxide films were isolated by dissolving the CDP interior which was achieved by dropping a droplet of water atop the carbon tape, allowing dissolution to occur for a few seconds before pouring off the water droplet. The process of adding and removing water droplets was repeated several times to ensure dissolution. The sample was then dried in an 85 °C oven for several hours. Silver sputtering was applied to both oxide | CDP particles and isolated oxide shells, depositing ~25 nm of Ag, in order to mitigate charge effects in the SEM. The SEM

images of the oxide | CDP particles reveal that the particle morphology is unchanged by the ALD process. The SEM images of the samples in which CDP was dissolved reveal oxide shells similar in size and shape to the original CDP particles. A majority of the oxide shells appear deflated, indicating that the CDP interior was indeed dissolved. It is unclear whether the solubility of the CDP interior is indicative of an incomplete oxide coating.

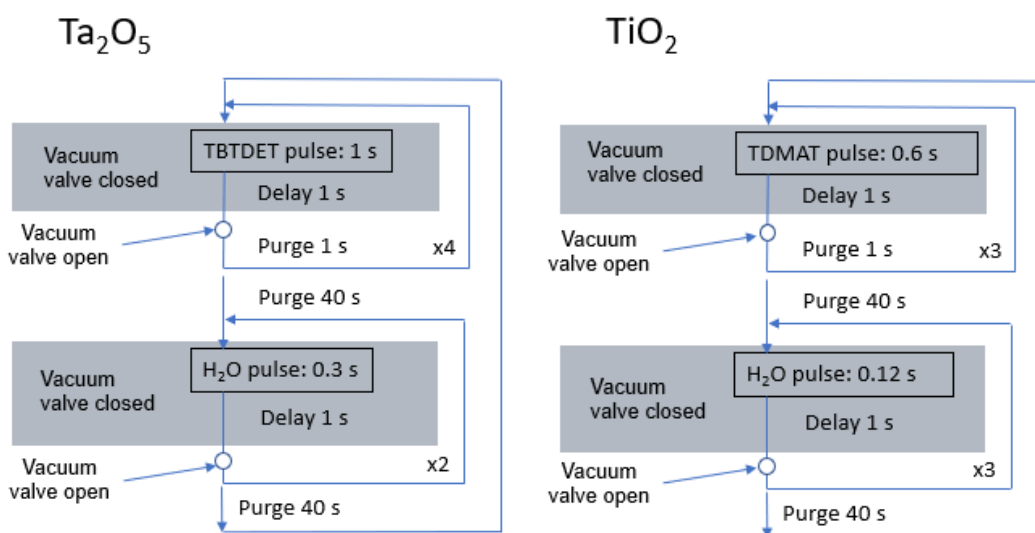


Figure B.2. ALD pulse sequences Ta_2O_5 and TiO_2 deposition. The sequences shown represent one cycle. There was a 0.1 s delay between the closing of the vacuum valve and the pulse of each precursor.

The stability of Pd | oxide | CDP powders were investigated by examining the ^{31}P NMR spectra of samples annealed at cathodic operating conditions. Two oxide coated CDP powder samples were produced by depositing 7.5 nm of TiO_2 and 10 nm of Ta_2O_5 independently on CDP powders. Pd nanoparticles were deposited on oxide coated and uncoated CDP powders using the MOCVD approach described in Chapter 5. The Pd mass loading for each sample was 14 wt%, 8 wt% and 8 wt% for the TiO_2 , Ta_2O_5 , and uncoated CDP samples respectively. The powders were

then annealed at 250 °C under humidified air ($p_{\text{H}_2\text{O}} = 0.38 \text{ atm}$) for 24 hrs. The stability of the Pd | oxide | CDP powders were determined by ex situ solid state NMR conducted on a 400 MHz Bruker Avance III HD 400 system equipped with a HX solid probe. After cooling to room temperature, the powders were packed into a 4 mm zirconia rotor and inserted into the NMR probe. The samples were spun at 12.5 kHz MAS and the ^{31}P spectra were collected using a simple zg experiment ($p1 = 3 \mu\text{s}$, $p1w1 = 104 \text{ W}$). Delay times were varied between 1 – 100 s.

The ^{31}P NMR spectra of the annealed Pd | CDP sample captured with various delay times are shown in Figure B.3. The anticipated phosphorus resonance of CDP is observed around -5 ppm. However additional resonances are observed between -5 – 10 ppm, indicative of reaction products between Pd and CDP, consistent with those observed by Papandrew et al.¹⁰⁵ The spectra in Figure B.3 have been renormalized to the maximum intensity, and the changes in intensity reflect a growing CDP resonance with increasing delay times as is anticipated by the phosphorus' T_1 of ~500 s,⁶⁷ whereas the intensity of the reactions products are relatively unchanged. The T_1 of the reaction products is therefore likely a few seconds.

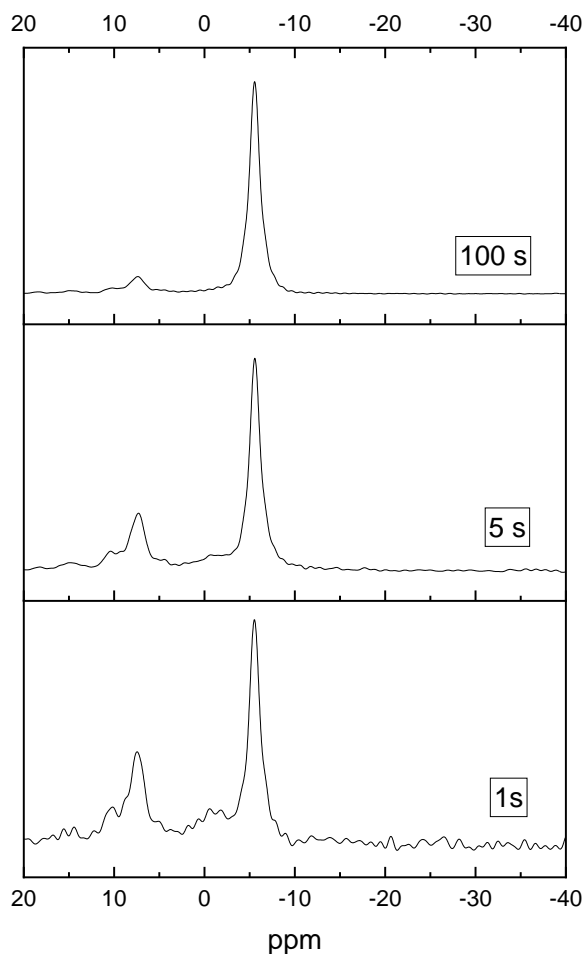


Figure B.3. ^{31}P NMR spectra of annealed Pd | CDP samples captured with the indicated delay times.

The ^{31}P NMR spectra shown in Figure B.3 for the Pd | oxide | CDP samples after annealing reveal that the TiO_2 oxide barrier layer was effective at preventing the reaction between Pd and CDP whereas the Ta_2O_5 layer was not. The Pd | TiO_2 | CDP spectra features only the CDP resonance with no new features associated with reaction products. In both the Pd | TiO_2 | CDP and standard CDP spectra there is a broad feature around -5 ppm that we believe to be attributed to an impurity introduced during sample synthesis or prep. In the Pd | Ta_2O_5 | CDP

sample, several new resonances are observed that were not present in the Pd | CDP sample, indicating that Ta is involved in the reaction products.

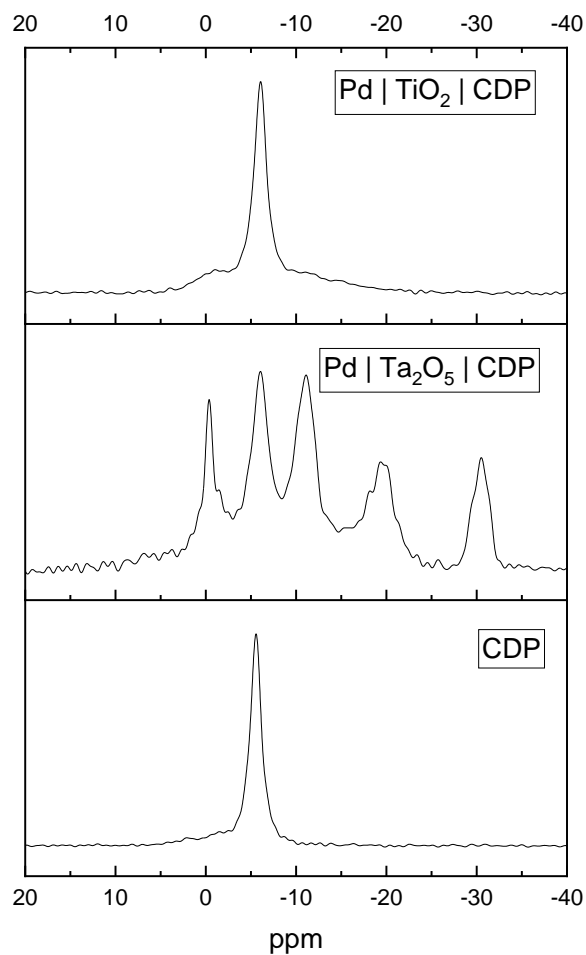


Figure B.4. ^{31}P NMR spectra of Pd | TiO₂ | CDP and Pd | Ta₂O₅ | CDP samples after annealing at 250 °C. The delay time for the TiO₂ spectra was 20 s whereas it was 1 s for the Ta₂O₅ and standard CDP samples.

B.3 Flat Cathodes

Having demonstrated that TiO₂ is capable of stabilizing Pd catalysts on oxide coated CDP particles, it was then appropriate to study the impact of introducing a TiO₂ layer on the electrochemical kinetics at the cathode. Focusing on electrochemical kinetics, we first study the impact of TiO₂ barriers in a flat cathode geometry in order to avoid the complications associated with complex microstructures in porous cathodes.

Flat cathodes were deposited on polished CDP pellets, fabricated using the methods described in Figure 5S.-2. For cathodes featuring TiO₂ barrier layers, the CDP pellet electrolyte was coated with TiO₂, independent of the anode and PTFE sealant, using the same ALD procedure described above for coating CDP powders. Catalyst films were then deposited on the cathodic face of the pellet either using the MOCVD approach described in Chapter 5 or DC sputtering. Sputtered catalyst films had a total target thickness of 15 nm. Sputtering was done on an Aja Orion sputter coater; the system was pumped down to 1.5e-5 Torr before sputtering and then operated at 25 W sputtering power at a base pressure of 3 mTorr with Ar leak gas. The sputtering rates of Pt and Pd were calibrated using XRR measurements on films sputtered on sapphire substrates; the rates for Pt and Pd were determined to be 0.023 nm/s and 0.041 nm/s respectively.

Flat cathode cells were then fabricated by joining the pellet with an anode supported on a gas diffusion layer (GDL) and sealing the two components together with PTFE tape. The procedure was largely identical to that described in Figure 5S.-2; however the procedure of isostatically pressing the MEA to seal the PTFE was developed during this work, and therefore some cells were isostatically pressed whereas others were sealed by uniaxially pressing to try to adhere the PTFE to the cathode face of the pellet. It was found during the development of these

procedures that even lightly uniaxially pressing the pellet and anode together would often result in cracks in the pellet. The occurrence of the cracks perhaps explains the low OCVs in several of the uniaxially sealed cells, but the issue was also observed in isostatically sealed cells.

We start by examining the performance of standard Pt cathode cells (Figure B.5). In both the cells that had sputtered and MOCVD Pt cathodes, there is an unsettling amount of variation in the observed performance. Despite my best efforts to eliminate variance in the sample preparation process, I was not able to achieve a convergence in cell performance. Possible factors contributing to variations in performance are poor sealing across the cell and imperfections in the polished cathode surface of the cell resulting in higher surface areas. Despite the high degree of variance in the data, there does appear to be a plurality of agreement in the performances from cells 97, 105, and 112.

The cells with sputtered cathodes were operated in humidified ($p_{\text{H}_2\text{O}} = 0.38 \text{ atm}$) H_2 – air environments at $250 \text{ }^\circ\text{C}$. The sputtered cathode cells on the whole displayed lower OCVs compared to the MOCVD cathode cells, whether the cells were prepared by isostatically pressing to seal (cells 102, 103, and 105) or uniaxially pressing (Trevor, and 97). The low OCVs observed in the sputtered cathodes cells, generally $< 0.9 \text{ V}$, makes drawing conclusions about the electrochemical kinetics uncomfortable. It was later found that the OCV increased when the anodic gas stream was switched from H_2 to 10% H_2 in Ar, indicating that hydrogen crossover leaks were responsible for the low OCV. Therefore, in the measurements on the MOCVD flat cathode cells, the anode gas stream was humidified 10% H_2 . However, despite the higher OCVs achieved in the MOCVD flat cathode cells, the cell performances were no more consistent than

in the sputtered cells. Perhaps this is attributed to the less controlled nature of the MOCVD process compared to sputtering.

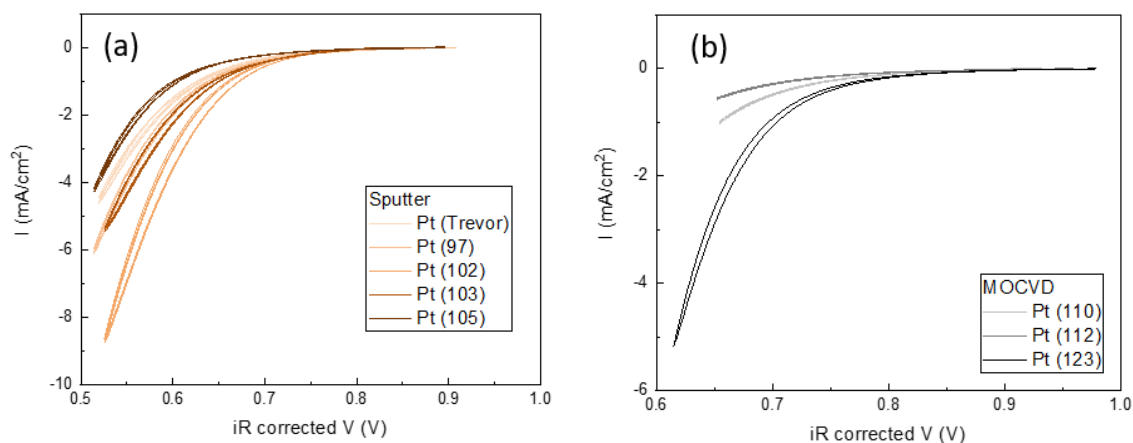


Figure B.5. Flat cathode cells with Pt catalyst films deposited either by (a) sputtering or (b) MOCVD. The values in parenthesis are my own internal identifiers.

The influence of a TiO₂ barrier layer on the activity of the Pt catalyst was examined (Figure B.5). Given the spread in the Pt cathode data and the singularity of the Pt | TiO₂ result here, it is not possible to make definitive conclusions about the impact of the TiO₂ layer. Comparing the polarization curves of cells 96 and 97, it appears that 7.5 nm of TiO₂ had minimal impact on the activity of a sputtered Pt film catalyst. However, an examination of the EIS spectra from the two cells reveals that the TiO₂ results in a new low frequency arc likely attributed to interfacial resistance arising from the TiO₂ layer. The spectra from the Pt electrode reveal only a single charge transfer arc, fit using an RQ circuit, whereas the Pt | TiO₂ spectra required two RQ circuits to account for the interfacial impedance.

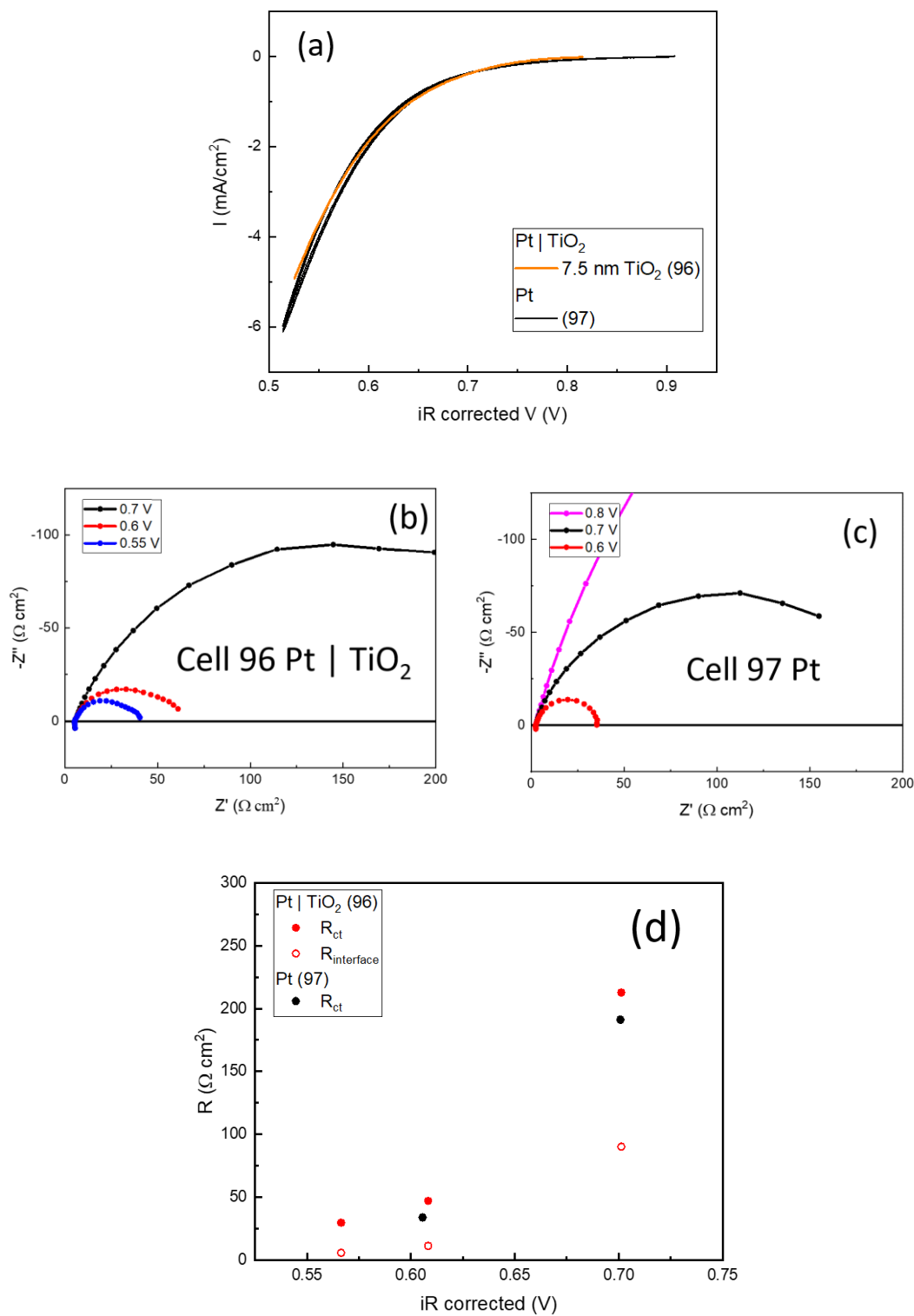


Figure B.5. (a) Comparison of the polarization curves collected from sputtered Pt flat cathodes with and without TiO₂ barrier layers. Cell 96 had 7.5 nm of TiO₂ deposited by ALD on the CDP

pellet electrolyte prior to Pt sputtering. EIS spectra collected from (a) cell 96 and (b) cell 97. (c) Comparison of the fitted resistance values from the two cells.

Next, cells with Pd-Pt bilayer catalyst films and TiO₂ barrier layers were examined. The TiO₂ layers were deposited by ALD on the CDP pellets in the same manner as in the previous Pt | TiO₂ cell (cell 96). In this case Pd-Pt bilayer catalyst films were deposited by subsequently sputtering Pd and Pt films, one atop the other. The overall composition of the film was selected to be 84 atomic % Pd and 16 atomic % Pt because this composition was identified by Papandrew et al as demonstrating the highest activity.¹⁰⁵ However, under SAFC operating conditions, the metallic films are not anticipated to form a solid solution, and thus the bilayer films are not expected to perform identically to the Pd-Pt alloys synthesized by MOCVD. The total catalyst film thickness was maintained at 15 nm with 12.6 nm of Pd and 2.4 nm of Pt. In cells 109 and TW01, the Pt film was sputtered first, followed by the Pd film. In cell 115 the order of the sputtering was reversed such that the Pt film was deposited on top of the Pd film. Each of the three cells was isostatically sealed.

In each of the Pd_{0.84}Pt_{0.16} | TiO₂ cathode cells, the performance was observed to improve in the chronopotentiometry/chronoamperometry data across the first 10 – 20 hrs before stabilizing. This is interpreted to mean that the TiO₂ has effectively prevented the reaction of Pd and CDP, as would be expected from the stability measurements of Pd deposited on oxide coated CDP powders. However, in each of the Pd_{0.84}Pt_{0.16} | TiO₂ cathode cells the polarization curves do not compare favorably with Pt at low cathode potentials or high overpotentials. There is surprisingly little downward curvature in the polarization curves of the Pd containing cathodes, which would translate to low alpha values in the Tafel framework. The Pd containing cathodes

all exhibited very low OCVs upon reaching operating temperature (< 0.8 V) and the OCV gradually increased to a value around 0.89 V over the course of the measurement. It is hypothesized that the low OCV is attributed to the oxidation potential of Pd, which is much more readily oxidized than Pt. However it would seem curious that the oxidation potential of Pd would increase over time, unless a less oxidation-prone Pd-Pt alloy was gradually forming in situ.

The near perfect agreement in the performances of cells 115 and TW01 is surprising given that the catalytic active sites are expected to be Pt in cell 115 and Pd in TW01. It has been suggested in aqueous systems that Pt skins on Pd should be more active than Pt alone for ORR.¹⁰⁷

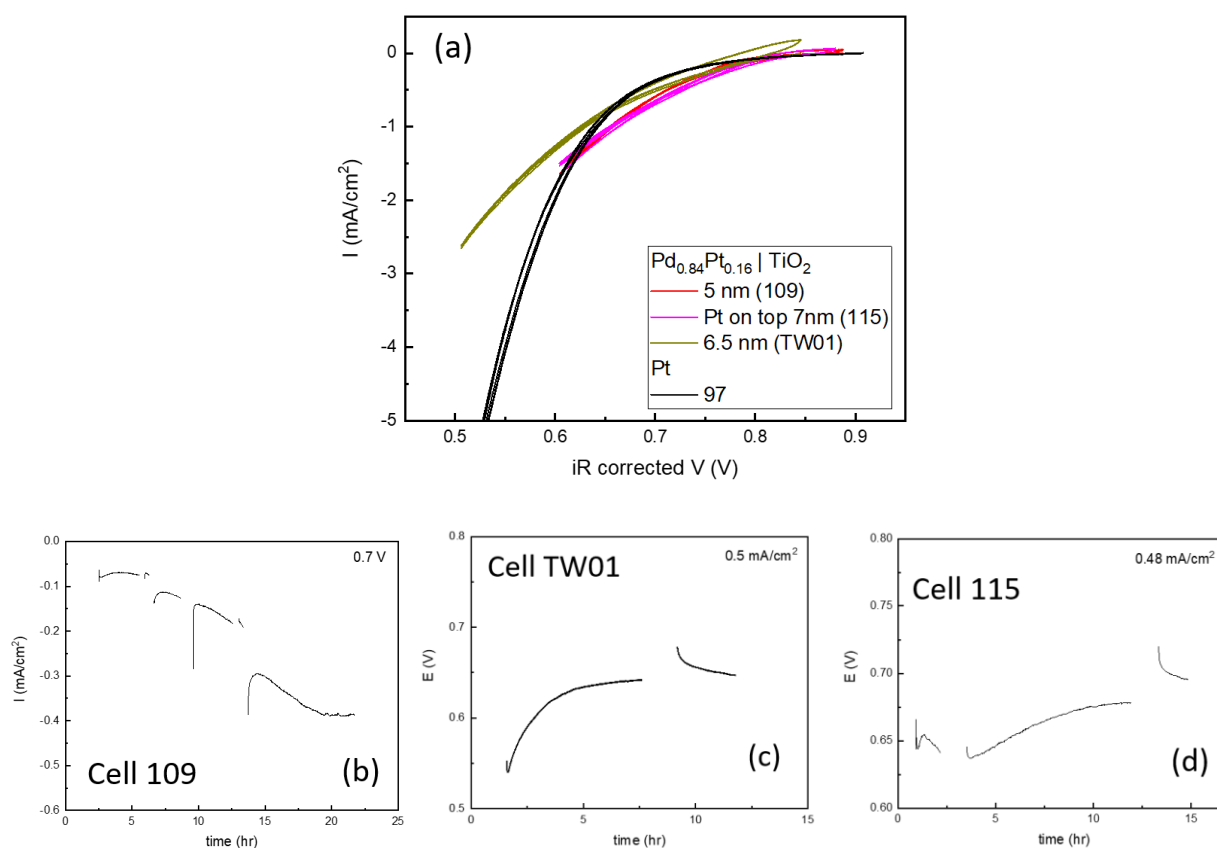


Figure B.6. (a) Comparison of the polarization curves of Pd_{0.84}Pt_{0.16} | TiO₂ flat cathodes with that of a standard Pt flat cathode. The thickness of the oxide layer is indicated in the legend. In cells

109 and TW01, the catalyst films were sputtered with the Pt layer first followed by the Pd layer. In cell 115 the order was reversed and Pd was deposited first. (b) Chronoamperometry from cell 109 at 0.7 V. (c) Chronopotentiometry from cell TW01 at 0.5 mA/cm². (d) Chronopotentiometry from cell 115 at 0.48 mA/cm².

The impedance spectra collected from the three Pd_{0.84}Pt_{0.16} | TiO₂ cells (cells 109, TW01, and 115) are shown in Figure B.7. The spectra are quite similar, both in form and magnitude. The spectra collected at 0.7 and 0.6 V can all be well fit using an RQ circuit, representing the charge transfer resistance, in series with a resistor, representing the ohmic resistance of the electrolyte. The additional interfacial resistance attributed to the TiO₂ barrier layer observed in the Pt | TiO₂ cathode (cell 96) is curiously not observed in these cathodes. The lack of interfacial resistance is especially odd considering that both the CDP – TiO₂ and TiO₂ – Pt interfaces are still present in cells 109 and TW01. Comparing the fit charge transfer resistances to those of a Pt catalyst (cell 97), it's clear that the R_{ct} values are higher for the Pd_{0.84}Pt_{0.16} | TiO₂ cathodes and less responsive to bias, consistent with the flatter polarization curves.

Thus while it appears that Pd has been stabilized by the TiO₂ barrier layer, the activity of the catalyst is now unfavorable in comparison to Pt. The lack of a distinct interfacial arc in the EIS spectra coupled with the observation of larger cathode resistances suggests that the inherent activity of the Pd_{0.84}Pt_{0.16} bilayer catalyst supported on TiO₂ is less than that of Pt.

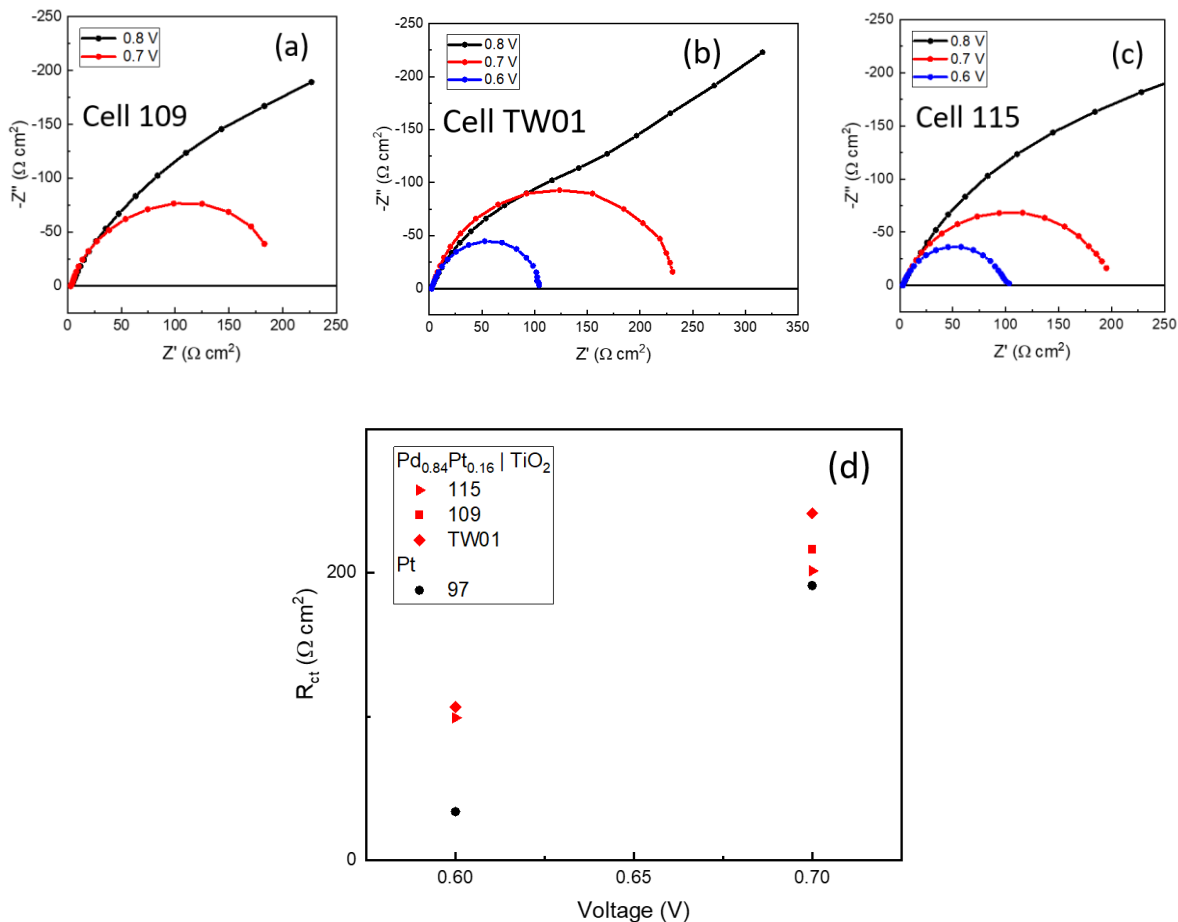


Figure B.7. (a-c) EIS spectra from cells with $\text{Pd}_{0.84}\text{Pt}_{0.16}$ | TiO_2 flat cathodes. (d) Comparison of the charge transfer resistance as fit from the spectra in a-c. The charge transfer resistance from a standard flat Pt cathode is shown for comparison.

A flat cathode cell was fabricated with a $\text{Pd}_{0.84}\text{Pt}_{0.16}$ | 3 nm TiO_2 cathode where the catalyst was deposited by MOCVD. The performance of the cell is shown in Figure B.8. The cell (cell 126) demonstrated a low OCV of 0.83 V, and the CV measurements in Figure B.8a were further restricted to an upper vertex potential of 0.75 V to prevent Pd oxidation on sweeping up the voltage. The chronoamperometry data in Figure B.8b reveals that the cell performance decreased over the first two hours of operation before then improving and eventually stabilizing

around 10 hrs. It is therefore unclear whether the TiO_2 film effectively prevented reaction in this cell.

The performance of $\text{Pd}_{0.84}\text{Pt}_{0.16} | \text{TiO}_2$ cathodes, both sputtered bilayer films and nanoparticle films, appears to be worse than Pt cathodes. It may be the case that the superior performance of the $\text{Pd}_{0.84}\text{Pt}_{0.16}$ catalyst demonstrated by Papandrew et al arose because of a reaction product or intermediate between Pd and CDP which temporarily boosted the activity of the catalyst. In the experiments here, the TiO_2 barrier layer may have prevented the reaction product formation and therefore no such increase in performance is observed.

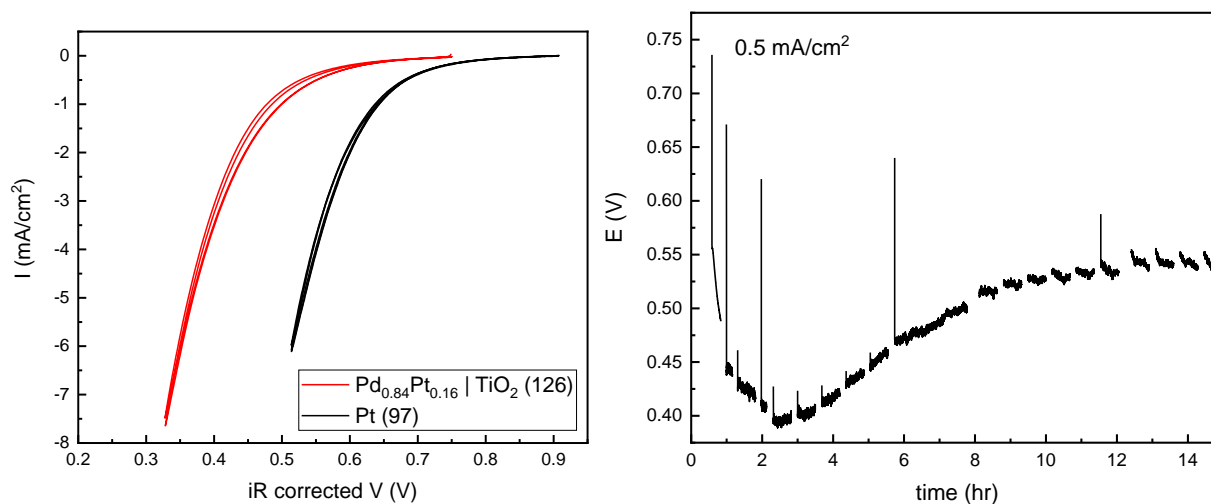


Figure B.8. (a) Polarization curve from cell 126 with a $\text{Pd}_{0.84}\text{Pt}_{0.16} | \text{TiO}_2$ cathode where the catalyst was deposited by MOCVD. The polarization curve of a sputtered Pt cathode cell (cell 97) is shown for comparison. (b) Chronoamperometry of cell 126 at 0.5 mA/cm^2 .

B.4 Porous Cathodes

Oxide barrier layers were also investigated in porous cathodes; however, first it is instructive to compare the performance of cathodes where the catalyst was Pt vs a PdPt alloy.

The synthesis of high activity PdPt alloy catalysts and the fabrication and operation of cells utilizing these catalysts turned out to be surprisingly nontrivial, and thus the lessons learned are described here.

PdPt alloys will begin reacting with CDP as soon as the particles are deposited.

Therefore, in order to observe the higher activity of PdPt alloys it is important that the reaction be kept to a minimum prior to fuel cell measurement. In performing MOCVD of PdPt alloys, it is very important to deoxygenate the deposition chamber as much as possible, as the presence of oxygen facilitates the degradative reaction between Pd and CDP. I would recommend pumping the chamber down to -660 mmHg and back filling with nitrogen at least five times prior to starting the deposition. Once the MOCVD has been done, it is important to measure the cathode powders as soon as possible, ideally the same day the deposition is completed. When measuring the cell, bring the cell up to operating conditions as quickly as possible to minimize the reaction occurring during ramping and only introduce air just before the measurement. During the heating stages, instead use nitrogen gas at the cathode. All fuel cell measurements were conducted at 250 °C with humidified ($p_{\text{H}_2\text{O}} = 0.38 \text{ atm}$) H_2 and air at the anode and cathode respectively.

Cathode powders with $\text{Pd}_{0.84}\text{Pt}_{0.16}$ catalyst nanoparticles were synthesized by MOCVD on CDP powders with gravimetric surface area of $3.5 \text{ m}^2/\text{g}$ to achieve a catalyst weight percent of 25.4%. The cathode powders were pressed onto a $\frac{3}{4}$ " standard SAFC half cell (anode and electrolyte layers supported on a stainless steel gas diffusion layer) at 1 ton for 3 s with a cathode loading of $19.0 \text{ mg}/\text{cm}^2$. The peak recorded performance of the cell (cell 80) is compared to a standard Pt catalyst cell in Figure B.9a. The polarization curve and $I@0.6 \text{ V}$ both reveal that cell 80 briefly exhibited superior performance to the standard Pt cathode cell. The Pt cell

demonstrated a $I@0.6\text{ V}$ of 230 mA/cm^2 , and so cell 80 achieved a superior $I@0.6\text{ V}$ for roughly the first hour of operation. The degradation of the $I@0.6\text{ V}$ occurred much more rapidly in cell 80 than reported by Papandrew for the same composition. I hypothesize that the degradation occurs more rapidly here because the CDP particles here are finer than those used in Papandrew et al. such that there is more surface area for the catalyst to react with CDP. It is likely the case that the polarization curve of cell 80 in Figure B.9a takes an odd shape with very little curvature at intermediate voltages because the cell is rapidly degrading during the measurement.

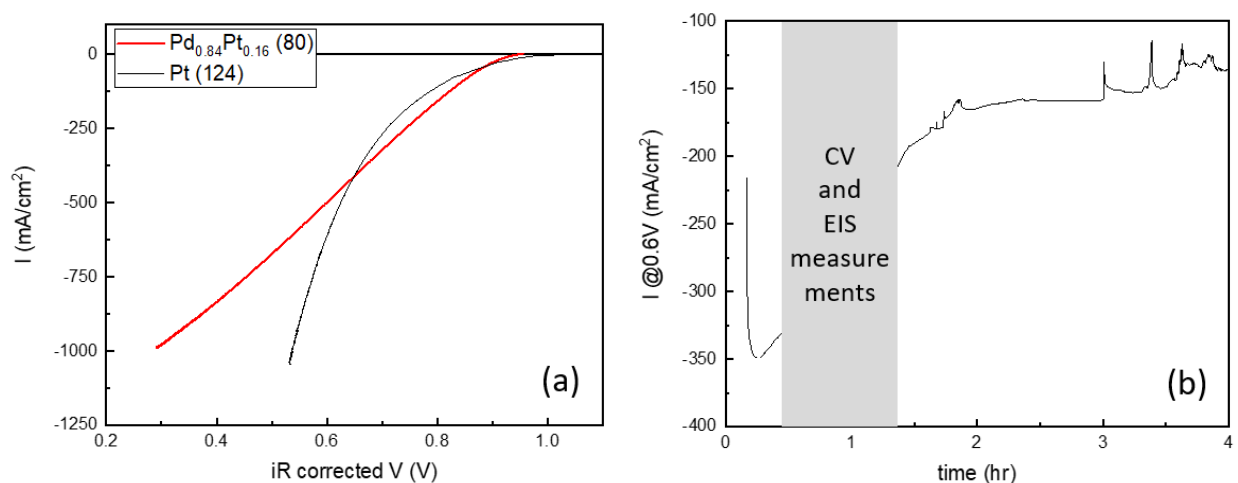


Figure B.9. Performance of cell 80 with $\text{Pd}_{0.84}\text{Pt}_{0.16}$ catalyst at the cathode. (a) Comparison of the polarization curve from cell 80 half an hour after the start of the measurement with the curve from a cell with the standard Pt cathode (cell 124). (b) Chronoamperometry measurements at 0.6 V. The shaded time period was used to collect CV data and EIS measurements at various biases.

We now examine cells with porous cathodes composed of catalyst | oxide | CDP particles. In order to stabilize Pd and prevent contact between CDP and Pd, it was also necessary to deposit an oxide thin film on the electrolyte layer. In order for the electrolyte to be amenable to vacuum deposition processes, such as ALD or PLD or sputtering, it was necessary to decouple the

electrolyte from the volatile components in the anode supported half cell. Thus a pellet CDP electrolyte was once again employed here in the cell geometry shown in Figure B.10. The cells were fabricated by pressing cathode powders onto the 3/4" pellet half cells at 1 ton for 3 s, where this uniaxial pressing step concurrently served to seal the PTFE tape to the pellet electrolyte. While uniaxially pressing the pellet electrolyte in the flat cathode cells was found to result in cracks through the electrolyte and low OCVs, the issue of low OCVs was curiously not observed in the porous cathodes. Difficulty in getting the cathode powders to adhere to the pellet electrolyte was frequently an issue, and to help address this issue in some instances the pellet face was lightly painted with a 10% polycarbonate in anisole solution to act as an adhesive. The anisole solvent was allowed to evaporate before spreading and pressing the cathode powders on the face of the pellet.

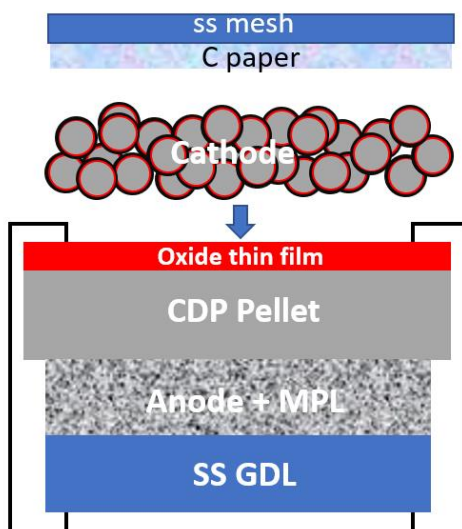


Figure B.10. Cell geometry employed in the measurement of catalyst | oxide | CDP cathodes.

Pt | TiO₂ | CDP cathode cells were fabricated using the procedure described above. Two different oxide thicknesses, 3 and 5 nm, were investigated – in both cases the CDP powders had a gravimetric surface area of 3.5 m²/g. In the case of 3 nm TiO₂, the oxide coated powders were then coated with Pt aiming for 23 wt% Pt. In the case of 5 nm TiO₂, Pt was deposited with a target 18 wt%. The Pt coated 3 nm TiO₂ | CDP and 5 nm TiO₂ | CDP cathode powders were then pressed onto half cells, cells 98 and 99 respectively, with cathode loadings of 22.4 mg/cm² and 25 mg/cm² respectively.

The polarization curves and impedance spectra collected from cells 98 and 99 are shown in Figure B.11. For comparison the data from two standard Pt MOCVD cathode cells are provided. Cell 124 was the porous cathode cell analyzed in Chapter 5, fabricated with a standard thin electrolyte cell geometry. Cell 90 was fabricated using the thick pellet electrolyte implemented in cells 98 and 99. Both cells used standard Pt cathode powders with 23 wt% Pt and the cathode loadings were 17.9 mg/cm² in cell 124 and 15.7 mg/cm² in cell 90. It is apparent that the polarization curves of the two Pt | TiO₂ | CDP cathodes are significantly worse than those of the standard Pt cathodes, which are relatively similar considering the differences in experimental OCV and cathode loading.

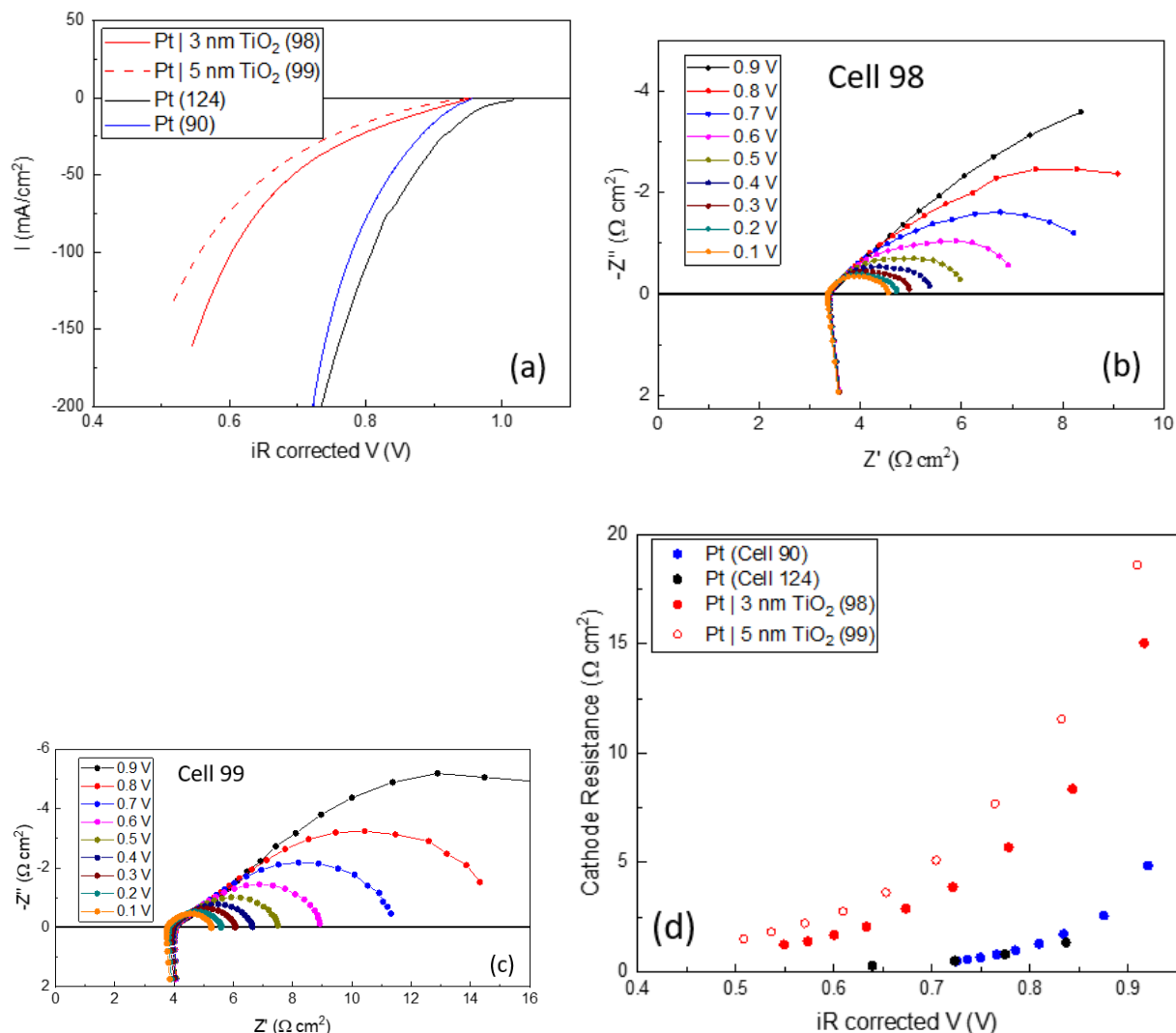


Figure B.11. (a) Polarization curves from cells 98 and 99, which featured cathodes of Pt | 3 nm TiO₂ | CDP and Pt | 5 nm TiO₂ | CDP respectively. Shown for comparison are the curves from cells with standard Pt cathodes. Cell 124 was analyzed in Chapter 5 and was fabricated as a standard SAFC with a thin electrolyte. Cell 90 was fabricated using the pellet electrolyte geometry used in cells 98 and 99. (b) and (c) Impedance spectra from cells 98 and 99 respectively.

The impedance spectra of the Pt | TiO₂ | CDP cathodes were also examined in comparison to those of the standard Pt cathodes. Although not dissimilar in shape, the spectra of the Pt | TiO₂ | CDP cathodes had significantly larger cathodic arcs. The cathodic arcs were fit

with two RQ circuits in series to extract the total cathode resistance as a function of bias. The fit resistance values were then compared to those from the standard Pt cathodes in Figure B.11d. It appears that the addition of a TiO₂ barrier layer significantly increased the cathode resistance, and that the added resistance scales with the thickness of the oxide film.

In an effort to extract physical properties of the cathode from the EIS spectra, the spectra were fit using the transmission line model (TLM) described in Appendix A. The TLM is most appropriate for spectra collected at or very near the OCV, however unfortunately for cells 98 and 99 spectra were not collected at OCV. Instead, I report the results for the two highest voltage spectra, 0.9 and 0.8 V. The cathode thicknesses in cells 98 and 99 were also not experimentally measured, but it was assumed that the thickness scaled with the cathode loading in comparison to cell 124. This assumption produced cathode thicknesses of 104 and 116 μm for cells 98 and 99 respectively, which were input into the TLM model.

	$\sigma^*_{\text{proton}} \text{ (S m)}$	$\sigma^*_{\text{electron}} \text{ (S m)}$	$r_{ct} \text{ (}\Omega \text{ m)}$
Cell 124 (OCV = 1.02 V)	0.633	2.13E13	3.5E-3
Cell 124 0.8 V	0.763	56.52	6.6E-5
Cell 98 0.9 V	0.040	1	5E-4
Cell 98 0.8 V	0.0549	3	4E-4

Cell 99 0.9 V	0.015	800	6.2E-4
Cell 99 0.8 V	0.028	600	4.4E-4

Table B.1. Transmission line model fitting results for EIS spectra from Pt | TiO₂ | CDP cathodes (cells 98 and 99) and standard Pt cathodes (cell 124).

The results of the TLM model fitting are summarized in Table B.1. The results illustrate that introducing a TiO₂ barrier layer significantly reduces the effective proton conductivity within the cathode, by an order of magnitude or more. Additionally, thicker oxide barrier layers appear to result in lower proton conductivities. The impact of the oxide film on the electronic conductivity is unclear, both because of the lack of trend in the fit $\sigma^*_{\text{electron}}$ values and the extreme fitting errors for this parameter which were often larger than the fit value itself. The model is insensitive to the conductivity values for the highly conductive electronic rail, because the behavior of the system is much more controlled by the limiting proton conductivity. For the fitting results of each spectra, the electronic conductivity is significantly higher than the protonic conductivity, and thus the important conclusion is that the regardless of the impact of the TiO₂ layer on electronic conductivity, losses due to electron transport remain minimal in comparison to those from proton transport. In comparing the charge transfer resistances, r_{ct} , it appears that the TiO₂ barrier layer may also have made the ORR rate less respondent to bias and therefore less active at lower cathode potentials.

References:

- 1 Truls Norby, M. F., Bengt Erik Mellander. Proton and deuteron conductivity in CsHSO₄ and CsDSO₄ by in situ isotropic exchange. *Solid State Ionics* **77**, 105-110 (1995).
- 2 Baranov, A. I. Crystals with Disordered Hydrogen-Bond Networks and Superprotonic Conductivity. Review. *Crystallography Reports* **48**, 1012-1037 (2003).
- 3 Yi, D., Sanghvi, S., Kowalski, C. P. & Haile, S. M. Phase Behavior and Superionic Transport Characteristics of (MxRb1-x)3H(SeO4)2 (M = K or Cs) Solid Solutions. *Chemistry of Materials* **31**, 9807-9818, doi:10.1021/acs.chemmater.9b03856 (2019).
- 4 Dane A. Boysen, S. M. H., Hongjian Liu, Richard A. Secco. Conductivity of Potassium and Rubidium Dihydrogen Phosphate at High Temperature and Pressure. *Chemistry of Materials* **16**, 693-697 (2004).
- 5 Botez, C. E. *et al.* High pressure synchrotron x-ray diffraction studies of superprotonic transitions in phosphate solid acids. *Solid State Ionics* **213**, 58-62, doi:10.1016/j.ssi.2011.08.015 (2012).
- 6 Calum R.I. Chisholm, R. B. M., Dane A. Boysen, Sossina M. Haile. Superprotonic Phase Transition in CsH(PO₃H). *Chemistry of Materials* **14**, 3889-3893 (2002).
- 7 Calum R.I. Chisholm, S. M. H. Superprotonic behavior of Cs₂(HSO₄)(H₂PO₄) - a new solid acid in the CsHSO₄-CsH₂PO₄ system. *Solid State Ionics* **136-137**, 229-241 (2000).
- 8 Uda, T. Thermodynamic, thermomechanical, and electrochemical evaluation of CsHSO₄. *Solid State Ionics* **176**, 127-133, doi:10.1016/j.ssi.2004.04.017 (2005).
- 9 Wang, L. S., Patel, S. V., Sanghvi, S. S., Hu, Y. Y. & Haile, S. M. Structure and Properties of Cs₇(H₄PO₄)(H₂PO₄)₈: A New Superprotonic Solid Acid Featuring the Unusual Polycation (H₄PO₄)⁺. *J Am Chem Soc* **142**, 19992-20001, doi:10.1021/jacs.0c08870 (2020).
- 10 Chisholm, C. R. I. *Superprotonic Phase Transitions in Solid Acids: Parameters affecting the presence and stability of superprotonic transitions in the MH_nXO₄ family of compounds (X=S, Se, P, As; M=Li, Na, K, NH₄, Rb, Cs)* Doctor of Philosophy thesis, California Institute of Technology, (2003).
- 11 Chisholm, C. R. I. & Haile, S. M. Entropy evaluation of the superprotonic phase of CsHSO₄: Pauling's ice rules adjusted for systems containing disordered hydrogen-bonded tetrahedra. *Chemistry of Materials* **19**, 270-279 (2007).
- 12 Haile, S. M., Chisholm, C. R. I., Sasaki, K., Boysen, D. A. & Uda, T. Solid acid proton conductors: from laboratory curiosities to fuel cell electrolytes. *Faraday Discussions* **134**, 17-39, doi:10.1039/b604311a (2007).
- 13 Dreßler, C., Kabbe, G. & Sebastiani, D. Proton Conductivity in Hydrogen Phosphate/Sulfates from a Coupled Molecular Dynamics/Lattice Monte Carlo (cMD/LMC) Approach. *The Journal of Physical Chemistry C* **120**, 19913-19922, doi:10.1021/acs.jpcc.6b05822 (2016).
- 14 Dreßler, C. & Sebastiani, D. Effect of anion reorientation on proton mobility in the solid acids family CsHyXO₄ (X = S, P, Se, y = 1, 2) from ab initio molecular dynamics simulations. *Phys Chem Chem Phys* **22**, 10738-10752, doi:10.1039/c9cp06473g (2020).
- 15 Hee-Seung Lee, M. E. T. The Structure and Proton Transport Mechanisms in the Superprotonic Phase of CsH₂PO₄: An Ab Initio Molecular Dynamics Study. *The Journal of Physical Chemistry C* **112**, 9917-9930 (2008).
- 16 Ayako Ikeda, S. M. H. The thermodynamics and kinetics of the dehydration of CsH₂PO₄ studied in the presence of SiO₂. *Solid State Ionics* **213**, 63-71 (2012).
- 17 Ikeda, A., Kitchaev, D. A. & Haile, S. M. Phase behavior and superprotonic conductivity in the Cs 1-xRbxH₂PO₄ and Cs 1-xKxH₂PO₄ systems. *J. Mater. Chem. A* **2**, 204-214, doi:10.1039/c3ta13889e (2014).

- 18 Ikeda, A. & Haile, S. M. Examination of the superprotonic transition and dehydration behavior of Cs_{0.75}Rb_{0.25}H₂PO₄ by thermogravimetric and differential thermal analyses. *Solid State Ionics* **181**, 193-196, doi:10.1016/j.ssi.2009.10.019 (2010).
- 19 Ponomareva, V. G., Bagryantseva, I. N. & Shutova, E. S. Effect of cation substitution in Cs_{1-2x}BaxH₂PO₄ on structural properties and proton conductivity. *Physics of the Solid State* **59**, 1387-1394, doi:10.1134/s1063783417070174 (2017).
- 20 Baranov, A., Grebenev, V., Khodan, A., Dolbinina, V. & Efremova, E. Optimization of superprotonic acid salts for fuel cell applications. *Solid State Ionics* **176**, 2871-2874, doi:10.1016/j.ssi.2005.09.018 (2005).
- 21 Wang, L. S., Patel, S. V., Truong, E., Hu, Y.-Y. & Haile, S. M. Phase Behavior and Superprotonic Conductivity in the System (1-x)CsH₂PO₄ - xH₃PO₄: Discovery of Off-Stoichiometric α -[Cs_{1-x}H_x]H₂PO₄. *Chemistry of Materials* **34**, 1809-1820, doi:10.1021/acs.chemmater.1c04061 (2022).
- 22 Matsui, T., Kukino, T., Kikuchi, R. & Eguchi, K. An Intermediate Temperature Proton-Conducting Electrolyte Based on a CsH₂PO₄ / SiP₂O₇ Composite. *Electrochemical and Solid-State Letters* **8**, A256-A258, doi:10.1149/1.1883906 (2005).
- 23 Yoshimi, S., Matsui, T., Kikuchi, R. & Eguchi, K. Temperature and humidity dependence of the electrode polarization in intermediate-temperature fuel cells employing CsH₂PO₄/SiP₂O₇-based composite electrolytes. *Journal of Power Sources* **179**, 497-503, doi:10.1016/j.jpowsour.2008.01.003 (2008).
- 24 Navarrete, L., Yoo, C. Y. & Serra, J. M. Comparative Study of Epoxy-CsH₂PO₄ Composite Electrolytes and Porous Metal Based Electrocatalysts for Solid Acid Electrochemical Cells. *Membranes (Basel)* **11**, doi:10.3390/membranes11030196 (2021).
- 25 Qing, G., Kikuchi, R., Takagaki, A., Sugawara, T. & Oyama, S. T. CsH₂PO₄/Polyvinylidene Fluoride Composite Electrolytes for Intermediate Temperature Fuel Cells. *Journal of The Electrochemical Society* **161**, F451-F457, doi:10.1149/2.052404jes (2014).
- 26 Qing, G., Kikuchi, R., Takagaki, A., Sugawara, T. & Oyama, S. T. CsH₂PO₄/Epoxy Composite Electrolytes for Intermediate Temperature Fuel Cells. *Electrochimica Acta* **169**, 219-226, doi:10.1016/j.electacta.2015.04.089 (2015).
- 27 Dane A. Boysen, C. R. I. C., Sossina M. Haile, Sekharipuram R. Narayanan. Polymer Solid Acid Composite Membranes for Fuel-Cell Applications. *Journal of The Electrochemical Society* **147**, 3610-3613 (2000).
- 28 Bagryantseva, I. N., Kungurtsev, Y. E., Dormidonova, D. O. & Ponomareva, V. G. Composite Electrolytes Based on Cesium Dihydrogen Phosphate and Fluoropolymers. *Russian Journal of Electrochemistry* **58**, 611-616, doi:10.1134/s1023193522070059 (2022).
- 29 Bagryantseva, I. N., Ponomareva, V. G. & Lazareva, N. P. Proton-conductive membranes based on CsH₂PO₄ and ultra-dispersed polytetrafluoroethylene. *Solid State Ionics* **329**, 61-66, doi:10.1016/j.ssi.2018.11.010 (2019).
- 30 Bagryantseva, I. N., Gaydamaka, A. A. & Ponomareva, V. G. Intermediate temperature proton electrolytes based on cesium dihydrogen phosphate and Butvar polymer. *Ionics* **26**, 1813-1818, doi:10.1007/s11581-020-03505-9 (2020).
- 31 Bagryantseva, I. N., Ponomareva, V. G. & Khusnutdinov, V. R. Intermediate temperature proton electrolytes based on cesium dihydrogen phosphate and poly(vinylidene fluoride-co-hexafluoropropylene). *Journal of Materials Science* **56**, 14196-14206, doi:10.1007/s10853-021-06137-0 (2021).
- 32 Bagryantseva, I. N., Kungurtsev, Y. E. & Ponomareva, V. G. Proton-conducting membranes based on CsH₂PO₄ and copolymer of tetrafluoroethylene with vinylidene fluoride. *Chimica Techno Acta* **9**, doi:10.15826/chimtech.2022.9.3.03 (2022).

- 33 Jensen, A. H., Li, Q., Christensen, E. & Bjerrum, N. J. Intermediate Temperature Fuel Cell Using CsH₂PO₄/ZrO₂-Based Composite Electrolytes. *Journal of The Electrochemical Society* **161**, F72-F76, doi:10.1149/2.063401jes (2013).
- 34 Bocchetta, P., Ferraro, R. & Di Quarto, F. Advances in anodic alumina membranes thin film fuel cell: CsH₂PO₄ pore-filler as proton conductor at room temperature. *Journal of Power Sources* **187**, 49-56, doi:10.1016/j.jpowsour.2008.10.088 (2009).
- 35 Guo, X. *et al.* Application of a composite electrolyte in a solid-acid fuel cell system: A micro-arc oxidation alumina support filled with CsH₂PO₄. *International Journal of Hydrogen Energy* **38**, 16387-16393, doi:10.1016/j.ijhydene.2013.09.127 (2013).
- 36 Ponomareva, V. & Shutova, E. High-temperature behavior of CsH₂PO₄ and CsH₂PO₄-SiO₂ composites. *Solid State Ionics* **178**, 729-734, doi:10.1016/j.ssi.2007.02.035 (2007).
- 37 Junichiro Otomo, N. M., Ching-ju Wen, Koichi Eguchi, Hiroshi Takahashi. Protonic conduction of CsH₂PO₄ and its composite with silica in dry and humid atmospheres. *Solid State Ionics* **156**, 357-369 (2003).
- 38 Ponomareva, V. G. & Shutova, E. S. Electrotransport properties of a high-temperature phase of CsH₂PO₄ and composite systems with silicon dioxide at different humidities. *Russian Journal of Electrochemistry* **43**, 513-520, doi:10.1134/s1023193507050035 (2007).
- 39 Ponomareva, V. G., Shutova, E. S. & Lavrova, G. V. Electrical conductivity and thermal stability of (1 - x)CsH₂PO₄/xSiPyOz (x = 0.2-0.7) composites. *Inorganic Materials* **44**, 1009-1014, doi:10.1134/s0020168508090185 (2008).
- 40 Ponomareva, V. G. & Shutova, E. S. Electrical conductivity and structural properties of proton electrolytes based on CsH₂PO₄ and silicophosphate matrices with low phosphorus content. *Inorganic Materials* **50**, 1056-1062, doi:10.1134/s0020168514100136 (2014).
- 41 Ponomareva, V. G. & Shutova, E. S. New medium-temperature proton electrolytes based on CsH₂PO₄ and silicophosphate matrices. *Inorganic Materials* **50**, 1050-1055, doi:10.1134/s0020168514100124 (2014).
- 42 Ponomareva, V. G. & Lavrova, G. V. New type of composite proton electrolytes based on CsH₂PO₄ synthesized by mechanical activation. *Materials Today: Proceedings* **12**, 9-12, doi:10.1016/j.matpr.2019.02.205 (2019).
- 43 Louie, M. W. C. *Electrocatalysis in Solid Acid Fuel Cells* Ph.D thesis, California Institute of Technology, (2011).
- 44 Wang, S. *et al.* Electrochemical impedance spectroscopy. *Nature Reviews Methods Primers* **1**, doi:10.1038/s43586-021-00039-w (2021).
- 45 Dane A. Boysen, T. U., Calum R.I. Chisholm, Sossina M. Haile. High-Performance Solid Acid Fuel Cells Through Humidity Stabilization. *Science* **303**, 68-70 (2004).
- 46 Uda, T. & Haile, S. M. Thin-Membrane Solid-Acid Fuel Cell. *Electrochemical and Solid-State Letters* **8**, A245-A246, doi:10.1149/1.1883874 (2005).
- 47 Uda, T., Boysen, D. A., Chisholm, C. R. I. & Haile, S. M. Alcohol Fuel Cells at Optimal Temperatures. *Electrochemical and Solid-State Letters* **9**, doi:10.1149/1.2188069 (2006).
- 48 Haile, S. M., Chisholm, C. R., Sasaki, K., Boysen, D. A. & Uda, T. Solid acid proton conductors: from laboratory curiosities to fuel cell electrolytes. *Faraday Discussions* **134**, 17-39, doi:10.1039/b604311a (2007).
- 49 Boysen, D. A. *et al.* From Laboratory Breakthrough to Technological Realization: The Development Path for Solid Acid Fuel Cells. *The Electrochemical Society Interface* **18**, 53-59, doi:10.1149/2.f06093if (2009).
- 50 Papandrew, A. B., Chisholm, C. R. I., Elgammal, R. A., Özer, M. M. & Zecevic, S. K. Advanced Electrodes for Solid Acid Fuel Cells by Platinum Deposition on CsH₂PO₄. *Chemistry of Materials* **23**, 1659-1667, doi:10.1021/cm101147y (2011).

- 51 Lim, D.-K. *et al.* Atomic layer deposition of Pt@CsH₂PO₄ for the cathodes of solid acid fuel cells. *Electrochimica Acta* **288**, 12-19, doi:10.1016/j.electacta.2018.07.076 (2018).
- 52 Baranov, A. I., Dolbinina, V. V., Lancers-Mendez, S. & Schmidt, V. H. Phase diagram and dielectric properties of mixed Cs_{1-x}(NH₄)_xH₂PO₄ crystals. *Ferroelectrics* **272**, 225-230, doi:10.1080/00150190211553 (2010).
- 53 Ponomareva, V. G. & Bagryantseva, I. N. The influence of Cs₂HPO₄·H₂O impurity on the proton conductivity and thermal properties of CsH₂PO₄. *Solid State Ionics* **329**, 90-94, doi:10.1016/j.ssi.2018.11.021 (2019).
- 54 Ponomareva, V. G. & Bagryantseva, I. N. Proton conductivity, structural and thermal properties of (1-x) CsH₂PO₄-xBa(H₂PO₄)₂. *Physics of the Solid State* **59**, 1829-1835, doi:10.1134/s1063783417090244 (2017).
- 55 Mohammad, N., Mohamad, A. B., Kadhum, A. A. H. & Loh, K. S. Effect of silica on the thermal behaviour and ionic conductivity of mixed salt solid acid composites. *Journal of Alloys and Compounds* **690**, 896-902, doi:10.1016/j.jallcom.2016.08.188 (2017).
- 56 Oh, S.-y., Kawamura, G., Muto, H. & Matsuda, A. Mechanochemical synthesis of proton conductive composites derived from cesium dihydrogen phosphate and guanine. *Solid State Ionics* **225**, 223-227, doi:10.1016/j.ssi.2012.02.058 (2012).
- 57 Ponomareva, V. G. & Lavrova, G. V. Effect of the excess protons on the electrotransport, structural and thermodynamic properties of CsH₂PO₄. *Solid State Ionics* **304**, 90-95, doi:10.1016/j.ssi.2017.03.026 (2017).
- 58 Arlman, E. J. The Basic Properties of Orthophosphoric Acid. *Recl. des Trav. Chim. des Pays-Bas* **56**, 912-922 (1937).
- 59 Mathew, M. & Wong-Ng, W. Crystal Structure of a New Monoclinic Form of Potassium Dihydrogen Phosphate Containing Orthophosphacidium Ion, (H₄PO₄)⁺1. *Journal of Solid State Chemistry* **114**, 219-223 (1995).
- 60 Minkwitz, R. & Schneider, S. Synthesis and Characterization of the Tetra-hydroxyphosphonium Hexafluorometalates P(OH)₄⁺MF₆⁻ (M = As, Sb). *Angew. Chem. Int. Ed.* **38**, 210-212 (1999).
- 61 Gillespie, R. J., Kapoor, R. & Robinson, E. A. The Sulfuric Acid Solvent System. *Adv. Inorg. Chem. Radiochem.* **1**, 385-423 (1965).
- 62 Addison, C. C. *et al.* Chemistry in fuming nitric acids—I. NMR spectroscopic study of PF₅, HPO₂F₂ and P₄O₁₀ in the solvent system 44 wt.% N₂O₄ in 100% HNO₃. *Polyhedron* **2**, 651-656 (1983).
- 63 Hibbert, R. C. & Logan, N. Multinuclear Nuclear Magnetic Resonance Study of the Interaction of Some Phosphorus(V) Compounds with Inorganic Acids. The Protonating Abilities of HNO₃, MeSO₃H, and HPO₂F₂ towards the Phosphoryl Group. *J. Chem. Soc., Dalton Trans.*, 865-866 (1985).
- 64 Sanghvi, S. S. *Superprotonic Solid Acids: Structure and Discovery* Ph.D thesis, Northwestern University, (2019).
- 65 Sheldrick, G. M. A short history of SHELX. *Acta Crystallogr A* **64**, 112-122, doi:10.1107/S0108767307043930 (2008).
- 66 Ichikawa, M. Dependence of the Distortion of the Tetrahedra in Acid Phosphate Groups H_nPO₄ (n= 1-3) on Hydrogen-Bond Length. *Acta Crystallographica Section B* **B43**, 23-28 (1987).
- 67 Kim, G., Blanc, F., Hu, Y.-Y. & Grey, C. P. Understanding the Conduction Mechanism of the Protonic Conductor CsH₂PO₄ by Solid-State NMR Spectroscopy. *The Journal of Physical Chemistry C* **117**, 6504-6515, doi:10.1021/jp312410t (2013).
- 68 Dillon, K. B. & Waddington, T. C. Behavior of Some Inorganic Phosphates in Strongly Acidic Solvents Studied by Phosphorus-31 Nuclear Magnetic Resonance Spectroscopy. *Journal of the Chemical Society A*, 1146-1150 (1970).

- 69 Boukamp, B. Electrochemical impedance spectroscopy in solid state ionics: recent advances. *Solid State Ionics* **169**, 65-73, doi:10.1016/j.ssi.2003.07.002 (2004).
- 70 Dane A. Boysen, S. M. H., Hongjian Liu, Richard A. Secco. High-Temperature Behavior of CsH₂PO₄ under Both Ambient and High Pressure Conditions. *Chemistry of Materials* **15**, 727-736 (2003).
- 71 Sato, Y., Shen, Y., Nishida, M., Kanematsu, W. & Hibino, T. Proton conduction in non-doped and acceptor-doped metal pyrophosphate (MP₂O₇) composite ceramics at intermediate temperatures. *Journal of Materials Chemistry* **22**, doi:10.1039/c2jm15335a (2012).
- 72 Merinov, B. V. Mechanism of proton transport in compounds having a dynamically disordered hydrogen bond network. *Solid State Ion.* **84**, 89-96 (1996).
- 73 Baranov, A. Crystals with disordered hydrogen-bond networks and superprotonic conductivity. Review. *Crystallography Reports* **48**, 1012-1037 (2003).
- 74 Haile, S. M., Boysen, D. A., Chisholm, C. R. I. & Merle, R. B. Solid acids as fuel cell electrolytes. *Nature* **410**, 910-913, doi:10.1038/35073536 (2001).
- 75 Boysen, D. A., Uda, T., Chisholm, C. R. I. & Haile, S. M. High-performance solid acid fuel cells through humidity stabilization. *Science* **303**, 68-70, doi:10.1126/science.1090920 (2004).
- 76 Merle, R. B., Chisholm, C. R. I., Boysen, D. A. & Haile, S. M. Instability of sulfate and selenate solid acids in fuel cell environments. *Energy Fuels* **17**, 210-215, doi:10.1021/ef0201174 (2003).
- 77 Baranov, A. I., Khiznichenko, V. P., Sandler, V. A. & Shuvalov, L. A. Frequency Dielectric-Dispersion in the Ferroelectric and Superionic Phases of CsH₂PO₄. *Ferroelectrics* **81**, 1147-1150 (1988).
- 78 Bronowska, W. & Pietraszko, A. X-ray Study of the High-Temperature Phase-Transition of CsH₂PO₄ Crystals. *Solid State Commun.* **76**, 293-298, doi:10.1016/0038-1098(90)90840-8 (1990).
- 79 Lavrova, G. V., Shutova, E. S., Ponomareva, V. G. & Dunyushkina, L. A. Proton conductivity and interphase interaction in CsH₂PO₄-SrZrO₃ composites. *Russian Journal of Electrochemistry* **49**, 718-724, doi:10.1134/s1023193513070094 (2013).
- 80 Leal, J. H. *et al.* Stability of the superprotonic conduction of (1-x)CsH₂PO₄/xSiO₂ (0 ≤ x ≤ 0.3) composites under dry and humid environments. *Materials Today Communications* **15**, 11-17, doi:10.1016/j.mtcomm.2018.02.021 (2018).
- 81 Otomo, J., Ishigooka, T., Kitano, T., Takahashi, H. & Nagamoto, H. Phase transition and proton transport characteristics in CsH₂PO₄/SiO₂ composites. *Electrochimica Acta* **53**, 8186-8195, doi:10.1016/j.electacta.2008.06.018 (2008).
- 82 Ponomareva, V. G., Bagryantseva, I. N. & Shutova, E. S. in *3rd All-Russian Conference (with International Participation) on Hot Topics of Solid State Chemistry - From New Ideas to New Materials*. SI edn 521-524 (Elsevier, 2020).
- 83 Boysen, D. A., Chisholm, C. R. I., Haile, S. M. & Narayanan, S. R. Polymer solid acid composite membranes for fuel-cell applications. *Journal of the Electrochemical Society* **147**, 3610-3613, doi:10.1149/1.1393947 (2000).
- 84 Ikeda, A., Kitchaev, D. A. & Haile, S. M. Phase behavior and superprotonic conductivity in the Cs_{1-x}Rb_xH₂PO₄ and Cs_{1-x}K_xH₂PO₄ systems. *J. Mater. Chem. A* **2**, 204-214, doi:10.1039/c3ta13889e (2014).
- 85 Ponomareva, V. G., Bagryantseva, I. N. & Shutova, E. S. Effect of Cation Substitution in Cs_{1-2x}Ba_xH₂PO₄ on Structural Properties and Proton Conductivity. *Phys. Solid State* **59**, 1387-1394, doi:10.1134/s1063783417070174 (2017).
- 86 Ponomareva, V. G. & Bagryantseva, I. N. The influence of Cs₂HPO₄ * H₂O impurity on the proton conductivity and thermal properties of CsH₂PO₄. *Solid State Ion.* **329**, 90-94, doi:10.1016/j.ssi.2018.11.021 (2019).

- 87 Singh, D. *et al.* Structural, thermal and electrical properties of composites electrolytes (1-x)CsH₂PO₄/xZrO₂ (0 ≤ x ≤ 0.4) for fuel cell with advanced electrode. *SN Appl. Sci.* **3**, 7, doi:10.1007/s42452-020-04097-9 (2021).
- 88 Wang, L. S., Patel, S. V., Sanghvi, S. S., Hu, Y. Y. & Haile, S. M. Structure and Properties of Cs₇(H₄PO₄)(H₂PO₄)₈: A New Superprotonic Solid Acid Featuring the Unusual Polycation (H₄PO₄)⁺. *J. Am. Chem. Soc.* **142**, 19992-20001, doi:10.1021/jacs.0c08870 (2020).
- 89 Kim, G., Blanc, F., Hu, Y. Y. & Grey, C. P. Understanding the Conduction Mechanism of the Protonic Conductor CsH₂PO₄ by Solid-State NMR Spectroscopy. *J. Phys. Chem. C* **117**, 6504-6515, doi:10.1021/jp312410t (2013).
- 90 Louie, M. W., Kislitsyn, M., Bhattacharya, K. & Haile, S. M. Phase transformation and hysteresis behavior in Cs_{1-x}Rb_xH₂PO₄. *Solid State Ion.* **181**, 173-179, doi:10.1016/j.ssi.2008.11.014 (2010).
- 91 Ikeda, A. & Haile, S. M. The thermodynamics and kinetics of the dehydration of CsH₂PO₄ studied in the presence of SiO₂. *Solid State Ion.* **213**, 63-71, doi:10.1016/j.ssi.2011.09.018 (2012).
- 92 Yamane, Y., Yamada, K. & Inoue, K. Superprotonic solid solutions between CsHSO₄ and CsH₂PO₄. *Solid State Ion.* **179**, 483-488, doi:10.1016/j.ssi.2008.03.031 (2008).
- 93 Matsunaga, H., Itoh, K. & Nakamura, E. X-ray Structural Study of Ferroelectric Cesium Dihydrogen Phosphate at Room Temperature. *J. Phys. Soc. Jpn.* **48**, 2011-2014, doi:10.1143/jpsj.48.2011 (1980).
- 94 Efremov, V. A., Trunov, V. K., Matschek, I., Gudinitza, E. N. & Fakeev, A. A. Non-Equivalence of H-Atoms in CsH₅(PO₄)₂ Crystals. *Zhurnal Neorg. Khimii* **26**, 3213-3216 (1981).
- 95 Yamada, K., Sagara, T., Yamane, Y., Ohki, H. & Okuda, T. Superprotonic conductor CsH₂PO₄ studied by H-1, P-31 NMR and X-ray diffraction. *Solid State Ion.* **175**, 557-562, doi:10.1016/j.ssi.2004.03.042 (2004).
- 96 O'Hayre, R., Cha, S.-W., Colella, W. & Prinz, F. B. *Fuel Cell Fundamentals*. 3 edn, (John Wiley & Sons, Inc., 2016).
- 97 Vilekar, S. A. & Datta, R. The effect of hydrogen crossover on open-circuit voltage in polymer electrolyte membrane fuel cells. *Journal of Power Sources* **195**, 2241-2247, doi:10.1016/j.jpowsour.2009.10.023 (2010).
- 98 Zhao, Z. *et al.* Graphene-nanopocket-encaged PtCo nanocatalysts for highly durable fuel cell operation under demanding ultralow-Pt-loading conditions. *Nat Nanotechnol.* doi:10.1038/s41565-022-01170-9 (2022).
- 99 Papandrew, A. B., Chisholm, C. R. I., Zecevic, S. K., Veith, G. M. & Zawodzinski, T. A. Activity and Evolution of Vapor Deposited Pt-Pd Oxygen Reduction Catalysts for Solid Acid Fuel Cells. *Journal of The Electrochemical Society* **160**, F175-F182, doi:10.1149/2.002303jes (2012).
- 100 Naumov, O., Naumov, S., Flyunt, R., Abel, B. & Varga, A. Fast Degradation for High Activity: Oxygen- and Nitrogen-Functionalised Carbon Nanotubes in Solid-Acid Fuel-Cell Electrodes. *ChemSusChem* **9**, 3298-3306, doi:10.1002/cssc.201601056 (2016).
- 101 Sasaki, K. A. *Electrochemical Characterization of Solid Acid Fuel Cell Electrodes* Ph.D. thesis, California Institute of Technology, (2010).
- 102 Xiong, L. & Manthiram, A. High performance membrane-electrode assemblies with ultra-low Pt loading for proton exchange membrane fuel cells. *Electrochimica Acta* **50**, 3200-3204, doi:10.1016/j.electacta.2004.11.049 (2005).
- 103 Orozco, D. C., Dyck, O., Papandrew, A. B. & Zawodzinski, T. A. A parametric study of the solid acid fuel cell cathode. *Journal of Power Sources* **408**, 7-16, doi:10.1016/j.jpowsour.2018.03.030 (2018).
- 104 Chisholm, C. R. I. *et al.* From Laboratory Breakthrough to Technological Realization: The Development Path for Solid Acid Fuel Cells. *The Electrochemical Society Interface* **18**, 53 (2009).

- 105 Papandrew, A. B. *et al.* Vapor-Deposited Pt and Pd-Pt Catalysts for Solid Acid Fuel Cells: Short Range Structure and Interactions with the CsH₂PO₄ Electrolyte. *Journal of The Electrochemical Society* **163**, F464-F469, doi:10.1149/2.0371606jes (2016).
- 106 Koenigsmann, C. *et al.* Enhanced electrocatalytic performance of processed, ultrathin, supported Pd-Pt core-shell nanowire catalysts for the oxygen reduction reaction. *J Am Chem Soc* **133**, 9783-9795, doi:10.1021/ja111130t (2011).
- 107 Minhua Shao, P. L., Junliang Zhang, Radoslav Adzic. Origin of Enhanced Activity in Palladium Alloy Electrocatalysts for Oxygen Reduction Reaction. *Journal of Physical Chemistry B* **111**, 6772-6775 (2007).
- 108 Paik, H., Berenov, A. V., Skinner, S. J. & Haile, S. M. Hydrogen oxidation kinetics on platinum-palladium bimetallic thin films for solid acid fuel cells. *APL Materials* **7**, doi:10.1063/1.5050093 (2019).
- 109 Tennyson, W. D. *et al.* Bottom up synthesis of boron-doped graphene for stable intermediate temperature fuel cell electrodes. *Carbon* **123**, 605-615, doi:10.1016/j.carbon.2017.08.002 (2017).
- 110 Wagner, M., Lorenz, O., Lohmann-Richters, F. P., Varga, A. & Abel, B. On the role of local heating in cathode degradation during the oxygen reduction reaction in solid acid fuel cells. *Sustainable Energy & Fuels* **4**, 5284-5293, doi:10.1039/d0se00842g (2020).
- 111 Wagner, M., Lorenz, O., Lohmann-Richters, F. P., Varga, Á. & Abel, B. Study on solid electrolyte catalyst poisoning in solid acid fuel cells. *Journal of Materials Chemistry A* **9**, 11347-11358, doi:10.1039/d1ta01002f (2021).
- 112 Thoi, V. S., Usiskin, R. E. & Haile, S. M. Platinum-decorated carbon nanotubes for hydrogen oxidation and proton reduction in solid acid electrochemical cells. *Chem Sci* **6**, 1570-1577, doi:10.1039/c4sc03003f (2015).
- 113 Lohmann, F. P. *et al.* The next generation solid acid fuel cell electrodes: stable, high performance with minimized catalyst loading. *Journal of Materials Chemistry A* **5**, 15021-15025, doi:10.1039/c7ta03690f (2017).
- 114 Varga, A. *et al.* Carbon nanotubes as electronic interconnects in solid acid fuel cell electrodes. *Phys Chem Chem Phys* **15**, 15470-15476, doi:10.1039/c3cp52586d (2013).
- 115 Varga, Á., Brunelli, N. A., Louie, M. W., Giapis, K. P. & Haile, S. M. Composite nanostructured solid-acid fuel-cell electrodes via electrospray deposition. *Journal of Materials Chemistry* **20**, doi:10.1039/c0jm00216j (2010).
- 116 Suryaprakash, R. C., Lohmann, F. P., Wagner, M., Abel, B. & Varga, A. Spray drying as a novel and scalable fabrication method for nanostructured CsH₂PO₄, Pt-thin-film composite electrodes for solid acid fuel cells. *RSC Adv.* **4**, 60429-60436, doi:10.1039/c4ra10259b (2014).
- 117 Louie, M. W. & Haile, S. M. Platinum thin film anodes for solid acid fuel cells. *Energy & Environmental Science* **4**, doi:10.1039/c1ee01889b (2011).
- 118 Rajalakshmi, N., Jayanth, T. T. & Dhathathreyan, K. S. Effect of Carbon Dioxide and Ammonia on Polymer Electrolyte Membrane Fuel Cell Stack Performance. *Fuel Cells* **3**, 177-180, doi:10.1002/fuce.200330107 (2003).
- 119 Halseid, R., Vie, P. J. S. & Tunold, R. Effect of ammonia on the performance of polymer electrolyte membrane fuel cells. *Journal of Power Sources* **154**, 343-350, doi:10.1016/j.jpowsour.2005.10.011 (2006).
- 120 Lim, D.-K. *et al.* Solid Acid Electrochemical Cell for the Production of Hydrogen from Ammonia. *Joule* **4**, 2338-2347, doi:10.1016/j.joule.2020.10.006 (2020).
- 121 Tian, X., Lu, X. F., Xia, B. Y. & Lou, X. W. Advanced Electrocatalysts for the Oxygen Reduction Reaction in Energy Conversion Technologies. *Joule* **4**, 45-68, doi:10.1016/j.joule.2019.12.014 (2020).

- 122 Danilovic, N. *et al.* Activity-Stability Trends for the Oxygen Evolution Reaction on Monometallic Oxides in Acidic Environments. *J Phys Chem Lett* **5**, 2474-2478, doi:10.1021/jz501061n (2014).
- 123 Qiao, J., Liu, Y., Hong, F. & Zhang, J. A review of catalysts for the electroreduction of carbon dioxide to produce low-carbon fuels. *Chem Soc Rev* **43**, 631-675, doi:10.1039/c3cs60323g (2014).
- 124 Liu, M. *et al.* Enhanced electrocatalytic CO₂ reduction via field-induced reagent concentration. *Nature* **537**, 382-386, doi:10.1038/nature19060 (2016).
- 125 Lamaison, S. & Wakerley, D. Don't cross the streams. *Nature Catalysis* **5**, 242-243, doi:10.1038/s41929-022-00774-7 (2022).
- 126 Christensen, E., Petrushina, I. M., Nikiforov, A. V., Berg, R. W. & Bjerrum, N. J. CsH₂PO₄ as Electrolyte for the Formation of CH₄ by Electrochemical Reduction of CO₂. *Journal of The Electrochemical Society* **167**, doi:10.1149/1945-7111/ab75fa (2020).
- 127 Andersen, S. Z. *et al.* A rigorous electrochemical ammonia synthesis protocol with quantitative isotope measurements. *Nature* **570**, 504-508, doi:10.1038/s41586-019-1260-x (2019).
- 128 Elgrishi, N. *et al.* A Practical Beginner's Guide to Cyclic Voltammetry. *Journal of Chemical Education* **95**, 197-206, doi:10.1021/acs.jchemed.7b00361 (2017).
- 129 Lasia, A. Modeling of hydrogen upd isotherms. *Journal of Electroanalytical Chemistry* **562**, 23-31, doi:10.1016/j.jelechem.2003.07.033 (2004).
- 130 Gasteiger, H. A., Kocha, S. S., Sompalli, B. & Wagner, F. T. Activity benchmarks and requirements for Pt, Pt-alloy, and non-Pt oxygen reduction catalysts for PEMFCs. *Applied Catalysis B: Environmental* **56**, 9-35, doi:10.1016/j.apcatb.2004.06.021 (2005).
- 131 Chaparro, A. M., Martín, A. J., Folgado, M. A., Gallardo, B. & Daza, L. Comparative analysis of the electroactive area of Pt/C PEMFC electrodes in liquid and solid polymer contact by underpotential hydrogen adsorption/desorption. *International Journal of Hydrogen Energy* **34**, 4838-4846, doi:10.1016/j.ijhydene.2009.03.053 (2009).
- 132 Jomori, S., Nonoyama, N. & Yoshida, T. Analysis and modeling of PEMFC degradation: Effect on oxygen transport. *Journal of Power Sources* **215**, 18-27, doi:10.1016/j.jpowsour.2012.04.069 (2012).
- 133 Lohmann-Richters, F. P., Abel, B. & Varga, Á. In situ determination of the electrochemically active platinum surface area: key to improvement of solid acid fuel cells. *Journal of Materials Chemistry A* **6**, 2700-2707, doi:10.1039/c7ta10110d (2018).
- 134 Heinzmann, M., Weber, A. & Ivers-Tiffée, E. Impedance modelling of porous electrode structures in polymer electrolyte membrane fuel cells. *Journal of Power Sources* **444**, doi:10.1016/j.jpowsour.2019.227279 (2019).
- 135 Bisquert, J. Influence of the boundaries in the impedance of porous film electrodes. *Physical Chemistry Chemical Physics* **2**, 4185-4192, doi:10.1039/b001708f (2000).
- 136 Siroma, Z. *et al.* Mathematical solutions of comprehensive variations of a transmission-line model of the theoretical impedance of porous electrodes. *Electrochimica Acta* **160**, 313-322, doi:10.1016/j.electacta.2015.02.065 (2015).
- 137 Springer, T. E., Zawodzinski, T. A. & Gottesfeld, S. Polymer Electrolyte Fuel Cell Model. *Journal of The Electrochemical Society* **138**, 2334-2341 (1991).
- 138 Springer, T. E., Wilson, M. S. & Gottesfeld, S. Modeling and Experimental Diagnostics in Polymer Electrolyte Fuel Cells. *Journal of The Electrochemical Society* **140**, 3513-3526 (1993).
- 139 Zhu, H. & Kee, R. J. A general mathematical model for analyzing the performance of fuel-cell membrane-electrode assemblies. *Journal of Power Sources* **117**, 61-74, doi:10.1016/s0378-7753(03)00358-6 (2003).

- 140 Zhu, H. & Kee, R. J. Modeling Distributed Charge-Transfer Processes in SOFC Membrane Electrode Assemblies. *Journal of The Electrochemical Society* **155**, B715-B729, doi:10.1149/1.2913152 ✕ (2008).
- 141 Harvey, D., Pharoah, J. G. & Karan, K. A comparison of different approaches to modelling the PEMFC catalyst layer. *Journal of Power Sources* **179**, 209-219, doi:10.1016/j.jpowsour.2007.12.077 (2008).
- 142 Welty, J. R., Wicks, C. E., Willson, R. E. & Rorrer, G. L. *Fundamentals of Momentum, Heat, and Mass Transfer*. 5 edn, (John Wiley & Sons, Inc, 2008).
- 143 Miccoli, I., Edler, F., Pfnur, H. & Tegenkamp, C. The 100th anniversary of the four-point probe technique: the role of probe geometries in isotropic and anisotropic systems. *J Phys Condens Matter* **27**, 223201, doi:10.1088/0953-8984/27/22/223201 (2015).
- 144 Tobochnik, J., Laing, D. & Wilson, G. Random-walk calculation of conductivity in continuum percolation. *Phys Rev A* **41**, 3052-3058, doi:10.1103/physreva.41.3052 (1990).
- 145 Cussler, E. L. *Diffusion: Mass Transfer in Fluid Systems*. 3 edn, (Cambridge University Press, 2009).
- 146 Neyerlin, K. C., Gu, W., Jorne, J. & Gasteiger, H. A. Determination of Catalyst Unique Parameters for the Oxygen Reduction Reaction in a PEMFC. *Journal of The Electrochemical Society* **153**, A1955-A1963, doi:10.1149/1.2266294 ✕ (2006).
- 147 Xu, H., Song, Y., Kunz, H. R. & Fenton, J. M. Effect of Elevated Temperature and Reduced Relative Humidity on ORR Kinetics for PEMF Fuel Cells. *Journal of The Electrochemical Society* **152**, A1828-A1836, doi:10.1149/1.1984351 ✕ (2005).
- 148 Guidelli, R. *et al.* Defining the transfer coefficient in electrochemistry: An assessment (IUPAC Technical Report). *Pure and Applied Chemistry* **86**, 245-258, doi:10.1515/pac-2014-5026 (2014).